THE UNIVERSITY
of EDINBURGH

Automatic Classification and 3D Visualisation of Abdominal Aortic Aneurysms to Predict Aneurysm Expansion

Yolanda Georgia S. Koutraki

Thesis presented for the degree of Doctor of Philosophy

University of Edinburgh

2018

Automatic Classification and 3D Visualisation of AAAs to Predict Aneurysm Expansion

Declaration

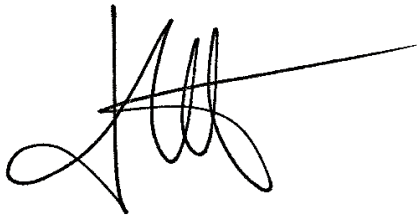I declare that this thesis has been composed by me and the work presented in it is my own except where otherwise stated.

This work has not been submitted for any other degree or professional qualification.

The publications/research output included in the Appendix are my own work.

Yolanda Georgia S. Koutraki

Automatic Classification and 3D Visualisation of AAAs to Predict Aneurysm Expansion

Contents

Acknowledgements

First and foremost, I would like to express my deepest gratitude to my supervisor Dr Scott Semple, for his constant support and valuable guidance throughout this PhD journey. I could not have asked for a better supervisor. His inexhaustible patience and encouragement until the very last hours before this thesis submission have been remarkable. Under his supervision, I was given the freedom to follow my scientific curiosity and develop my own hypotheses and get involved in very interesting scientific discussions.

I am deeply grateful to my second supervisor Dr Tom MacGillivray, for his immense support, guidance and motivation throughout my PhD. His deep knowledge of Medical Image Processing and his valuable insights have been of great benefit to this work.

I would like to express my gratitude to Prof Dave Newby for his encouragement and for always finding time through his hectic schedule to offer his valuable insights and to review chapters of this thesis.

I would like to thank the MA³RS study investigators, this great team I worked with throughout my studies. Special mention to Dr Rachael Forsythe, for always being available to offer help, insights, a second opinion and brainstorming over the massive data we were dealing with. A big thank you also to Dr Olivia McBride and special thanks to Dr Jenny Richards, who, even though not in CRIC anymore, was always very keen to offer advice and support.

Special thanks to Dr Calum Gray for sharing his immense knowledge and always offering the most helpful suggestions for the most complicated image processing problems. Most importantly though, I'd like to thank him for always managing to cheer me up, even when work felt overwhelming.

I would like to thank all the great people in CRIC and the CVS, who made this PhD a more positive and enjoyable experience and a special thanks to the ever-

In memory of my Grandfather, Miltiadis K. Koutrakis

Abstract

Abdominal aortic aneurysms (AAA) are a major cause of death in men above the age of 65 in the western world. Currently decisions for AAA management are based on the size of maximum AAA diameter (>5.5cm), measured using ultrasound imaging. However, as a proportion of AAAs rupture whilst still below this diameter threshold, while larger AAAs may never rupture, better methods for AAA expansion and rupture prediction are required. Previous research suggested that the presence of "hotspots" (focal areas) of inflammation as detected with USPIO-enhanced MRI may have potential in identifying faster-growing AAAs. However, the identification of these USPIO "hotspots" had been up to this point restricted to manual processing of the MRI data in a time-consuming and laborious slice-by-slice method, which only used 2D information. Inter- and intra- observer variability were an issue, as well as the use of empirically-defined signal thresholds which were dependent on each acquisition protocol.

The work presented in this thesis aimed to evaluate current methodologies for AAA assessment and growth prediction and to contribute to improved prediction models by introducing novel techniques. Ultrasound was found to undermeasure AAA size and the use of maximum AAA diameter was found to be problematic, especially for growth calculations. Automatically calculated alternatives which account for the total size and shape of the AAA, as measured with MRI, were introduced for more reproducible measurements. Furthermore, automation and standardisation of the previously-employed manual methods for hotspot detection and AAA classification were achieved, with the development of an efficient algorithm with excellent agreement levels. Taken a step further, two improved algorithms were introduced, adaptive to the data and USPIO distribution of individual AAAs and eliminating the universal threshold previously used. These algorithms incorporated information on 3D USPIO distribution along the length of the AAAs to detect and visualise 3D hotspots of inflammation for the first time. Novel 2D and 3D metrics were introduced, while the algorithms were also incorporated into a GUI for ease of clinical use.

Additional aneurysm metrics automatically derived by the algorithms were incorporated into multiple linear regression models to investigate prediction of AAA growth rate. This investigation introduced three significant predictors which have not been used in previous predictive models of AAA expansion: the "mean thrombus major axis" metric, which reflected baseline size of AAA throughout multiple axial slices of the AAA; the "eccentricity WT" metric which reflected the relationship between wall shape and thrombus; and the presence of "3D hotspots" which may potentially reflect transported USPIO within a network of vascular channels along the length of the aneurysm. In line with previous literature, family history of AAA and high diastolic BP were also found to be significant predictors, but larger cohorts are needed for more reliable assessment of the predictive models suggested in this thesis.

Lay Summary

An Abdominal Aortic Aneurysm (AAA) is an enlargement of the aorta, the largest blood vessel of the body, in the abdominal area. Currently, only large AAAs (wider than 5.5cm) are immediately considered for surgery. However, sometimes smaller aneurysms will rupture, so better methods for prediction of growth and rupture are required. Using Magnetic Resonance Imaging (MRI) and a contrast agent made of iron particles, it was previously shown that inflammation in AAAs could be visualised, and that AAAs which had areas of concentrated inflammation ("hotspots") on their wall grew faster. This analysis of the data was done in a laborious and time-consuming way by experienced clinicians, slice-by-slice throughout the length of the aneurysm, in which the images also had to be filtered for the clinicians to be able to easily detect the inflammation and classify the patients in groups to allow AAA growth predictions. Additionally, there is some level of variability in the way different clinicians would process the data, as they had to rely on relatively subjective visual observations to make decisions.

In this thesis, I created a series of computer software programs that perform all the of the analysis explained above in an automatic way. My software detects the "inflammatory hotspots", and then classifies the patients into groups automatically. The software also includes automatically calculated measurements of the shape of the AAAs and checks the patterns of inflammation along the length of the aneurysm, rather than slice-by-slice as before, to try to help to predict growth of AAAs more accurately. The images do not need to get filtered for my software, so it uses all of the available information about inflammation, while the program is much faster than the manual processing. Since no visual observations or manual processing are needed with this software, the results are objective and always identical, regardless of how many times they are performed or with different operators using the software. I also identified some variables that show some potential in helping to predict the AAA growth rate: a novel way of measuring the size of AAAs, the novel way of measuring the relative shape of its different parts (the aortic wall and thrombus/aneurysm

itself) and whether the aneurysm might have a network of tiny vessels that allows blood to go through the AAA thrombus and reach the wall. High blood pressure and a family history of AAAs were also found to predict AAA expansion rate, but larger numbers of patients are needed to provide adequately reliable prediction using these measurements.

My software may provide clinicians with a more robust and faster tool to assist with the assessment of future AAA patients. The techniques used in this software can also be adapted in the future to contribute in the imaging of inflammation in different parts of the body in other clinical applications.

Abbreviations

2D	2-Dimensional
3D	3-Dimensional
ΔT_2*	Change in T_2*
%ΔT_2*	Percent Change in T_2*
AAA	Abdominal aortic aneurysm
ANOVA	Analysis of Variance
AP	Antero-Posterior
CRIC	Clinical Research Imaging Centre (in Edinburgh)
CT	Computed Tomography
CV	Coefficient of Variation
CVD	Cardiovascular Disease
Diam	Diameter
EVAR	Endovascular Aneurysm Repair
FEA	Finite Element
FEA	Finite Element Analysis
FEM	Finite Element Method
FID	Free Induction Decay (signal)
FDA	Food and Drug Administration (United States of America)

FN   False Negative

FP   False Positive

GUI   Graphical User Interface

HASTE   Half-Fourier Acquisition Single-shot Turbo spin-Echo

HSC   Health and Social Care in Northern Ireland

ILT   Intraluminal Thrombus

MA³RS   MRI for Abdominal Aortic Aneurysms to predict Rupture or Surgery

MASS   Multicentre Aneurysm Screening Study

Max   Maximum

maxAP   Maximum Antero-Posterior (diameter)

Min   Minimum

MLR   Multiple Linear Regression

MPIO   Micron-sized Particles of Iron Oxide

MRI   Magnetic Resonance Imaging

MRS   Magnetic Resonance Spectroscopy

NMV   Net Magnetisation Vector

NHS   National Health Service (of the United Kingdom)

NRI   Net Reclassification Index

PET   Positron emission tomography

PET-CT	Positron emission tomography –computed tomography
R^2	Coefficient of determination
RF	Radio Frequency
RIE	Royal Infirmary of Edinburgh
ROI	Region of interest
SEM	Standard Error of the Mean
SD	Standard Deviation
SI	Signal intensity
SPECT	Single photon emission computed tomography
SPIO	Superparamagnetic Particles of Iron Oxide
SPSS	Statistical Package for the Social Sciences
SSE	Sum of squared deviations due to error
SVS	Society for Vascular Surgery
T	Tesla
T_2W	T_2-weighted
T_2*W	T_2*-weighted
TE	Echo time
TN	True Negative
TP	True Positive
UK	United Kingdom

UKSAT   United Kingdom Small Aneurysm Trial

US   Ultrasound

USA   United States of America

US   Ultrasound

USPIO   Ultrasmall Superparamagnetic Particles of Iron Oxide

VSPIO   Very Small Superparamagnetic Particles of Iron Oxide

Chapter 1   Introduction

1.1 Definition of the Problem and Study Objectives

Despite a considerable decrease in the number of deaths caused by cardiovascular disease (CVD) in recent years, CVD remains the leading cause of death globally, claiming 17.5 million lives in 2012 [1]. According to the most recently published European cardiovascular disease statistics, CVD causes over 4 million deaths in Europe, reaching the significant percentage of 47% of total deaths [2].

Early diagnosis of CVD is undoubtedly advantageous but, in some cases, it is considered crucial in order to save lives. Abdominal Aortic Aneurysms (AAAs) are such a case. Aneurysm, from the Greek 'ανεύρυσμα', meaning widening, is a permanent and irreversible localised dilatation of a vessel to more than 1.5 times its normal diameter. Abdominal aortic aneurysms are found in the aorta, the largest artery in the human body, usually distal to the renal arteries, although they may extend up past the point of renal arteries [3], as depicted in the schematic in Figure 1.1. and in the gross anatomy image of a large unruptured AAA extending to the aortic bifurcation in Figure 1.2. The process of aneurysm progression is expansion, leading to possible eventual rupture [4].

AAA deaths pose a considerable burden in the western world, being responsible for 1- 3% of deaths of men between the age of 65 and 80 [5]. Given that the mortality rates for ruptured AAAs reach 80%-90% [6], early diagnosis and successful management are necessary. However, elective surgery (open surgical treatment or endovascular repair) has considerable risks, with 30-day post-intervention mortality reaching 27.1% , so the expected risk of rupture has to be weighed against the risk of procedural complications [7]–[10].
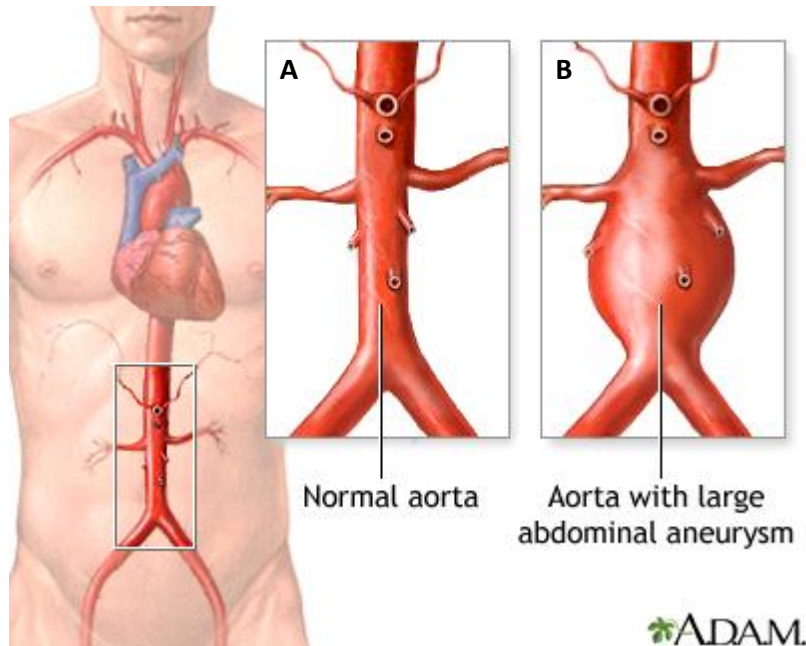
Figure 1.1: An Abdominal Aortic Aneurysm (AAA): Normal aorta (A), as opposed to aorta with large AAA (B) [11]*.*

AAAs are most often asymptomatic until rupture and are therefore identified either by chance, or via national screening programs [12]. After detection, decisions for the management of asymptomatic AAAs are based on their size, which is calculated by measuring the maximum anterior-to-posterior (AP) diameter with ultrasound: only AAAs with diameters larger than 5.5 cm, or with annual growth of more than 1.0 cm are considered for surgical intervention. However, this criterion is insufficient, as 60% of AAAs with max AP diameters surpassing the 5.5 cm threshold will never rupture [13], while 10-20% of AAAs with max AP diameters under the 5.5 cm threshold will still rupture [3], [14]. There are currently no alternative methods used to better predict the progress of AAAs, so novel approaches are urgently required.

Previous research into AAA growth and rupture [15] suggested that the presence of localised inflammation on the aortic wall of AAAs, also known as "hotspots", may allow to distinguish faster growing AAAs from less active ones. For the visualisation of inflammation, Magnetic Resonance Imaging (MRI) enhanced with Ultrasmall Superparamagnetic Particles of Iron Oxide (USPIO) was used. From

the scans acquired, USPIO-uptake maps corresponding to inflammation were created for each slice of the AAA.
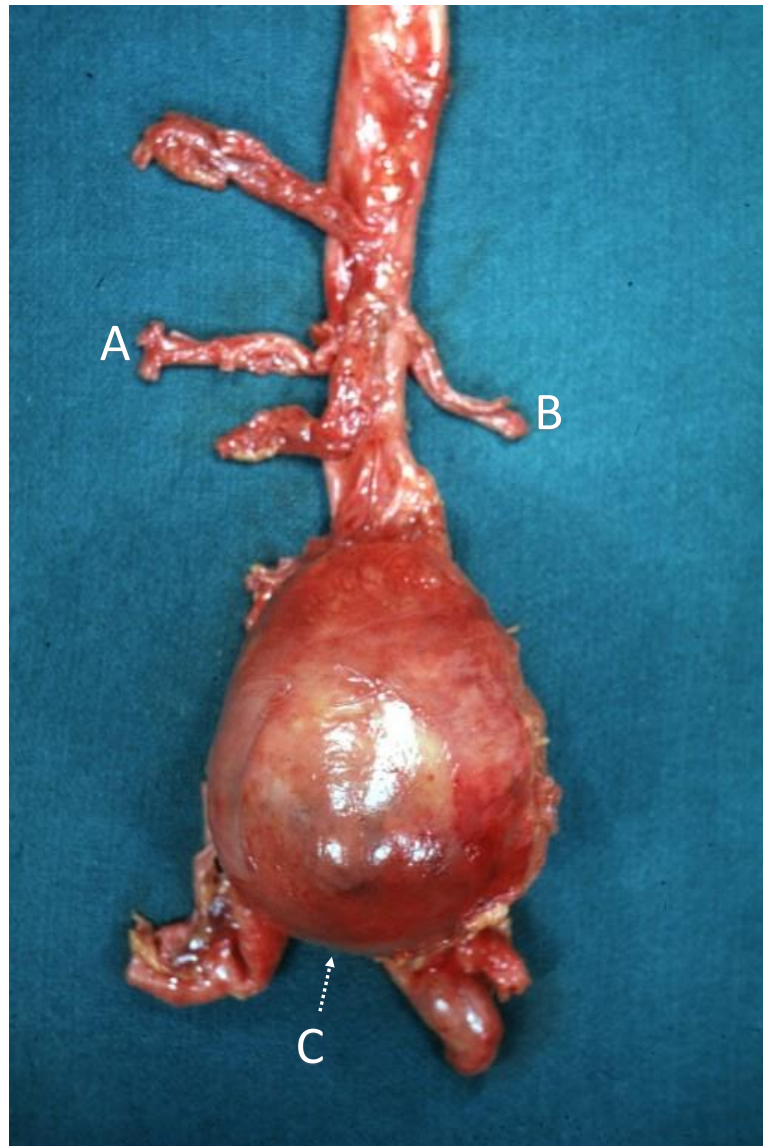
Figure 1.2: Unruptured and unopened, large typical AAA (gross, natural colour). *The AAA extends from below the renal arteries(A), (B) to the aortic bifurcation(C) (Image source: PEIR Digital Library 2017).*

For the identification of the hotspots, an empirically-determined threshold was applied to the inflammation maps and clinicians manually processed each individual slice. This threshold was specific to the scanning protocol of the study, thus not applicable to differently acquired datasets and, hence hindering

reproducibility. Furthermore, the threshold approach possibly excluded important information about USPIO distribution throughout the aneurysm.

This manual processing methodology was time-consuming and laborious, while introducing inter- and intra-observer variability to hotspot detection and AAA classification. Importantly, being restricted to manual analysis, clinicians were not able to utilise the full extent of data produced by the MRI scanning: they only used 2D images without taking 3D information of the entire AAA mass into consideration, and they could not efficiently calculate any reproducible anatomical or functional metrics which could potentially assist with further AAA stratification.

The objective of the work presented in this thesis was to evaluate current methodologies for AAA assessment and growth prediction and to contribute to improved prediction models by introducing novel automated techniques.

More specifically, this thesis aimed to:

- Investigate the accuracy and reproducibility of currently used AAA size and growth measurement methods and suggest better alternatives.
- Automate the current hotspot identification and classification method for greater efficiency and reproducibility.
- Replace the threshold technique used by clinicians in manual processing with less restrictive alternative.
- Introduce algorithm which makes use of 3D data for hotspot assessment and visualisation.
- Identify alternative variables extracted from the data, which can further describe AAAs and assist in their classification.
- Introduce new growth prediction models.

1.2 Thesis Outline

In **Chapter 2**, the necessary background and context within which this PhD research lies is provided. A literature review on AAA disease is presented, describing the anatomy, underlying pathophysiology, epidemiology, demographics, aetiology, and risks associated with AAAs. The currently standard protocols for assessment and management are introduced, along with a summary of the alternative methods suggested in the literature. An overview of anatomical imaging methods for AAAs is provided, with a special focus on MRI and its use for inflammation tracking with USPIO.

The pilot study, which first introduced the hotspots of inflammation as a potential AAA growth predictor and upon which the MA³RS trial expanded, is described. As the research described in this thesis was conducted mainly under the MA³RS study umbrella, with use of its data and techniques, an extensive description of the MA³RS protocols and methods is also presented.

In **Chapter 3**, some basic image processing background is presented, mainly aimed at readers with clinical training. The main concepts behind clustering generally, and k-means clustering specifically are introduced, as they are required for a better understanding of the methods applied in Chapter 5.

The results of this thesis are presented in the three following chapters. Each of these chapters is structured in a stand-alone format, containing the necessary context and background information, the individual materials and methods, the findings, discussion and conclusion.

More specifically, in **Chapter 4**, the currently practised methods for AAA size and growth measurement are described and critically evaluated, with a special focus on the accuracy and reproducibility of maximum AP diameter. The agreement levels between ultrasound, CT and MRI data are explored with the use of MA³RS subsets. Adjustments to the current threshold of 5.5cm are investigated, and

alternatives to the use of max AP diameter with ultrasound are introduced. These alternative metrics will consequently be used in the following chapters.

Chapter 5 focuses on the process towards building the main algorithms created in this work and on their validation on MA³RS and pilot study subsets. An algorithm for the accurate replication of the manual processing is described and evaluated, followed by two more advanced algorithms. These two algorithms take the AAA classification a step further, by eliminating the previously used threshold, incorporating 2D and 3D data, offering options for visualisation and introducing novel 2D and 3D metrics for AAA stratification.

In **Chapter 6**, building upon the work presented in the previous chapters, the prediction of AAA growth rate is investigated. The findings from Chapter 4 on improved measurement techniques are used to calculate AAA expansion rates and use them as output for prediction models. The 2D and 3D classifications produced with the algorithms described in Chapter 5 are used to assess the influence of inflammation on AAA growth rate. Furthermore, several metrics derived from these algorithms are evaluated as potential AAA growth rate predictors. Finally, a multiple linear regression model is introduced as a starting point upon which further investigation with larger sample sizes may be undertaken in the future.

In **Chapter 7** the conclusions derived from this thesis are presented, and potential paths for further investigation are described.

In **Appendix 1**, research outcomes derived from the work presented in this thesis are presented.

Finally, in **Appendix 2**, detailed tables of the Multiple Linear Regression models described in Chapter 6 are presented.

Chapter 2   Background

In this chapter, the context within which this research lies is presented. An overview of the pathophysiological background, the demographics and the risks associated with Abdominal Aortic Aneurysms (AAAs) are introduced. The current commonly used assessment and management protocols and methodologies for this condition are described, including a synopsis of alternative methods and hypotheses described in the literature.

The necessary background information on Magnetic Resonance Imaging is presented, as well as the way in which it is combined with the application of contrast agents to image cellular inflammation in cardiovascular applications, with a particular focus on AAAs.

A brief description of the pilot study (previously conducted by members of the MA³RS research team) that introduced inflammatory patterns as a potential predictor of AAA expansion and rupture follows, upon which the MRI for Abdominal Aortic Aneurysms to predict Rupture or Surgery (MA³RS) trial later expanded. The protocols and methods implemented in MA³RS and the necessary technical background are also introduced and discussed in relation to the work presented in this thesis.

The work presented in this thesis mainly used data acquired within the MA³RS trial to further develop and automate the techniques employed in these research trials and offer alternative approaches for AAA classification and growth prediction.

2.1   Abdominal Aortic Aneurysms: Background

2.1.1 Anatomy of an AAA

2.1.1.1 Normal Aorta

The typical size of a healthy aorta is between 2.0 cm and 3.0 cm. A wall thickness of less than 4mm is considered normal [17]. The healthy aorta consists of the aortic wall and the aortic lumen. The aortic **lumen** is the tubular cavity of the aorta, which is the normal passageway of blood, as shown in Figure 2.1.
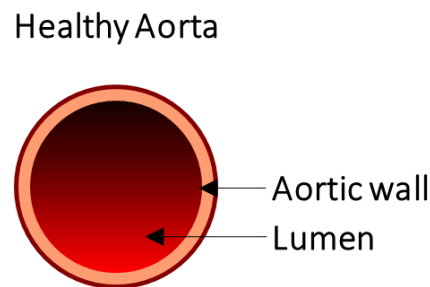
Figure 2.1: Schematic of cross section of healthy aorta. Its size ranges between 2.0cm and 3.0 cm and there is normal blood flow in the lumen.

The **aortic wall** consists of three distinct layers: the tunica adventitia, which is the outermost layer, the tunica media and the tunica intima, which is the innermost, as shown in Figure 2.2.

The **tunica intima** is the thinnest of the three layers and is composed of a layer of simple squamous epithelium, known as endothelium [18], [19]. The endothelial cells rest on a basement membrane and a thin subendothelial extracellular matrix consisting of elastic and collagenous fibres bound together [20]. The endothelium acts as a physical boundary between the blood and the surrounding tissue, but also engages in the regulation of inflammation, coagulation and vessel tone.
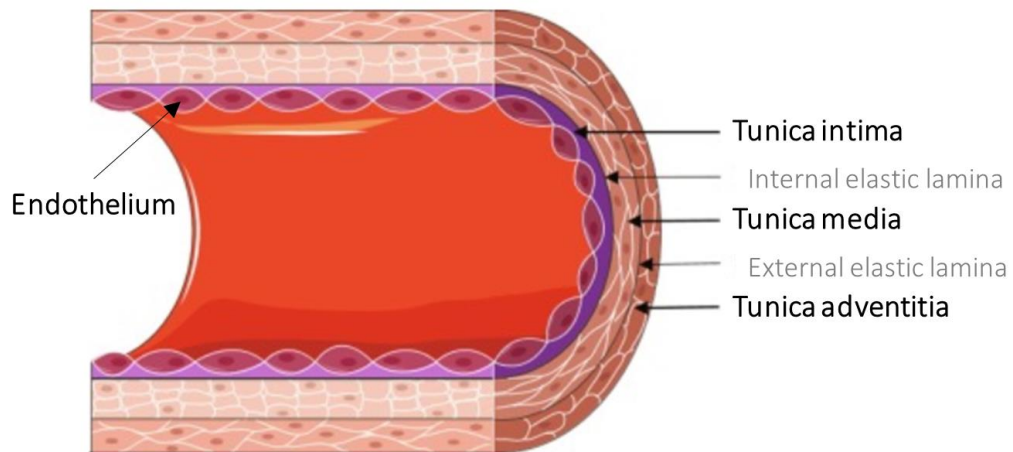
Figure 2.2: Cross section of healthy abdominal wall. *The three wall layers can be seen, from outer to inner: tunica adventitia, tunica media and tunica intima. The endothelium, which comprises part of the tunica intima, is also visible. An external elastic lamina separates the tunica adventitia from the tunica media and an internal elastic lamina separates the tunica media from the tunica intima. (Image adapted from (Brown et al., 2017)).*

The **tunica media** is made up of organised layers of vascular smooth muscle cells, set in a subendothelial extracellular matrix comprising of elastin, collagen, and proteoglycans. This layer mainly contributes to the structural and elastic properties of the aorta [19].

The **tunica adventitia** is primarily composed of collagenous connective tissue, but it also includes other cells (e.g. immunomodulatory cells and fibroblasts) and adrenergic nerves. The vasa vasorum (network of small blood vessels) deliver nutrients and oxygen to the blood vessel itself [21].

An internal elastic lamina separates the tunica intima and media, and an external elastic lamina separates the tunica media and adventitia [19].

2.1.1.2 The Intraluminal Thrombus

The **intraluminal thrombus (ILT)** can be found in at least 70-80% of AAA patients [22] and it is believed to be created via the deposition of blood components during aortic dilation (Figure 2.3) [23]. It is a complex laminated, non-occlusive fibrin structure, permeated by a network of canaliculi, platelets, red blood cells and other hematopoietic blood cells [24]–[27].
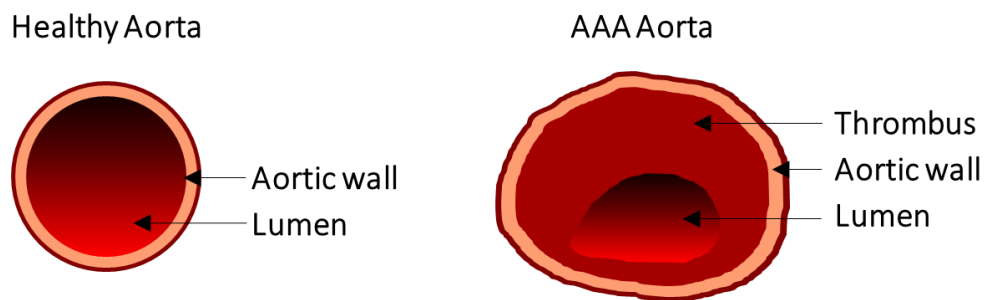
Figure 2.3: Schematic of cross section of a healthy aorta and an aorta with an abdominal aortic aneurysm. Compared to the healthy aorta, the AAA aorta is dilated, it has a non-circular shape and the wall is distorted. Thrombus is occupying a large proportion of the aorta and the lumen is smaller and distorted, affecting the blood flow.

The size and location of the thrombus vary among different patients, as well as the percentage of wall covered by it: as demonstrated in Figure 2.4, the thrombus may cover the entire wall (Figure 2.4 A), or only parts of it (Figure 2.4 B) [28].

The thrombus is in constant contact with the blood flow and undergoes continuous remodelling, with its size commonly increasing concurrently with AAA growth [24], [29], [30]. Two main layers can be approximately distinguished within the thrombus: first, a luminal layer, which is rich in red blood cells due to its contact with the lumen, and second, a brown-coloured fibrinolysed layer adjacent to the aortic wall [27].
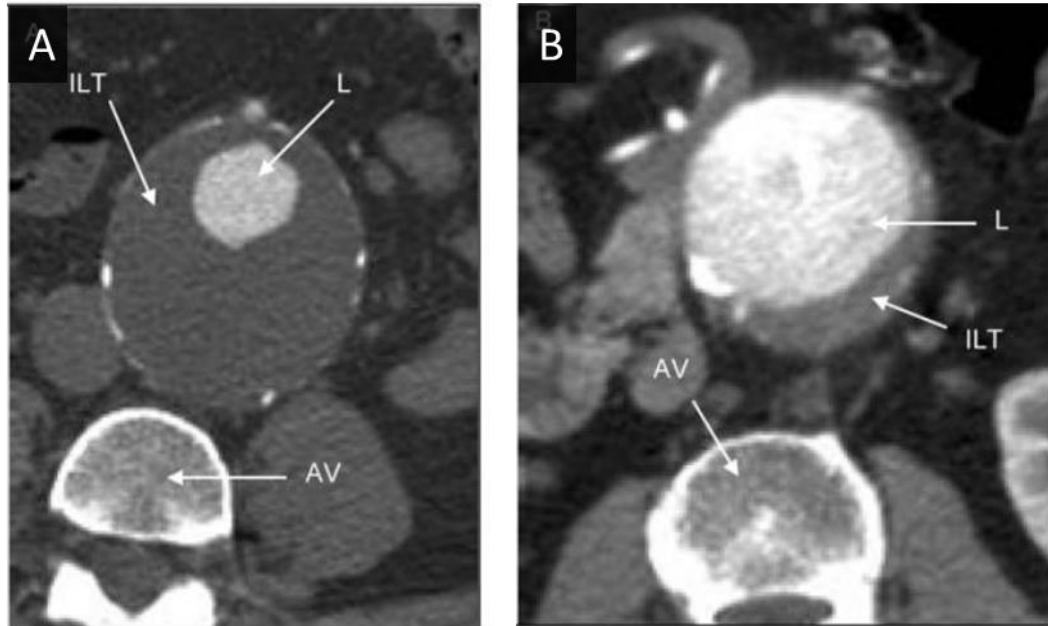
Figure 2.4: A) Axial CT image of AAA demonstrating substantial quantity of posterior-eccentric thrombus. B) Axial CT image of AAA with moderate quantity of posterior-eccentric thrombus. L=lumen; ILT=intraluminal thrombus; AV=abdominal vertebra (Moxon et al., 2010).
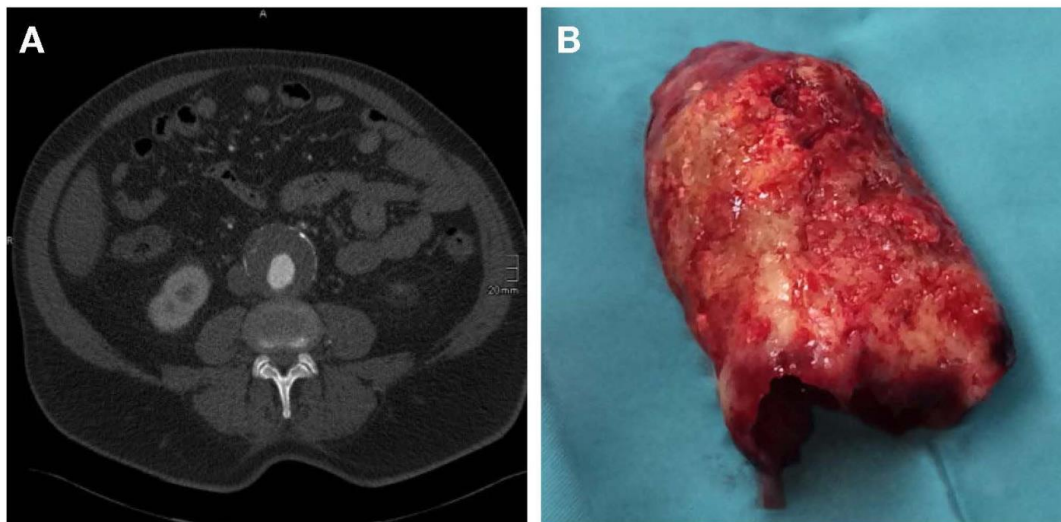
Figure 2.5: A) Axial CT image of infrarenal AAA with intraluminal thrombus. B) Corresponding intraluminal thrombus removed during open surgical repair (gross, natural colour) [31].

2.1.2 Epidemiology

AAAs are commonly asymptomatic until rupture [12]. Detection of AAAs frequently occurs as an incidental finding during investigation of some other more symptomatic pathology. With an overall mortality from ruptured AAAs reaching 80%-90% [6], early identification and prognosis of dilation and rupture becomes a necessity. Studies between 2002 and 2005 indicated a prevalence of AAAs in 4-8% of men aged 65 to 80 in the western world [32]–[34], with AAAs being overall responsible for between 1 and 3% of deaths of men in this age group [5]. According to statistics from 2013, in the UK AAAs cause 1.5% of deaths in men over 55 years [35], while the United States Centre for Disease Control reported for the same year AAAs as the 15th leading cause of death for American men of ages 60 to 64 [36].

In recent years the prevalence of AAAs appears to be declining in the western world, potentially because of reduction in risk factor levels, especially a decrease in smoking [37], [38]. However, a large global epidemiological study in 2013 concluded that AAA mortality has not declined at a global level, since there are large variations between countries, with some (e.g. Austria, Hungary) showing an increase in AAAs [39].

2.1.3 Aetiology - Risk Factors

The underlying biological mechanisms of AAAs have been investigated for many years but are still not well understood. Both genetic and epigenetic factors are believed to be involved in aneurysm disease [40]–[42]. AAAs had traditionally been considered to be a direct result of atherosclerosis [43], but research in recent years suggests that atherosclerosis is either not the sole factor, or a non-causal event that happens in parallel to the AAA disorder [44], [45].

Tobacco has been strongly associated with the pathogenesis behind AAA development [46]–[48], with a recent longitudinal study [49] reporting a 6 to 7 times higher risk of AAA in current smokers compared with those who never smoked. Furthermore, it has been demonstrated [47], [50] that smoking increases the rate of expansion and the risk of rupture of already existing AAAs. Norman and Curci [47] suggested that long-lasting alterations in vascular smooth muscle and inflammatory cell function caused by smoking are implicated in the underlying mechanisms of AAA development.

Other risk factors suggested in the literature include male gender, advanced age, hypertension, chronic obstructive pulmonary disease, hyperlipidaemia, obesity, and family history of AAA, [37], [45], [51], [52]. More recently two more risk factors were introduced, namely ethnicity (Caucasian) and height, with >5-fold incidence of AAAs observed in subjects in the top tertile group for height [49]. Diabetes mellitus appears to have a negative association with AAA incidence, for reasons not yet defined [53]–[55].

It should be noted that although male gender is considered a risk factor for AAA development, women appear to have higher rupture rates for small AAAs (<5.5cm) [56], [57] and it has been suggested that aneurysm size indexed to body surface area is a more reliable predictor of rupture in women than aneurysm size alone [58]. A 2017 study indicated that women have higher mortality rates after elective AAA repair (either open or endovascular) compared to men [59]. Additionally, current female smokers have a higher risk than males who have never smoked, equal to the risk of male former smokers [49].

2.1.4 Pathophysiology

2.1.4.1 Biomechanical Factors

2.1.4.1.1 Law of Laplace

The development of AAAs is connected to changes of the connective tissue in the aortic wall. The mechanical properties of the aorta are determined by fibrillar collagens and elastic fibres [5], [60]. The **Law of Laplace**, according to which the wall tension required to withstand the internal fluid (in this case blood) pressure is proportional to the radius of the vessel (aorta), was previously used to describe the mechanical properties of AAAs [61], [62]. This law however assumes that the vessel is of strictly cylindrical shape with consistent wall thickness and uniform mechanical properties throughout and, as demonstrated in a number of studies [63]–[66], these assumptions cannot be accurately applied to AAAs. AAAs are characterised by a more complex geometry, being often asymmetrical and with variations in wall thickness, tortuosity, potential presence and variable thickness of intraluminal thrombus (ILT) and are affected by a range of heterogeneous biological processes [67]–[71].

2.1.4.1.2 Finite Element Analysis (FEA)

On the other hand, **Finite Element Analysis (FEA)** appears to be a more promising methodology for wall stress calculation in AAAs [64], [72], [73]. FEA, as a practical application of Finite Element Method (FEM), focuses on solving highly complex problems by breaking them down into smaller (and easier) sub-problems. In the case of AAAs, FEA combines CT scan data to initially produce 3D (geometrical) models of the AAAs. These 3D models are thereupon segmented into smaller components, i.e. Finite Elements (FEs), with the use of FE mesh generation algorithms. The Finite Elements extracted can then be studied separately focusing on individual characteristics and micro-environments. This way a more detailed and accurate description of the intricate stress patterns of the entirety of the AAA can be achieved.

However, despite the higher accuracy of the wall stress estimations that FEA provides, it does not offer any information on the tensile strength of the AAA wall (i.e. the amount of force that would be required for the wall to rupture). Interestingly, Tanios et al. recently demonstrated that adaptive biological mechanisms may be counteracting increased localised wall stress and strain through elevated production of collagen and proteoglycans [74]. It would hence be erroneous to solely rely on FEA for rupture prediction, unless it was combined with other techniques capable of determining the weakened areas of the aortic wall non-invasively. Such non-invasive techniques however are not yet routinely available, despite some promising recent studies that used Bayesian regression for the calculation of wall strength distribution [75]–[77].

2.1.4.1.3 Role of thrombus

Intraluminal thrombus (ILT) is present in the majority of AAAs and it comprises many layers of heterogeneous consistency [24], [78]. It is not yet certain whether the presence of thrombus hinders or advances AAA growth, or whether it has little influence. ILT has been found to affect wall stress [63], [79] and specifically decrease peak wall stress [63], [80], [81]. Accelerated ILT growth was proposed as a probable predictor for rupture [82] in 2000, and in 2015, Virag et al suggested that the complex biomechanical nature of the ILT could cause either rupture or a halt of AAA growth and should therefore be taken into consideration in growth and rupture predictions [83]. In the case of ILT failure, blood from the lumen infiltrates the thrombus through the resulting fissure and in the next stage the blood penetrates the aortic wall. This haemorrhagic phenomenon appears as a **high-attenuating crescent sign** within the AAA on computed tomography (CT) scans (Figure 2.6) and is considered a potential predictor of acute or impending rupture [84]–[89].
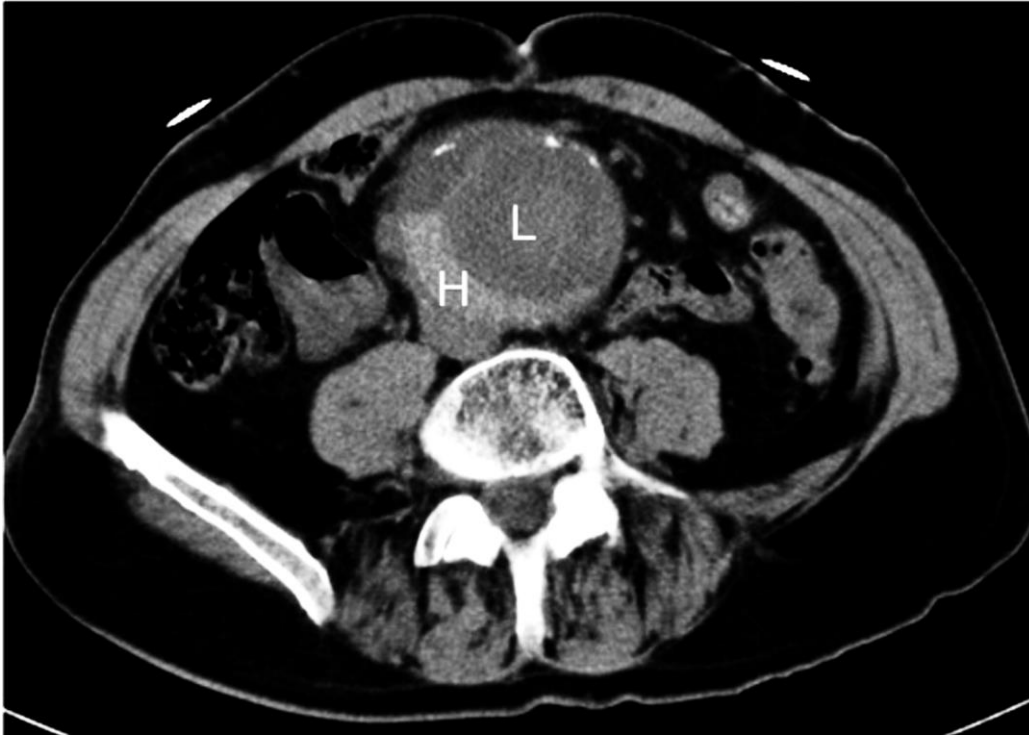
Figure 2.6: Hyperattenuating crescent sign. *Axial unenhanced CT scan presenting crescent-shaped intramural haematoma (H) of higher attenuation than the aortic lumen (L)* [90] *.*

2.1.4.2 Biological Factors

In the abdominal part of the aorta, with no microvasculature available, the wall relies on direct supply of oxygen through the lumen. The presence of intraluminal thrombus (ILT) is hypothesised to be hindering normal diffusion of oxygen towards the wall and consequently inducing **cellular hypoxia** at various degrees, leading to **wall thinning** [63], [91]. These conditions are believed to trigger **inflammation** and **neovascularisation** [4], [91].

Inflammation has been accepted as a critical factor contributing to AAA development and growth [5], [92]–[95]. Through a series of mechanisms, inflammation drastically alters the pathology of the AAA, eventually rendering the wall more susceptible to AAA development and rupture.

Concentrations of **macrophages** are found in the aortic wall from the early stages of AAA formation and contribute to its pathogenesis in a number of ways [96], [97] which are out of the scope of this thesis. Importantly, activated macrophages promote an increase of **oxidative stress** which thereupon intensifies **tissue damage** [98].

Amidst the processes taking place around the enlargement of the aortic wall and the AAA formation and progress, **elastin and collagen** levels are disrupted, leading to **wall stiffness** and **reduction of tensile strength** [99]–[101].

2.1.5 Biological "Hotspots" of Inflammation

The pathological mechanisms present within the AAA (see section 2.1.4), namely cellular hypoxia, wall thinning, inflammation, neovascularisation, oxidative stress, tissue damage, wall stiffness and reduction of tensile strength, do not develop uniformly throughout the aorta, but rather have been demonstrated to appear in a focal manner, suggesting areas at high risk of rupture [64], [97], [102]–[104].

Being so biologically active, these areas may prove to be rich sources of predictive information, if novel analysis techniques are applied to them. Non-invasive techniques are obviously preferable when considering the aorta, so targeted imaging applications are very attractive for the assessment of AAAs.

2.1.6 Risk of Rupture and AAA Management

2.1.6.1 Risk of Rupture

AAAs can either be managed with **open surgical treatment**, **endovascular repair (EVAR)**, or **non-invasive prevention** of growth and rupture [105]–[107].

Given that elective repair has an estimated mean overall 30-day mortality between 0.5% and 27.1%, surgical and endovascular interventions are only considered when the perceived risk of rupture is higher than the risk of procedural complications [7]–[10].

For many years and still currently in practice, the universally recognised metric to predict AAA rupture has been **maximum aortic diameter**. It should be noted that symptomatic AAAs, with symptoms including abdominal pain, back pain and limb ischemia, are considered to be at a higher risk of rupture and are therefore considered for surgical treatment regardless of their size [5], [108], [109]. Asymptomatic AAAs with diameters smaller than 5.5cm are not considered for surgical or endovascular intervention. The diameter threshold was accepted after two large studies, the United Kingdom Small Aneurysm Trial (UKSAT, n=1090) and the United States Aneurysm Detection and Management study (USADAM, n=1136) concluded that there was no survival benefit for immediate surgery for patients with AAAs of 4-5.5cm diameter size [13], [110]. This measurement is made by serial ultrasound monitoring, with CT imaging commonly being applied as part of surgical planning when the 5.5cm antero-posterior (AP) diameter threshold has been reached on ultrasound.

However, this criterion is currently under debate, because 60% of AAAs larger than 5.5 cm in diameter which are under surveillance do not appear to rupture [13], and 10-20% of AAAs presenting at point of rupture are found to be under 5.5 cm in diameter [3], [14].

Alternative criteria for rupture risk prediction suggested in the literature mainly focus on mechanical properties of the AAA, such as **wall tension** [62], **wall stiffness** [100], **peak AAA wall stress** [65], [66], [69] and **intraluminal thrombus (ILT) growth** [63], [79], [82], with none of them having yet proved to be a better rupture predictor than the diameter criterion [73].

There are currently no other methods used to successfully augment rupture prediction in aneurysms under surveillance, so novel methods for rupture stratification are urgently needed.

2.1.6.2 NHS AAA Screening Programme (NAAASP)

Screening is the process of assessing whether individuals without any signs or symptoms may have a disease or may be at increased risk of developing it.

In the case of aneurysm disease, most patients experience no symptoms throughout AAA development until rupture [5]. Research has shown that AAA screening has the potential to reduce AAA rupture-induced deaths by 53% to 73% [32], [111], [112].

In the United Kingdom (UK), the National Health Service (NHS) introduced the NHS AAA Screening Programme (NAAASP) in 2010, which has ever since been inviting all men aged above 65 to attend local hospitals for an AAA assessment [113]. Women are not invited to be screened because occurrence of AAAs in female individuals appears to be up to six times less prevalent than occurrence in males [114]; the exclusion of women from AAA screening has however been challenged [59], [115], [116].

In the first instance of the screening, all eligible men are offered an abdominal ultrasound scan (US) in order to examine whether they have an aortic diameter of size larger than 3 cm, which then qualifies as an AAA.

Based on the aortic diameter measurement, individuals are then classified into three groups:

1. If their aorta is found to be **smaller than 3cm**, the individual is discharged.

2. If their aorta is found to be **between 3.1 cm and 5.4 cm** (small or medium AAAs), they are invited for ongoing surveillance, with surveillance intervals depending on the size of the AAA. Surveillance is terminated when:

   a. The AAA reaches 5.5 cm, so the individual is moved to group 3 (detailed below).

   b. Referral for treatment is decided based on other factors (e.g. appearance of symptoms).

   c. The aortic diameter is found to be smaller than 3 cm in three successive ultrasound scans.

   d. The size of the AAA diameter remains smaller than 4.5 cm after 15 yearly scans.

   e. The individual declines participation, fails to attend, moves to another area or passes away.

3. If they are found to have a large AAA (**at least 5.5 cm**), they are referred to a vascular surgeon to be considered for treatment options, including surgery.

The same AAA screening programmes are also offered by NHS Scotland, NHS Wales and HSC (Health and Social Care) Northern Ireland [117].

2.2 Abdominal Aortic Aneurysm (AAA): Anatomical Imaging Methods

Various methods may be used for AAA imaging, focusing either on anatomical, functional or molecular properties [118].

The established methods for **anatomical imaging** are Ultrasound (US) Scanning, Computed Tomography (CT) and Magnetic Resonance Imaging (MRI). All three modalities were used to image AAAs for the analysis activities described in this thesis and will be introduced in the following sections.

In an anatomical examination of an AAA, of interest is the size of the aneurysm, but also its position and shape. In a typical AAA scan, 3 main components can be discerned and segmented for further scrutiny: namely the aortic wall (which is commonly widened throughout the AAA length), the intraluminal thrombus (ILT) and the luminal area (lumen), as depicted in the cross section of an AAA in Figure 2.7.

More detailed metrics describing the AAA anatomy may also be of interest, e.g. the relative size of lumen or thrombus compared with the total AAA size, the thickness of thrombus and wall and how these vary throughout the AAA and the variations in shape and symmetry, as they can be possible sources of information for growth and rupture prediction, as discussed in sections 2.1.4 and 2.1.6 and further explored in results Chapter 5.
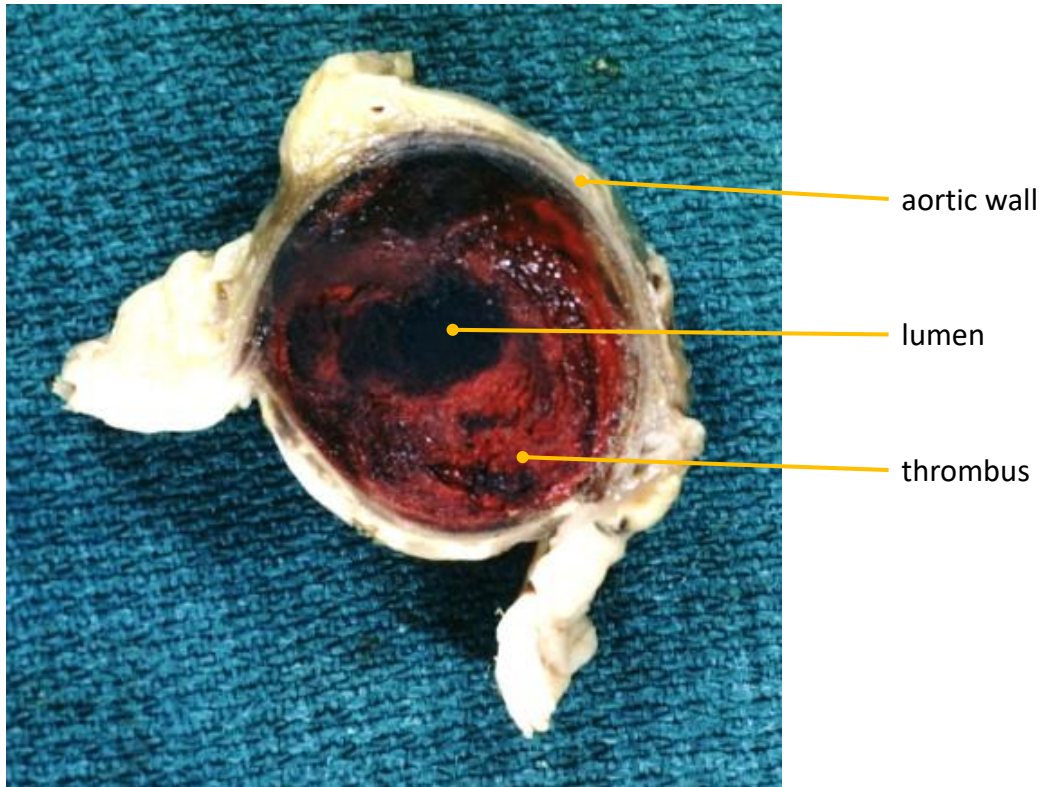
Figure 2.7: Cross section of AAA. The main anatomical features of interest include the aortic wall, the lumen and the thrombus (Image source: PEIR Digital Library 2017a).

Functional/Molecular imaging, applied to study biological mechanisms, is commonly performed, among others, with MRI, Magnetic Resonance Spectroscopy (MRS), optical fluorescence and bioluminescence imaging, SPECT and Positron Emission Tomography (PET) [118], [120]. In the research presented here, the interest was in studying the anatomy of AAAs as well as functional information that can be derived from MRI scans. MRI combined with the application of a particular type of imaging contrast agent (USPIO) affords the opportunity to look at inflammation, one of the key factors observed in AAA histology samples; this mechanism will be discussed in section 2.3.2.

2.2.1 Ultrasound Scanning

Figure 2.8: Abdominal ultrasound scan performed as part of the NHS AAA Screening Programme [121]*. The US technician can be observed as she moves the US transducer against the skin of the subject, while simultaneously assessing the real-time images produced on the screen.*

Ultrasound (US) scanning (Figure 2.8) is characterised by ease of use, safety and wide availability, while being the most inexpensive imaging modality applied to AAAs. It is thus commonly preferred as a first-stage diagnostic and monitoring tool [5], [118].

US scanning, also known as Ultrasonography, uses high-frequency sound waves above 20,000 Hz to create images of tissues, vessels and organs within the human body. During a US scan, a hand-held transducer (or probe) is placed directly against the skin of the subject and moved accordingly so that the whole area of interest is scanned. Water-based gel is applied on the skin, to ensure there is no attenuation of the sound waves through air interfaces.

Ultrasound waves are emitted from the transducer through the gel, via the skin and into the body structures. The transducer receives the soundwaves that bounce back (echoes), converts them into an electrical signal and sends that to a computer where real-time images are produced on a screen. US has the advantage of being non-invasive and providing real-time scanning. The resolution of the output images is of acceptable standards, but only within the limited view of the manually operated probe [122].

A typical US scan of an AAA can be seen in Figure 2.9.
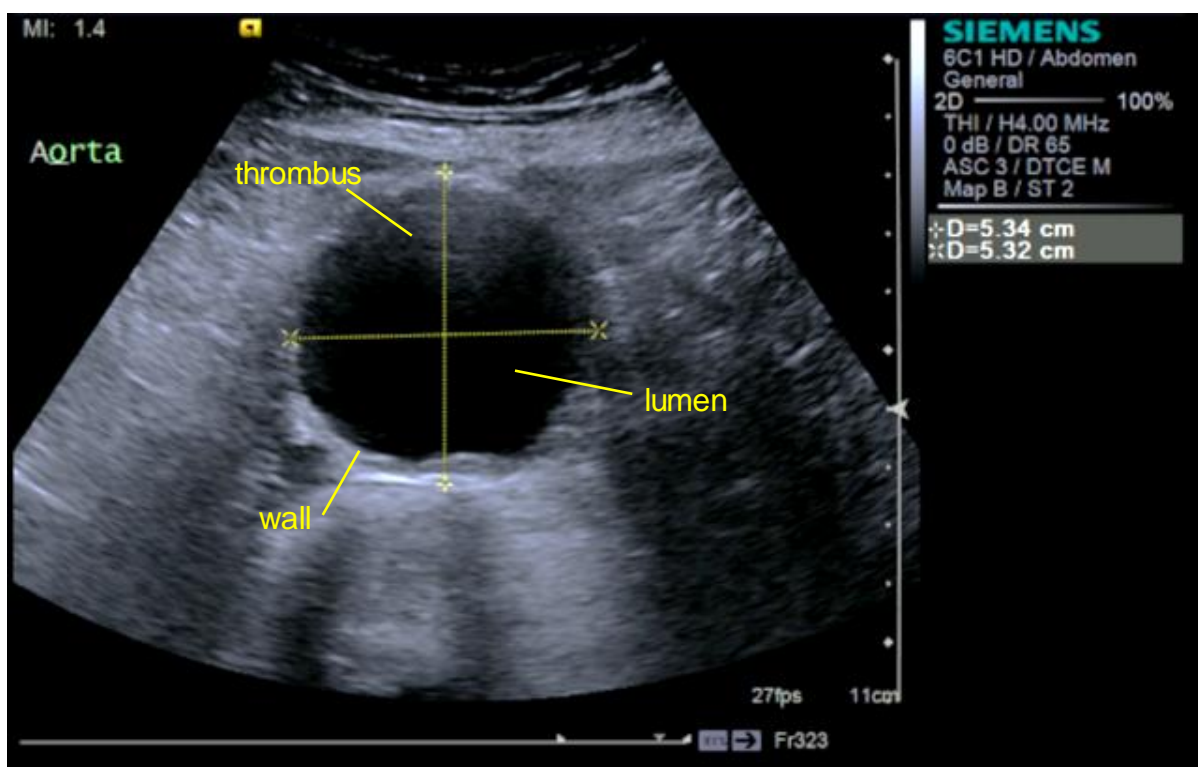
Figure 2.9: Ultrasound Imaging of an AAA. Transabdominal transverse US scan of the aorta of an AAA patient, concentrating on the aneurysm mass. The maximum antero-posterior diameter is the distance marked between the "+" symbols, and the lateral diameter is the distance marked between the "*" symbols. (Image source: MA³RS trial).

A considerable disadvantage of US imaging lies in the fact that the image quality is non-isotropic and susceptible to noise. The fact that the US probe is manually operated introduces inter- and intra-observer variability, and makes the comparison between separately acquired US scans challenging. [3]. US scans

consist of "screenshots" of the real-time view that the sonographer selects to save and there is commonly no information regarding the third dimension (which level of the aorta length is being imaged) saved with the scan [123]–[125].

Other limitations of US are caused by the soundwave properties: US waves cannot adequately penetrate dense bone tissue, and are disrupted by gas and air (making it thus difficult to image through air-filled bowels). Issues also arise in the case of obese patient imaging, as higher US wave attenuation is caused by the greater mass of tissue needing to be penetrated by the waves [125]–[128].

A more detailed analysis of US compared to CT and MRI is presented in Chapter 4 (AAA Measurements: US vs. CT vs. MRI).

2.2.2 Computed Tomography

Computed Tomography (CT), sometimes referred to as "CAT scanning" (Computerised Axial Tomography), consists of a series of high resolution 2D X-ray images that when combined together produce high quality 3D data (Figure 2.10).

CT images have very good spatial resolution, particularly in the z-axis, or slice width, and produce very detailed 3D geometry. A major advantage of CT is that it can image bone, soft tissue and blood vessels at the same time. It generally has good vascular differentiation, but inferior soft tissue differentiation compared to MRI [88], [89], [129].

CT is relatively fast, with approximately one second (actual scanning time) required per slice. AAA imaging with CT usually consists of 70-90 slices (so under 2 minutes actual scanning time) and the total scan time is around 5 minutes [130]. The fast imaging speed of CT warrants fewer motion artefacts and higher

resolution, although the presence of calcium or metal do tend to cause artefacts that obscure anatomical features in the images [131], [132].
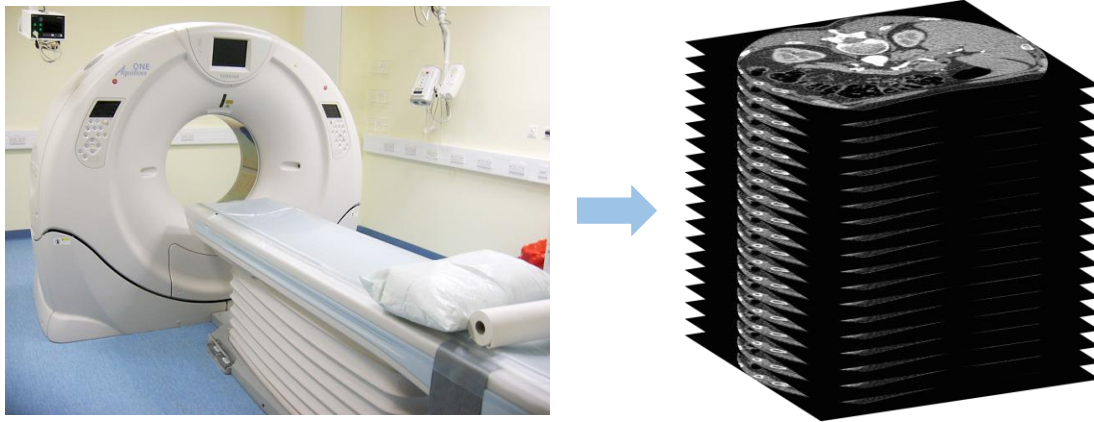
Figure 2.10: CT scanner and stack of CT slices produced (Photograph of CT scanner source: Edinburgh Wellcome Trust Clinical Research Facility, CT images source: MA³RS trial)

CT is not used for routine AAA monitoring due to the associated relatively high ionising radiation exposure. It is however the preferred method for pre-surgical assessment [3]. Contraindications against CT include allergies to intravenous contrast agents (which are considered rare, but more common than with MRI), risk of contrast-induced nephropathy, especially in cases of subjects suffering from renal insufficiency, diabetes and dehydration [118], [133].

A typical slice of a transverse CT scan of an AAA can be seen in Figure 2.11.
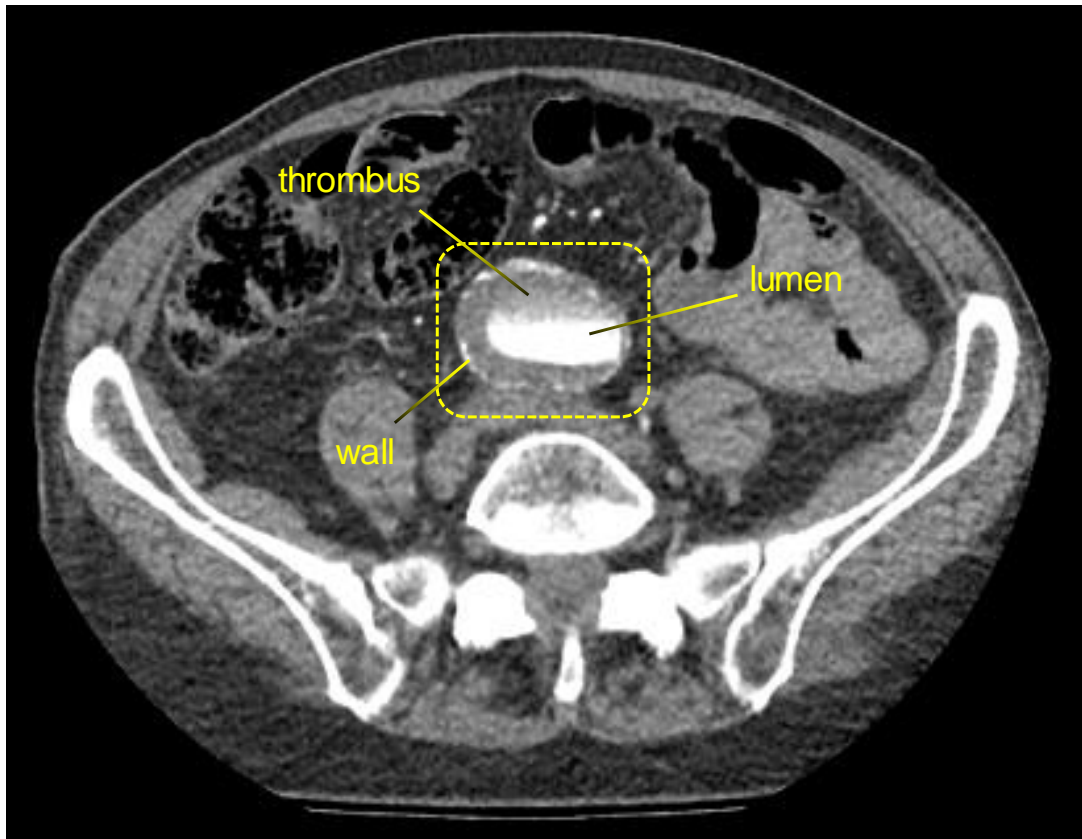
Figure 2.11: CT Imaging of an AAA. Transabdominal transverse CT scan slice of the aorta of an AAA patient, with AAA depicted within the yellow rectangle. *The luminal area appears in white colour and parts of the aortic wall surrounding the thrombus (grey area) are subtly visible. Standard CT iodine-based contrast agent, Iomeron 400 (BRACCO, USA) used. (Image source: MA³RS trial).*

2.2.3 Magnetic Resonance Imaging

Magnetic Resonance Imaging (MRI) makes use of the spinning nuclear magnetisation of the hydrogen atoms within tissues and how they interact with magnetic fields created by the scanner in order to create images. MRI is a very effective imaging modality system due to its non-invasive nature, while the absence of ionising radiation makes it an ideal modality for serial imaging research [134].

MRI has not yet been established as a routine clinical practice for AAA, but it may well become systematically used for serial AAA screening in the near future. The main reason preventing its prevalence is its relatively high cost compared to US and CT: in 2016, a US scan of an AAA would cost £43, a CT scan £77, while an MRI scan would cost £123 [135].
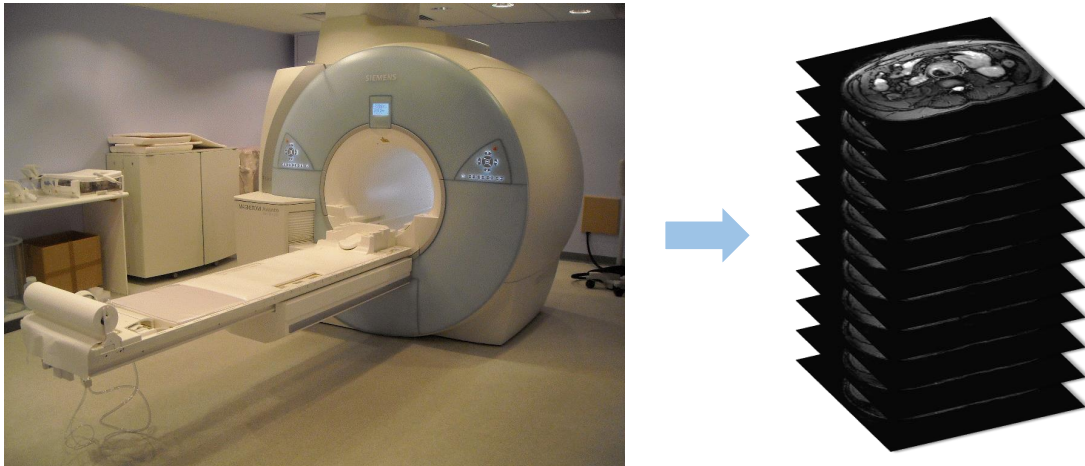
Figure 2.12: MRI scanner and stack of MRI slices produced. (Photograph of MRI scanner source: Weston Area Health NHS Trust, MRI images source: MA³RS trial).

MRI scanners can generate images in any plane, with exceptional 3-dimensional sub-millimetre spatial resolution in some applications (Figure 2.12). The strongest advantage of MRI is its excellent and user-variable soft tissue contrast, allowing the illustration of subtle differences within tissues. Compared to CT, MRI provides less details of bony structures, but offers far superior soft tissue contrast [127], [129], [132], [136].

Additionally, MRI can be used in combination with the application of contrast agents, which allow more detailed imaging, provide additional soft tissue contrast, and can demonstrate biological functions of the tissues as well as indicate pathological processes. Some MRI contrast agents have the additional benefit of comparatively long half-lives, allowing studies with several-day follow-up scans to take place. More details on MRI contrast agents can be found in section 2.3.2.1.

A typical slice of a transverse MRI scan of an AAA can be seen in Figure 2.13.
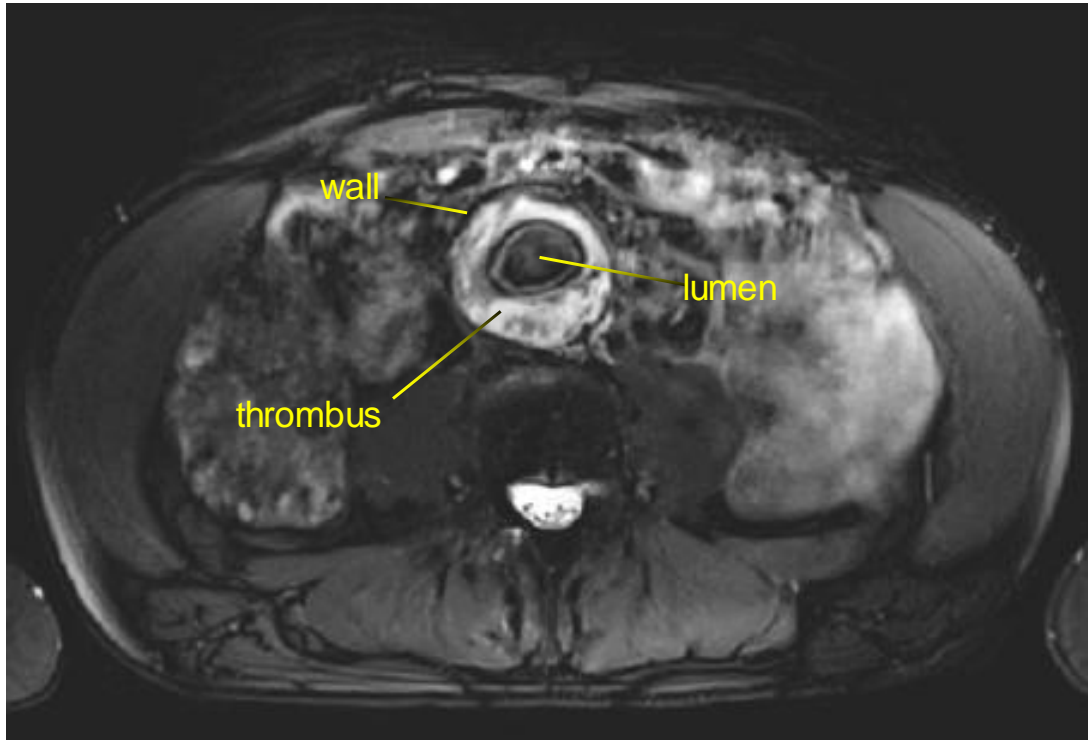
Figure 2.13: MRI Imaging of an AAA. Transabdominal infrarenal transverse T₂W MRI slice of MA³RS cohort patient, with AAA regions clearly visible, by virtue of the exceptional soft tissue contrast. The luminal area (bloodflow) appears dark and is clearly distinguishable from the lighter thrombus. The aortic wall appears to be distinct as well. The bright signal level is cerebrospinal fluid (CSF) in the vertebral canal. (Image source: MA³RS trial).

MRI is susceptible to motion-related artefacts, and abdominal and thoracic imaging may require repeated breath holds by the patient, resulting in relatively long (and tiring for old patients) imaging protocol times compared to CT and US. Indicatively, a routine MRI scanning procedure of an AAA lasts approximately 30 minutes, while the corresponding CT scan would require less than 5-10 minutes and a US AAA assessment would last 10 to 15 minutes. However, the US data acquired within this time comprise only a few (2 to 4 usually) images of the AAA, while the data acquired during an MRI session may consist of hundreds of slices: within one MRI session, the same AAA volume may be imaged several times with

separate acquisitions with differing soft tissue contrasts obtained, with a mixture of 2D and 3D images obtained [137], [138].

MRI might be unsuitable for some categories of patients, such as people who suffer from claustrophobia (even in the case of short-bore or open MRI) [139], or subjects containing metal implants, pacemakers or other devices that would be a safety concern or interfere with the magnetic field of MRI and therefore cause imaging artefacts. Additional considerations arise in the case of contrast agent administration, affecting subjects who are allergic to the agent (even though this is a very rare phenomenon), pregnant, breastfeeding or suffering from kidney or liver disorders [14], [118].

2.2.4 Discussion

There are many factors that affect the choice of imaging modalities in AAA scanning, including availability, cost, and safety, but the most important factor in the context of this AAA research is spatial resolution.

CT has exceptional spatial resolution in the z-axis, thus producing high-quality 3D reconstructions. It can simultaneously image bone, soft tissue and vessels. The short scanning times required for CT ensure minimal presence of motion artefacts. The vascular differentiation of CT is good, but it underperforms in soft tissue differentiation, especially when compared to MRI. This weakness is evident in AAA imaging, where the differentiation between the aortic wall and the luminal thrombus is very challenging. CT scans may also suffer from artefacts in the presence of metal or calcium. As a typical example of achievable spatial resolution of CT for imaging in the torso, the resolution achieved in the MA3RS trial was 0.6 mm.

The spatial resolution of MRI is highly dependent on the specific area of the body being scanned. In the case of abdominal scans, non-rigid coils with less

elements are used, generating a smaller signal to noise ratio compared to other body parts. The acquisition of high-quality images with MRI in the abdominal area is further challenged by the comparatively long scanning times, which make the scans susceptible to movement artefacts (respiratory, cardiac, gastrointestinal). Scanning within the time of a breath-hold and other artefact minimisation techniques such as gating to cardiac and respiratory motion can significantly improve resolution. The strongest point of MRI is soft tissue differentiation, which makes it an ideal imaging modality for AAA research. The resolution of the MRI scans of AAAs in the MA[3]RS study was 1 mm.

The spatial resolution of ultrasound in the abdominal area is generally very good, typically achieving values of 1mm or lower with the use of standard 3.5MHz transducers. However, ultrasound waves cannot penetrate dense bone tissue and are distorted by the presence of air or gas. Additionally, as ultrasound resolution is dependent on beam attenuation, imaging at great depth, e.g. in the case of obese patients, can be challenging. The spatial resolution of ultrasound scans acquired for the MA[3]RS study was 1 mm.

Among the three modalities described, MRI appears to be the best suited for the needs of this study, especially when enhanced with contrast agents to visualise underlying physiological mechanisms like inflammation.

2.3   Abdominal Aortic Aneurysm: Molecular Imaging with MRI

2.3.1 Basic Principles of Magnetic Resonance Imaging

Following is a brief description of the relevant background information relating to MRI. For a more in-depth discussion, please refer to: [138], [140], [141].

Human tissue consists of 60-80% of water (H_2O), with each molecule of water containing two atoms of hydrogen (H) and each atom of hydrogen containing one proton. The spinning nuclear charge of each of these **protons** creates a tiny magnetic field known as **magnetic moment**. Thus, for simplification, each hydrogen nucleus can be regarded as a small magnet with its own magnetic moment or spin.

In the absence of magnetic fields in their environment, the millions of magnetic moments within a tissue have random orientations, resulting in no net magnetic field. When a strong external magnetic field B_0, like the one created with an MRI scanner, is introduced, the magnetic moments of the hydrogen nuclei align along with the magnetic field, either parallel or anti-parallel. Quantum physics dictates that hydrogen nuclei have only two possible energy states: **Low energy** nuclei align parallel to B_0 and **high energy** nuclei align anti-parallel. The net magnetic moment of hydrogen is **called net magnetisation vector (NMV)**.

The introduction of the external field B_0 causes an additional spin of the NMV around B_0 at a characteristic frequency called the **precessional frequency ω_0** or Larmor frequency, and given by the Larmor equation: $\omega_0 = \gamma B_0$

Where γ is a constant called the *magnetogyric ratio.*

When a radio frequency (RF) pulse of energy is applied, energy is transferred to the NMV; this process is called **excitation**. During excitation, the protons gain energy such that the magnetic moments start spiralling in a motion away from

the direction of B_0, resulting in the NMV turning towards the transverse plane (xy plane) when viewed in the "rotating frame of reference" (which rotates at the Larmor frequency). A receiver coil can be used to detect the magnetic field fluctuations caused after the excitation of the protons; a voltage is generated within this receiver coil, which is then used to form the **MR signal**.

When the RF pulse is removed, the NMV loses energy and returns to realign with B_0, in a process called **relaxation**. Relaxation consists of two simultaneous but independent processes.

The first is **spin-lattice relaxation**, which occurs as nuclei release their energy to their environment. This process is also called **T_1 recovery,** and it results in regaining magnetisation in the longitudinal plane, as depicted in Figure 2.14. T_1 recovery has an exponential rate.
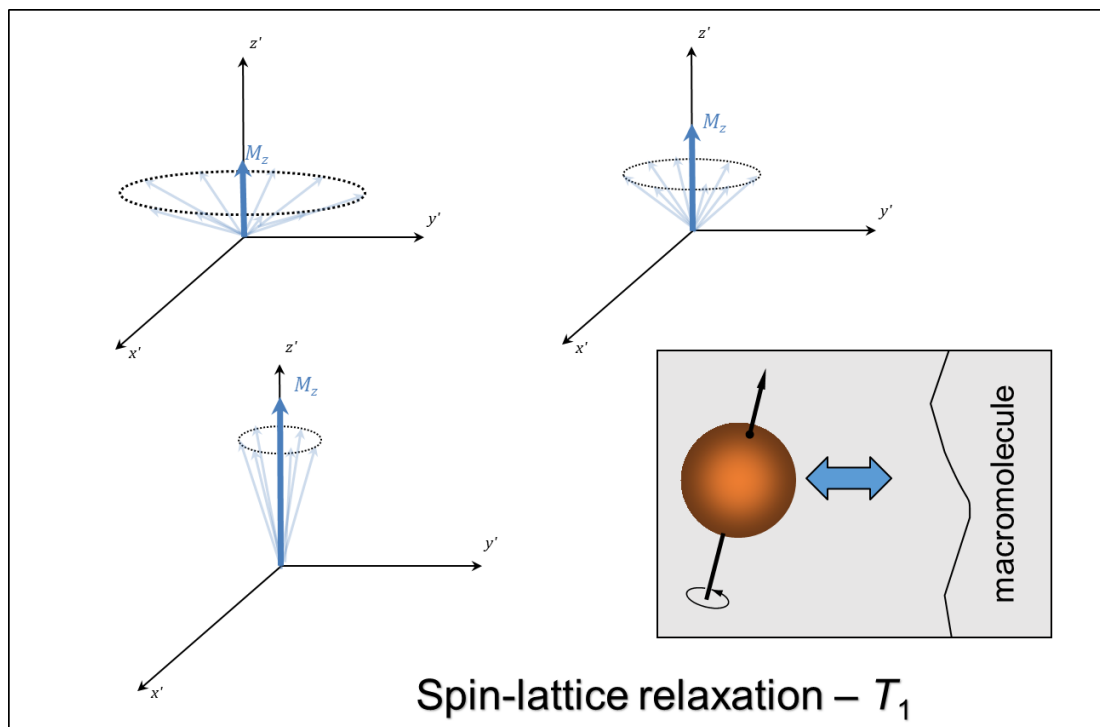
Figure 2.14: Spin-lattice relaxation/T_1 recovery: Energy is transferred from the nuclear spin system to the environment, resulting in relaxation in the longitudinal (z') plane. *(Image credit: Scott Semple)*

The second process is **spin-spin relaxation,** and it occurs when nuclei exchange energy with their neighbouring nuclei. It is also known as **T_2 decay**, and it results in loss of magnetisation in the transverse plane, as shown in Figure 2.15. This relaxation process is also described by an exponential rate.
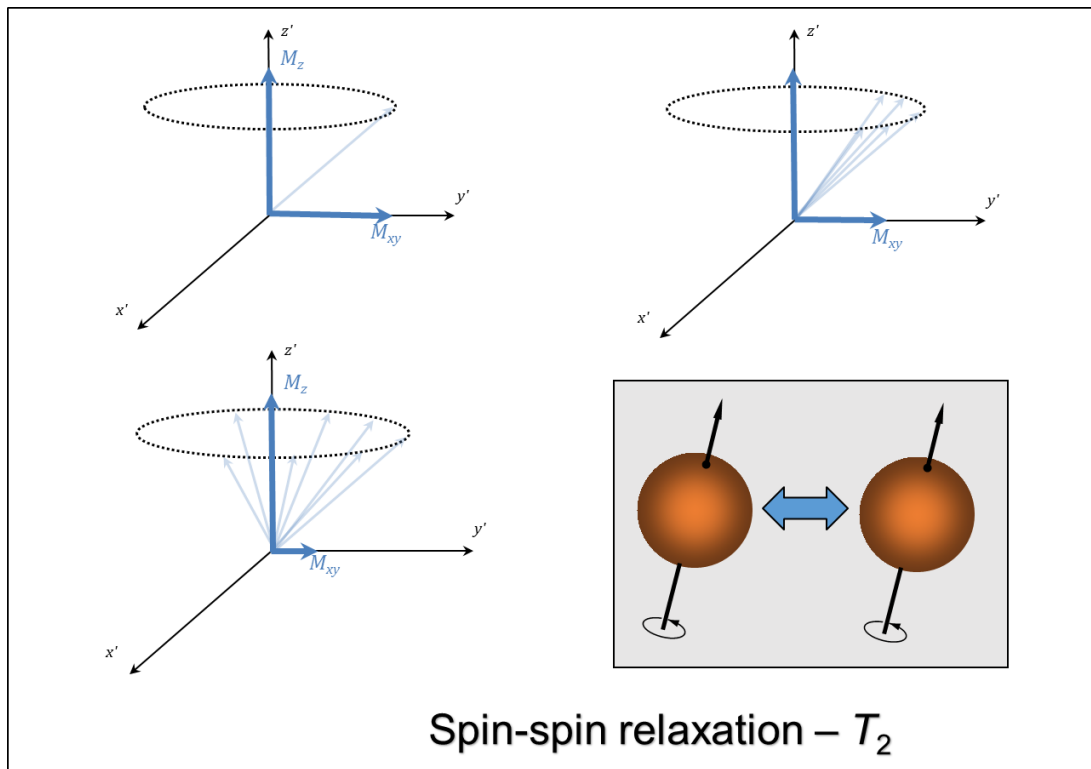
Figure 2.15: Spin-spin relaxation/T_2 decay: Nuclei exchange energy with neighbouring nuclei, leading to loss of magnetisation in the transverse(x'-y') plane. (Image credit: Scott Semple)

Simultaneous to the decay of transverse magnetisation, the magnitude of the voltage created within the coil is also reduced. This transient oscillation is known as **free induction decay (FID)** signal.

2.3.1.1 Weighting

In order to illustrate the differences in T_1 relaxation times or alternatively in T_2 relaxation times in different tissues, the timing of the application of the radiofrequency pulse and other magnetic field gradients of the imaging sequence can be altered so that one relaxation contrast mechanism predominates, giving T_1-weighted (T_1W) or T_2-weighted (T_2W) images. Two of the most common sequence parameters used to influence the contrast weighting of the imaging sequence are the repetition time (TR) and the echo time (TE) of the sequence (outlined further below).

In the protocols used for this research, T_2-weighted (T_2W) scans were used for extraction of anatomical information.

2.3.1.1.1 T2-weighting

A T_2-weighted (T_2W) image demonstrates the differences found between the T_2 relaxation rates of different soft tissues. The amount of T_2 decay taking place is strongly regulated by the choice of the imaging sequence parameter TE.

2.3.1.2 T2* decay

There is a further component of proton magnetisation relaxation associated with actual applications of scanning. T_2^* decay consists of the combination of the T_2 decay and dephasing caused by local magnetic field inhomogeneities. These local field inhomogeneities may be caused by the varying magnetic properties of different tissues within the body. These effects are often therefore particularly strong at the boundary between two tissues with significantly different magnetic susceptibilities. The presence of ferrous objects or paramagnetic (possessing magnetisation in direct proportion to field strength of externally applied magnetic field; paramagnetism appears in atoms that have unpaired electrons) or superparamagnetic (characterised by a large magnetic moment in the presence of a static external field, no magnetic memory, suitable for MRI) contrast agents will strongly contribute to increased, localised T_2^* decay, as shown in

Figure 2.16. T_2^* decay is therefore always faster than T_2 decay. T_2^* decay may be thought of in practical terms as the decay of the FID that occurs after the RF pulse is switched off.
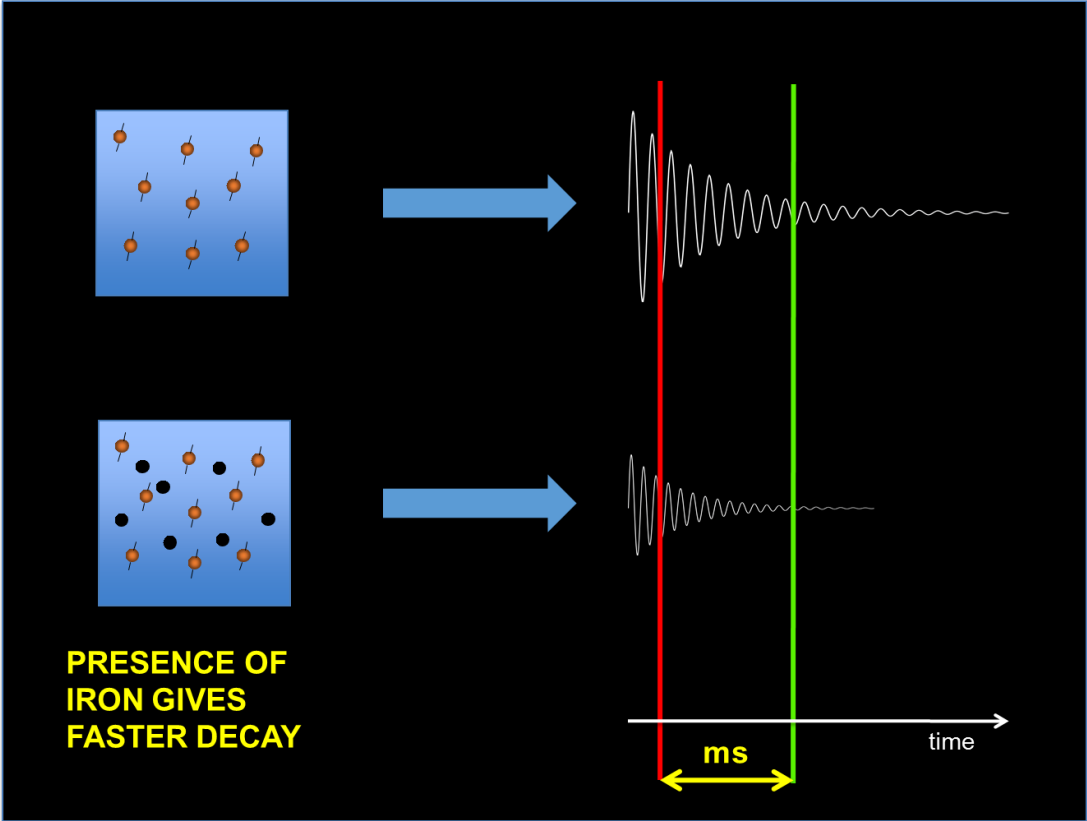
Figure 2.16: The presence of iron causes faster T2 decay. (Image credit: Scott Semple)*
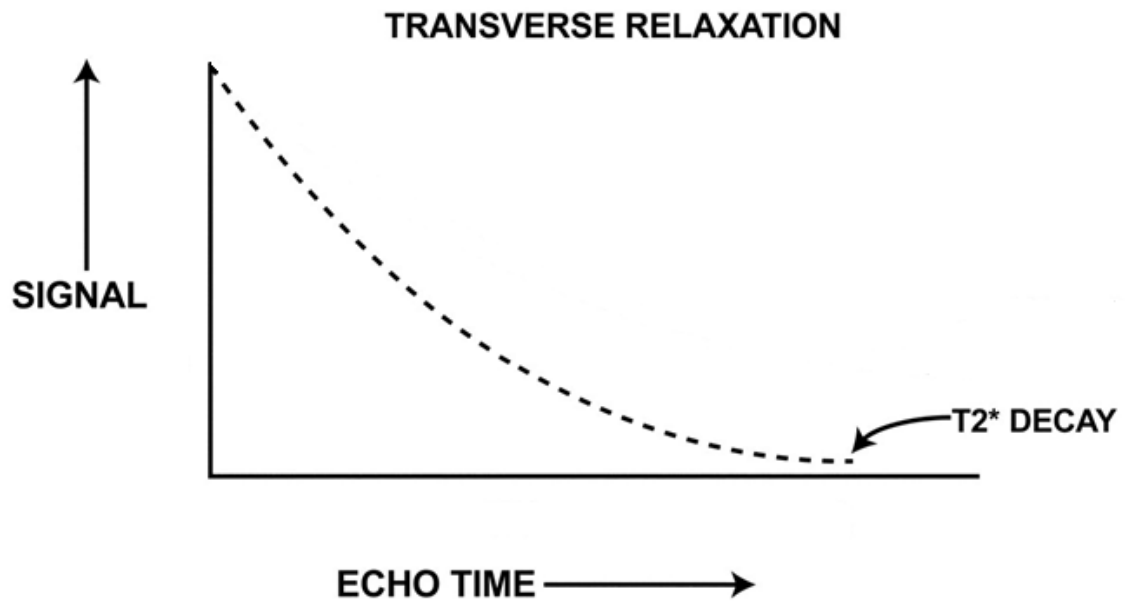
Figure 2.17: T₂* exponential decay of the signal intensity against gradient echo time (TE) (adapted from [142]*.*

The T_2* value is the time constant of the decay rate of transverse magnetisation (signal intensity) against echo time (TE), as can be seen in Figure 2.17. The relationship is described by the Equation 2.1:

$$S(t) = S(0)e^{-t/T2^*}$$

Equation 2.1

Where $S(t)$ is the signal intensity at time t and $S(0)$ is the signal intensity at starting time ($t = 0$).

The calculation of the T_2* value is useful for the estimation of USPIO accumulation, as explained in section 2.2.3.

2.3.1.3 Spin echo pulse sequence

The spin echo pulse sequence uses a 90° RF excitation pulse in order to flip the longitudinal NMV to the transverse plane. Voltage is then induced within the receiver coil and after the 90° RF pulse is switched off, T_2 dephasing begins and the signal decays.

A 180° RF pulse is introduced, and it has enough energy to compensate for the dephasing, thus causing protons to recover their transverse magnetisation and producing a spin echo.

Echo time (TE) corresponds to the time between the application of the 90° RF excitation pulse and the spin echo (the time of MR signal sampling). The TE determines the amount of T_2 decay that is allowed to happen.

Repetition time (TR) is the time interval between each 90° RF excitation pulse.

2.3.1.4 Gradient echo pulse sequence

A gradient echo pulse sequence uses a single RF excitation pulse of variable degree, so the NMV can flip to a variable angle. If the flip angle used is other than 90°, then only a part of the longitudinal magnetisation is converted to transverse magnetisation (and therefore to MR signal). After the removal of the RF pulse, T_2^* dephasing immediately begins. This decaying signal is sampled after time TE and this signal is termed a gradient echo, as shown in Figure 2.18

An advantage of gradient echo pulse sequences is their shorter scan times compared to spin echo pulse sequences.

A disadvantage of gradient echo pulse sequences is their sensitivity to magnetic field inhomogeneities, which sometimes causes imaging artefacts, but may be exploited to make gradient echo specifically T_2^*-weighted.
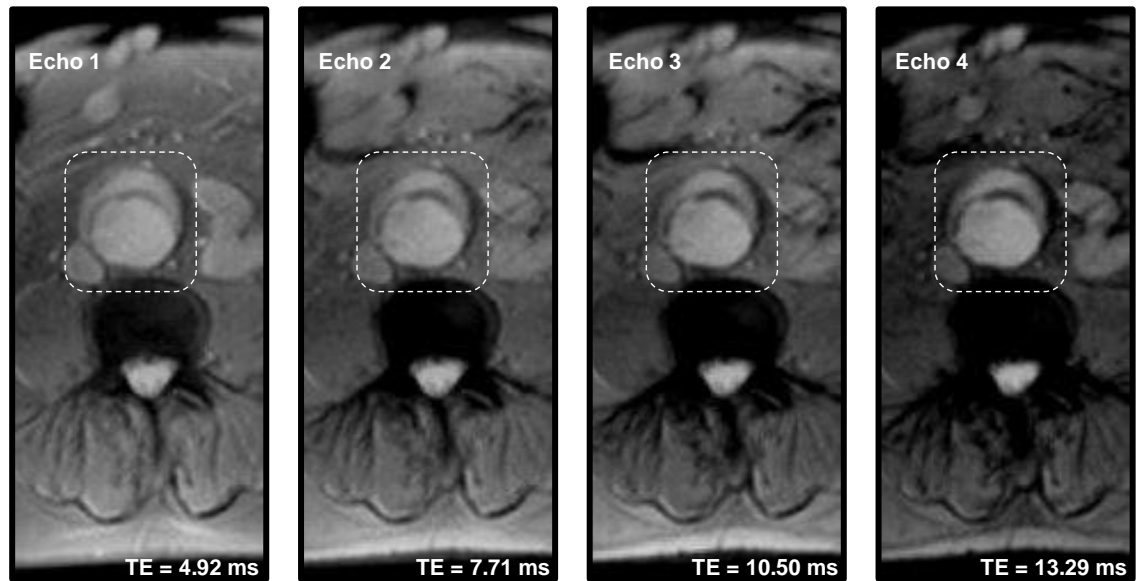
Figure 2.18: A multi-echo gradient-echo sequence, consisting of 4 echoes at TE=4.92ms, TE=7.71ms, TE=10.50ms and TE=13.29ms acquired axially through the AAA demonstrating differential T_2* decay in different soft tissue of the AAA. The AAA area has been annotated. The T_2* decay can be seen, as the signal appears increasingly darker in the echoes, the relaxation rate is faster in some tissues than others. (Source of data used for this image: The MA³RS trial)*

2.3.2 Inflammation tracking with MRI

2.3.2.1 MRI Contrast Agents for Imaging of Inflammation

The ability of MRI to provide good soft tissue contrast relies on the differences in water content locally (proton density), but also importantly on the regional differences in the longitudinal (T_1) and transverse (T_2) relaxation times [143]. The differences in T_1 and T_2 can be intensified by adapting the scanning parameters accordingly, as briefly outlined above. Diseased tissue can sometimes be differentiated from healthy tissue based on these differences, but many conditions will not be detected without the introduction of a contrast agent [144].

MRI contrast agents are pharmaceutical substances which are administered to subjects before or during an MRI scan in order to improve soft tissue discrimination and allow more targeted imaging [145]. The introduction of

contrast agents has been demonstrated to increase sensitivity and specificity in diagnostic MRI [146], [147].

Based on their magnetic behaviour, MRI contrast agents can be commonly classified into two main groups. The first group is **paramagnetic agents**, which shorten the T_1 relaxation times of the tissues in which they concentrate and are mostly **Gadolinium (Gd^{3+})** – based. The second group is **super-paramagnetic agents**, which shorten T_1, T_2 and particularly T_2^* relaxation times of the tissues and are most commonly based on **iron oxide** (FeO) particles [143], [144].

Gadolinium (Gd^{3+}) contrast agents have been successful in identifying atherosclerotic plaque components, such as calcified plaque, fibrous cap and lipid core [148]–[150], as well as assessing neovascularisation in human vascular tissue [151]. In the case of AAAs, gadolinium-based contrast agents have been found to distinguish between the fibrous cap and the thrombus, but have failed to provide any information about the underlying pathophysiological mechanisms [152].

2.3.2.2 USPIO Structure and Use

Ultrasmall Superparamagnetic Particles of Iron Oxide (USPIO) are a range of contrast agents that can offer additional insights into underlying biological processes. Additionally, USPIO have the advantage of being trackable in lower concentrations than gadolinium-based contrast agents [153].

USPIO have been used in many applications, such as myocardial and renal perfusion assessment, macrophage activity detection, atherosclerosis imaging, detection of inflammation and identification of unstable lesions within carotid atheroma [154]–[159]. Of special interest to our team's research has been the ability of USPIO agents to identify areas of inflammation as demonstrated by Howarth et al in 2009 [160]. Specifically for AAA disease, USPIO were found to function as a marker of cellular inflammation, first in pre-clinical models and small clinical studies [161]–[163] and in 2011 with the pilot study (described in

section 2.4.1) conducted within our department [15] which further confirmed this role in the specific application of AAAs.

Iron oxide particles are clinically used in a variety of sizes, comprising of: very small (VSPIO, <20 nm in diameter), ultrasmall (USPIO, 20–50 nm in diameter), small (SPIO, 60–250 nm in diameter) nano-sized superparamagnetic particles of iron oxide and micron-sized (MPIO, 1-8 µm in diameter) particles of iron oxide [134]. Iron oxide particles generally consist of a nonstoichiometric microcrystalline magnetite core and have a coating of carbohydrate or polymer [164].

2.3.2.3 Cellular Uptake of USPIO

Since iron oxide particles are administered intravenously, their size and coating influence their uptake by cells [165]. USPIO have a blood pool half –life between 16 and 24 hours, which is significantly longer than SPIO (2-6 hours) or gadolinium (approximately 1.5 hours) [166]–[170]. Having a longer circulating time, USPIO are thus more effective in the imaging of vessel walls. Although USPIO are mainly found within the blood pool, they also enter inflamed tissues; the mechanism behind their migration however is not fully understood. It has been hypothesised that the small size of the USPIO allows them to transport across the endothelium, especially in cases when the latter is compromised and inflammatory neovasculature is present. After entering the tissues, the USPIO are ingested by resident macrophages [134], [171]. The alternative theory suggests that USPIO are engulfed by monocytes or macrophages in the blood circulation and are consequently transported to sites of inflammation [172], [173].

2.3.2.4 Detection of USPIO with MRI

In AAAs, the co-localisation of superparamagnetic particles of iron oxide (SPIO) and macrophages within the aortic wall has been previously verified histologically [15] within the pilot study described in section 2.4.1. As a result of the high concentration of USPIO in inflamed sites, local magnetic disturbances shorten T_2 and T_2^* relaxation times. The inflamed areas therefore appear darker than the non-inflamed sites in the T_2 and T_2^*W images [134]. The MRI signal reduction observed has been previously demonstrated to be proportionate to macrophage density [174], hence the local differences in signal in T_2^* maps before and after administration of USPIO can be used to calculate the extent of inflammation within the tissues.

2.4   From the Pilot Study to the MA³RS Study

2.4.1 Introduction

In 2009, a pilot study [15] was set up to evaluate a novel way of predicting AAA expansion, which would potentially replace or supplement the diameter-measuring method described in section 2.1.6.

As described in 2.1.4 and 2.1.5, among other mechanisms, cellular inflammation has been shown to play a critical role in AAA development and expansion, by altering the pathology of the aortic wall through proteolytic degradation. This mechanism appears to function locally, in focal areas of the wall.

Based on this, the hypothesis of the pilot study was that the presence of concentrated cellular inflammation in the wall of AAAs would correlate with the rate of AAA expansion more strongly than diameter size alone did. MRI with USPIO contrast was ideally suited to directly assess the inflammation process within AAAs (see 2.3.2). 29 patients with asymptomatic AAAs measuring 4.0-6.6cm (as measured with US) were imaged using a 3-T MRI scanner before and 24 to 36 hours after administration of USPIO to visualise areas of USPIO uptake, corresponding to regions of inflammation.

2.4.2 Visualisation of Inflammation in AAAs

In the pilot study, regions of interest (ROIs) depicting the lumen, thrombus and aortic wall were manually labelled on anatomical T_1W or T_2W scans for each slice, using Mayo Analyze software (AnalyzeDirect, Overland Park, KS, USA).

4-echo gradient T_2* sequences of axial scans were combined to generate pre-USPIO T_2* maps (Figure 2.19 A) and post-USPIO T_2* maps (Figure 2.19 B) for each slice of each AAA. USPIO uptake within AAA tissues was identified by calculating percent change ($\%\Delta T_2$*) of the T_2* values before and after USPIO injection (Figure 2.19 C).

All images were registered to T_2W using a semi-automatic rigid 3-dimensional voxel registration protocol in Mayo Analyze. The ROIs that had been defined on the T_2W images could then be applied to the T_2*-weighted images and resulting T_2* maps.

The percent change ΔT_2* was visualised in the form of colour maps superimposed over anatomical T_2W AAA slices. The areas with higher concentration of USPIO (higher inflammation level) appeared "warmer", as illustrated in Figure 2.19 C. The colour scale expanded from blue (cold), representing insignificant change in T_2* values (thus no USPIO uptake) to red (warm), representing significant change in T_2* values (thus highest USPIO uptake). Percent change smaller than 59% was considered insignificant and was thus depicted as 0% change (blue colour on map). The methodology used for the 59% threshold decision and the colour map generation is presented next.
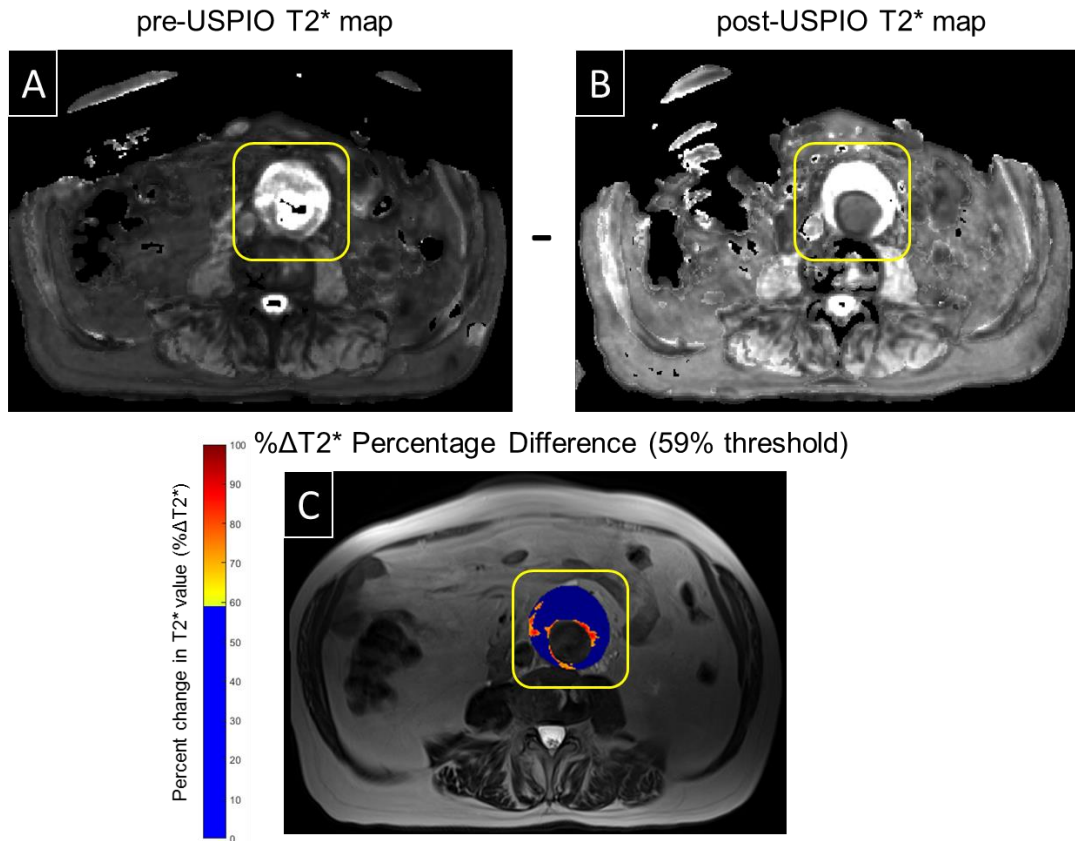
Figure 2.19: Representation of ΔT_2* as a means of USPIO uptake visualisation within the AAA. *The AAA can be seen within the highlighted yellow area. A representative AAA slice is used for this example of $\%\Delta T_2*$. The pre-USPIO (A) and the post-USPIO (B) T_2* maps are calculated from the combination of 4 corresponding gradient echoes. The percent change in T_2* values (ΔT_2*) between them is then calculated and visualised in form of a colour map (jet scale) superimposed on the corresponding T_2W anatomic image (C). As can be seen in the colour bar, changes smaller than 59% are considered insignificant and are represented as 0% (blue). (Source of data used for this image: The Pilot Study [15]).*

2.4.2.1.1 ΔT_2* threshold method

Repeatability was examined by performing two consecutive scans on patients without moving them and the bias was established with the Bland & Altman method.

Reproducibility scans were consequently used to establish a threshold, above which any ΔT_2* change would be attributed to USPIO uptake, rather than noise. 8 patients had an initial scan (without USPIO administration), with T_2* values

measured, then they were moved out of the MRI scanner and later repositioned in the scanner and had the same scanning sequence and T_2^* measurements repeated. The per cent change in T_2^* value ($\%\Delta T_2^*$) was calculated for each voxel. The threshold was derived by calculating the 95th percentile value for the (non-USPIO) $\%\Delta T_2^*$ and averaging over all 8 patients, thus resulting in the significance threshold value of 59.1%.

2.4.3 Classification: Groups explained

The AAAs were classified into three groups based on inflammation patterns as identified at baseline through MRI scanning with USPIO. These groups were hypothesised to represent different underlying biological mechanisms, with Group3 being the one of greatest interest, as it was thought to correspond to the biological "hotspots" of inflammation previously described in section 2.1.5.

More specifically, the 3 classification groups were as follows:

- Group1: no mural or thrombus USPIO uptake, except for isolated periluminal T_2^* enhancement (see 2.4.3.1) occurring immediately adjacent to, and in continuity with the lumen, as illustrated in Figure 2.20 A.

- Group2: diffuse USPIO uptake that was distinct from the periluminal thrombus (see 2.4.3.1) and the aortic wall, as depicted in Figure 2.20 B.

- Group3: concentrated areas consisting of at least 10 contiguous voxels of USPIO uptake within the aortic wall of the aneurysm distinct from periluminal area and thrombus (see 2.4.3.1), representing "inflammatory hotspots", as shown in Figure 2.20 C.
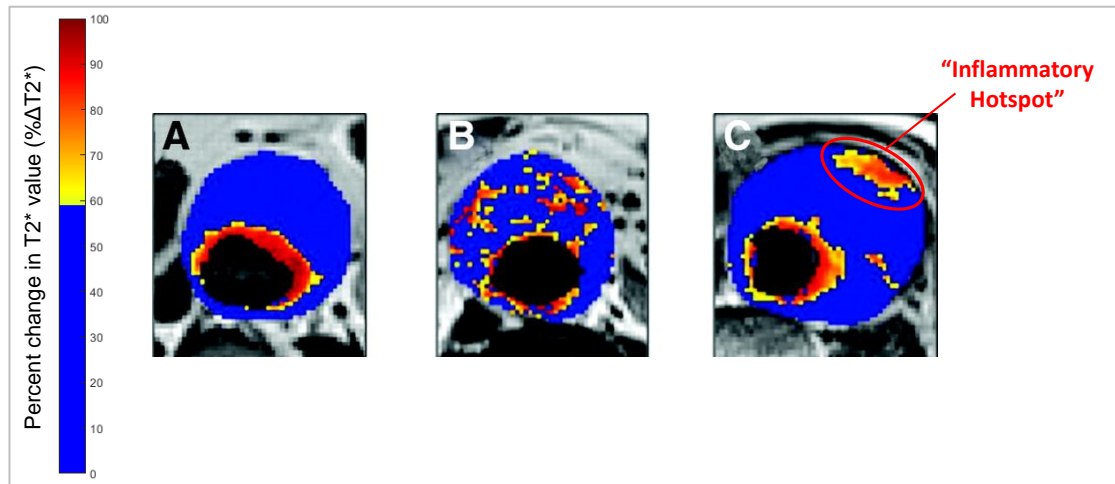
Figure 2.20: Colour maps illustrating representative slices from AAAs of each of the 3 groups. The colour scale corresponds to the degree of difference between pre-USPIO and post-USPIO T_2 values (%ΔT_2*). Differences smaller than 59% are considered insignificant and are thus replaced by 0% values (depicted in blue colour). The colour maps have been superimposed on T_2W anatomic images. The three AAA groups based on patterns of inflammation consist of: A) Group1, with only periluminal USPIO uptake. B) Group2, with diffuse USPIO uptake (distinct from periluminal area and wall area). C) Group3, with an "inflammatory hotspot", consisting of at least 10 contiguous voxels of USPIO uptake, within the AAA wall and distinct from the periluminal area. (Image source: Pilot Study (Jennifer M J Richards et al. 2011)).*

2.4.3.1 USPIO uptake in Periluminal Area

A high change in T_2* value in the periluminal area of the AAA was a constant finding in all patients (forming a "halo shape" around the lumen). This was attributed to physical trapping of USPIO in fresh, possibly gelatinous and permeable thrombus which is found close to the blood flow [15], [24], rather than being considered a manifestation of inflammation. Periluminal enhancement was therefore not used as a contributing factor in the AAA classification.

2.4.4 Findings and Limitations of the Pilot Study

To account for the "staccato" growth pattern of the AAAs, the annual growth rate of the AAAs was calculated from the baseline ultrasound scan and 2 further ultrasound scans performed at 6 and 12 months. Potential correlation between

the AAA classifications and yearly growth was subsequently investigated, to evaluate the prognostic power of this method in predicting AAA growth.

It was found that the AAAs of the third group (Figure 2.21 - highlighted bars) grew significantly faster than the other two groups, while the initial diameters (as measured at baseline) of all 3 groups were of similar range, as demonstrated in Figure 2.21.
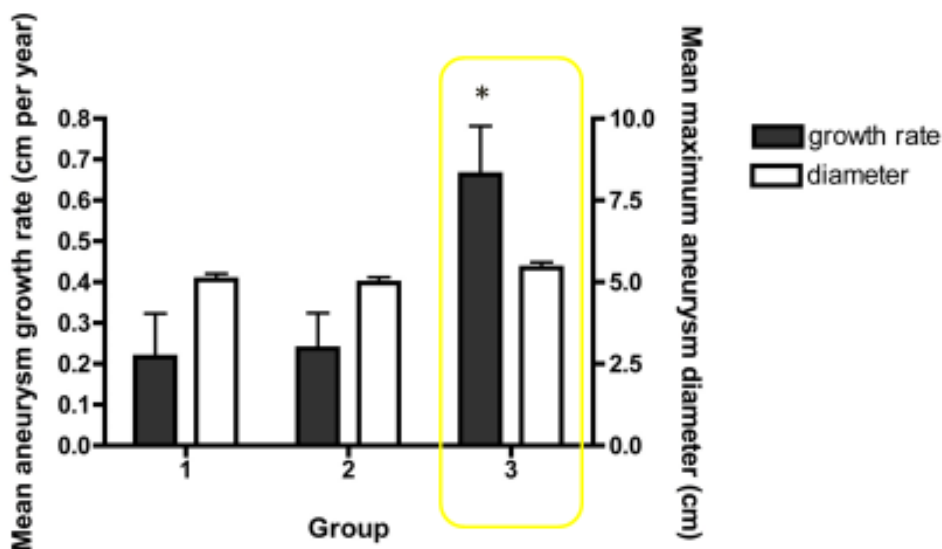
Figure 2.21: Relationship between baseline diameter and annual growth for each of the 3 AAA groups. It is clearly shown that the initial AAA diameters are of similar sizes for all 3 groups, while the growth rate for AAAs of the 3rd group is significantly higher (0.66cm/y) than that of group 1 AAAs (0.22 cm/y) and that of group 2 AAAs (0.24 cm/y), (P=0.020). No significant difference between 1st and 2nd group growing rates is observed.(Image source: Pilot Study [15]).

Importantly, histological staining with CD68 and Prussian-blue verified that the areas of concentrated USPIO uptake corresponded to areas high macrophage concentration. It was thus demonstrated that uptake of USPIO in AAAs identifies cellular inflammation.

Additionally, this proof-of-concept study proposed for the first time that the presence of focal areas of inflammation ("inflammatory hotspots") adjacent to the

AAA wall appear to distinguish patients at risk of more rapidly progressive AAA expansion.

2.4.4.1.1 Limitations

This pilot study appeared to give new promise for a more effective way of stratifying AAA patients, compared to the established diameter-size criterion. Being however the first clinical study in this niche area, it had some limitations:

- The sample size was considerably small (only 29 patients).

- Growth of the AAAs was calculated for a period of only 6 months.

- Most of the data processing was done manually, including:

  o Semi-manual registration of all images (pre-USPIO and post-USPIO T_2*W) to anatomical T_2W images.

  o Manual inflammation pattern ("hotspot") identification on %ΔT_2* colour maps.

  o Manual AAA classification

- The methodology in this pilot study also did not account for the 3D nature of the MRI data, but rather processed all available slices as independent 2D images. This had the disadvantage that the information contained in each slice could not be easily combined with the information from the adjacent slices. In this way, crucial pieces of information could have been omitted during the manual segmentation and hotspot identification.

- The definition of "hotspot" of inflammation as requiring to exhibit a 10-voxel sized area was somewhat arbitrary (based approximately around assumptions relating to the intrinsic spatial resolution of the images as compared to thrombus/AAA size). Different sized area thresholds of significance could have been tested.

- No sub-classification of Group3 patients was conducted (the small sample hindered this as well), e.g. based on size or shape of hotspots.

- AAA shape and anatomical metrics were not taken into consideration, as this was out of the scope of the pilot study.

2.5   The MA³RS Study

2.5.1 Introduction

The MA³RS (MRI for Abdominal Aortic Aneurysms to predict Rupture or Surgery) study aimed to expand on the pilot study by validating the previous findings and providing additional information to the current simplistic gold-standard of ultrasound measurement of aneurysm diameter.

 The study design of MA³RS has been previously presented in detail [175]. A description of the main points that are relevant to this PhD work are presented here.

2.5.2 Methods

2.5.2.1 Study Cohort

342 patients were recruited between November 2012 and December 2014 from 3 centres in Scotland (Royal Infirmary of Edinburgh, Western Infirmary of Glasgow and Forth Valley Royal Hospital in Lambert). The **inclusion criteria** were: age above 40 years, maximum antero-posterior (AP) AAA diameter of at least 40mm and being under ultrasound surveillance programmes. **Exclusion criteria** included patients with renal failure, inflammatory AAAs, AAAs resulting from connective tissue disorders, scheduled imminent AAA repair and women of childbearing potential.

2.5.2.2 Study protocol

The study flowchart, as published by the Edinburgh group in 2015 [175] is presented in Figure 2.22.

Briefly, the **baseline** assessment involved a full clinical assessment, collection of clinical data such as medical history and cardiovascular risk profile (e.g. smoking status, hypertension, family history of AAAs, diabetes mellitus), blood sample collection, pulse wave analysis, an ultrasound scan, a CT scan and two MRI scans.

Every six months after the baseline (at 6th, 12th and 18th month), a clinical assessment and an ultrasound scan took place in all 3 centres.

Additionally, out of the 342 patients in the study, 20 had repeat USPIO-enhanced MRI scans within a month of baseline in order to evaluate **reproducibility of the technique**. A further group of 59 subjects had MRI scans repeated 1 year after baseline and 20 patients were scanned 2 years after baseline.

The **final 2-year** assessment included a clinical assessment, an ultrasound scan, a CT scan, blood sample collection and pulse wave analysis for all the patients still participating in the study.
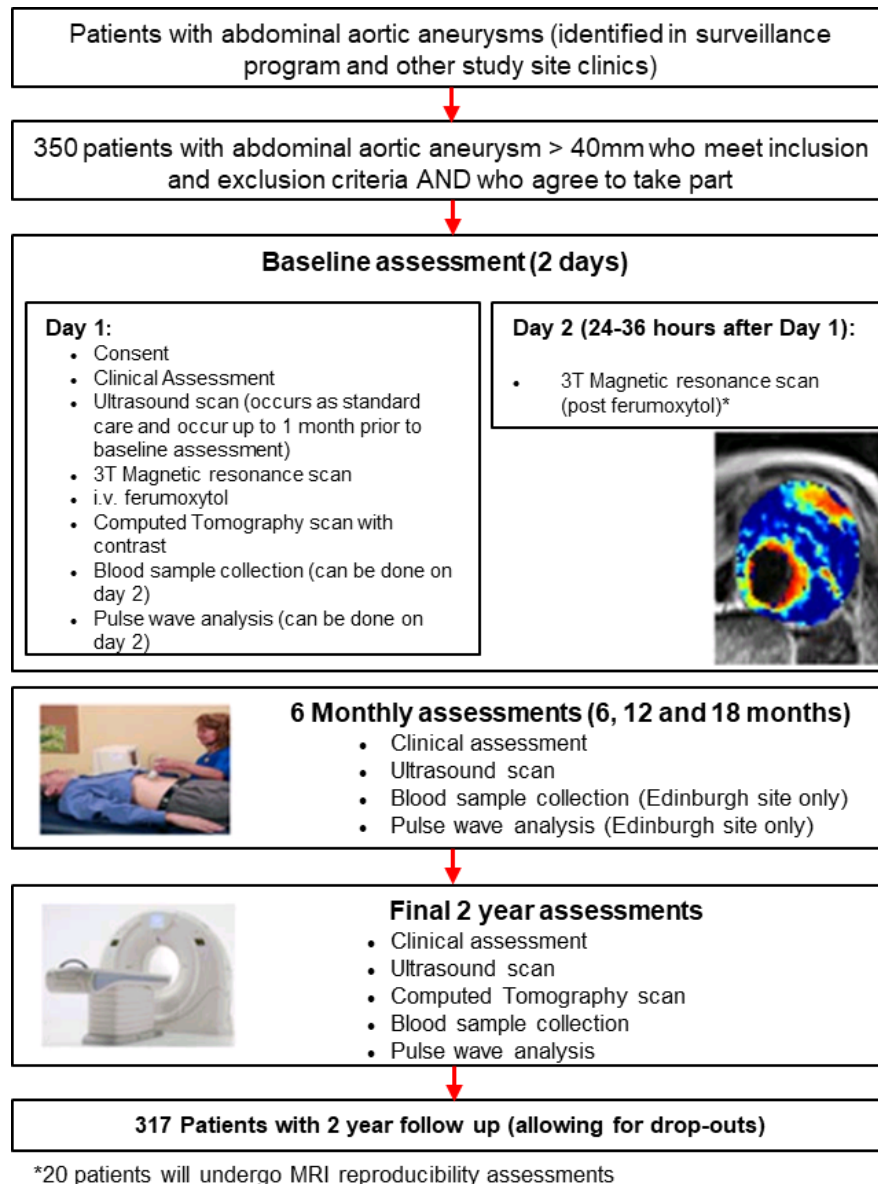
Figure 2.22: MA3RS study protocol flow chart. (i.v. stands for intravenous)[175].

2.5.2.2.1 Ultrasound

Recruited patients received a baseline ultrasound scan (3.5 MHz linear array transducer) as part of the screening process, which provided longitudinal B-scan images of the AAAs to determine maximum antero-posterior (AP) diameter at baseline. After this, ultrasound scans were conducted every 6 ±2 months by accredited clinical vascular scientists in the 3 participating centres.

2.5.2.2.2 CT

Patients underwent contrast-enhanced CT imaging at baseline (or within 1 month) and at 2 years. A 320-multidetector CT scanner (Aquilion ONE; Toshiba) was used in Edinburgh, and a 64-multidetector CT scanner (Brilliance 64; Philips) was used in Glasgow. Anatomical regions of interest (ROIs) were manually segmented on the resulting CT images. The length of the max AP diameter for each AAA was also documented.

2.5.2.2.3 MRI

2.5.2.2.3.1 Anatomical

The position of the AAA was initially identified with the use of coronal and sagittal T_2-weighted (T_2W) multi-slice HASTE sequences with breath-holding.

Anatomical information was obtained with the use of T_2W turbo spin echo sequences, with and without Spectral Attenuated Inversion Recovery fat suppression (TR/TE 2500/252 ms; 365x384 matrix; slice width 5mm; field of view 300x400 mm).

2.5.2.2.3.1.1 Manual Segmentation of ROI

Regions of interest (ROIs) corresponding to the lumen, thrombus and aortic wall were manually drawn on each slice of the anatomical T_2W scans (Figure 2.23 and Figure 2.24) by clinical observers using SliceOmatic 4.3 (TomoVision). Scans with or without fat suppression would be used, depending on the quality of the images.
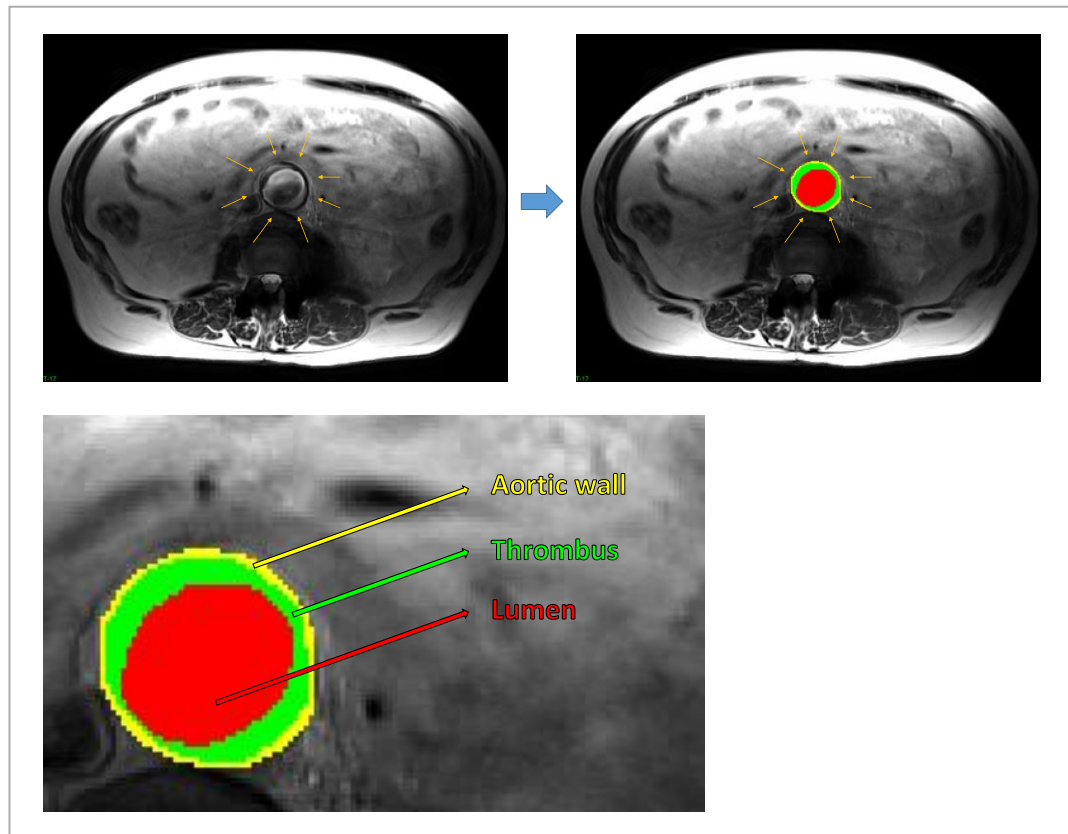
Figure 2.23: Regions of Interest in AAA. *Transabdominal transverse T_2W MRI slice on a level near the centre of AAA (cross-section of AAA). The ROIs have been manually segmented (using SliceOmatic software by TomoVision): the aortic wall is depicted in yellow, the thrombus in green and the lumen in red.*

All available sets of scans were registered to the anatomical T_2W images using bespoke automatic multi-parametric registration software created by members of our research group [176]. The ROIs that had been defined on the T_2W images were then applied to the registered sequences of MRI scans available (e.g. pre-USPIO T_2*W, post-USPIO T_2*W).
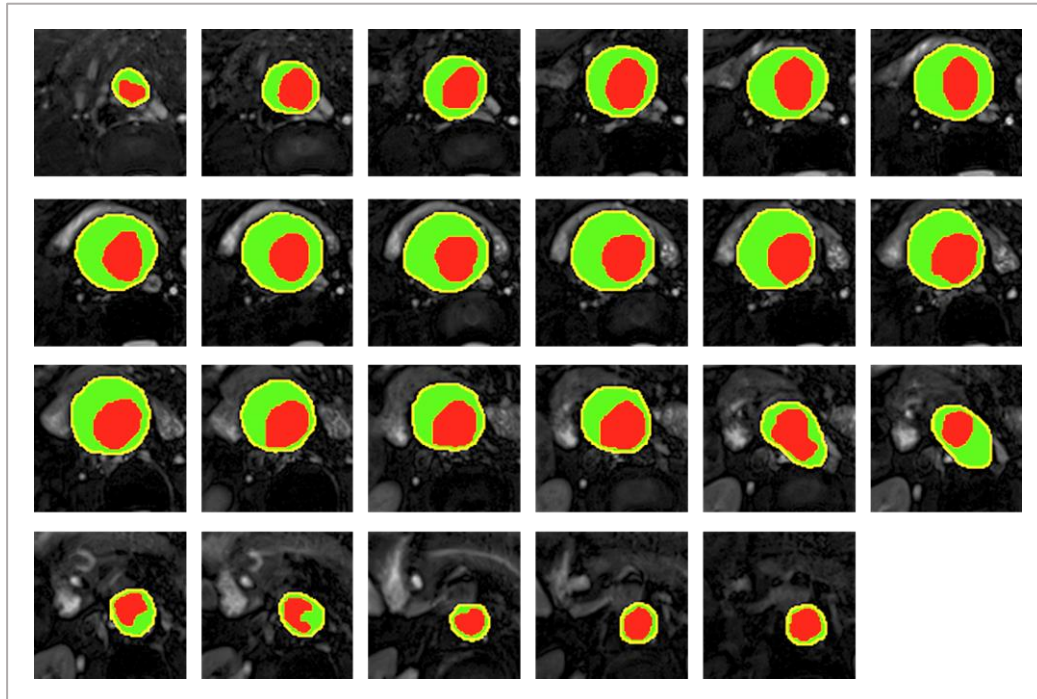
Figure 2.24: Regions of Interest (ROIs) throughout whole AAA. *Example of all manually segmented ROIs on all 23 transabdominal transverse MRI slices of an AAA.*

2.5.2.2.3.1.2 USPIO detection

Participants had a baseline 3-T MRI scan (Magnetom Verio 3T scanner, Siemens Healthcare, Erlangen, Germany), followed by a USPIO injection (4 mg/kg of ferumoxytol; Rienso). They subsequently underwent a second MRI scan within 24 to 36 hours of the USPIO administration.

For the USPIO detection, a multi-echo, gradient echo T_2*W sequence (TE 4.9, 7.7, 10.5, 13.3 ms; TR 133 ms; flip angle 15°; matrix 192x256; field of view 400x400 mm; slice width 5 mm) was used for the pre-contrast and post-contrast scans.

2.5.2.2.3.1.3 T_2* map generation from echoes and noise filtering

An algorithm accompanied with a GUI (Graphical User Interface) for T_2* map generation had been previously created in-house in MATLAB R2015a (The

MathWorks, Inc., Natick, MA, USA), in order to ensure that we had full control of all the levels of image processing applied on the MRI data after extracting them from the scanner.

For the generation of T_2* maps, the four echoes in the multi-echo T_2*W sequence were combined, as described in section 2.3.1.4. The T_2* mapping software imports the four echoes for each patient and initially applies a Gaussian smoothing filter on each echo to reduce noise. The selected filter has a window size of [3x3], which was determined experimentally.

Next, the r^2 coefficient of determination (the proportion of the variance in the dependent variable that is predictable from the independent variable) is used to identify data that do not present an acceptable straight line fit when the log of signal intensity is plotted against echo time. These data points are then excluded from the T_2* processing.

A threshold for noise level is also applied to further identify voxel eligibility. For the voxels excluded from the processing, an effort to replace them is made, by extracting information from the surrounding voxels and interpolating [15]. Any voxels that cannot be reliably replaced with interpolated values, are replaced with zero values, as illustrated in Figure 2.25. These zero values can be later selected and excluded from further processing.
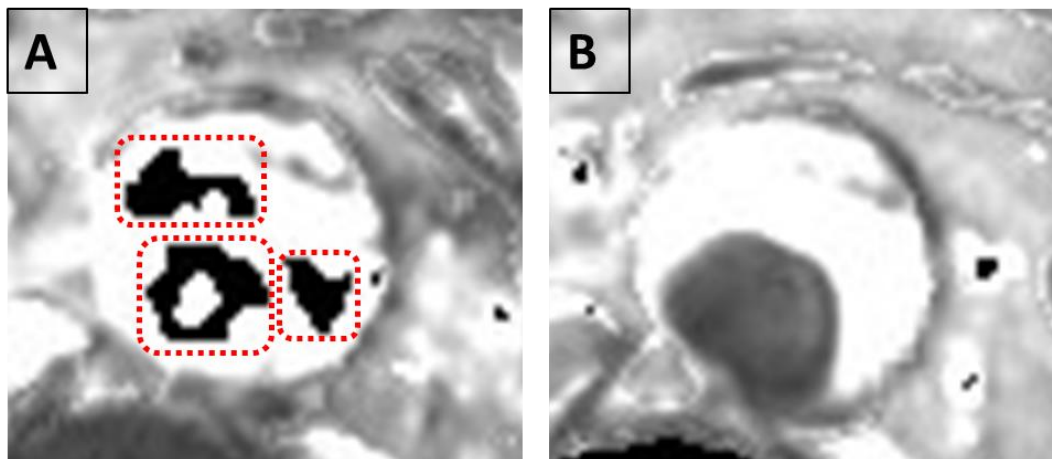
Figure 2.25: Low quality voxels in T$_2$* map generation from echoes. *A pre-USPIO T$_2$* map is shown in A and the corresponding post-USPIO T$_2$* map is shown in B. In A, the marked voxels could not be reliably replaced with interpolated values, so were replaced with zero values, thus appear black in the image.*

The output of the software is a pre-USPIO T$_2$* map, depicting T$_2$* values for each voxel (Figure 2.26 A) and the corresponding post-USPIO T$_2$* map (Figure 2.26 B). Colour maps (of change) are also produced, showing the percentage change per voxel in T$_2$* value (%ΔT$_2$*) after the administration of USPIO, as shown in Figure 2.26 C.

The regions with very significant changes (significance level here considered above 71%) represented USPIO uptake. Histology was also conducted on samples of aortic wall from patients undergoing surgical repair within 28 hours of USPIO administration and the presence of USPIO was verified.
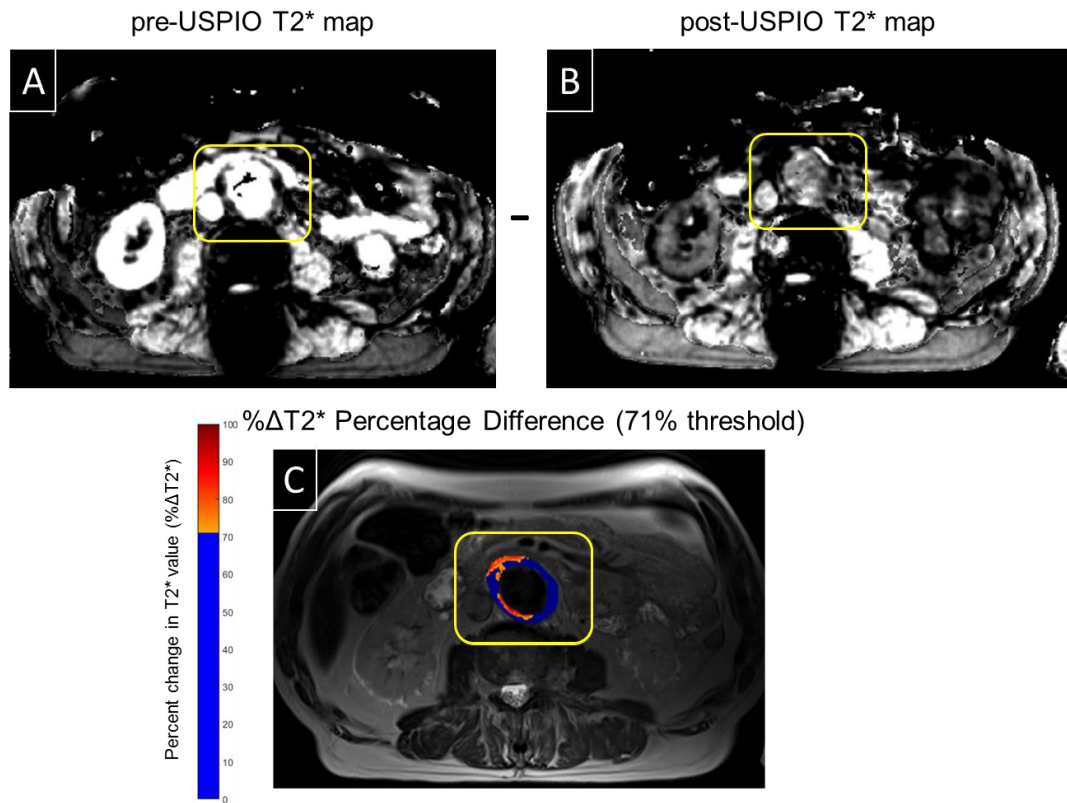
Figure 2.26: Representation of ΔT_2^* as a means of USPIO uptake visualisation within the AAA. *The AAA can be seen within the highlighted yellow area. A representative AAA slice is used for this example of $\%\Delta T_2^*$. The pre-USPIO (A) and the post-USPIO (B) T_2^* maps are calculated from the combination of 4 corresponding gradient echoes. The percent change in T_2^* values (ΔT_2^*) between them is then calculated and visualised in form of a colour map (jet scale) superimposed on the corresponding T_2W anatomic image (C). As can be seen in the colour bar, changes smaller than 71% are considered insignificant and are represented as 0% (blue). (Source of data used for this image: The MA^3RS Study.*

"Dropout" areas

In the ΔT_2^* map depicted in Figure 2.27, two dark areas have been marked, corresponding to voxels that had to be excluded from further processing (due to low quality, as described in the previous section). These areas will hereafter be referred to as "**dropout areas**"; they appear black in the figure because their intensity values have been replaced with zeroes.
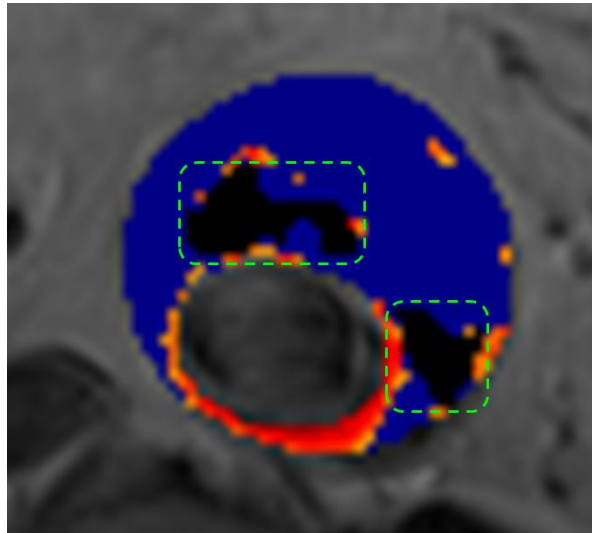
Figure 2.27: Two "dropout" areas on ΔT₂* map. *The voxels corresponding to these areas have been replaced with zeroes (and thus appear black) in order to be excluded from further processing.*

2.5.2.2.3.1.4 ΔT₂* Threshold Decision

In order to identify a threshold above which the USPIO uptake would be considered significant, the methodology applied in the pilot study was used, as described in section 2.4.2. For the MA³RS study, a group of 20 patients underwent reproducibility MRI scans within one month of the baseline scan. The percent change in T_2* values (%ΔT_2*) was calculated for each voxel. The threshold was produced by calculating the 95th percentile value for the %ΔT_2* and averaging it for all 20 patients, thus resulting in the value of 71%.

2.5.2.2.4 Classification

The manual classification methodology applied on the MA³RS dataset was similar to the methodology implemented in the Pilot Study (section 2.4.3).

The %ΔT_2* colour maps were reviewed by two independent observers, blinded to patient demographics, AAA diameter, and growth rate. The AAAs were subsequently classified into 3 groups depending on USPIO enhancement:

1. AAAs without USPIO enhancement (Group 1 of pilot study, Figure 2.20 A)

2. AAAs with indeterminate USPIO enhancement (Group 2 of pilot study, Figure 2.20 B)

3. AAAs with USPIO enhancement (Group 3 of pilot study, Figure 2.20 C)

If there was significant disagreement over classification of a subject, additional review of the data was performed, and group consensus was agreed upon.

Very few cases of Group 2/ indeterminate USPIO enhancement were detected in the MA[3]RS study, possibly due to the comparatively higher quality of data (improved scanning protocol, no gaps between slices in MRI scanning sequences). It should also be noted that the outcome (annual AAA growth) of AAAs labelled as Group 2 was not significantly different to Group1 AAAs in the pilot study.

Chapter 3   Image Processing Background

This chapter introduces some basic image processing background, covering methods such as clustering and more specifically k-means clustering. These concepts may be useful to the reader for better comprehension of the techniques applied in Chapter 5.

3.1 Introduction

One of the aims of this thesis was to automate the manual detection of concentrated inflammation ("hotspots") within the AAA. Hence, a computerised segmentation method was desirable for application to the calculated %ΔT$_2$* difference maps of USPIO uptake in order to identify and "single out" candidate areas, particularly when employed in large studies, such as the MA[3]RS trial.

Image segmentation techniques can be broadly grouped into three categories [177]:

- Edge-based methods
- Pixel-based methods
- Region-based methods

The %ΔT2* difference maps in the previous pilot study were presented in the form of colourmaps to assist easier visual interpretation and presentation [15]; but the underlying data consisted of grayscale images which corresponded to signal intensity values. The percentage change in T$_2$* within a pixel was then related to the degree of localised USPIO uptake. Since the %ΔT2* difference maps were therefore created on a pixel-by-pixel basis, a **pixel-based** segmentation method was reasoned to be appropriate to explore in this thesis. The most commonly used pixel-based segmentation techniques are **optimal global thresholding** and pixel classification through **clustering** [178]. An optimal global threshold was applied in the MA[3]RS project after empirical determination of a suitable threshold level (i.e. 71%) to %ΔT2* difference maps [179], as detailed in (Chapter 12.4.2). However, applying a global threshold in this manner may remove some potentially significant information that could describe the range of USPIO uptake within and around a "hotspot". In particular, application of a global threshold may also remove some interconnectivity between areas of uptake when subsequently viewed in three dimensions. It is potentially

important to classify an aneurysm as having several small hotspots of inflammation, or one large interconnected area of inflammation throughout the aneurysm. Automatic detection of USPIO uptake using non-thresholded data has the potential to yield more useful information than analysis that has had a global threshold applied. In a bid to therefore avoid the use of a global threshold in the automatic processing, clustering of non-thresholded data was one of the methods tested (see Chapter 5) and the one eventually used in the final algorithm. Therefore, additional relevant background of clustering is outlined below.

3.2 Clustering

Organising information into meaningful groups is one of the most intuitive and fundamental ways of understanding and solving problems with complex data [180].

Clustering or ***Cluster Analysis*** is the study of methods and algorithms used in order to organise data by discovering and representing an underlying structure of "natural groups" or hierarchies [180], [181]. The given number of objects or variables is thus classified into groups based on their common characteristics or similarities [182]. Alternatively, rather than a search for similarities, observations of differences among the data could also be used to create mutually exclusive groupings for Clustering [183].

After being clustered, the objects within each group, called a ***cluster***, have more similar defined "traits" with each other rather than with objects belonging to different clusters [184].

A first step to be taken in the application of clustering the objects within the group is to observe the group and decide which object feature would enable the best classification to achieve a desired result (in this case, "appropriate" grouping of the objects). Such a choice of object feature among the characteristics available for a dataset is known as ***feature selection***.

In general, clustering algorithms attempt to reveal hidden patterns, which would be impossible for the human eye to discern, among large unlabelled datasets that are more complicated than this simple example, (i.e. without any prior class knowledge or category labels as a prerequisite).

3.2.1 History of Clustering - Applications

Clustering started being popular in computer science in the 1970s, with applications in feature selection demonstrated on a speaker identification database presented as early as 1978 [185].

More specifically for **medical image segmentation applications**, various types of clustering have been previously used. A brief overview of common methodologies is presented (not exhaustively) in: [186]–[190][191], [192][193]–[195][196][197].

Despite the fact that Clustering can contribute to highly automated processes, it is important to allow a certain degree of human control and intervention in the processing, especially in cases where data analysis may have significant ramifications (e.g. analysis of medical data). Clusters can be best defined and interpreted by experts in the field of the specific application being considered [180] In the case of medical data clustering, clinical experts should be involved in the assessment of the clustering output, to help ensure clinical validity of the results of the analysis.

3.2.2 Types of Clusters

Clusters can be categorised in different types, depending on the relationships between the objects belonging to the same or different clusters. Different kinds of clusters have been previously described [198], [199]. In the case of the k-means clustering applied to medical imaging described in this thesis the focus lies on "prototype" or "centre-based" clusters.

Prototype-based or centre-based clusters

In the case of **prototype-based** or **centre-based clusters**, each object is closer to the centre of the cluster it belongs to than to the centre of any other clusters, as depicted in the simplified case of 4 clusters in Figure 3.1 [199].
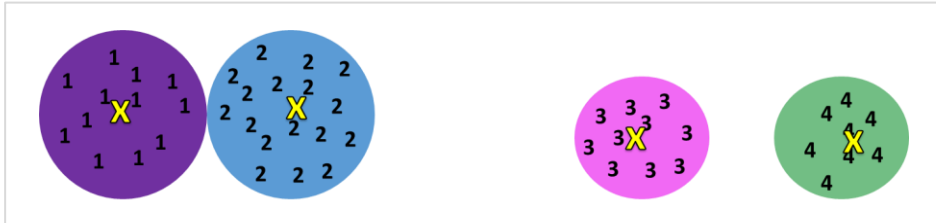
Figure 3.1: Four prototype-based/centre-based clusters. *Each object is closer to the centre of the cluster it belongs to than the centre of any other clusters. The centres of the clusters correspond to the cluster centroids and are marked with yellow "x" symbols.*

3.2.3 Number of Clusters

Since in most clustering applied to medical imaging we generally do not have pre-labelled data (i.e. we are performing "unsupervised" learning), the choice regarding the number of clusters, k, to be used to bin the data is an important issue. This number depends on factors such as the type of data available, the total number of objects in the group, the features selected, and the noise levels. There are some documented efforts to standardise the selection of the number of clusters but with varying levels of success, and there is to date no universal rule [200]–[202].

In the simplified example depicted in Figure 3.2, the initial points get classified in different groups depending on the number of clusters used in the algorithm. Different shapes represent membership to different clusters.
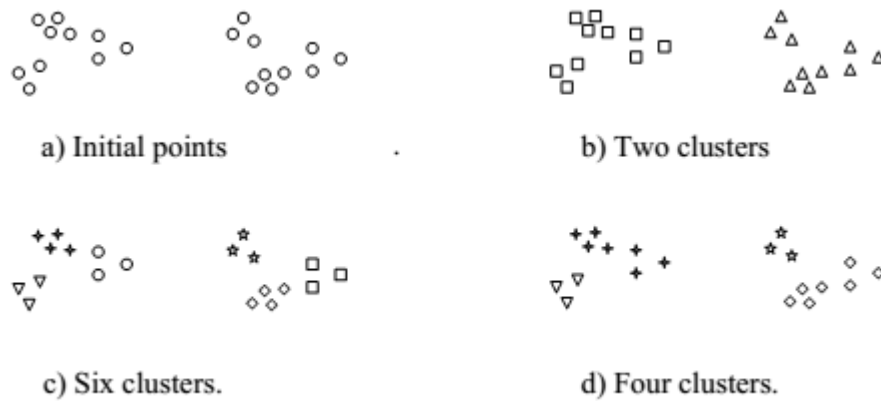
Figure 3.2: Simple example of clustering a set of an initial set of points using 2, 3 or 4 clusters per classification [203]*.*

It should be noted that clustering algorithms always give results, meaning that even an 'irrational' choice of cluster number (e.g. choosing too many clusters while trying to segment a low-quality image) will give a classified version of the initial points. Additionally, all objects are forced into one of the available clusters unless specific exceptions are defined to allow any objects to remain unclustered.

3.2.4 Operational Definition – Clustering Steps

An operational definition of Clustering could be described as:

"Given a representation of *n* objects, find K groups based on a measure of similarity such that the similarities between objects in different groups are low" [182].

Further to this definition, the Clustering process can be broken down into a set of steps, based on which Clustering Algorithms can be designed. A typical sequence of tasks to be followed for pattern Clustering would be [180], [184]:

A. Pattern Representation (potentially with feature extraction and/or feature selection included)

B. Proximity Measure Definition (depending on data type/characteristics)

C. Clustering of data

D. Data Abstraction (only if necessary)

E. Output Evaluation (only if necessary).

These tasks are covered in more detail in the following sections.

A. Pattern Representation

Pattern Representation pertains to the choice of number of clusters selected, the patterns available, as well as the characteristics or *features* (size, type, scale) of the data that are accessible to the specific clustering algorithm.

With the input in this case being in the form of grayscale images, the dataset available is usually a 2D matrix of intensity values. In the case of a colour image, it is represented as a 3D matrix, with each pixel represented by 3 colour values (red, green, blue).

Feature extraction is the process of applying various processing techniques to the initial given features, in order to obtain a set of new features, more suitable for the clustering algorithm at hand [204], [205].

Feature selection is the process of selecting an optimal subgroup of features based on a specific criterion [206].

Importantly, in real life applications of Clustering, the data are seldom as easy to classify as in the simplified example described in this chapter. Commonly, there is noise present among the datasets, outliers in the groupings, and the objects to be processed are much more diverse.

B. Proximity Measure Definition

Proximity in Clustering is usually measured by calculating a distance or similarity between pairs of patterns [184], [207]. There are various different methods for calculating proximity [184], [208], [209], but in this context, the interest is in distance measures between points.

Here, Euclidean distance is introduced, as it is the method used in the algorithms developed in this work.

Euclidean Distance

Also known as *Pythagorian distance* or *Beeline distance*, the *Euclidean metric* calculates the "as-the-crow-flies" distance between two points [210], [211]. It is probably the most widely-used metric for continuous features, as it provides an intuitive way of calculating the proximity between subjects in two-dimensional and three-dimensional environments [184].

In Cartesian coordinates, if $x = (x_1, x_2, \dots, x_n)$ and $y = (y_1, y_2, \dots, y_n)$ are two points in the Euclidean n-space, then the *Euclidean Distance* $d(x, y)$ between x and y is depicted in Equation 3.1:

$$d(x,y) = \sqrt{\sum_{i=1}^{n}(x_i - y_i)^2}$$

Equation 3.1
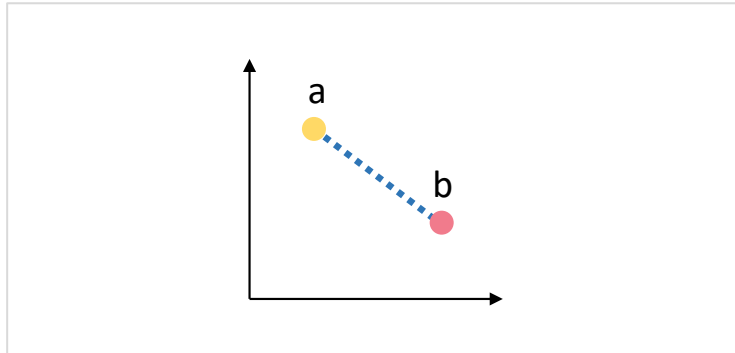
Figure 3.3: Euclidean distance between two points a and b.

In Clustering, the Euclidean distance is a good metric to be used when the dataset to be clustered has "compact", or "isolated" clusters [184], [212].

Depicted in Figure 3.3 in the dashed line, are the Euclidean distances between different points.

C. Clustering of data

The Clustering step can utilise a wide variety of clustering methods which are too varied to adequately cover within this thesis [198]. The k-means clustering applied in this thesis specifically uses partitional clustering.

In *partitional clustering*, the dataset is divided into non-overlapping clusters, such that each point only belongs to one cluster, as shown in Figure 3.4.
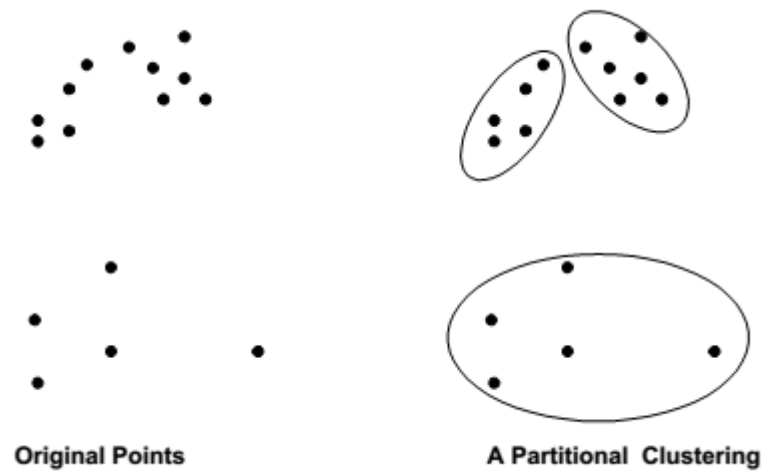
Figure 3.4: Partitional Clustering [199]*.*

Among partitional algorithms, *k-means clustering* is the most widely used and will be described later in this chapter in detail [182].

D. Data Abstraction

Data abstraction is the process of discovering representative patterns or prototypes among the datasets [184]. A common example is the use of *centroids* and *medoids* as data abstractions: the data belonging to a cluster can be represented by the average of all the objects within the cluster (centroid), or the most representative object (medoid) [208].

Depicted in Figure 3.5 is an example of the centroids of two clusters.
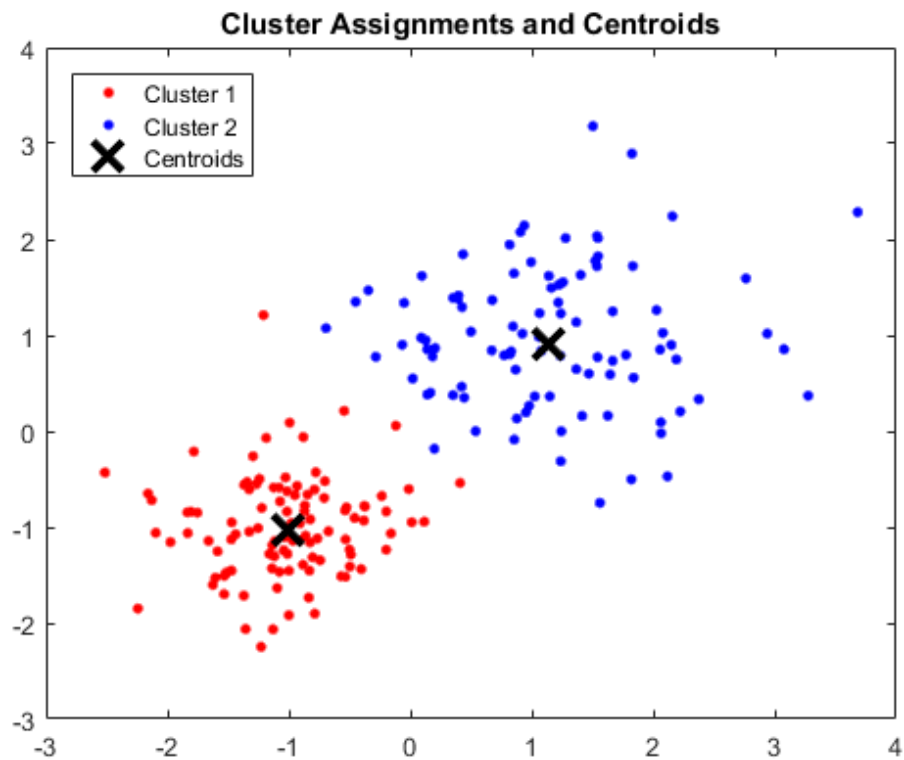
Figure 3.5: Centroids of two clusters. *The datapoints have been assigned to two clusters (depicted in red for cluster 1 and blue for cluster 2) and the centroids of the clusters are marked with an "x" symbol. The centroids can be used to represent the corresponding clusters (Image source: MATLAB Documentation* [213]*).*

E. Output Evaluation

Output evaluation, or *Cluster validity analysis* [184] can be described as the assessment of the resulting clusters of the process, based on certain chosen criteria.

Very often a "gold standard" or "ground truth" is used as output evaluation. In the case of medical image analysis, clinical feedback from appropriately trained experts provides a degree of ground truth for output evaluation.

Regarding the specific algorithms created within this PhD work for the automatic detection of areas of inflammation ("inflammatory hotspots"), the output was evaluated against the output of the manual processing of the same datasets, as executed by trained clinicians.

In the case of binary predictive output, a *confusion matrix* (or *table of confusion*) as shown in Figure 3.6, can be used for evaluation. In a confusion matrix, the predicted outcomes are compared against the actual outcomes, with 4 possible combinations:

- *True Positive (TP):* correctly predicted event/positive outcome

- *False Positive (FP):* incorrectly predicted event/positive outcome

- *True Negative (TN):* correctly predicted non-event/negative outcome

- *False Negative (FN)*: incorrectly predicted non-event/negative outcome

False Positive (FP) is also known as *Type I error* and False Negative (FN) is known as *Type II error*.

Predicted Outcome

	Positive	Negative
Positive	True Positive (TP)	False Negative (FN)
Negative	False Positive (FP)	True Negative (TN)

True Outcome

Figure 3.6: A confusion matrix used to evaluate the output of predictive binary clustering. The predicted outcome is compared against the true outcome, resulting in 4 combinations: TP, FN, FP, and TN.

With the use of TP, FP, TN, FN, common metrics can be calculated for further analysis of the output [214]. The most commonly used metrics are *Sensitivity* and *Specificity*. In a diagnostic context, sensitivity evaluates the ability of a test (or algorithm) to correctly detect the patients who do have a condition as positive to this condition [215]. Specificity assesses the ability of an algorithm to correctly identify the patients who do not have a condition as negative for the condition.

- *Sensitivity* or *Recall* or *True Positive Rate (TPR):*

$$TPR = \frac{TP}{P} = \frac{TP}{(TP + FN)}$$

- *Specificity (SPC)* or *True Negative Rate:*

$$SPC = \frac{TN}{N} = \frac{TN}{(TN + FP)}$$

Some other metrics used for output evaluation are:

- *Precision* or *Positive Predictive Value (PPV)*:

$$PPV = \frac{TP}{(TP + FP)}$$

- *Negative Predictive Value (NPV)*:

$$NPV = \frac{TN}{(TN + FN)}$$

- *Fall-out* or *False Positive Rate (FPR)*:

$$FPR = \frac{FP}{N} = \frac{FP}{(FP + TN)} = 1 - SPC$$

- *False Negative Rate (FNR)*:

$$FNR = \frac{FN}{(TP + FN)} = 1 - TPR$$

- *False Discovery Rate (FDR)*:

$$FDR = \frac{FP}{(TP + FP)} = 1 - PPV$$

where P = (number of) positive events, N = (number of) negative events.

3.2.5 K-means Clustering

I make use of k-means clustering in the work presented in this thesis, as it is a standardised clustering methodology [177]. Its robustness to applications in medical imaging and the unsupervised nature of the processing made it an appealing choice. Methodologies developed in my thesis would not be dependent on sourcing large volumes of training data and potentially more easily transferable to images from other scanners and databases.

The k-means algorithm finds a partition in which objects within each cluster are as close to each other as possible, and as far from objects in other clusters as possible. The choice among the different distance measures available depends on the kind of data being handled. K-means uses centroids of clusters as data abstraction (see Figure 3.5).

3.2.5.1 Basic Algorithm

The basic steps of the k-means algorithm are as follows [216]:

Basic K-means Algorithm

1. Select K points as initial centroids.

2. **repeat**

3.   Form K clusters by assigning each point to its closest centroid.

4.   Recompute the centroid of each cluster.

5. **until** Centroids do not change.

3.2.5.2 Initialisation

Application of K-means algorithms may give different results on each application, as the algorithm selects centres (cluster centroids) at random. This can be avoided by performing an initialisation step at the beginning of the algorithm. There are many options to choose from, always dependent on the nature of the data at hand: the initial centroids can be selected at random, or using a specially adapted approach, or popular algorithms such as Kaufman, Forgy, or MacQueen [217]–[219].

In the case of the k-means clustering applied for the hotspot segmentation presented in this thesis, the initial centroids were spaced uniformly along the grey level axis.

3.2.5.3 Number of clusters

There are a variety of methods that can be used to decide the number of clusters to be used in k-means (see section 3.2.3). For example, a popular technique described by Matthew Fawcett in 2015, uses Histogram Analysis: the basic theory involves plotting the histogram of the initial data and, after some thresholding and de-noising, counting the number of peaks which should give the number of clusters to be used [220].

The number of clusters in this application was experimentally determined, as will be explained in more detail in Chapter 5.

3.3 Summary

This chapter provides an overview of the basic theory of clustering, key steps in the application of the methodology, and the specific case of using k-means clustering in the analysis and segmentation of medical imaging data. The application of k-means clustering to develop an automated detection method of "hotspots" of inflammation within the aneurysms of the MA³RS cohort is discussed in later chapters.

Chapter 4   AAA Measurements: US vs. CT vs. MRI

4.1 Introduction

In this chapter, the currently available methods used to assess AAA size and growth are briefly described, followed by a critical evaluation of the most common currently used tools for clinical assessment, maximal AP (anterior to posterior) diameter measured with ultrasound.

Using subsets of the MA³RS clinical trial data, I compared AAA measurements obtained with the use of ultrasound (US), computed tomography (CT) and magnetic resonance imaging (MRI), in order to determine the level of agreement between the different modalities. Using CT as a gold standard, adjustments to the currently used 55mm threshold with ultrasound were investigated. I explored alternative measurement and analysis options, aiming to assess which method would be the most reliable to use for AAA size assessment, as well as generating AAA growth calculations, to use as ground truth for the classification of AAAs in subsequent analyses in later chapters (Chapter 6 and Chapter 7).

4.2 Background

4.2.1 Use of maximum anteroposterior diameter and reproducibility of measurements

The clinical method currently most commonly used for AAA surveillance involves the recording of two anterior-posterior (AP) measurements of the maximum aortic diameter (max AP) with US: one measurement is acquired in the transverse plane and the other one in the longitudinal plane. The largest value of these two measurements is used to describe the "maximum diameter" of the AAA. Within current NHS clinical pathways, the use of CT imaging is mainly confined to pre-operative assessments of AAAs, as detailed in section 2.2.2.

There is considerable variation in the specific imaging methodologies applied in many of the published trials assessing patients with AAAs which have contributed to defining current standard clinical care. Different research groups have employed locally defined protocols or clinical services or practices, and it is not uncommon for the detailed methods of US or CT employed to be unreported in publications. In 2012, a review [221] of 56 studies that employed either US or CT for AAA size measurement found that only 32 of them (57%) had fully reported the methods used. In this review, the four specifications of the methodology that were considered essential were: "plane of acquisition", "axis of measurement", "position of callipers" (whether inner or outer aortic wall was used as starting and finishing point of measurement) and "selected diameter" (e.g. maximum AP, maximum in either axis, etc.). The great diversity of AAA size measurement methodologies combined with the lack of detailed description introduces a very serious issue of reproducibility between different trials and importantly, problems with setting global threshold values used for clinical assessments and interventions between different centres [222].

Maximum AP diameter (regardless of the imaging modality used to measure it) became the common clinically adopted gold standard for AAA size measurement

most probably because of its adoption by the UK Small Aneurysms Trial (UKSAT) [110], [223], [224] which took place between 1991 and 1998 and was considered a landmark trial. However, the selection of the maximum AP diameter as the most appropriate method employed in that trial was based on a pilot study with only 10 patients [225], which measured the reproducibility of AP measurements and transverse measurements, finding the AP measurements to be more reproducible.

Previously to this, Nevitt [226] had used "maximal transverse diameter", **either anteroposterior or lateral**, measured in centimetres, for AAA size assessments, in order to keep consistency with older studies.

More recently, in another milestone trial, namely the Multicentre Aneurysm Screening Study (MASS) [227], the maximal transverse diameter of the aorta in transverse (axial) plane was measured, followed by the maximal AP in longitudinal plane. The **largest** diameter of these two was reported.

4.2.1.1 AAA Growth

The rate of AAA growth is one of the criteria considered for surgical review, with growth over 1.0 cm per year being the threshold [110]. Additionally, a study on growth rates of AAAs in Japanese patients with a sample of 124 patients concluded that AAAs growing by at least 3 mm per year should be considered for surgery, even if their AAA is smaller than 5.0 cm (their suggested threshold for intervention is 5.0 cm rather than the 5.5 cm level used by the NHS in the UK) [113], [228].

Importantly, many studies [80], [82], [236], [228]–[235] use growth as an outcome in the absence of rupture events, but measure it with different imaging modalities and protocols.

It is therefore important to establish the bias between different measurement methods in calculating AAA growth.

4.2.1.2 Agreement between US, CT and MRI

A number of studies have assessed the levels of agreement in AAA measurements between US and CT [128], [225], [237]–[242], with 7 out of 8 demonstrating that US underestimates the aortic diameter by mean differences of 0.1 to 9.4 mm. Only one study found the US to overestimate the diameter size compared with CT [225]; this was however based on a sample of only 10 subjects, which was the smallest sample among the 8 studies.

A more recent study [241] validated the accuracy of CT measurement of AAAs by scanning a silicone AAA replica phantom of known size and finding no significant difference between the real and the CT-acquired measurements. It then proceeded to identify the bias between CT and US measurements of AAA diameters of 123 patients and found significant differences between the two modalities, with US underestimating the aortic diameter by a mean difference of 2.1 (±3.9) mm (mean difference ± 1.96 SD). Subgroup analysis revealed a greater mean difference of 3.9 (±3.5) mm for AAAs of size 5.0 to 5.4 cm, compared with AAAs of size ≥5.5 cm. With the threshold for surgical management in the UK at 5.5 cm [113], this bias would cause 31% of that study cohort to be misclassified when screened with US.

More recently in 2014, another study [242] which looked into the reproducibility of US measurements for AAA Screening found that, compared with CT, US consistently under-estimated the size of the aorta, with mean differences ranging from 2 mm to 5 mm, depending on the specific protocols used. This group therefore suggested that this underestimation could be reducing the sensitivity of the tests used by the NHS AAA Screening Programme (NAAASP) [113].

In the literature, a few studies have explored the difference between CT and MRI measurements in various tissue types. For example, in a 2012 study [136], measurements of visceral adipose tissue in humans obtained with CT and MRI were compared: a mean bias of -2.9% as a portion of total abdominal area was found in visceral adipose tissue and +0.4% for subcutaneous adipose tissue. A comparison between MRI and CT [243] imaging of the thoracic aorta concluded that MRI may satisfactorily replace CT for aortic measurements.

A study more specific to AAAs [244] that compared aortoiliac arterial measurements before endovascular abdominal aortic aneurysm repair (EVAR), demonstrated that the inter-modality agreement between contrast-enhanced CT and unenhanced MRI was good-to-excellent and adequately high compared to inter-observer and intra-observer intra-class correlation coefficients. The authors of the study concluded that even though contrast-enhanced CT continues to be the gold standard for pre-EVAR assessment, it can be successfully replaced by unenhanced MRI in the presence of contraindications for CT.

4.2.1.3 Use of maximum anteroposterior diameter

As will be shown in the Results section (4.5.3), the use of maximum AP diameter (max AP) might be a very restrictive method, as it does not take the shape of the AAA into consideration, which may be non-circular in cross-section. This can be seen in the case of the axial MRI AAA slice in Figure 4.1, where the length of the max AP diameter (55.2mm) is smaller by 11.8 mm than the maximum general (regardless of direction) diameter (67mm).
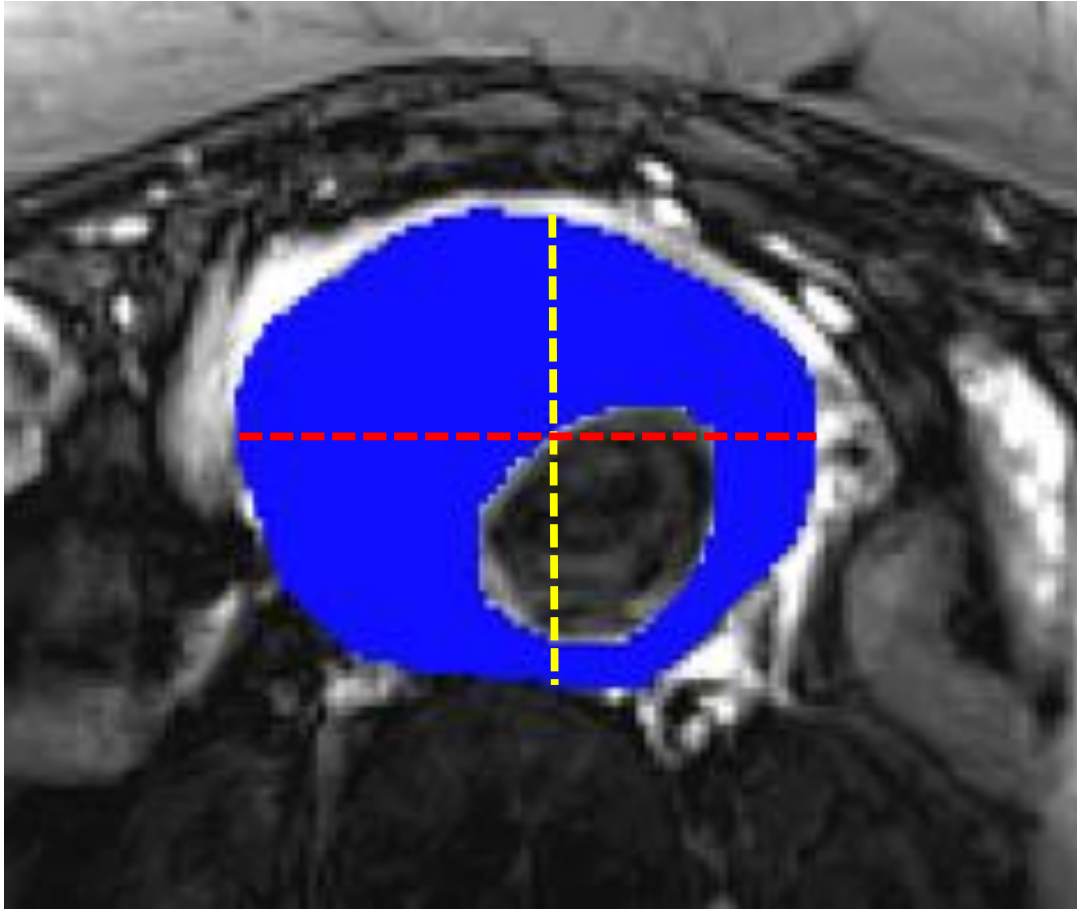
Figure 4.1: Maximum AP Diameter vs. Maximum General Diameter. *Segmented T₂-weighted cross-sectional axial MRI slice of an AAA which appears non-cylindrical. The blue area represents the thrombus and aortic wall combined and the lumen area has been left uncovered. In yellow, the max AP measurement is measured as 55.2mm. In red, the maximum diameter of the AAA shape (regardless of direction) is 67mm, and therefore 11.8 mm larger than the max AP.*

AAAs appear in a variety of shapes, and measurements based solely on the AP axis in the transverse plane cannot differentiate between AAAs of significantly different total sizes, as shown in the example cases in Figure 4.2, where, despite the almost identical values of AP diameters of the two slices as measured with MRI (0.1 mm difference between them), the total area of the slice (as shown in blue) on A is smaller than the total area of the slice on B by 434.1 mm², as well as the lateral diameter of A being obviously smaller than that of B.
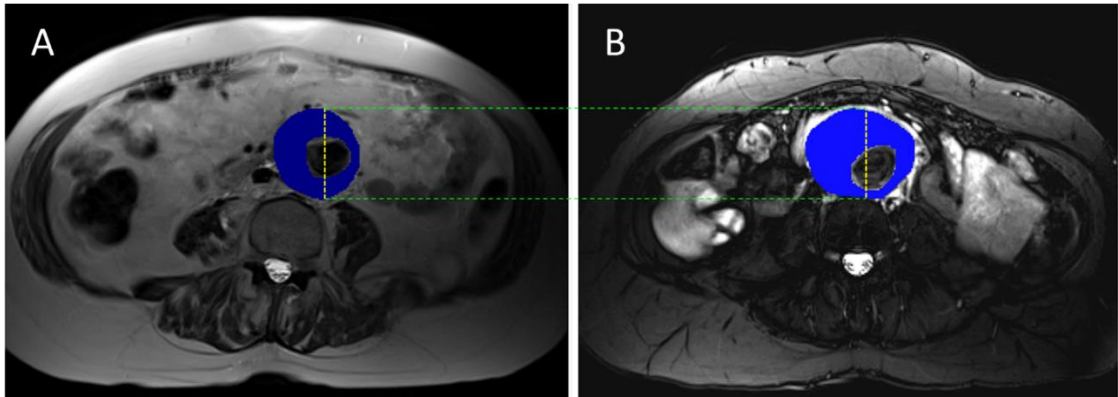
Figure 4.2: Two different AAAs with equal max AP diameters, but different max Areas (max slice Area per AAA). *T_2-weighted MRI scans, with the blue superimposed area representing thrombus and aortic wall combined and the lumen area in the centre uncovered. **A:** MRI max AP diam = 55.3mm, max Area = 2517.5mm². **B:** MRI max AP diam = 55.2mm, max Area = 2951.6mm². Difference between max AP diameters = 0.1 mm; difference between max Areas = 434.1 mm²*

In a similar manner, growth calculated as the change in maximal AP diameter does not necessarily reflect the growth of the entire AAA: there is no "guarantee" that growth would happen proportionately throughout the whole AAA mass. By using the change in maximal AP diameter to estimate growth, cases of AAAs growing significantly in directions other than AP may incorrectly be classified as stable.

4.3 Aims

For several assessments carried out in this thesis, I needed max AP diameter measurements corresponding varying time points in order to calculate max AP diameter growth and to validate whether AAA diameter is a predictor of AAA growth (see chapter 6). Such measurements were already available as manually-derived US measurements. However, as the literature indicated that US consistently underestimated AAA diameter size compared to CT, while MRI highly agreed with CT measurements, I decided to perform a comparison between the US and MRI measurements in a MA³RS sub-sample. I used CT as point of reference, since it is the currently accepted gold standard for AAA measurement.

The main problem with extracting max AP diameter measurements from MRI or CT is that both MRI and CT AAA scans consist of a very large number of slices, which makes manual calculation of diameter size time-consuming, and with high user-dependent variability. For this reason, it was deemed necessary to design an algorithm which automatically calculates max AP of any previously segmented dataset and to validate it against manual measurements. All MA³RS MRI scans had already been manually segmented by suitably experienced observers, so the algorithm could be applied to these segmentations. The MA³RS CT had not yet been segmented at the time of writing this thesis.

Further to comparing measurements, I was interested in the effect that the use of max AP with US, MRI or CT would have on the calculation of growth and on the classification of patient risk. Finally, I aimed to explore alternative methods of AAA size and growth calculation and compare them against max AP measurements.

4.4 Methods

4.4.1 Statistical Methods

GraphPad Prism version 6 (GraphPad Software, Inc., CA.) and SPSS version 22.0 (IBM Corp.) were used for the statistical analysis in this chapter.

Bland-Altman plots were used to compare different clinical measurement methods, e.g. differences between AAA diameter measurements as measured with MRI, CT and US. Correlation coefficients and regression were also used.

Bland-Altman plots with unit differences and percentage differences were both included in most cases.

Pearson correlation was used, with *correlation coefficient R* ranging from -1 to +1 (with values close to ±1 suggesting perfect correlation and values approaching 0 suggesting no correlation).

The R *squared* (R^2) *coefficient of determination* was also reported for better interpretation of the R value.

In graphs where it was applicable, the *identity line* $x = y$ was plotted with a dashed line to further illustrate the agreement levels of the values plotted (with higher agreement levels being closer to the identity line).

Linear regression was applied when a linear relationship was suggested by the scatterplots of the data. The line of best-fit was plotted with a black line and the 95% confidence intervals were represented by error bars which formed a "confidence band", depicted in light blue.

4.4.2 Ultrasound (US) Measurements

For the MA[3]RS study (described in section 2.5) carried out at the Royal Infirmary of Edinburgh (RIE), standard NHS Lothian protocols were followed. A 3.5 MHz

linear array transducer was placed on the abdomen and an anterior-posterior (AP) measurement of the maximum aortic diameter was reported in centimetres to one decimal place. The measured diameter was taken between the outside edges of the aortic wall, through the lumen. It should be noted that for some of the subjects, there was also a recording of the lateral aortic diameter size as measured at the same level/transverse plane where the maximum AP diameter had been recorded (as seen in Figure 4.3). The lateral measurements however were not incorporated into the MA³RS study, as there was not an adequate number of measurements available for reliable statistical processing.

It was useful for the work presented in this thesis to calculate the maximum AP diameter with MRI using a similar approach to the one manually employed by the sonographers with US scanning so that direct comparison between the two modalities could be made.

To achieve this, close inspection of the US scanning process was necessary. After "shadowing" the sonographer appointed on the MA³RS project during several aneurysm scanning sessions, I created a schematic approximating the various positions and angles that the US transducer might take during an aneurysm examination.

Briefly described, the sonographer scans the AAA axially throughout the length of the abdominal aorta to gain an 'insight' of the aneurysm shape and to locate the widest part of the aorta. After visually identifying the broadest area in the antero-posterior axis on the screen, they record the corresponding maximum AP diameter measurement. The diameters are manually measured on the ultrasound monitor with callipers provided by the software supplied on the various US units used through the lifetime of the study, as shown on Figure 4.3, where the callipers have been placed to measure the maximum AP (A) diameter and the corresponding maximum lateral (B) diameter. Sometimes, several measurements are taken to accurately determine the largest one as identified by the sonographer. It should be noted that this process of scanning the entire AAA

throughout the length of the abdominal aorta to determine the level at which the maximum AP measure is made, is employed during each scanning session for each patient, without reference to any previous scans for that individual. This means that the sonographer may not be calculating the maximum AP measurement at the same head-foot position of the aorta between subsequent scans. Therefore, "growth" of the aneurysm is clinically defined as the change in the maximum AP of the aneurysm, regardless of the exact location in the aneurysm that the maximum AP diameter appears.
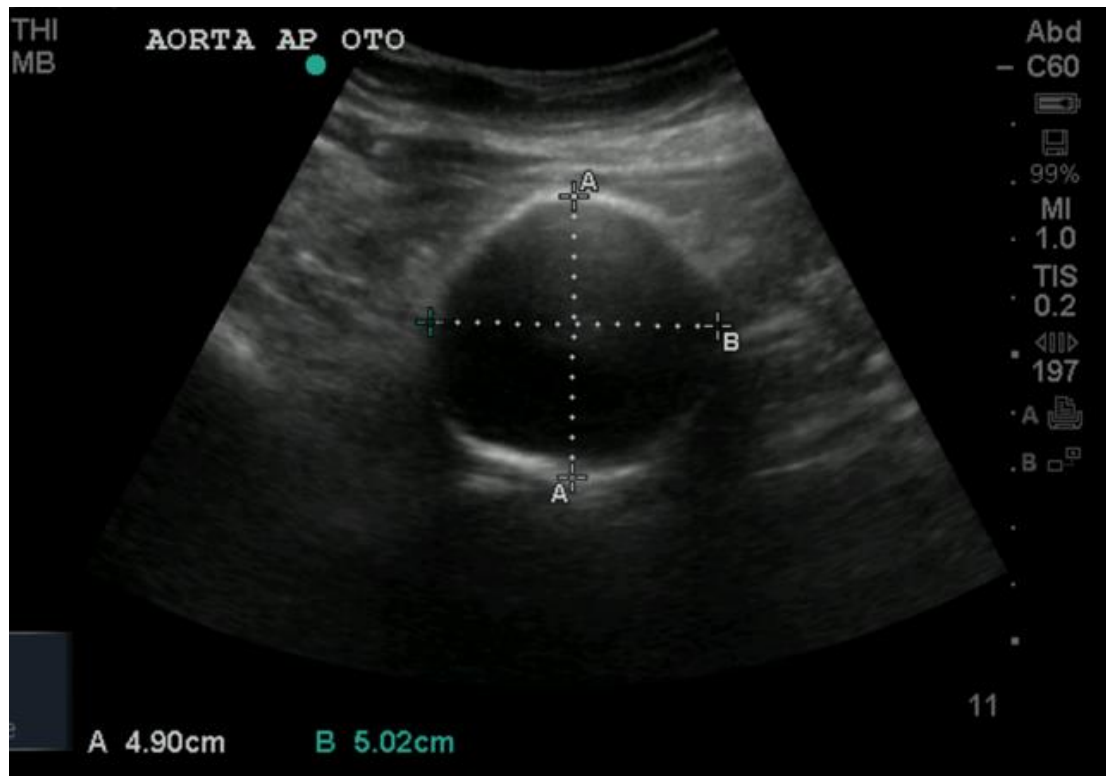
Figure 4.3: US scan of an AAA. *This is a typical transabdominal transverse US scan of the aorta of a MA³RS trial patient, concentrating on the aneurysm mass. Maximum anteroposterior (A) and lateral (B) diameters have been marked and measured (AP diameter size=4.90 cm, lateral diameter size=5.02 cm).*

Importantly, the sonographer who guided me through the US scanning process reported that in cases of doubt over the exact position of the aortic wall due to

noisy scanning, they would select the largest of the possible diameter measurements to record.

According to NHS guidelines [245] the transducer must be held at a 90° angle against the skin. In practice however, issues of reproducibility can be introduced, as the position of the US transducer highly depends on the specific size and shape of the body of the subject being scanned. In the case of AAA screening, factors such as the size and shape of the abdominal area or the presence of gas within the abdominal area can influence the position of the transducer since it is manually operated.

The inter-observer coefficient of variation of 3.5% for AAA diameter measurements has previously been reported [124].

It would be impossible to calculate all variations of the transducer position, but generally they would be expected to consist of a combination of **translation** (Figure 4.4 A) in two axes (the area created between axis x and axis y – the transducer always touches the skin, so no translation in the z axis is present) and **rotation** (Figure 4.4 B) (in all directions, "roll, pitch and yaw", which would appear like "tilting"), or a **combination of both** (Figure 4.4 C).
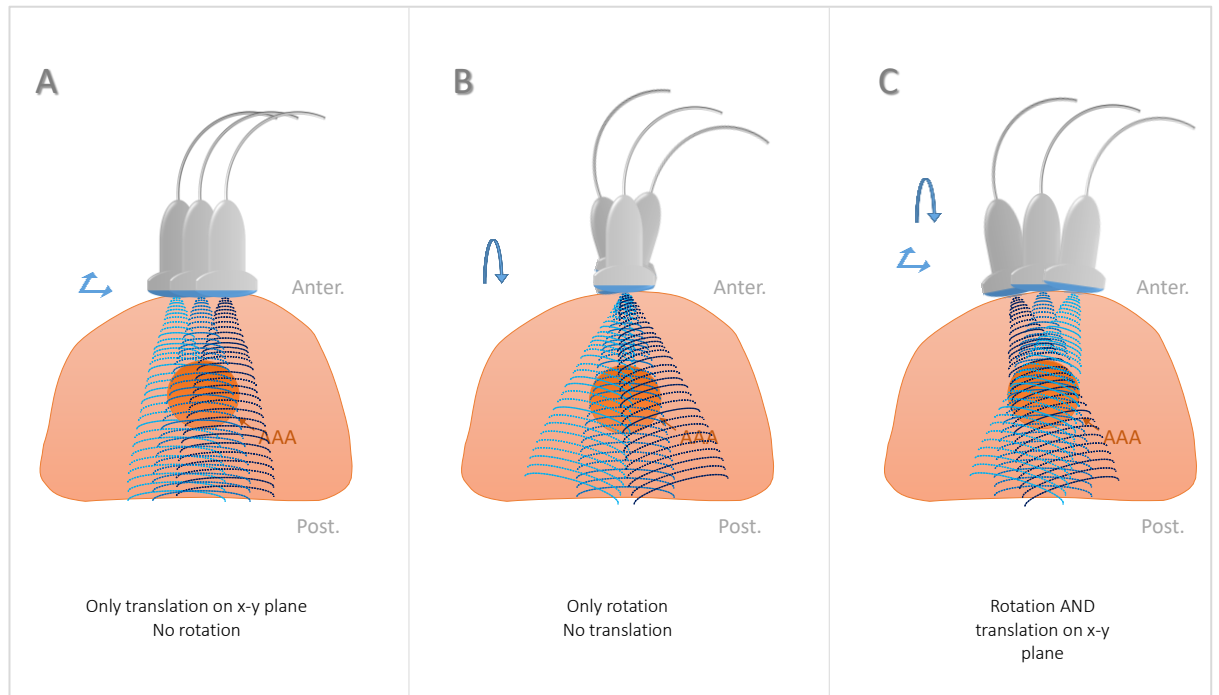
Figure 4.4: Axial orientation schematic with approximations of different angles/positions at which the ultrasonic transducer can be placed on the patient's abdomen during AAA measurement. *During the measurement, the transducer can be moved in the plane created by x and y axes (**A**), or rotated towards different directions (**B**), or a combination of both (**C**).*

4.4.3 Magnetic Resonance Imaging (MRI) Measurements

4.4.3.1 Maximum AP Diameter

In order to obtain maximum AP diameter measurements from MRI scans, comparable to those performed with US by sonographers, I created an algorithm that imitates the movements of the transducer on the patient's abdomen, to account for the most likely variations in position and angle. This algorithm was coded in MATLAB to create a tool for efficient and automatic processing in batch mode.

The algorithm uses previously segmented datasets, specifically it only needs the segmentation map which distinguishes between the AAA area and its background. Therefore, it can be applied on any similar type of segmented dataset, regardless of imaging modality.

Within the algorithm, I chose to separate the AAA into 3 equal rectangles and to confine the measurements within the central one on each slice, as shown in Figure 4.5 B. The transducer would not be expected to deviate much outside the central part of the AAA, so a smaller central segment could have been selected (by separating into 5, 7 or more rectangles), but I selected the most conservative case of 3, to account for large deviations. Within the selected central section, all points belonging to the outer perimeter of the wall of the aneurysm are connected to each other as depicted Figure 4.5 C, forming all possible diameters that could potentially be drawn by the sonographers on the US scans. The largest among these is selected as the maximum AP diameter of the slice.
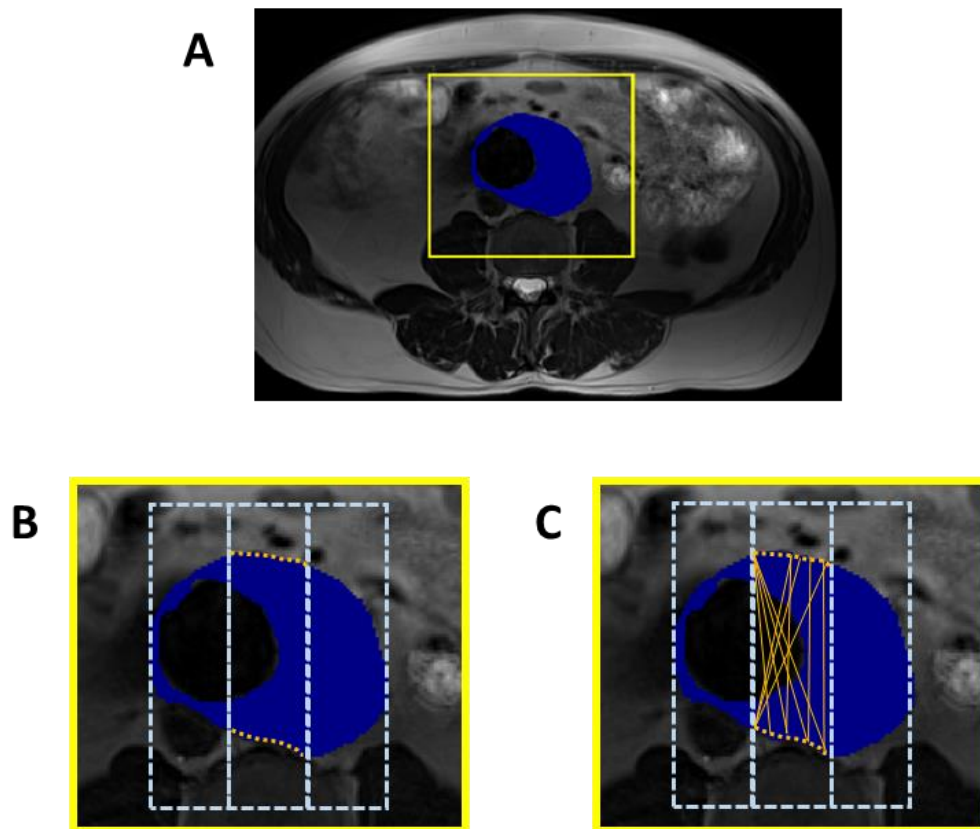
Figure 4.5: Max AP diameter Calculation method for MRI. *The AAA area (**A**) is divided into 3 equal sections (**B**), and the max AP diameter calculations are applied only on the middle section. All the points of the perimeter or the AAA belonging to the selected section are then connected to each other in all possible combinations of "diameters" (**C**). (T$_2$-weighted MRI scan, blue area represents thrombus and wall, while lumen has been left uncovered (black)).*

This method of creating all possible diameters from all points available works well in "regular" or "cylindrical" aneurysms AAAs (with the perimeter of each slice being circular), similar to the one depicted in Figure 4.6 B. In this figure, the red line corresponds to the "true vertical" AP diameter (in reference to the orientation that we label the subject position in the scanner bore). The yellow line corresponds to an extreme case of the largest diagonal diameter that can arise from the connection of all available points. This type of diameter shown in yellow must be excluded from the maximum AP diameter selection, as they are too oblique to qualify as being on the AP axis and they would be unlikely to be

selected by a sonographer as AP diameters, based on the feedback I obtained from the MA³RS sonographer I shadowed.

In Figure 4.6, three cases of aneurysm shapes (slices) are presented to further explore if these diagonal lines can distort the max AP measurements. It seems that in most common cases of AAAs seen in Figure 4.6 A and Figure 4.6 B, there are no issues with these, as the vertical line is larger or equal to the diagonal line. In the less-common (at least within the MA³RS dataset) case of a slice with a shape similar to the one in Figure 4.6 C however, the diagonal line is much larger than the vertical one and if not excluded, it will be chosen as the max AP of the slice. This is avoided in my algorithm, through a simple comparison: if any candidate maximum diameter is found to be larger than the vertical line, it is excluded. This process is further illustrated in the flowchart in Figure 4.7.

A   Vertical > Diagonal   **B**   Vertical ≈ Diagonal   **C**   Vertical < Diagonal
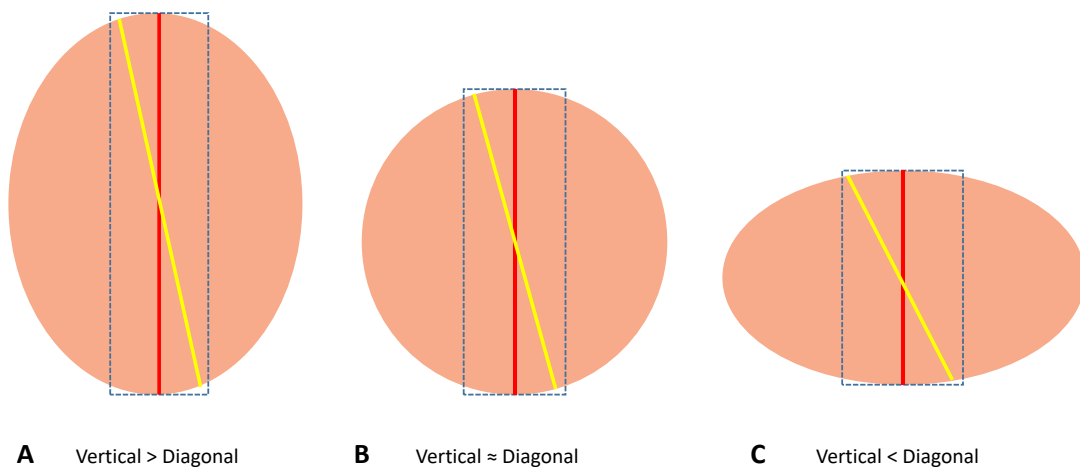
Figure 4.6: Different forms the aorta could potentially take (at the level of the AAA). The shape of the aorta is often not perfectly cylindrical. Approximations of 3 representative shapes can be seen here in cross-sectional cuts at the level of the AAA, with A and C presenting elliptical shapes and B a circular shape. Within the middle third of the AAA depicted within the blue rectangular area, the red line corresponds to the vertical diameter and the yellow line corresponds to the largest diagonal diameter, considered as the most extreme case of the automatically determined diameters. In the algorithm, cases A and B do not cause problems, as the vertical diameter is larger or equal to the diagonal diameter and will be the one selected as the maximum AP diameter. In case C, the diagonal diameter is too oblique to be considered an AP diameter; to avoid selection of such extreme maximum diameters in the algorithm, any diagonal diameters larger than the vertical diameter are automatically excluded.
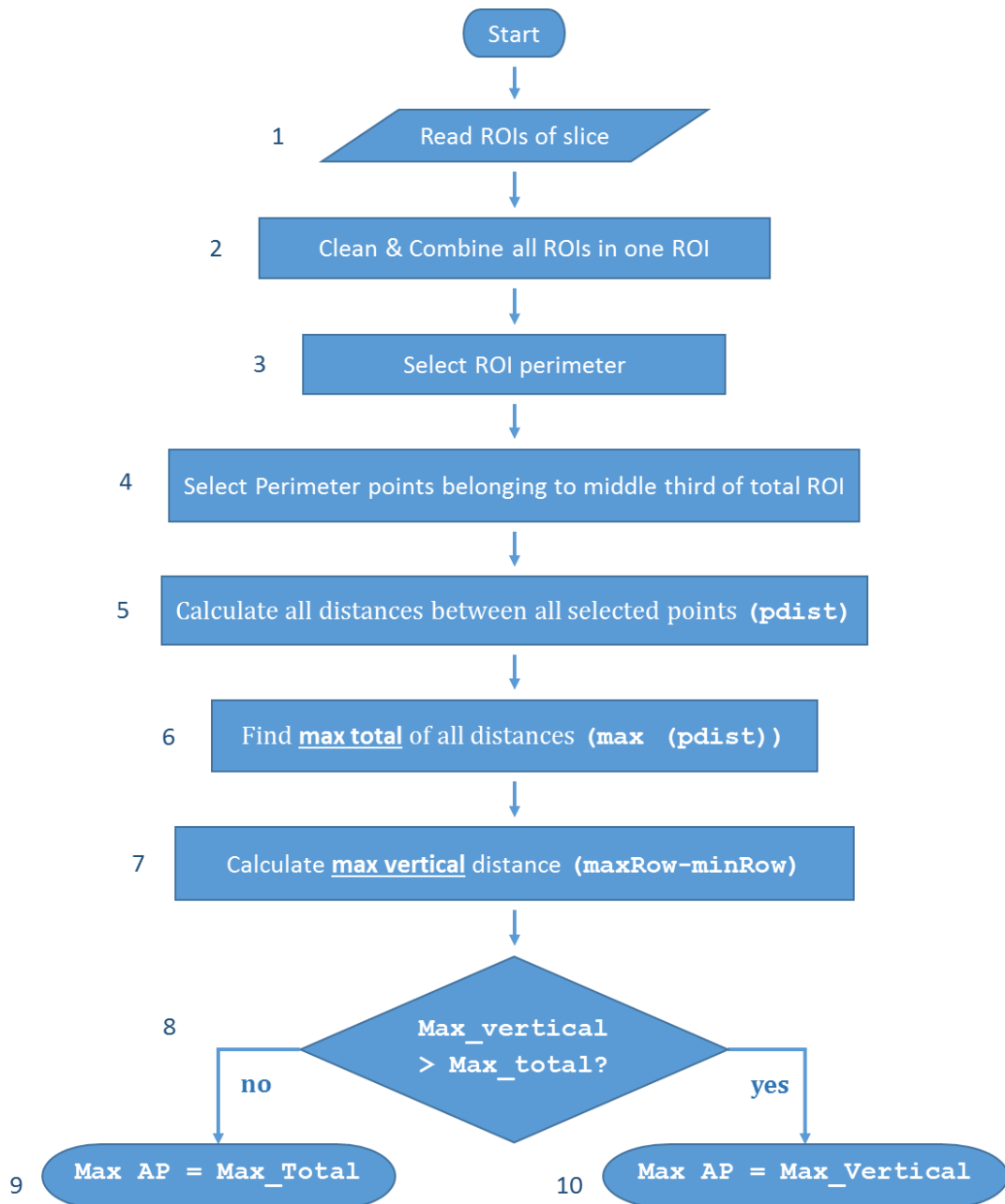
Figure 4.7: Flowchart of algorithm (summarised) for automatic maximum AP diameter calculation on MRI data per slice. *The algorithm was programmed in MATLAB. First, the user is asked to provide the location of the folder where the ROIs of any number of AAAs are stored. It then automatically iterates for every AAA and for every slice per AAA. The iteration for one such slice is depicted in the figure.* ***1)*** *The coordinates of the pixel locations of all ROIs (wall, thrombus, and lumen) per slice are read into the program.* ***2)*** *ROIs are cleaned by filling in any accidentally omitted pixels within the ROIs and deleting any drawn areas outside the AAA using MATLAB's functions bwmorph and bwconncomp. All ROIs (wall, thrombus and lumen) per slice are combined in one ROI corresponding to the whole AAA.* ***3)*** *The perimeter of the ROI is found with MATLAB's bwperim*

function 4) Among the perimeter points selected, the ones belonging to the middle third of the total ROI are selected. 5) The distances between all the selected points are calculated using the function 'pdist'. 6) Among these distances, the largest one is named 'max_total'. 7) The largest vertical distance within the ROI is calculated by subtracting the smallest row (minRow) of the ROI matrix from the largest row (maxRow) and named 'max_vertical'. 8) A comparison between max_vertical diameter and max_total diameter is made. 9) If the max_vertical diameter is larger than the max_total diameter, the max_vertical is selected as max AP diameter. 10) If the max_vertical diameter is smaller or equal to the max_total diameter, the max_total is selected as max AP diameter.

In order to evaluate the method for automatically calculating the maximum AP diameter of AAAs from MRI scans, this algorithm was applied to a randomly selected subset of the MA^{3}RS cohort. MRI data (ROIs defined on T$_2$-weighted data by expert observers) corresponding to 20 patients were used, with two independent subsets available for each patient: one acquired from an MRI scan at baseline and one from an MRI scan a year later. Therefore, a total of 40 maximum AP measurements were automatically produced by my algorithm.

As a reference, I also made the same maximum AP diameter measurements per slice for each patient manually, using Mayo Analyze (version 12, AnalyzeDirect, Overland Park, KS, USA). These measurements were also checked by two expert observers in our team. One maximum diameter measurement per slice was collected and consequently the largest of all AP diameters per AAA was saved, as depicted in Figure 4.8. This resulted in a total of 40 maximum AAA AP measurements, corresponding to the automatically calculated ones. The MRI manual measurement process closely imitated the US diameter measurement methodology described in 4.4.2.
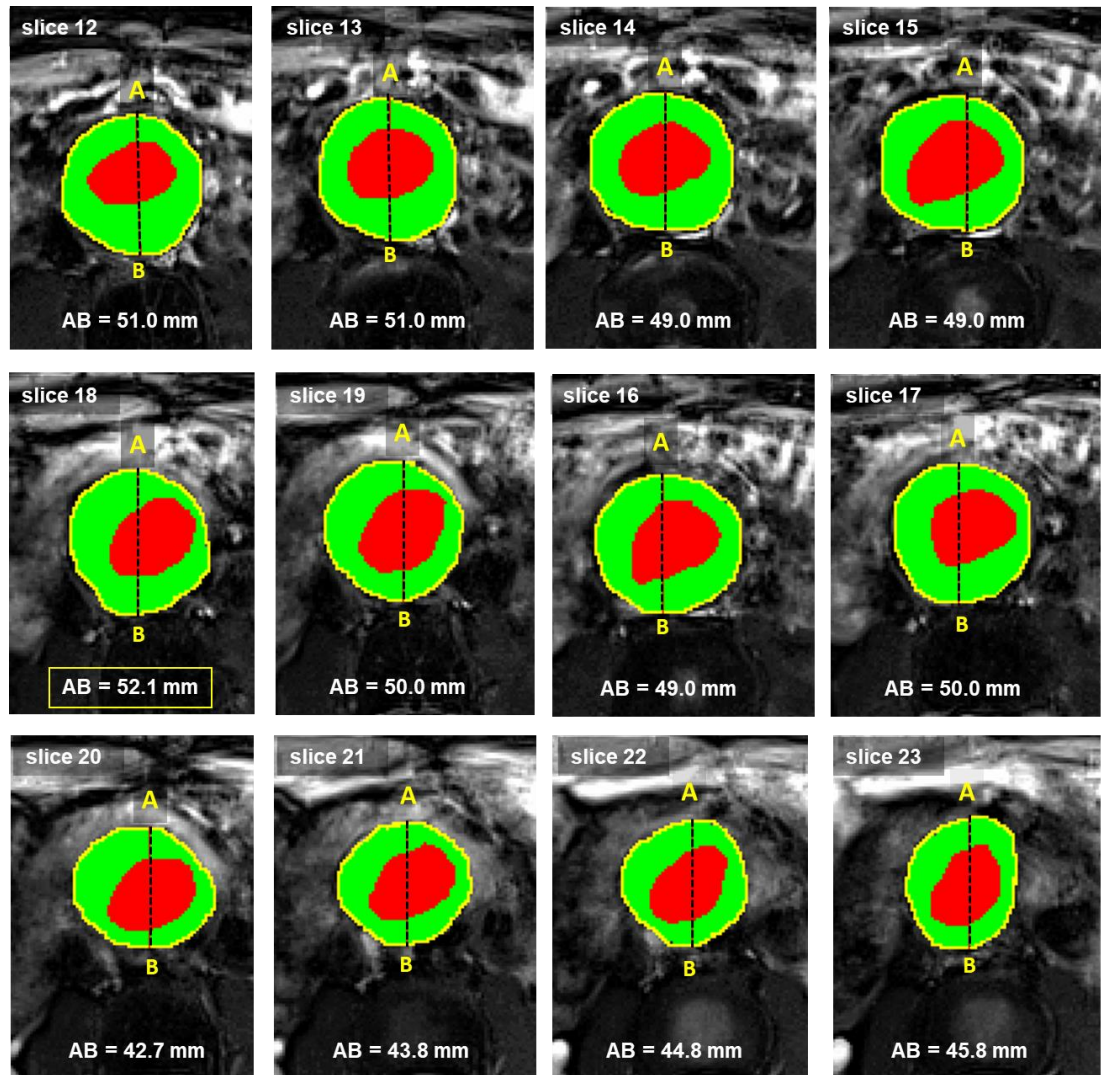
Figure 4.8: Manual calculation of maximum AP diameter in MRI axial slices of AAA. *Example of the measurements applied on consecutive slices (slices 12-23) of the AAA of one MA³RS patient. The ROIs have been superimposed on T₂-weighted scans, with red corresponding to lumen, green for thrombus and yellow for the aortic wall. The AP diameter of each slice is marked with a dashed black line (AB), revealing the largest (max AP) diameter of the AAA to be in slice 18, with AB₁₈=52.1mm.*

4.4.3.1.1 Evaluation of automatic measurement of max AP Diameter in MRI (MRI auto vs. MRI manual)

The evaluation of the automatic MRI max AP measurement was required so that if successful it could be used to automatically calculate max AP aortic diameters to compare against US and CT.

Scatterplots and the Bland-Altman method were used to compare the 40 maximum AP measurements calculated either manually or automatically (Figure 4.9). A strong linear correlation was found, with correlation coefficient R=0.996 and coefficient of determination R^2=0.993, p<0.0001. The bias of differences was only 1.4 mm with 95% Limits of Agreement from -2.9 mm to 5.7 mm.

These results verified that the automatic calculation of the maximum AP diameter in the MRI data was a very successful reproduction of the manual selection employed in the MRI data, and could therefore be used in the following experiments as an adequate replacement for manual selection. This saved processing time and made processing the MRI data more robust and reproducible.
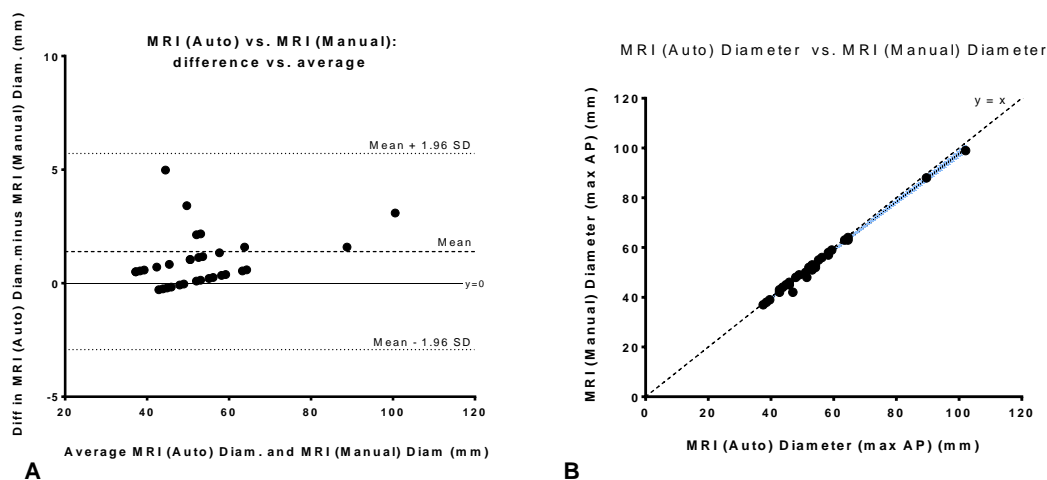
Figure 4.9: Comparison of Manual vs. Auto Measurements of 1-year Change in max AP Diameter (mm). *Auto MRI vs. Manual MRI measurements of max AP diameter (mm).*
A: Bland Altman plot of Difference (MRI auto diameter – MRI manual diameter) (mm) versus Average (average of MRI auto diameter and MRI manual diameter) (mm) for n=40 measurements of maximum AP diameter, corresponding to 2 measurements per patient for 20 patients, with bias=1.4mm, SD of bias=2.20 mm; 95% Limits of Agreement from -2.92 mm to 5.71mm.
B: Pearson correlation for n=40 measurements of maximum AP diameter, R=0.996; identity (dashed) line y=x. Blue lines correspond to 95% C.I. of linear regression; R^2 =0.993, equation: Y = 0.9672*X + 0.9803, p<0.0001.

For the same datasets, the change in max AP diameter could be calculated, as $Change$ (Equation 4.1), or $Percentage\ Change$ (Equation 4.2).

$$Change = (maxAPdiameter\ at\ Year1) - (maxAPdiameter\ at\ Baseline)$$

Equation 4.1

$$Percentage\ Change = \frac{(maxAPdiameter\ at\ Year1) - (maxAPdiameter\ at\ Baseline)}{(maxAPdiameter\ at\ Baseline)} * 100\%$$

Equation 4.2

The 1-year change in max AP (mm) as measured manually was compared against the automatically calculated change to assess the level of agreement between the two methods. As demonstrated in Figure 4.10, a strong correlation was observed between the manually processed and the automatically processed changes, with correlation coefficient R=0.95 and coefficient of determination R^2=0.89 (p<0.0001) for the change in mm (Figure 4.10 A) and R=0.91 and R^2=0.83 for

percent change (Figure 4.10 B). Additionally, the line of regression was very close to identity (x=y) in both cases, demonstrating a high level of agreement.
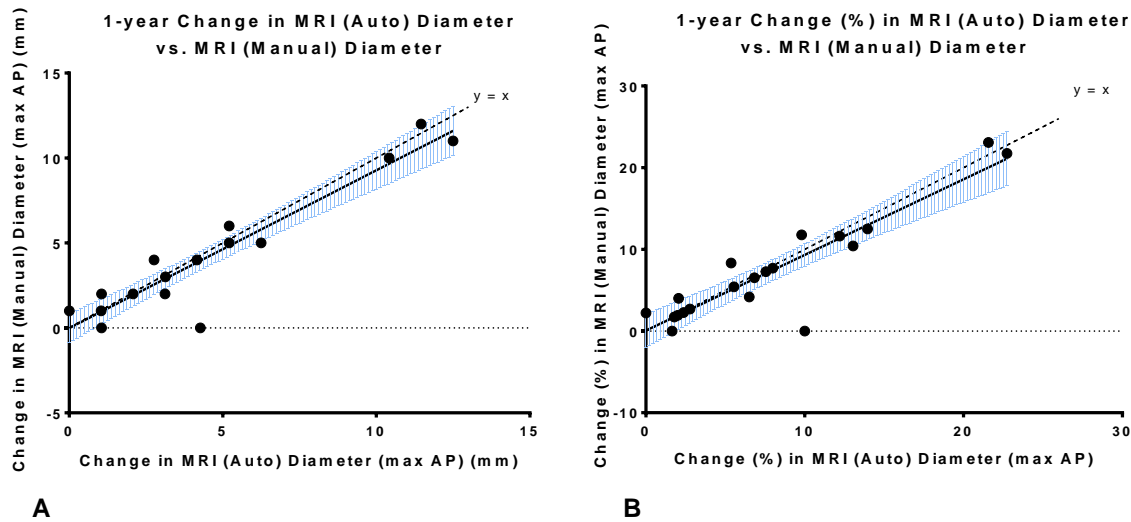
Figure 4.10: Comparison of Manual vs. Auto Measurements of 1-year Change in max AP Diameter (mm).
A: Pearson correlation for 1-year Change in manual MRI diameter vs. Auto MRI diameter, n=20 measurements of maximum AP diameter, r=0.95. Blue lines correspond to 95% C.I. of linear regression, equation: Y = 0.9289*X - 0.01192, R^2=0.89, p<0.0001, identity (dashed) line y=x.
B: Pearson correlation for 1-year %Change in manual MRI diameter vs. Auto MRI diameter, n=20 measurements of maximum AP diameter, R=0.91. Blue lines correspond to 95% C.I. of linear regression, equation: Y = 0.9256*X + 0.06034, R^2=0.83, p<0.0001, identity (dashed) line y=x.

4.4.3.2 Other Metrics

In-house software (developed in MATLAB) that was able to generate additional aneurysm metrics was available in our lab, developed for a previous project by Dr Calum D. Gray in the Image Analysis Core Laboratory of the Clinical Research Facility joint with CRIC. I additionally adapted this code for the needs of the data processing for my study and an overview of the different metrics generated by this modified code is provided below. The code uses the same ROIs described above that had been previously segmented.

4.4.3.2.1 Maximum General Diameter of AAA (with MRI)

The **maximum general diameter** refers to the largest diameter per aneurysm, as measured on MRI T_2-weighted data, regardless of diameter direction.

Briefly, for each slice the algorithm projects lines starting from the centroid of the shape (Figure 4.11 A) and stopping when they meet the outer perimeter, while rotating from a 0° to 180° degrees. This way, 180 lines are created, connecting the centroid with the points on the perimeter of one side of the shape (continuous lines in Figure 4.11 B). These lines comprise one half of the diameters only. To define the second half, the lines are then extended from the centroid towards the other side of the shape until they meet points of the perimeter on the other side (dashed lines in Figure 4.11 B).

The sizes of all the resulting diameters per slice are calculated and the maximum and minimum diameters (depicted with green and red lines in Figure 4.11 C respectively) of each slice is saved.
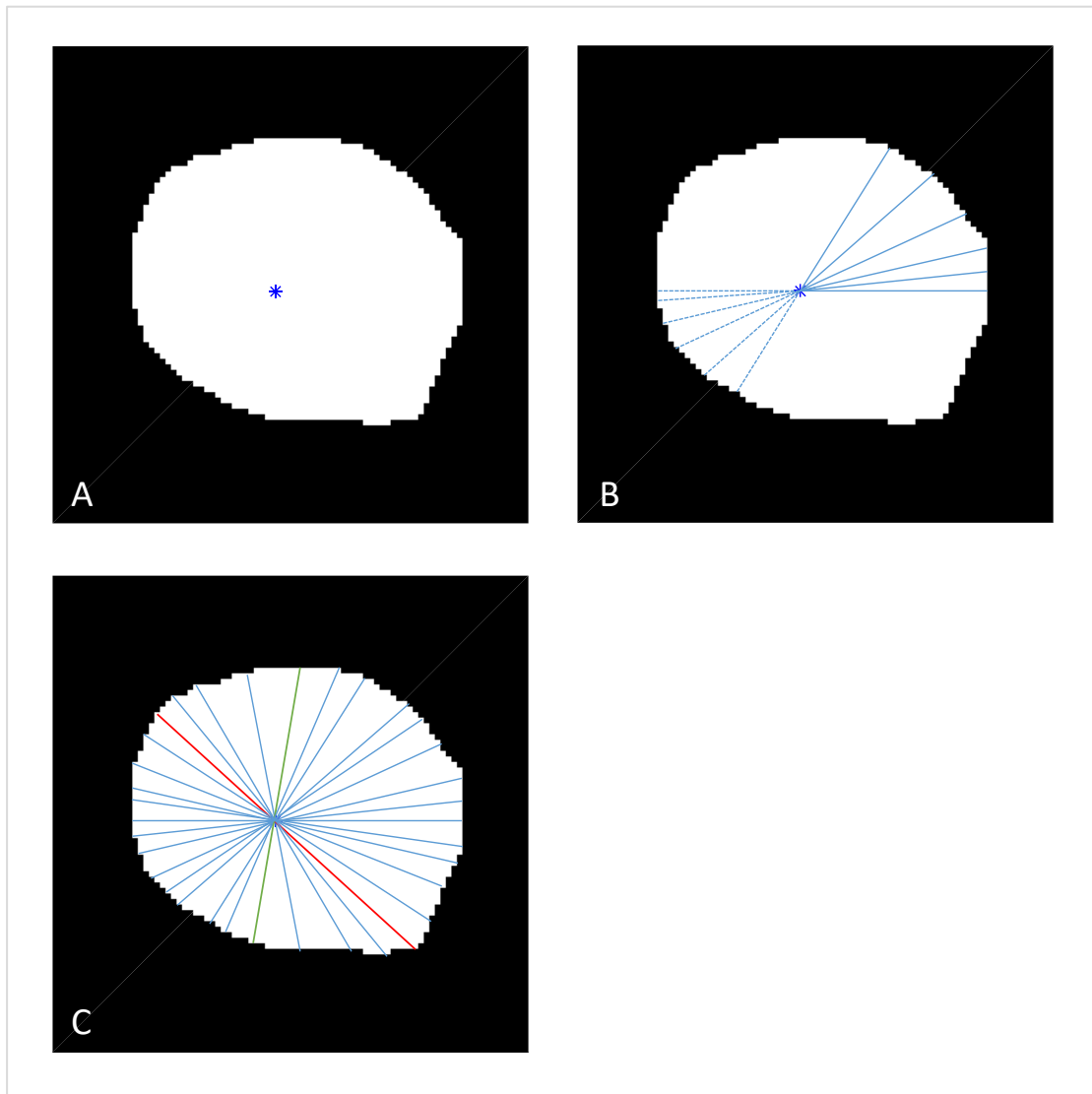
Figure 4.11: Measurement of Min and Max Diameters. *First, the centroid of the shape is found as seen in (A), then the diameters are created as lines starting from 0° to 180° and passing through the centroid, as seen on (B). After all diameters are created(C), the minimum diameter (green line), in this case measuring 41.6mm and the maximum diameter (red line), in this case measuring 53mm per slice are selected.*

4.4.3.2.2 Maximum Area of AAA (with MRI)

The total number of 2D pixels within a region gives an **Area metric**, measured in pixels (Equation 4.3) and applied to MRI T$_2$-weighted data.

$$Area(pixels) = Number\ of\ Pixels$$

Equation 4.3

The size per pixel (in mm) can then be used to calculate the Area metric in millimetres (mm) (Equation 4.4):

$$Area(mm) = Number\ of\ Pixels * Pixel\ Size(mm)$$

Equation 4.4

4.4.3.2.3 Top5 Area Average of AAA (with MRI)

This method calculates the cross-sectional area for each slice in the MRI T_2-weighted data of an AAA and then selects the 5 largest areas per AAA (Figure 4.12). This way, a larger area of the AAA is taken into consideration in the measurements, thus diminishing the effects of any possible human errors in the manual ROI drawing.
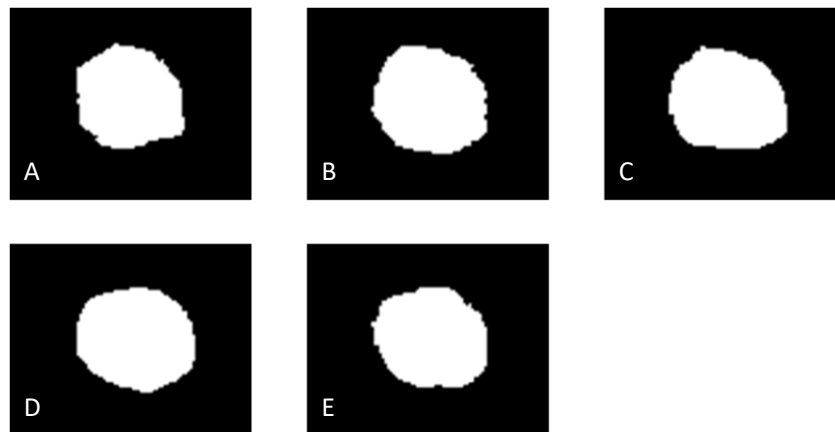
Figure 4.12: Top 5 area average. The slices with the 5 largest areas of an AAA (total areas, including wall, thrombus and lumen) are selected and their average is used. Here, area(A)= 1211mm², area(B)=1278mm², area(C)= 1290mm², area(D)= 1268mm² and area(E)= 1250mm². Thus, the average area value of 1260mm² is used.

4.4.3.2.4 Volume of AAA (with MRI)

The Top5 Area Average of AAA method described above is used as an alternative to total AAA Volume measurements, which would require all slices of each AAA to be included in the processing. The underlying issue with including all MRI slices when comparing AAAs is the high dependence of the final result on the exact number of slices included in each AAA: the exclusion or addition of just a

single slice due to low quality (e.g. breathing artefact, see 2.2.3 Introduction) or due to the variation in the exact level of the aorta that is selected as the upper and lower boundaries of the AAA, can alter the volume measurement greatly and thus hinder accurate size reporting in clinical settings and conclusive comparison between aneurysms.

4.4.4 Computed Tomography (CT)

It was important to include CT measurements in the comparison between US and MRI, as CT is considered to be the gold standard in the evaluation of AAA size [246]. A subset of 15 patients among the MA³RS cohort had two CT scans performed, the first one at the beginning of the study (baseline scan) and the second one 2 years later.

At the time of my work on this thesis, the CT scans had not been annotated with ROIs by a clinical expert, hence the maximum AP diameters could not be extracted from them automatically (the automatic algorithm utilises segmented data only at this stage). Manual diameter measurements were conducted instead. The methods used were identical to the ones used for manual measurements of maximum AP diameters on MRI scans described in section 4.4.3.1. For each AAA, the maximum diameter for each slice was measured on axial CT slices and the largest selected as the maximum AP diameter of the AAA. The measurements were carried out twice and the average values of each two instances were accepted.
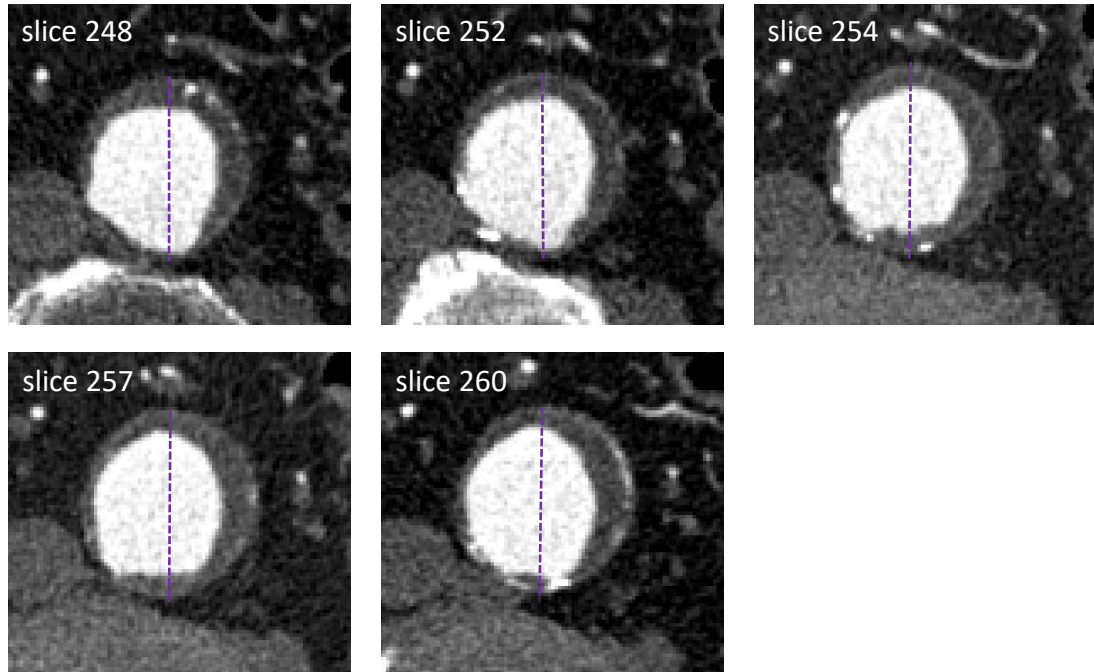
Figure 4.13: Manual calculation of maximum AP diameter in CT axial slices of AAA. *Example of the measurements applied on 5 slices (slices 248, 252, 254, 257, 260)) of the AAA of one MA³RS patient. In the absence of pre-defined ROIs for these scans, the AP diameter has been drawn directly on the CT scans. The AP diameter of each slice is marked with a dashed line, and the largest (max AP) diameter will be detected after all available slices have been measured.*

4.5 Results

4.5.1 Measurement of AAA size: max AP diameter

4.5.1.1 Maximum AP Diameter: Comparison between US, CT and MRI

In order to perform a direct comparison of US, CT and MRI diameter measurements, a subset of 15 patients from the MA³RS trial, for which I had access to datasets acquired with all modalities at two timepoints (baseline and 2-year follow-up) for each patient was selected.

As explained in the Methods (4.4.3.1.1 and 4.4.4), the maximum AP diameter measurements in the CT data were manually calculated by an expert observer. In the MRI datasets, the maximum AP diameter was measured automatically using the previously validated technique presented in 4.4.3.1.

In Figure 4.14, all 30 max AP diameter measurements available (2 per patient, for 15 patients) from US, CT and MRI are plotted for comparison. The measurements follow similar trends, but do not agree on exact values. The graph suggests that the diameters measured with US have systematically lower values, while MRI and CT are numerically closer to each other.
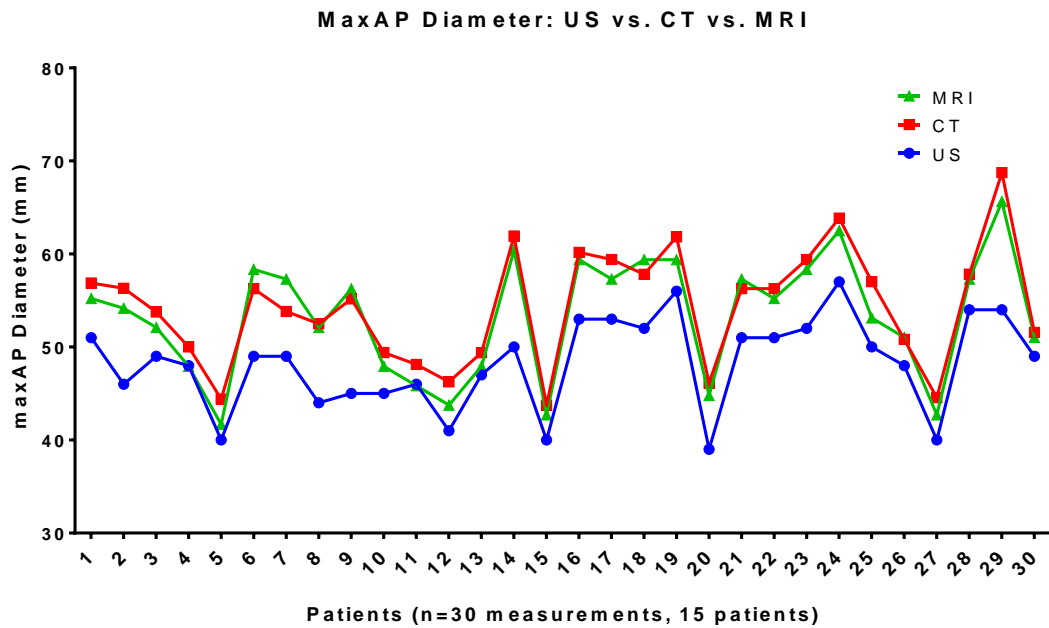
Figure 4.14: Maximum AP diameter (mm): US vs. CT vs. MRI. *N=30 measurements of maximum AP diameter in mm, corresponding to 2 measurements per patient (one at baseline and one 2 years later) for 15 patients. US Diameter measurements for US were manual (sonographer), for CT manual (trained observer) and for MRI automatically calculated.*

This is further demonstrated in Figure 4.15 with the comparison of the mean values (±SEM) of max AP diameter for each modality: The mean max AP diameter with US was 48.3±0.9 mm, with CT it was 54.3±1.1 mm and with MRI it was 53.3±1.2 mm. A repeated measures one-way ANOVA, (F= 86.33, DF=2, p< 0.0001) followed by Tukey's multiple comparisons test showed that the difference between the mean US values and the mean CT values was highly significant (p < 0.0001), as well as the difference between US values and mean MRI values (p < 0.0001). The difference between the mean CT values and the mean MRI values was not significant (p > 0.05).
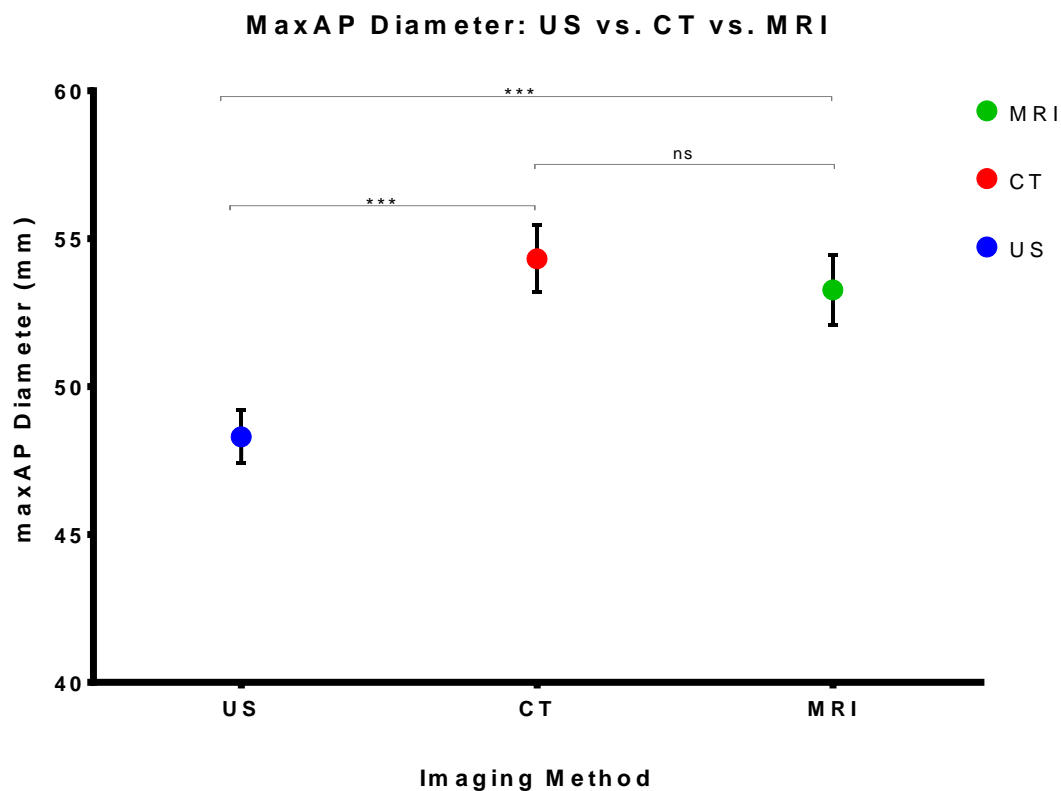
Figure 4.15: Comparison of maximum AP diameter measurements: US vs. CT vs. MRI. *Data show the mean ± SEM, n=30, (15 patients, with 2 measurements for each); **US:** mean=48.3 mm, SD=4.9mm, SEM=0.9mm; **CT:** mean=54.3mm, SD=6.2mm, SEM=1.1mm; **MRI:** mean=53.3mm, SD=6.5mm, SEM=1.2mm; Repeated measures one-way ANOVA, F= 86.33, DF=2, p< 0.0001 followed by Tukey's multiple comparisons test; ns=not significant; *p<0.05, **p<0.01, ***p<0.001.*

In a more detailed analysis, the three methods were compared against each other in pairs (Figure 4.16), using Bland-Altman plots and with scatterplots depicting correlation, linear regression and the identity line (x=y) for reference (if the measurements were in agreement, they should not only correlate, but also be in very close proximity to the identity line).
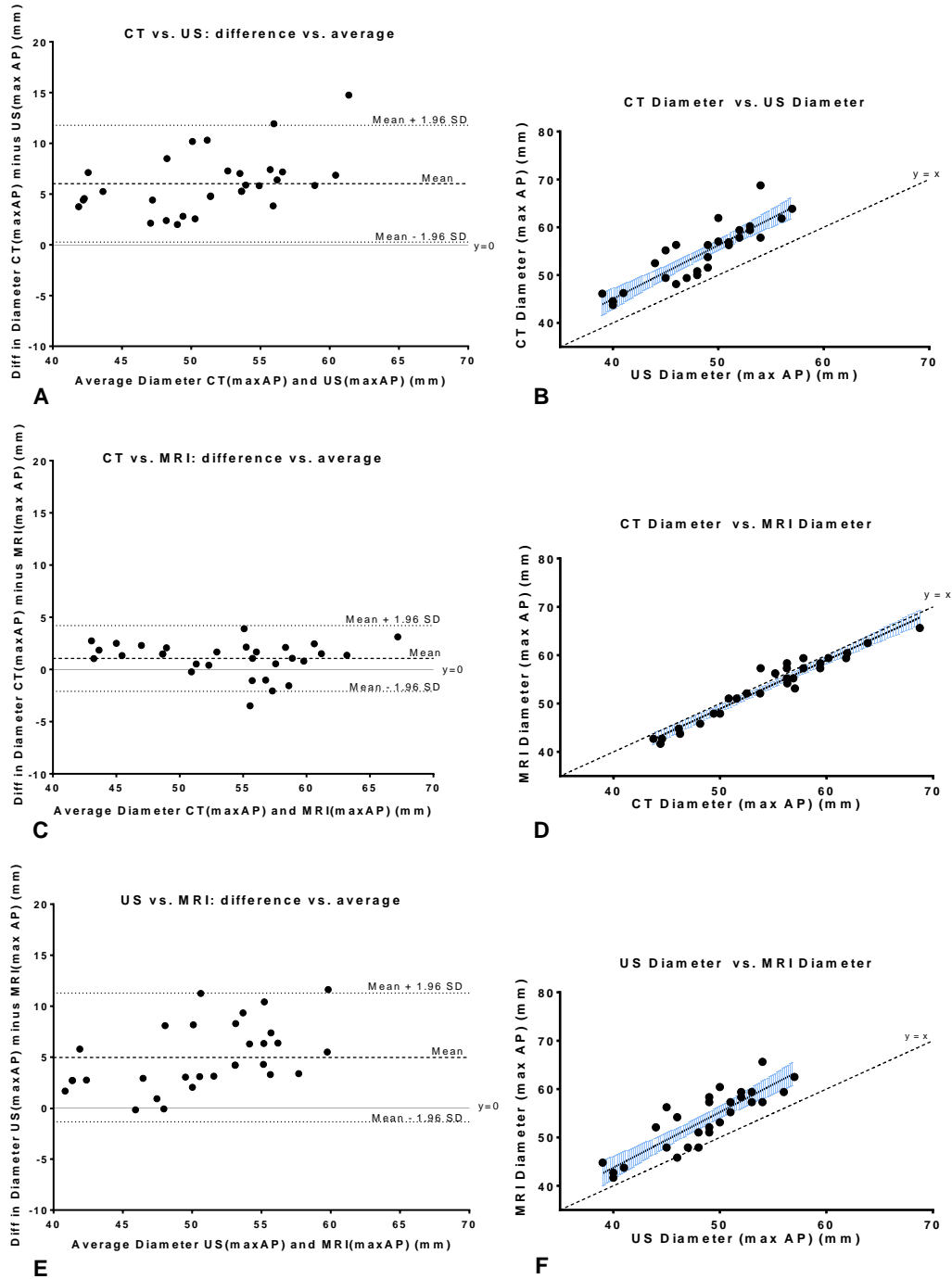
Figure 4.16: Bland-Altman plots and Scatterplots with Correlation and Linear Regression for comparison between US, CT and MRI max AP diameter measurements. *A: CT vs. US: Bland-Altman plot: bias=6.0 mm, SD of bias=2.9 mm. 95% Limits of Agreement from 0.3 mm to 11.8 mm, n=30 measurements (2 measurements per patient) for 15 patients.*
B: CT vs. US: Pearson Correlation with correlation coefficient R=0.8868, coefficient of determination R^2=0.7865, p<0.0001, n=30 measurements (2 measurements per patient) for 15 patients, identity (dashed) line y=x, blue lines correspond to 95% C.I. of linear regression. *C: CT vs. MRI: Bland-Altman plot: bias=1.1mm, SD of bias=1.6mm. 95% Limits of Agreement from -2.1mm to 4.2mm, n=30 measurements (2 measurements per patient) for 15 patients.* *D: CT vs.*

MRI: Pearson Correlation with correlation coefficient R=0.9685, coefficient of determination R²=0.9381, p<0.0001, n=30 measurements (2 measurements per patient) for 15 patients, identity (dashed) line y=x, blue lines correspond to 95% C.I. of linear regression. **E:** *US vs. MRI: Bland-Altman plot: bias=5.0mm, SD of bias=3.2mm. 95% Limits of Agreement from -1.3mm to 11.3mm, n=30 measurements (2 measurements per patient) for 15 patients* **F:** *US vs. MRI: Pearson Correlation with correlation coefficient R=0.8740, coefficient of determination R²=0.7639, p<0.0001, n=30 measurements (2 measurements per patient) for 15 patients, identity (dashed) line y=x, blue lines correspond to 95% C.I. of linear regression.*

As shown in Figure 4.16 D, the CT and MRI values correlated very strongly (R=0.97, R^2=0.94, p<0.0001) and were very close to the identity line (x=y), presenting good agreement levels. The correlation between US and CT was less strong but still significant (R=0.89, R^2=0.77, p<0.0001) as seen in Figure 4.16 B, but more importantly the level of agreement appeared considerably lower than that of CT-MRI agreement, as indicated by the larger distance between the datapoints in the scatterplot and the identity line. Similarly, for the association between US and MRI in Figure 4.16 F, there were similar levels of correlation as those of US-CT (R=0.87, R^2=0.76, p<0.0001), and a considerable distance between the datapoints and the identity line suggested a low agreement level between the two modalities.

The exact levels of disagreement are presented in the Bland-Altman plot analysis. The bias (average of differences) between MRI and CT as shown in Figure 4.16 A is only 1.1 mm, while the bias observed between US and CT demonstrated in Figure 4.16 C is 6.0 mm. The bias between US and MRI (Figure 4.16 E) is slightly smaller, with a value of 5.0 mm.

4.5.2 Effects of use of maximum anteroposterior diameter in classifying patient risk: Comparison between ultrasound, CT and MRI

As discussed previously, the current threshold for patients to be considered for surgery is 5.5 cm and it is commonly measured with US. In Figure 4.17 the group of 30 AAAs was classified as either "small" AAAs (AAAs <5.5 cm) or "large" AAAs

(AAAs ≥ 5.5 cm), based on US, CT, or MRI max AP diameter measurements. When classified based on the US values, 28 of the 30 AAAs were categorised as small and only 2 as large. The CT measurements grouped 14 AAAs as small and 16 as large, while MRI classified 15 AAAs as small and 15 as large. This way of presenting the data suggests discordance between the US and the other two modalities, in the number of patients that would be described as exhibiting a "large" AAA according to this criterion; it does not however examine the agreement on a case-by-case level (i.e. which specific AAAs are classified as large or small per modality).
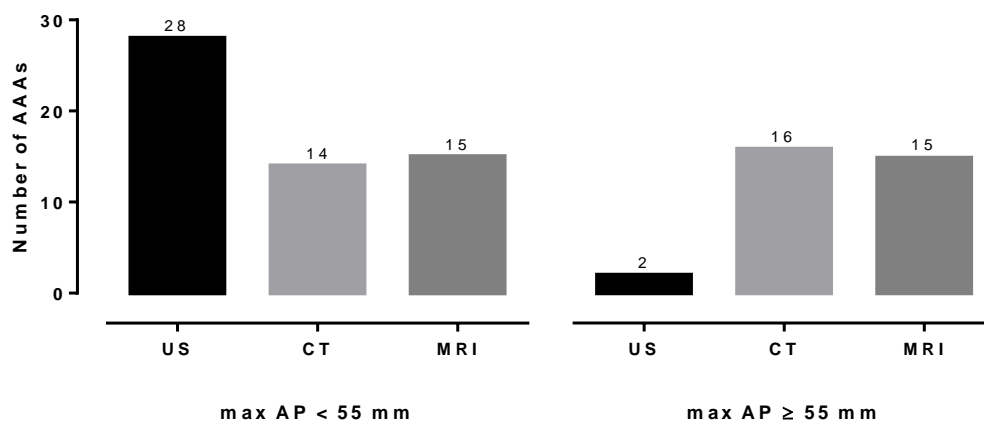
Figure 4.17: Classifying patients with small or large AAAs with US vs. CT vs. MRI. *Measurements conducted with US classified 28 out of 30 AAAs (93.33 %) as small (max AP diameter < 55mm), and 2 out of 30 (6.67%) as large (max AP diameter ≥55mm). For the same patients, measurements with CT classified 14 out of 30 (46.67%) as small (max AP diameter < 55mm), and 16 out of 30 (53.33%) as large (max AP diameter ≥55mm). MRI classified 15 out of 30 (50%) as small (max AP diameter < 55mm), and 15 out of 30 (50%) as large (max AP diameter ≥55mm).*

Since CT is considered the gold standard for pre-operative AAA assessment, it was selected here to be used as the ground truth against which the accuracy of the US and the MRI measurements in classifying AAAs could be verified. In this way, the cross-tabulation (confusion matrix) of the US classification outcome against the CT classification outcome identified the degree of agreement as shown in Table 4.1. When compared with CT classification, the US classification resulted in 2 true positives (TN), 0 false positives (FP), 14 false negatives (FN)

and 14 true negatives (TN), thus achieving 100% specificity, but only 12.5% sensitivity.

Table 4.1: Confusion matrix to evaluate Outcome of AAA classification based on US measurements of max AP diameter against CT classification Outcome. *TP=True Positive, FP=False Positive, FN= False Negative, TN=True Negative; Sensitivity=TP/(TP+FN); Specificity=TN/(TN+FP).*

CT Outcome		Positive	Negative
	Positive	TP = 2	FP = 0
	Negative	FN = 14	TN = 14
	Sensitivity	12.5%	
	Specificity	100%	

(US Outcome)

The confusion matrix of the MRI classification outcome against the CT classification outcome is depicted in Table 4.2, with 14 true positives (TP), 1 false positive (FP), 2 false negatives (FN) and 13 true negatives (TN), hence resulting in 92.9% specificity and 87.5% sensitivity.

Table 4.2: Confusion matrix to evaluate Outcome of AAA classification based on MRI measurements of max AP diameter against CT classification Outcome. *TP=True Positive, FP=False Positive, FN= False Negative, TN=True Negative; Sensitivity=TP/(TP+FN); Specificity=TN/(TN+FP).*

CT Outcome		Positive	Negative
	Positive	TP = 14	FP = 1
	Negative	FN = 2	TN = 13
	Sensitivity	87.5%	
	Specificity	92.9%	

(MRI Outcome)

There is a notable difference of 75% between the sensitivity results of the US and the MRI when each is compared to the gold standard of CT, while the difference in specificity is considerably less pronounced, at 7.1%. This discrepancy in sensitivity is further illustrated in the Receiver Operating Characteristic (ROC) curve analysis in Figure 4.18, where it becomes obvious that, assuming the CT as the gold standard, and with the use of the 55-mm threshold, US performs very poorly, as demonstrated by the low and statistically insignificant Area Under the ROC Curve (AUC) of AUC=0.56 (p=0.561).
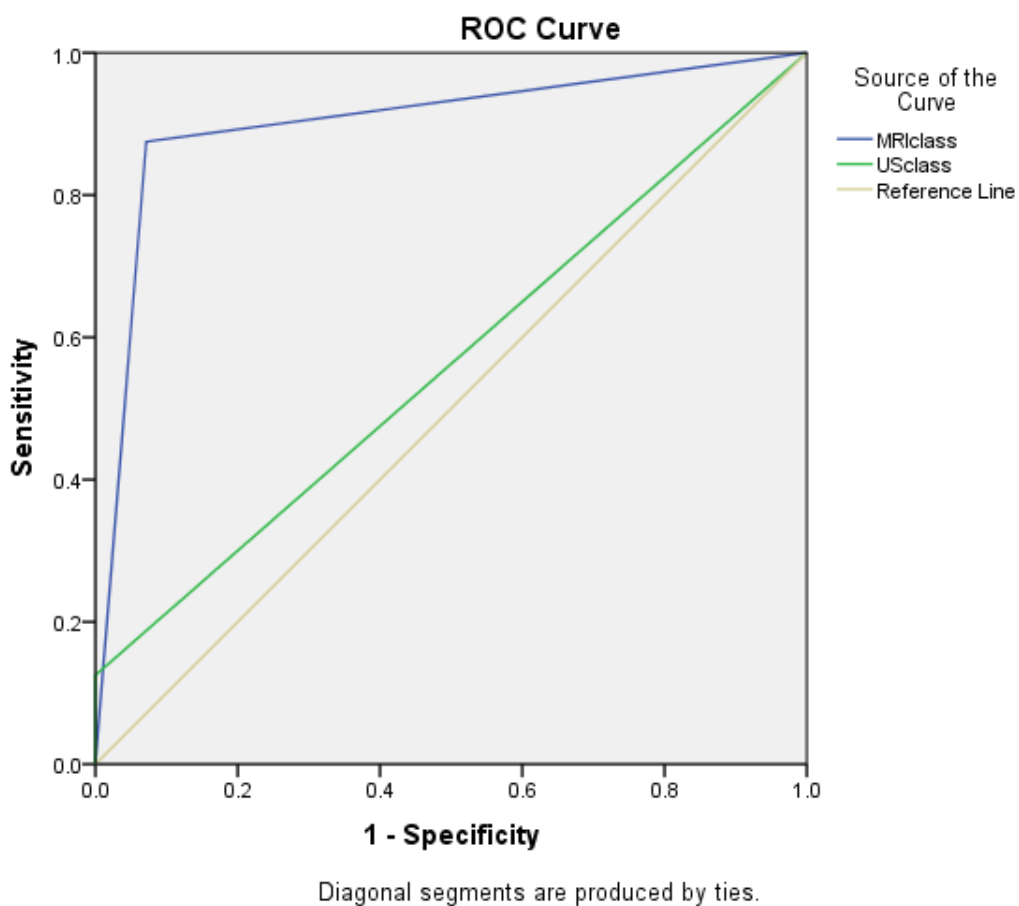
Figure 4.18: Receiver operating characteristic (ROC) for the US and MRI classifications of AAAs, assuming the CT classification as the gold standard. *The 55 mm threshold was used in the classification of all modalities for n=30 AAAs. The area under the ROC curve (AUC) for the US classification was AUC= 0.56, not significant (p=0.561). For the MRI classification, AUC=0.90 (p<0.0001).*

Since the results of this work indicated that US largely underestimated the size of AAAs when compared with CT (Figure 4.14, Figure 4.15), a logical next step was to determine whether an adjustment of the current 55 mm threshold would improve the agreement between the US and CT classifications in this dataset and allow measurements with the different modalities to be comparable. ROC curve analysis was performed (Figure 4.19), this time including the raw US max AP diameter values against the CT classification. The coordinates of the ROC curve (Table 4.3 A) could then be used to identify the most appropriate threshold for maximising both Sensitivity and Specificity.

Regarding the MRI measurements, the levels of agreement with CT had previously been satisfactorily high. The MRI values were included in the ROC analysis (Figure 4.19 and Table 4.3 B) in order to investigate whether the 55 mm threshold was the best option to be used with MRI data, assuming again CT as the gold standard.

The ROC curve analysis (Figure 4.19) showed that the ultrasound had potential for more accurate AAA classifications based on max AP diameter size, with AUC= 0.93, (p<0.0001). The MRI still scored slightly higher with AUC= 0.97, (p<0.0001). According to the analysis of the coordinates of the ROC curve in Table 4.3 A, the optimal threshold that should be used in Ultrasound classifications is ≥48.5 mm (>48 mm) which corresponds to 87.5% Sensitivity and 78.6% Specificity (calculated from difference: 1.0 - 0.214). Alternatively, if a higher level of Specificity was deemed more important, the ≥49.5 mm (>49 mm) threshold, corresponding to 81.3% Sensitivity and 100% Specificity (calculated from difference: 1.0 - 0.0) could be selected.
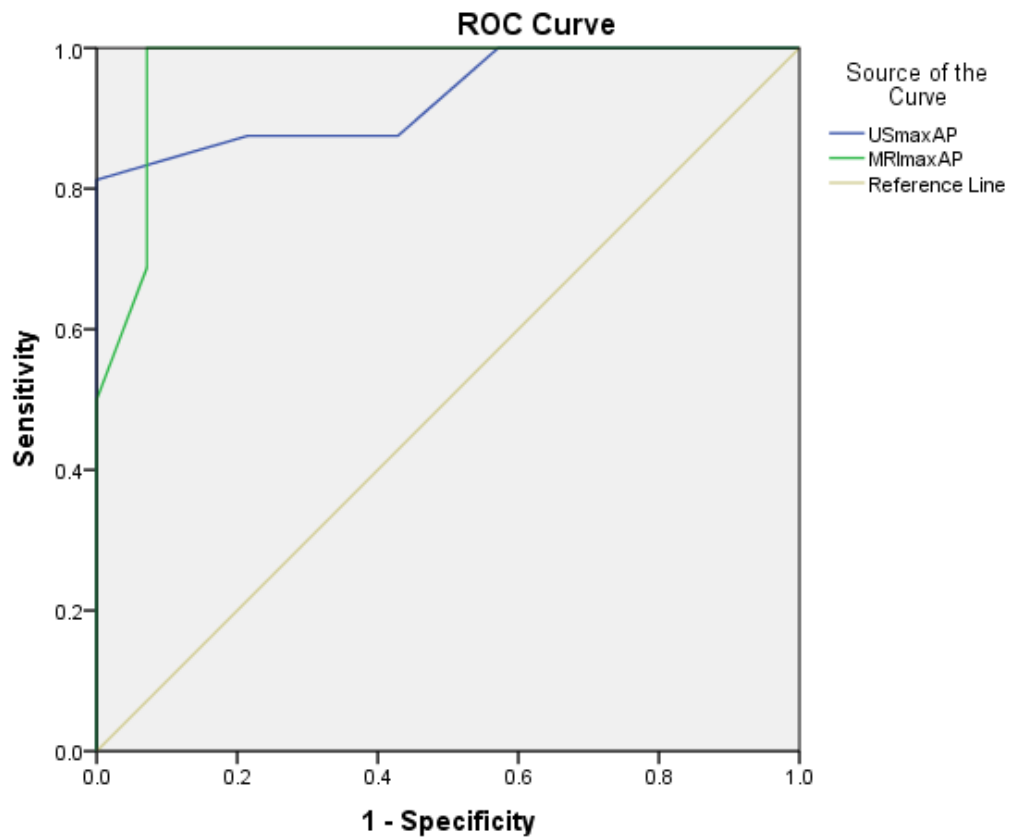
Figure 4.19: Receiver operating characteristic (ROC) for the Ultrasound and MRI classifications of AAAs, assuming the CT classification as the gold standard. *N=30 AAAs. The area under the ROC curve (AUC) for the Ultrasound was AUC= 0.93, (p<0.0001). For the MRI, AUC=0.97, (p<0.0001).*

As shown in the analysis of the coordinates of the ROC curve in Table 4.3 B, the optimal threshold that should be used in MRI classifications is ≥52.6 mm (>52.5 mm) which corresponds to 100% Sensitivity and 92.9% Specificity (calculated from difference: 1.0 - 0.071).

Table 4.3: Coordinates of the ROC curve for A) US max AP diameter B) MRI max AP diameter.
The CT classification (with 55 mm threshold) is assumed as gold standard. In each sub-table, the True Positive Rate (Sensitivity) and the False Positive Rate (1-Specificity) corresponding to all the potential threshold values are listed. The currently used threshold and corresponding Sensitivity and 1-Specificity values have been highlighted in blue and the optimal thresholds and corresponding values have been highlighted in yellow. In A, two different thresholds have been suggested and the option between them can be made based on the level of Specificity considered acceptable.

A Coordinates of the Curve

Test Result Variable(s): **USmaxAP**

Positive if Greater Than or Equal To	Sensitivity	1 - Specificity
38.0000	1.000	1.000
39.5000	1.000	.929
40.5000	1.000	.714
42.5000	1.000	.643
44.5000	1.000	.571
45.5000	.938	.500
46.5000	.875	.429
47.5000	.875	.357
48.5000	.875	.214
49.5000	.813	.000
50.5000	.688	.000
51.5000	.500	.000
52.5000	.375	.000
53.5000	.250	.000
55.0000	.125	.000
56.5000	.063	.000
58.0000	.000	.000

B Coordinates of the Curve

Test Result Variable(s): **MRImaxAP**

Positive if Greater Than or Equal To	Sensitivity	1 - Specificity
40.6700	1.000	1.000
42.1900	1.000	.929
43.2300	1.000	.786
44.2700	1.000	.714
45.3100	1.000	.643
46.8750	1.000	.571
49.4800	1.000	.357
51.5650	1.000	.214
52.6100	1.000	.071
53.6500	.938	.071
54.6900	.875	.071
55.7300	.750	.071
56.7700	.688	.071
57.8150	.500	.000
58.8600	.375	.000
59.9000	.188	.000
61.4600	.125	.000
64.0650	.063	.000
66.6300	.000	.000

4.5.3 Measurement of AAA size: Alternative Methods of measuring AAA size using MRI

4.5.3.1.1 Maximum General Diameter

As previously discussed (4.2.1.3) and illustrated in Figure 4.1, Figure 4.2 and Figure 4.6, the suitability of the max AP diameter to be used as a representative value for the whole AAA can be debated. As AAAs are often non-perfectly cylindrical, the *max general diameter* (maximum diameter per slice, regardless of direction, see 4.4.3.2.1) can be found to be larger than the max AP diameter. The two types of measurements, as automatically calculated with MRI (see 4.4.3.1), are compared here.

Interestingly, as can be observed in the plot of the max AP diameter against the max general diameter in Figure 3.20 A, the fitted regression line and the identity line (x=y) are close to converging, with coefficient of determination $R^2=0.85$, p<0.0001. However, further assessment with the Bland-Altman method (Figure 4.20 B), revealed that the bias was high enough (bias=2.2mm, SD of bias=2.7mm, with 95% limits of agreement from -3.1mm to 7.5mm, giving a range of 10.6mm) to suggest that max AP diameter and max general diameter are not interchangeable as clinical AAA size assessment methods.
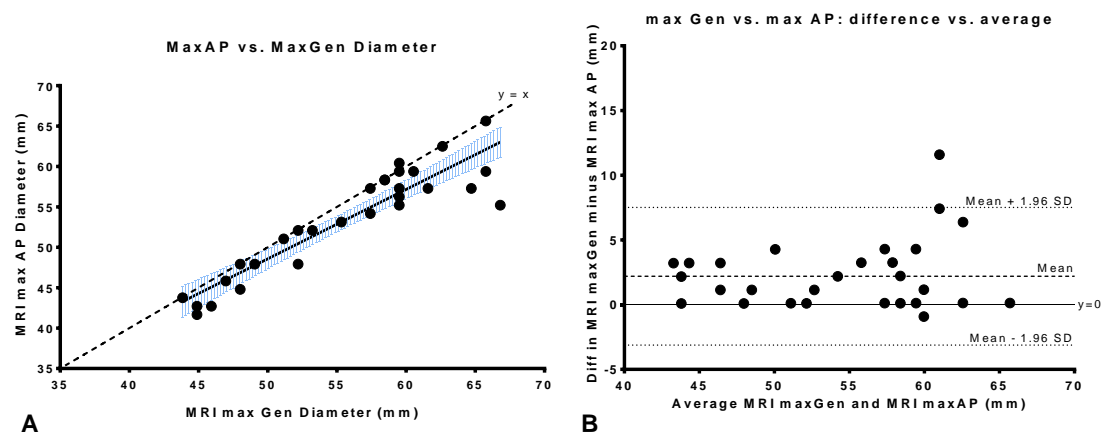
Figure 4.20: Relationship between MRI max AP diameter (maxAP) and MRI max general diameter (maxGen).
A) Pearson Correlation with correlation coefficient R=0.92, coefficient of determination $R^2=0.85$, p<0.0001, n=30 measurements (2 measurements per patient) for 15 patients, blue lines correspond

to 95% C.I. of linear regression with Y = 0.8591*X + 5.619, identity (dashed) line y=x.
B) *Bland-Altman plot: bias=2.2mm, SD of bias=2.7mm, 95% Limits of Agreement from -3.1mm to 7.5mm, n=30 measurements (2 measurements per patient) for 15 patients.*

4.5.3.1.2 MRI Maximum Area (per slice)

Intuitively, the MRI max general diameter might appear to be a better way of representing the AAA size compared to max AP diameter; its calculation however can be challenging (especially when applied using manual processing). Using any single maximum diameter measure to represent an entire AAA will also always be a method highly influenced by the shape of the individual slices and be highly influenced by way the AAA slice has been segmented.

In contrast, using the **MRI maximum area** as a metric for AAA size may give more accurate estimations, as it accounts for the entire region comprising the slice and does not get affected by shape, irregularities or symmetry.

In Figure 4.21 A, the MRI max area metric and the max AP diameter, as measured with MRI, appear to be very strongly correlated as one might expect (R=0.95, p<0.0001) and with a coefficient of determination R^2=0.89, p<0.0001. The agreement however between the MRI max area metric and the max general diameter (Figure 4.21 B) is even stronger, with almost perfect alignment, with R=0.98, p<0.0001 and R^2=0.97, p<0.0001, therefore suggesting the two methods could be used interchangeably. Because, however, of the difficulty in determining the max general diameter and the potential issues with reproducibility if the process is not automated, it may be preferable to use the max area to measure AAA size. Additionally, as further explained in 4.4.3.2.3 and 4.4.3.2.4,

incorporating more values than just the maximum of the whole AAA (e.g. top 5 values) could contribute even more representative values for the entire AAA.
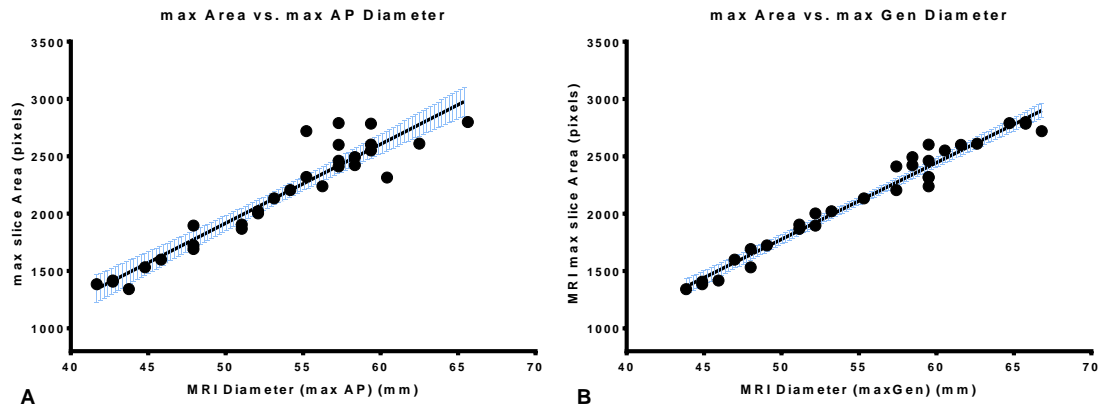
Figure 4.21: Relationship between Max Area and max diameters (max AP and maxGen) as measured with MRI.

*A) Max Area vs. max AP diameter: Pearson Correlation with correlation coefficient R=0.95, coefficient of determination R^2=0.89, p<0.0001, n=30 measurements (2 measurements per patient) for 15 patients, blue lines correspond to 95% C.I. of linear regression with Y = 68.85*X - 1526. All measurements automatically calculated from MRI data.*

*B) Max Area vs. max General diameter. Pearson Correlation with correlation coefficient R=0.98, coefficient of determination R^2=0.97, p<0.0001, n=30 measurements (2 measurements per patient) for 15 patients, blue lines correspond to 95% C.I. of linear regression with Y = 66.84*X - 1566. All measurements automatically calculated from MRI data.*

4.5.4 Measurement of AAA growth

The change in max AP diameter size after 2 years, as measured with all 3 modalities for the same 15 patients (as described in 4.5.1, 4.5.2, and 4.5.3) is depicted in Figure 4.22. As previously, the US and CT diameters were measured manually, and the MRI diameters were automatically calculated. It can be observed that in most cases, the changes follow the same overall trends, but for some subjects there are large difference in the changes calculated by different modalities, e.g. for patient ID=2 in Figure 4.22, MRI and CT values for change overlap, while the US value is notably larger by 5mm.

A more detailed analysis of the relationships between 2-year growth as measured with the 3 different modalities is presented in Figure 4.23. The US changes appear to be in disagreement with CT and MRI changes, while the MRI and CT show higher levels of correlation, with Pearson correlation coefficient R=0.859, coefficient of determination R^2=0.738, p<0.0001. More specifically, the bias between CT and US was 0.3mm, but with 95% limits of agreement from -4.2mm to 4.8mm, a range of 9mm. The bias between CT and MRI was 0.2mm, with 95% limits of agreement from -3.8mm to 4.2mm, a range of 8mm. The bias between MRI and US was 0.1mm with 95% limits of agreement from -6.2mm to 6.5mm, a range of 12.7mm.

The ranges of the 95% limits of agreement appear to be very wide in all above cases, suggesting that max AP diameter might not be the optimal measurement for growth estimations in AAAs. As suggested previously in 4.5.3.1.2 for AAA size measurement, the use of max Area metrics, ideally including more than values (e.g. top 5 largest areas of AAA) may provide a more accurate method for growth estimation.
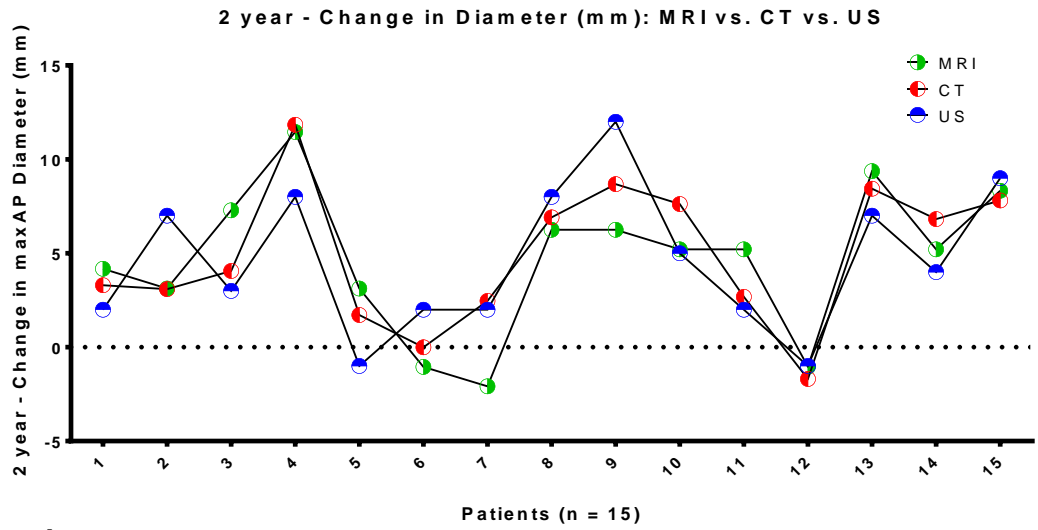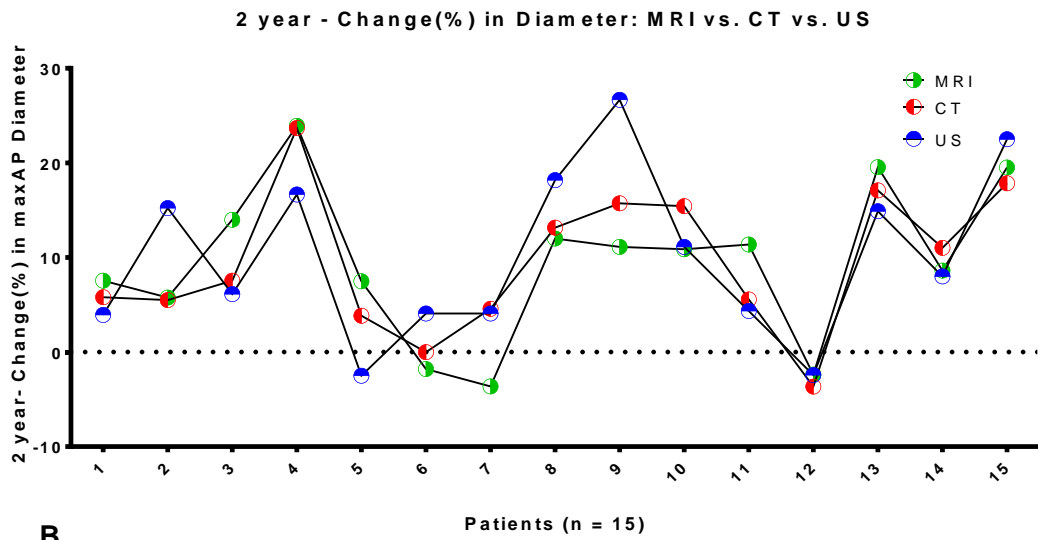
Figure 4.22: 2-year Change and %Change in max AP Diameter (mm): MRI vs. CT vs. US. *The patients had one scan with each modality in baseline (±2 months) and then had a repetition of measurements 2 years later (±2 months), n=15 patients; Change calculated as 2year-diameter minus baseline diameter. Percentage change calculated as (2year-diameter minus baseline diameter)/baseline diameter*100.*
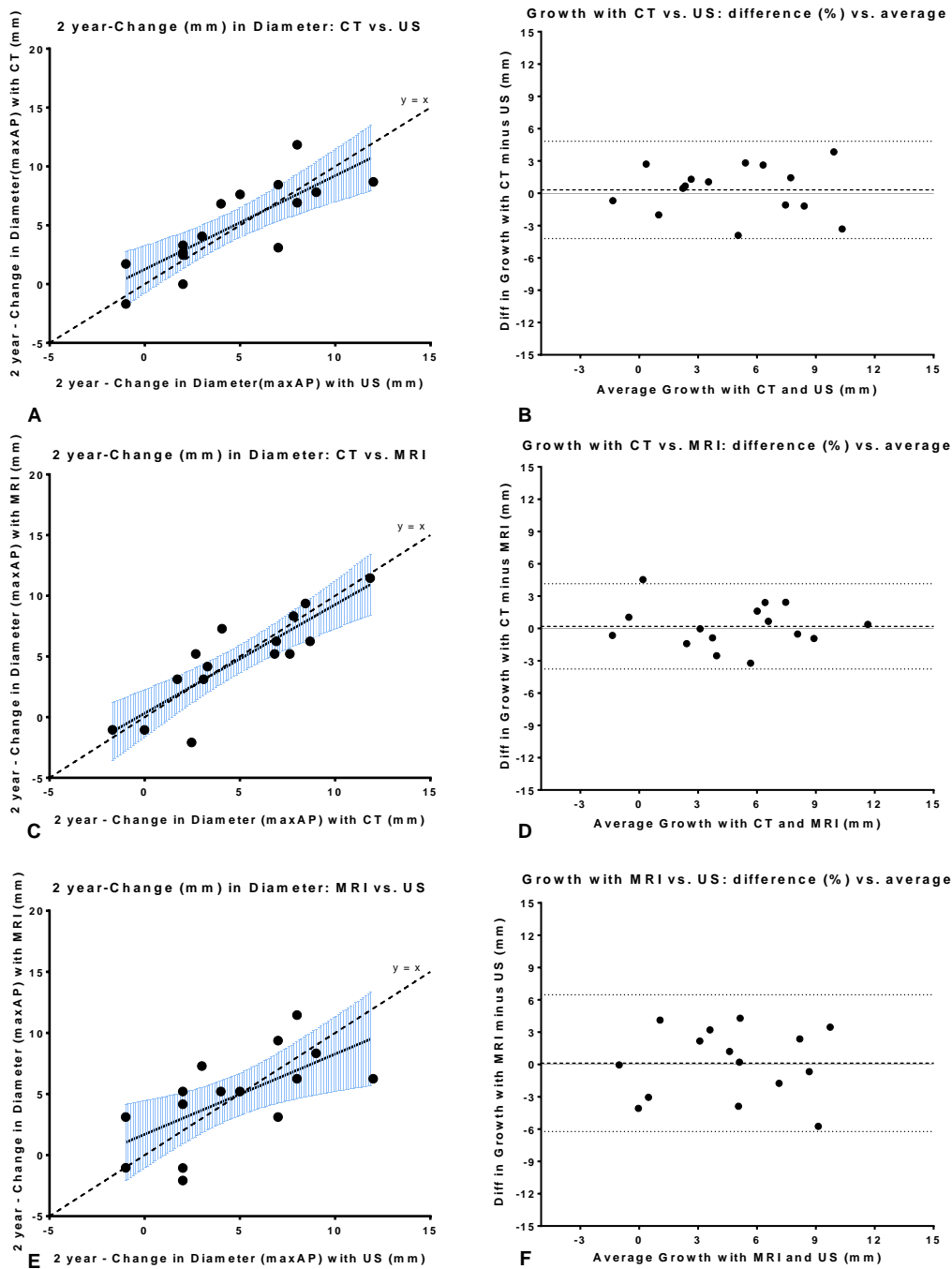
Figure 4.23: 2-year Change (mm) as calculated from max AP diameter: US vs. CT vs. MRI.
A: 2-year Change in Max AP diameter: CT vs. US: Pearson Correlation with correlation coefficient R=0.811, coefficient of determination R²=0.659, p<0.0002, n=15 patients, blue lines correspond to 95% C.I. of linear regression, identity (dashed) line y=x.
B: CT vs. US: Bland-Altman plot: bias=0.3mm, SD of bias=2.3mm. 95% Limits of Agreement from -4.2mm to 4.8mm, n=30 measurements (2 measurements per patient) for 15 patients.
C: 2-year Change in Max AP diameter: CT vs. MRI: Pearson Correlation with correlation coefficient R=0.859, coefficient of determination R²=0.738, p<0.0001, n=15 patients, blue lines correspond to

95% C.I. of linear regression, identity (dashed) line y=x.
D: *CT vs. MRI: Bland-Altman plot: bias=0.2mm, SD of bias=2.0mm. 95% Limits of Agreement from -3.8mm to 4.2mm, n=30 measurements (2 measurements per patient) for 15 patients.*
E: *2-year Change in Max AP diameter: MRI vs. US: Pearson Correlation with correlation coefficient R=0.643, coefficient of determination R^2=0.414, p<0.0096, n=15 patients, blue lines correspond to 95% C.I. of linear regression, identity (dashed) line y=x.*
F: *MRI vs. US: Bland-Altman plot: bias=0.1mm, SD of bias=3.2mm. 95% Limits of Agreement from -6.2mm to 6.5mm, n=30 measurements (2 measurements per patient) for 15 patients.*

4.6 Discussion

4.6.1 Measurement of AAA size and growth

Accurate identification of aortic size is of great importance, because it is the main criterion upon which AAA detection and management is based: according to current diagnostic criteria [246] maximum AP diameter measurements performed with US are most commonly used, with max AP sizes of 3.5 cm or higher signifying the existence of an AAA, while max AP sizes of >=5.5 cm or annual max AP growth of >=1cm qualify AAAs for surgical treatment. CT is almost exclusively used for pre-operative assessments and MRI is predominantly used for research purposes. However, the literature indicates that US regularly underestimates aortic measurements, compared to CT or MRI, with the last two being so accordant that MRI has been suggested as a potential replacement for CT altogether [243].

The results of this chapter (4.5.1.1) confirmed the literature findings in the MA³RS cohort. When 30 max AP diameters from the MA³RS trial data were compared, US measurements systematically under-measured diameter values compared to the other two modalities, with the mean US measurements at 48.3±0.9 mm, mean CT at 54.3±1.1 mm and mean MRI at 53.3±1.2 mm (Figure 4.15).

The bias (average of differences) between US and CT (Figure 4.16 C) was found to be 6.0 mm, thus exceeding the maximum acceptable bias of 5 mm for US reproducibility, as set by the UK AAA screening programme (NAAASP) [113]. The bias between US and MRI (Figure 4.16 E) was 5.0 mm, being exactly on this limit. The bias between MRI and CT was 1.1 mm, which is excellent, since it is 4.5 times smaller than the maximum acceptable bias of 5mm.

In order to demonstrate the effects of the disagreements between US, CT and MRI, the 30 AAAs were classified as small (<55mm) or large (>=55mm), based on the

measurements of each modality. US identified 2 of the AAAs as large, while CT identified 16 cases and MRI 15 cases.

Using CT as ground truth (and the ≥55 mm threshold which defined "large" AAAs or "positive" cases), US achieved 100% specificity, but just 12.5% sensitivity, with 14 false positives. In areas like medical diagnosis, a high level of sensitivity is more important that a high level of specificity. On the other hand, MRI had 92.9% specificity and 87.5% sensitivity, with only 2 false negatives and 1 false positive.

These results highlight the variability between the different imaging methods and the danger of applying thresholds defined with one imaging modality to measurements performed with different modalities. Accurate documentation of the imaging methodologies of research studies should thus be considered of uttermost importance.

The high bias between US and the other 2 modalities could be attributed to the intrinsic differences in the imaging methods, for example the difference in soft tissue contrast evident between the modalities (Figure 4.2, Figure 4.3 and Figure 4.13). The differences in size observed would not constitute such a significant problem so long as they were consistent, if e.g. CT measurements were consistently 3mm larger than the corresponding US measurements, it would be possible to use both methods interchangeably after a small adaptation, but this was not the case.

In order to explore the discordance between US and CT or MRI further, ROC analysis was performed, and it identified adjustments of the 55 mm threshold, which improves the classification agreement and provides a formula for US, CT and MRI classifications to be comparable (i.e. with a different threshold for each modality: >48mm for US and 52.5mm for MRI). Given that the sample size was only n=30, further analysis with larger sample sizes in the future would be advisable for more accurate thresholds.

Given the fact that max AP diameter growth of ≥1 cm/year qualifies AAAs for surgical treatment, it was of great interest to establish the bias between US, CT and MRI growth measurements. The comparisons were applied on a sample of 15 subjects for whom I had access to 2-year growth data available in all 3 modalities.

The US growth did not correlate well with CT and MRI growth, while CT and MRI demonstrated a stronger correlation (R^2=0.738, p<0.0001). The bias (average of differences) between modalities was low, with CT-US bias of 0.3 mm, CT-MRI bias of 0.2 mm and MRI-US bias of 0.1 mm. However, the ranges of 95% limits of agreement derived from Bland-Altman analysis painted a different picture: very wide ranges, with CT-US range of 9 mm, CT-MRI range of 8 mm and MRI-US range of 12.7 mm revealed a very high discordance between the 3 imaging modalities in growth calculation.

This finding may suggest that max AP diameter might be a restrictive method for calculating AAA growth, with reproducibility issues between the different imaging modalities.

4.6.2 Alternatives to max AP

AAAs are rarely perfectly cylindrical, thus the use of max AP diameter to represent their size may be debatable, because it does not account for variations in AAA shape. This was illustrated with specific examples from the MA^{3}RS dataset (4.2.1.3 and Figure 4.1, Figure 4.2 and Figure 4.6,) and further demonstrated by comparing the max AP diameter against the max general diameter of AAAs. The max general diameter was defined as an alternative measurement to max AP diameter, representing the largest diameter of the AAA without being limited only to the AP axis.

Comparison between the two types of diameter (automatically calculated with my algorithm) in a sample of 30, revealed as expected, that even though their

values correlated (R^2=0.85), the bias between the values (bias=2.2mm, SD of bias=2.7mm, 95% Limits of Agreement from -3.1mm to 7.5mm,) is too high for them to be used as interchangeable methods of AAA measurement.

The max general diameter may be a more suitable metric for AAA size, but nevertheless its calculation is not standardised and can introduce reproducibility issues. Additionally, neither max AP nor max general diameter metrics are ideal for growth calculations: max AP diameter growth cannot detect growth happening in directions other than on the AP axis, while max general diameter can be influenced by the shape of individual AAA slices.

MRI maximum area was introduced as a more appropriate AAA size metric, unaffected as it is by the shape or symmetry of individual slices, while most importantly, being highly reproducible. The max area of 30 MA³RS subjects was automatically calculated and compared with max AP diameters and max general diameters. The max area measurements correlated better with the max general diameter measurements (R^2=0.97, p<0.0001) than with the max AP diameter measurements (R^2=0.89, p<0.0001). This was anticipated, as the max AP diameter, being restricted to the AP axis, would miss any large diameters occurring at different directions, hence underestimating the size of some AAAs.

This weakness of the max AP diameter becomes more detrimental in AAA growth calculations, where the AP-axis restriction can fail to reflect 3-dimensional growth that may have occurred on different planes or directions. Max general diameter and max area can be used almost interchangeably, but max area may be preferred due to its higher reproducibility.

4.7 Summary

In conclusion, US appears to under-measure AAA size compared to MRI and CT. MRI showed very high levels of agreement with CT, indicating it can be successfully used to replace CT measurements. The currently used thresholds for AAA stratification should be revisited for more accuracy. MRI measurements for AAA appear better suited for the work presented in the remainder of this thesis. These metrics also benefit from being able to be automatically calculated via an objective computational approach (developed for this thesis).

The use of max AP diameter to measure AAA size proved to be potentially problematic, especially for growth calculations. Alternative metrics, namely max general diameter and max area were found to be more reliable for growth measurements, among which the max area metric is more reproducible and was thus selected to be used for the growth calculations required in the following chapters of this thesis.

Chapter 5   Automatic Detection of "Hotspots" of Inflammation

5.1   Introduction

In this chapter I introduce a process towards building efficient algorithms for the automatic detection of inflammatory hotspots in USPIO-enhanced MRI images of AAA. Building upon the concepts described in Chapter 2, an algorithm which closely replicates the manual hotspot detection and AAA classification used in the pilot and MA³RS trials was created (Replication algorithm), followed by two improved algorithms (Evolution 2D and 3D), which take the inflammation analysis a step further by using non-thresholded data and investigating the use of additional metrics available within the image data. For the first time, 3D hotspot detection and visualisation of AAA hotspots are achieved, supplemented with 3D metrics to assist further AAA analysis and stratification. Finally, two Graphical User Interfaces created to combine the data assessment, visualisation and automatic processing of the algorithms by the clinical research team for the MA³RS trial (and potential follow-up trials) are showcased at the end of the chapter.

5.1.1 The transition from Manual to Automatic Hotspot Segmentation

As described in the methods sections of the pilot and MA[3]RS study (see 1.4.2 and 1.5.2), in order to identify the inflammatory hotspots in each AAA, the clinical observers would visually inspect colourmaps that were calculated to correspond to $\%\Delta T_2^*$ values between scans which visually represented focal USPIO uptake. The $\%\Delta T_2^*$ maps used for the manual hotspot segmentation had previously been thresholded (59% threshold in pilot protocol, 71% threshold in MA[3]RS protocol, see 1.4.2 and 1.5.2). As can be seen in Figure 5.1, the areas corresponding to $\%\Delta T_2^*$ values below the threshold therefore appeared uniform (blue colour) and made the differentiation between inflammatory and non-inflammatory areas more visually obvious for manual segmentation by the clinical observers. The criteria for an inflammatory area to be considered a hotspot have been introduced in section 1.4.3 and are briefly summarised in Figure 5.1.
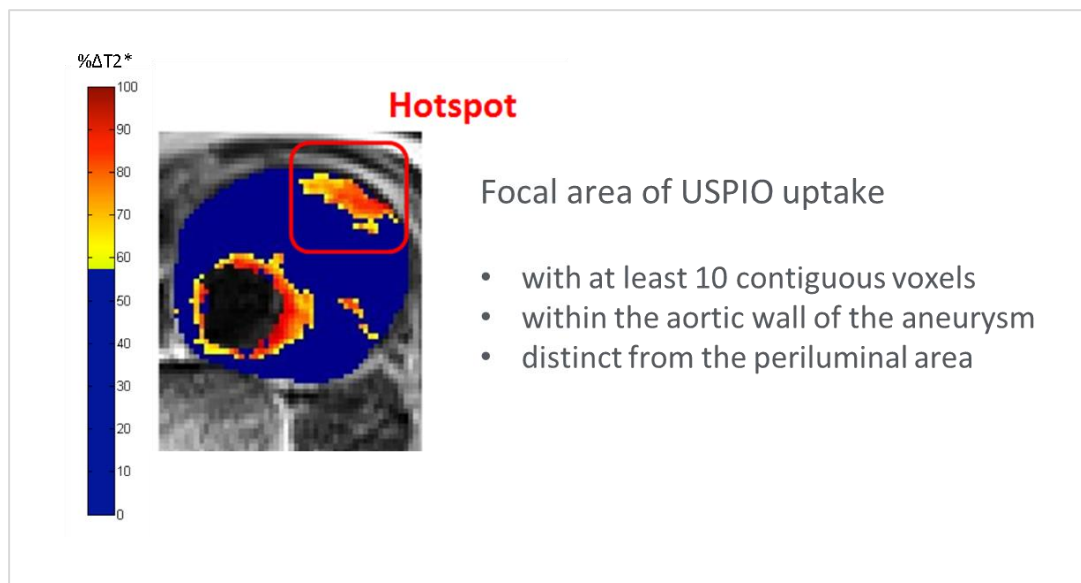
Figure 5.1: Criteria for an area to be considered an "inflammatory hotspot". $\%\Delta T_2^*$ map with colour map superimposed on T_2-weighted cross-sectional axial MRI slice of an AAA. The blue area represents the thrombus and aortic wall combined and the lumen area has been left uncovered are used to visualise the areas of USPIO uptake, reflecting inflammation. The criteria depicted in the figure had to be fulfilled during the visual assessment for the areas to be considered "hotspots". This was taken from the pilot study, hence the threshold applied to the $\%\Delta T_2^*$ map is 59%.

5.2　　Algorithm definition and pre-processing

Three algorithms will be presented in this chapter (Figure 5.2). Firstly, the "Replication of Manual Hotspot Detection Algorithm" (5.3) was created to imitate previous manual hotspot selection and automate it so that it could be applicable on a large scale reproducibly. The output was 2D hotspots similar to those selected by the clinical observers and exported as *.tiff image files for visual presentation.
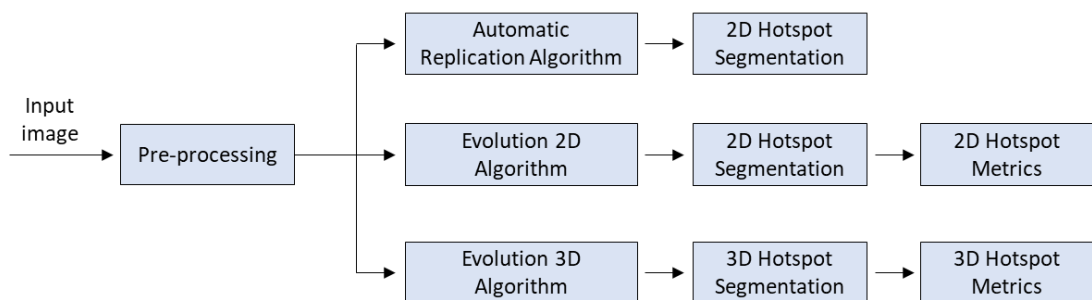
Figure 5.2: The three algorithms created. *All three algorithms shared the same input and pre-processing.*

The second algorithm, presented here as "Evolution 2D Algorithm", introduced some changes into the process, firstly and most importantly by using non-thresholded %ΔT_2* maps for hotspot detection and also by introducing additional hotspot metrics.

The third algorithm ("Evolution 3D Algorithm") was very similar to the 2nd, but segmenting 3-dimensional hotspots instead, something that would be impossible to be accurately performed with manual processing, as well as calculating additional 3D hotspot metrics.

5.2.1 Prior to input

As previously detailed in the description of the MA^{3}RS study protocol (1.5.2.2), some data processing took place after the MRI scanning and before the input of the images to my algorithm. Briefly, these tasks comprise of:

- Data registration

- Noise filtering

- T$_2$* map generation

5.2.2 Input

As demonstrated in the flowchart in Figure 5.3, the data imported by the algorithm are, for each patient:

- The manually segmented **Regions of Interest** (ROIs), in which the lumen, thrombus and aortic wall have been identified on all available slices of each AAA by clinical observers. These manual segmentations have been extracted from SliceOmatic 4.3 (TomoVision) where they were originally created as *.tag files and processed with in-house software so that they can be imported to MATLAB R2015a (The MathWorks, Inc., Natick, MA, USA), as DICOM files. The ROIs come in the form of a mask with values 0 to 3, with 0 for background, 1 for lumen, 2 for thrombus and 3 for wall.

- The **T$_2$-weighted** scans for each AAA. These are used for anatomical reference upon which functional information is to be superimposed.

- The **T$_2$* maps** for scans **pre-USPIO** administration, which have been calculated with the T$_2$*mapping software previously developed in-house.

- The **T$_2$* maps** for scans **post-USPIO** administration, which have been calculated with the T$_2$*mapping software previously developed in-house (see 1.5.2.2).

All the aforementioned datasets were spatially co-registered as described previously. The process followed for the Input of data is presented in the flowchart in Figure 5.3.
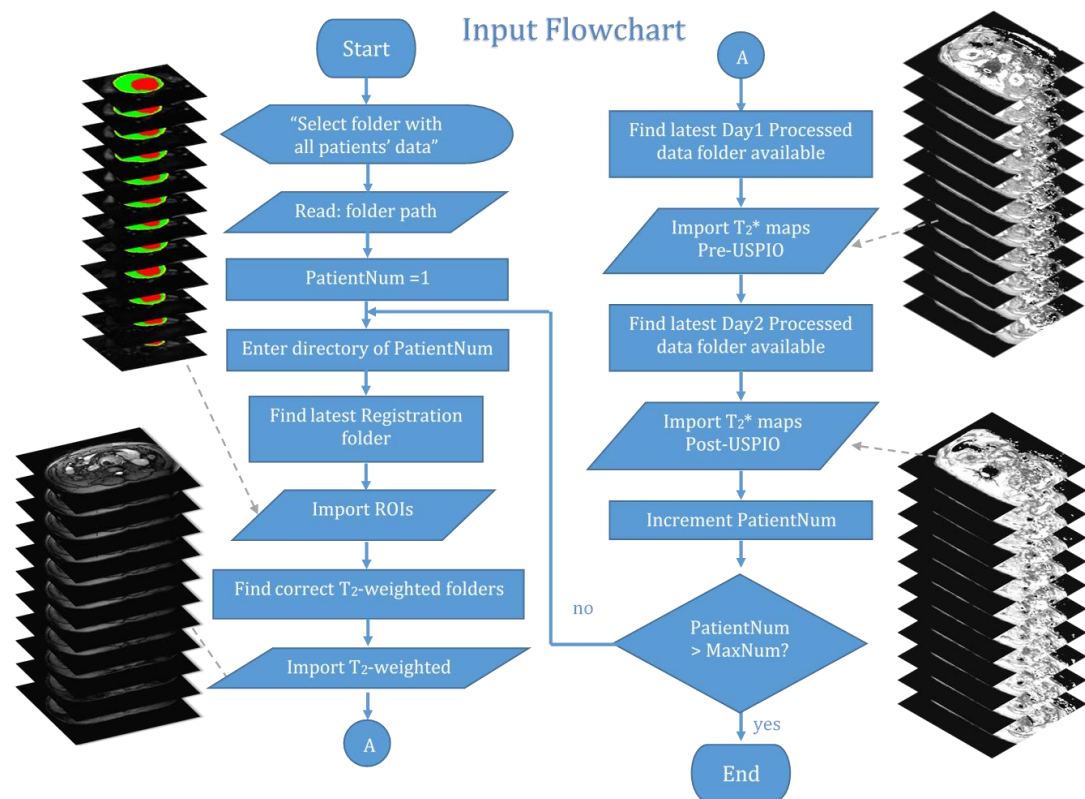
Figure 5.3: Input Flowchart. *The code includes two loops, with the external loop executing one iteration per patient, as seen here, while the internal loop executes one iteration per slice for every action (e.g. importing ROIs), but it is not shown in this flowchart for simplification.*

5.2.3 Pre-processing of data

Generally, *pre-processing* of the data in image analysis systems refers to the application of techniques for noise suppression and artefact removal. As explained in 5.2.1 and 1.5.2.2, some noise removal had already been deployed prior to input of the data into these algorithms. Here, pre-processing dealt with correcting the data produced from manual segmentations.

The pre-processing stage was the same for all 3 versions of the algorithm.

5.2.3.1 Corrections of manual ROI segmentations

5.2.3.1.1 Accidental marking of pixels as ROI

There were many instances among manually segmented ROIs of the datasets at hand, where small areas or just single pixels outside the ROI had been marked accidentally by the clinical observers. In Figure 5.4, a representative example is presented, where the three colours (red for lumen, green for thrombus, yellow for aortic wall) have been used to manually mark the ROIs, but two small individual areas outside the AAA have also been selected: a cluster of pixels has been marked as part of the lumen in red colour (Figure 5.4 A), and less visible, but causing problems in the automatic calculation, there is one isolated pixel (Figure 5.4 C) marked as part of the wall in yellow colour. This sort of "accidental" marking of pixels, which then incorrectly contribute to regional masks, is relatively common in tasks that involve manual segmentation of images, so it was important that my software had an automated method of checking the data for these errant pixels and removing them from further processing.
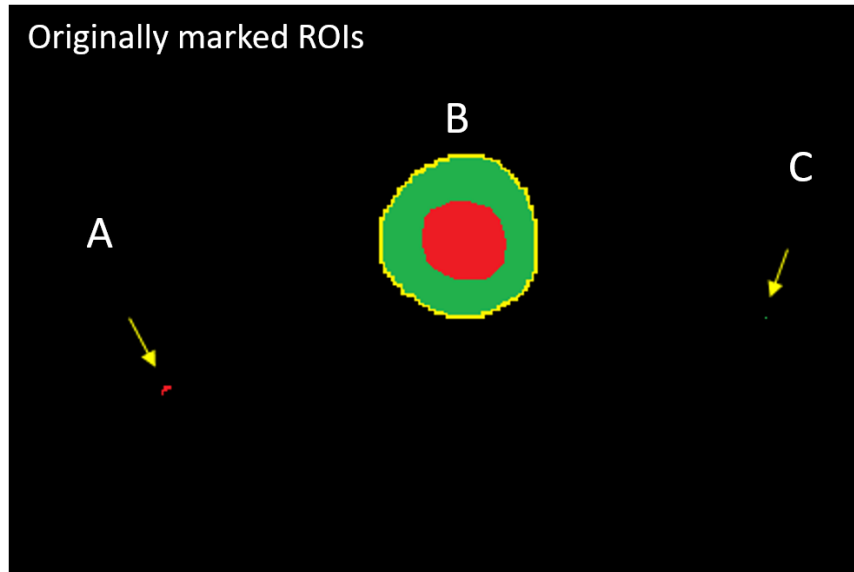
Figure 5.4: Accidental marking of pixels as ROI. *During the manual segmentation, some pixels (A and C) external to the ROI (lumen in red, thrombus in green and aortic wall in yellow) were sometimes marked as members of the ROI. Here, the cluster of pixels at A was marked as part of the lumen (red) and the pixel at C was marked as part of the wall (yellow).*

To correct this recurring ROI issue, the algorithm creates a binary mask that divides all pixels into two groups: pixels marked as belonging to the ROI during the manual segmentation are assigned the value '1' and all other pixels, marked as background, are assigned the value '0', as shown in Figure 5.4. Then MATLAB function *bwmorph* is used to remove any isolated binary objects such as the one marked in Figure 5.5 C.
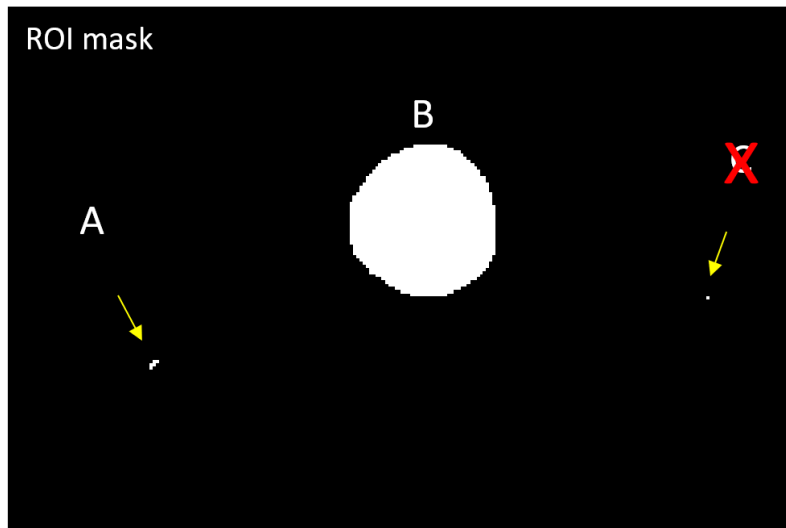
Figure 5.5: Mask of originally segmented ROIs. *All pixels that had been marked as members of the ROI during the manual segmentation are assigned the value 1 and appear here in white, while the background pixels have been assigned the value 0 and appear black. MATLAB's bwmorph function is applied and isolated pixels are "cleaned", thus C is deleted.*

Next, all inter-connected areas (non-background) are identified using MATLAB's *bwconncomp* function with 2-dimensional connectivity for n=8 neighbourhood. It is expected that the actual ROI that includes lumen, thrombus and wall will be the largest interconnected area, as the accidentally marked areas were consistently much smaller. By sorting all interconnected areas according to size, the biggest area (in this case B) can be safely selected as the ROI and all remaining interconnected areas (in this case just A, as C had already been excluded previously) can be masked and excluded from further processing.

5.2.3.1.2 Accidental omission of ROI pixels

Another common issue in manual segmentation data that was recurrently present in some of the datasets here was the accidental omission of some pixels within the AAA, as depicted in Figure 5.6. To correct this during the pre-processing, after the algorithm defined all interconnected areas as explained in 5.2.3.1.1, all "holes" within them were closed, using MATLAB's *imfill* function.
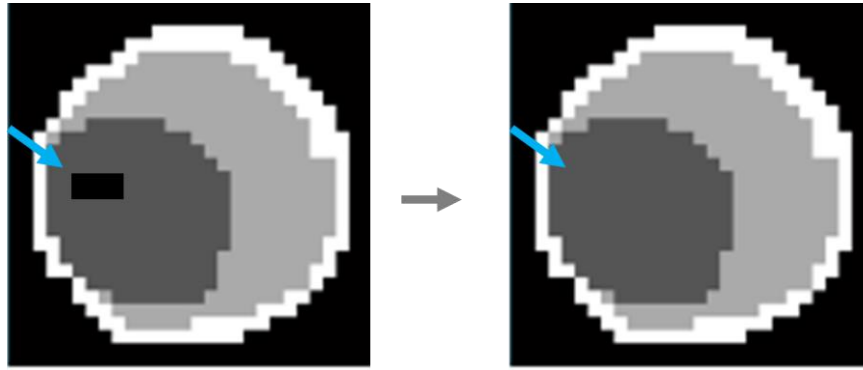
Figure 5.6: Accidental omission of pixels during manual segmentation. In this ROI representation, the dark grey area corresponds to the lumen, the light grey to the thrombus and the white to the wall. Sometimes pixels like the ones shown within the lumen here (arrow) were accidentally left unmarked during manual segmentation. MATLAB's imfill function was applied on such cases and the unmarked pixels were assigned to the ROI they belonged to.

All of the above steps of the pre-processing part of the algorithm are presented as a flowchart in Figure 5.7.
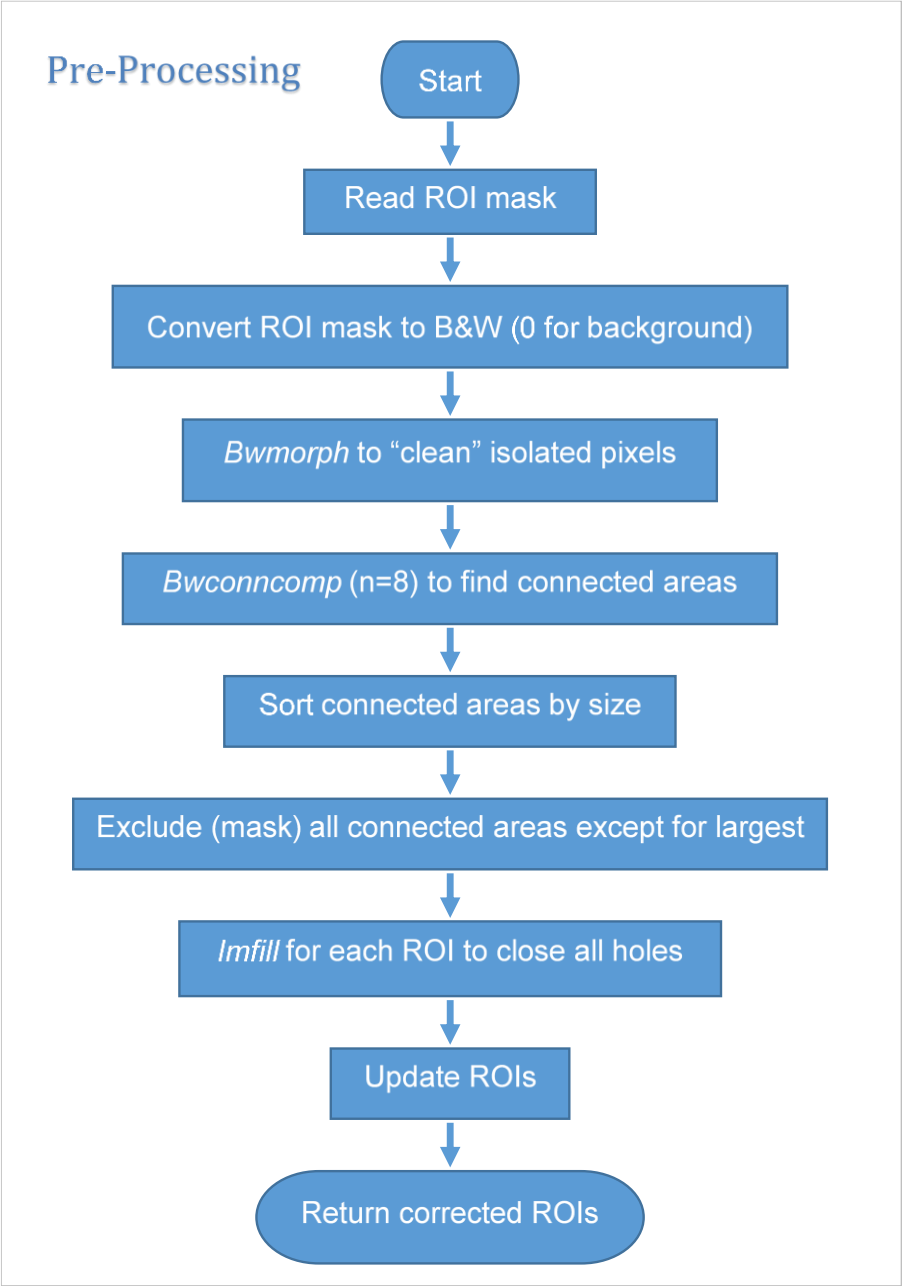
Figure 5.7: Pre-processing flowchart

5.3 The "Automatic Replication" Algorithm

As a starting point, I focused on creating an algorithm that would automatically "replicate" the manual processing as performed by the clinical observers. In order to achieve a successful "imitation" of the manual hotspot detection, processing rules had to be identified, as well as the order in which they were being manually applied, so that they could then be coded into an algorithm for automation. The rules of the manual detection and the corresponding functions are presented in Table 5.1.

Table 5.1: Manual Detection Rules and the corresponding functions in the Replication Algorithm, as detailed later in this chapter

	Manual Detection Rules	Corresponding functions in Replication Algorithm
1	$\%\Delta T_2^*$ maps have **71% threshold**	$\%\Delta T_2^*$ maps creation • 71% threshold applied
2	Hotspots not touching **dropout** areas neighbouring with lumen	Dropout Processing • Dropout areas map created. • Dropout areas in contact with lumen detected. • Hotspots in contact with these Dropout areas excluded
3	Hotspots distinct from **periluminal area**	Periluminal method • Hotspots in contact with lumen excluded (number of contact points allowed is adjustable)
4	Hotspots **>=10** contiguous voxels	Hotspot Detection • Detection of all contiguous areas (2D) on thresholded $\%\Delta T_2^*$ maps • Only areas >=10 voxels selected as potential Hotspots
5	Hotspots within **aortic wall**	Mural USPIO uptake • Detection of outer wall Perimeter • Only Hotspots neighbouring with outer perimeter selected

6	AAA **Classification in 3 groups**: • positive USPIO enhancement • negative USPIO enhancement • indeterminate USPIO enhancement	AAA Classification in 2 groups • positive USPIO enhancement • negative USPIO enhancement

5.3.1 Percentage ΔT2* Thresholding

As described in the 1.4.2 and 1.5.2 (Pilot and MA^{3}RS methods), in the case of manual data processing, thresholding was applied to the values of the $\%\Delta T_2*$ maps before visually reviewing them and identifying inflammatory hotpots.

Specifically, the threshold applied on the MA^{3}RS data was 71%, so after importing the datasets, a 71% threshold was applied on the $\%\Delta T_2*$ maps, as illustrated in Figure 5.8.
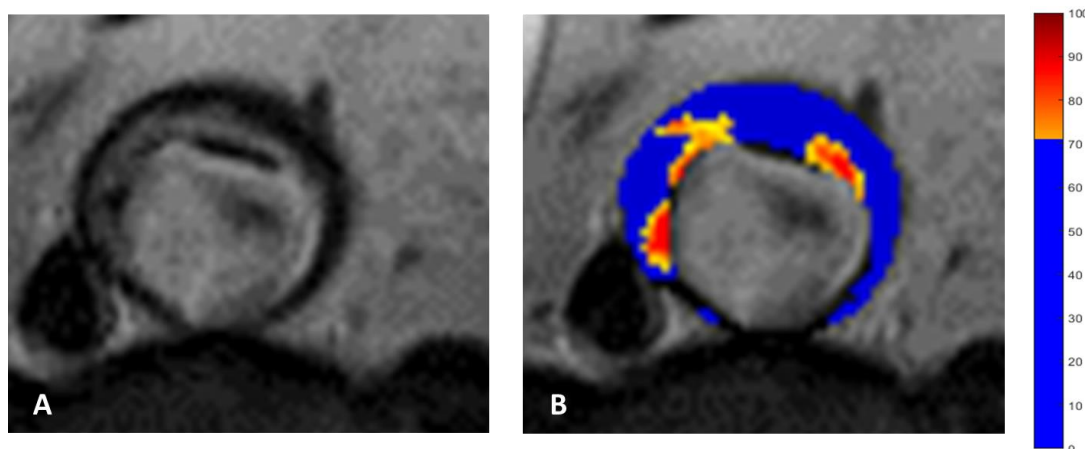
Figure 5.8: Application of 71% threshold on %ΔT2* map. A) *Anatomical T$_2$W MRI slice of MA^{3}RS cohort patient.* **B)** *The corresponding %ΔT$_2$* values are calculated and visualised in form of a colour map (jet scale) superimposed on the T$_2$W image (A). As can be seen in the colour bar, changes smaller than the 71% threshold are considered non-significant and are represented as a uniform value (blue). (Image source: MA^{3}RS trial).*

5.3.2 Hotspots touching "Dropout" areas

As described in 1.5.2.2., during the process of the T_2* map creation from the 4 individual gradient echo images, pixels which could not provide a reliable T_2* decay fit were identified and excluded, forming "dropout" areas [15]. These areas could be found anywhere within the AAA, but one case stood out: dropout areas touching the lumen. These were of special interest, because in some cases they expanded from the luminal area as far as to reach a candidate hotspot. An example of this is shown in Figure 5.9 B. It can be seen that there would be no way to reliably assess whether the hotspot was actually distinct from the periluminal area. For this reason, all candidate hotspots touching a dropout area which went on to neighbour with the lumen, were excluded.
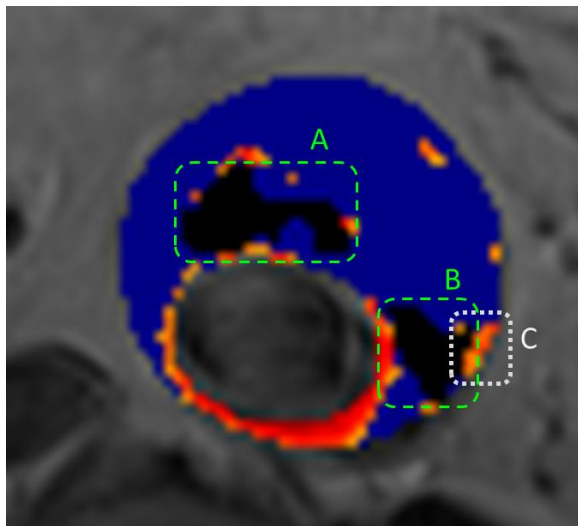
Figure 5.9: Two "dropout" areas within one AAA slice. *%ΔT₂* map superimposed on anatomical T_2W MRI slice of MA^{3}RS cohort patient. Both (A) and (B) dropouts are touching the lumen, but (B) is of special interest because it is also touching a candidate hotspot (C). This hotspot (C) will be excluded, as we cannot assess whether it is connected with the lumen through the periluminal area, because of the dropout pixels found in-between.*

This rule was also coded into the hotspot detection algorithm. After the %ΔT$_2$* map creation (Figure 5.10 A), the dropout areas were identified and a mask for them was created (Figure 5.10 B). Next, a mask for the lumen area was created based on the manual segmentation performed previously and it was dilated by

one pixel, using the MATLAB function *bwmorph* (Figure 5.10 C). The dilated lumen mask (Figure 5.10 C) was then combined with the map of dropouts (Figure 5.10 B) as shown in Figure 5.10 D. Having dilated the lumen by 1 pixel, the intersection points between lumen and dropouts were identified and the exact number of overlapping pixels per intersection was calculated. By calculating this number, instead of using simply a positive/negative answer to whether each dropout touched the lumen, the strictness of neighbouring rules could further be adapted and investigated. A threshold, for example, of 2 neighbouring pixels could be set, allowing dropout areas with less than 2 overlapping pixels to be considered separate from the lumen.
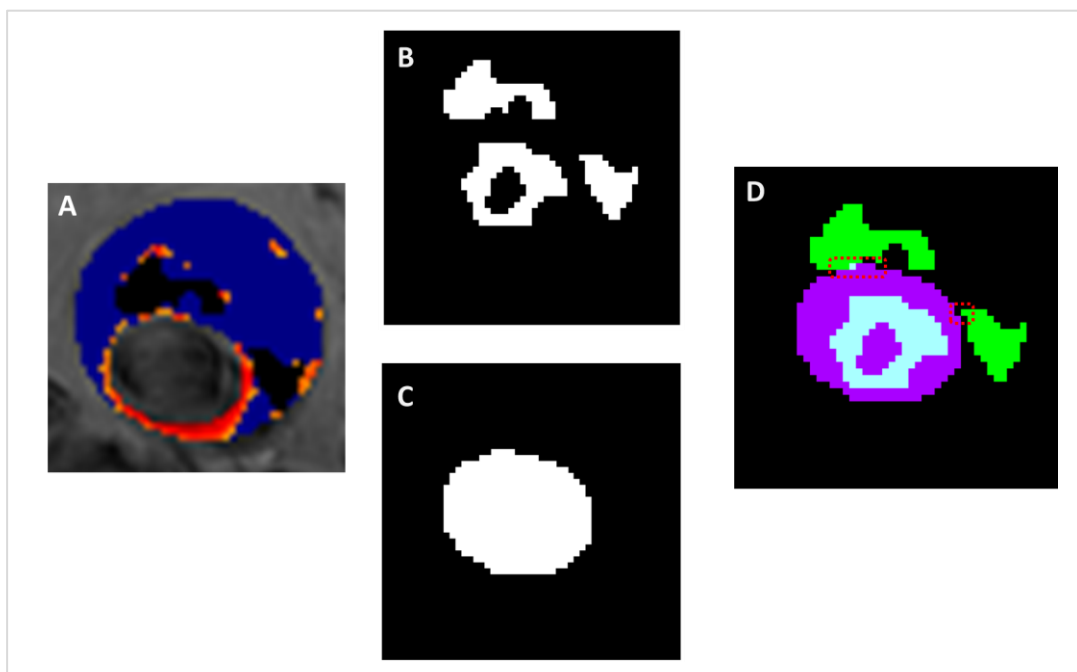
Figure 5.10: Identification of dropout areas in contact with lumen. A) *%ΔT$_2$* map with 71% threshold applied. The dropout areas are visible in black colour.* *B)* *Mask of all dropout areas identified within the same slice (illustrated in white).* *C)* *Mask of the lumen of the same slice.* *D)* *Combining the masks of dropouts (B) and lumen (C) to find points of contact (8-pixel neighbourhood), marked here within the red lines.*

In the next step, each candidate hotspot would be checked to assess whether it was in contact with any of the dropout areas that were touching the lumen, in a similar manner: For each hotspot, after dilating the hotspot by 1 pixel with the

bwmorph function, a mask of the slice was created (with 1 for hotspot pixels and 0 for background) and was overlapped with the mask of each single dropout area that was touching the lumen. If the hotspot was found to be in contact with any of the specific dropout areas, it was discarded.

The whole process followed for the exclusion of hotspots that were in contact with dropout areas is presented in Figure 5.11.
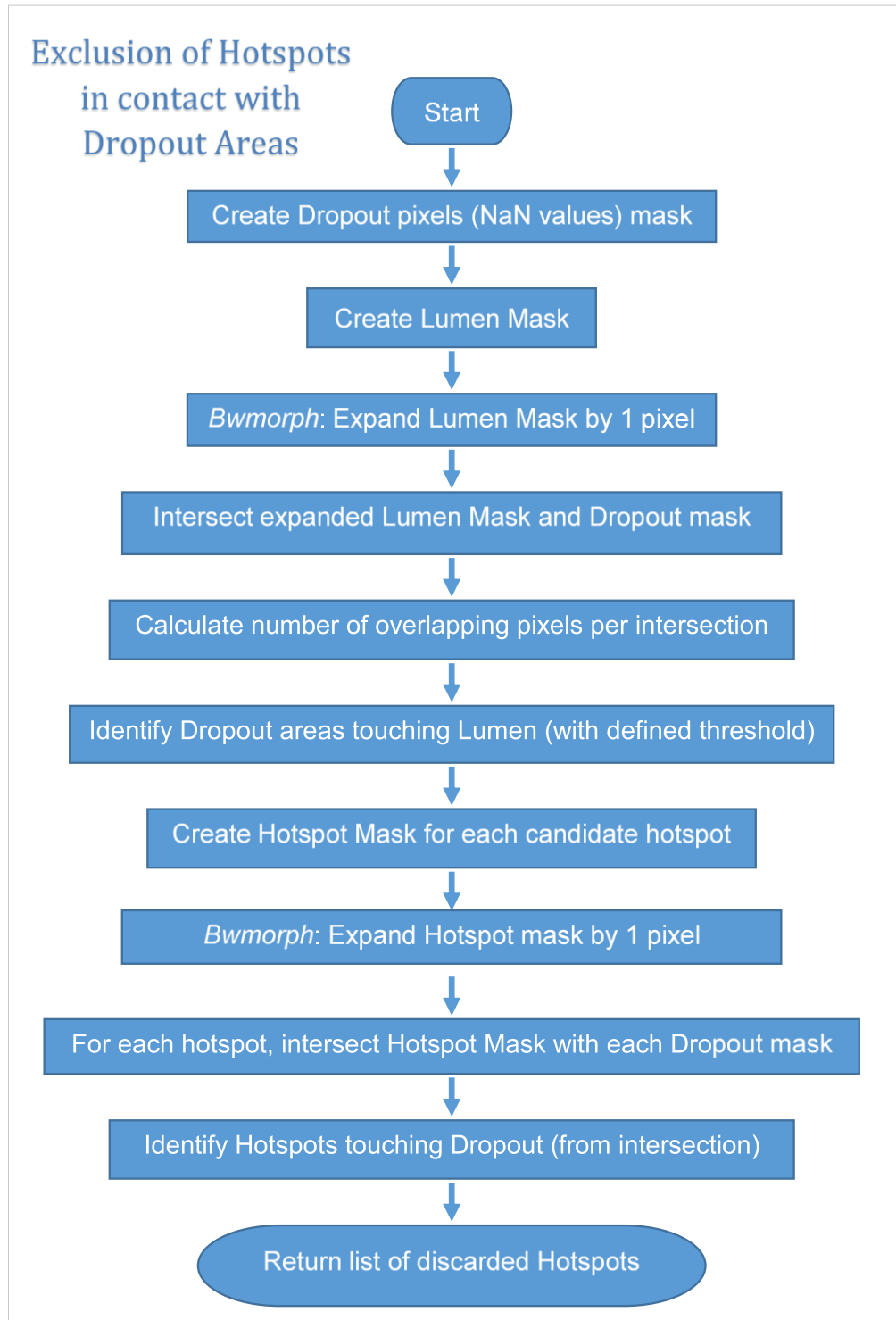
Figure 5.11: Flowchart of Dropout Exclusion.

5.3.3 Detection of Hotspots within Periluminal Area

One of the criteria for an inflammatory area to be considered a hotspot during manual segmentation was that it should not be part of the periluminal area. In order to incorporate this rule in the automatic processing, the following steps were taken.

For the 71% thresholded data (Figure 5.12 A), the perimeter of the luminal area (as defined in the manually segmented ROIs) was identified. Each candidate hotspot (e.g. the hotspot in Figure 5.12 B) was dilated by 1 pixel (e.g. the hotspot has been dilated in Figure 5.12   C) and its constituent pixels consequently intersected with the pixels of the lumen's perimeter (marked in red in Figure 5.12 C). This way, the number of contact points between the lumen and each hotspot (marked in blue in Figure 5.12 C) was identified and the hotspots could be further stratified, as either not touching the lumen, or touching with a known number of pixels.
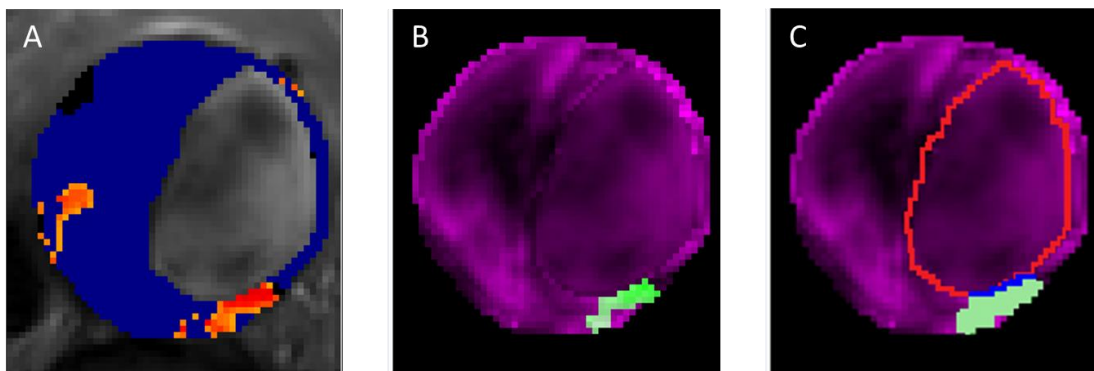
***Figure 5.12: Detection of Hotspots touching the periluminal area. A)** %ΔT$_2$* map with 71% threshold applied. **B)** Candidate hotspot detected, marked in green colour. **C)** Perimeter of lumen (red line) and thickened hotspot (by one pixel with MATLAB bwmorph function) combined and overlapping pixels are marked in blue.*

5.3.4 Hotspot Size

As explained in section 1.4.3.1, a minimum of 10 contiguous pixels were required for an area of inflammation to be considered a "hotspot" during manual segmentation, even though this number was to some extent arbitrary, having been empirically selected for the original pilot AAA project data. The same number was used in the replication algorithm.

5.3.5 Mural USPIO uptake

After applying the Automatic Replication Algorithm, there were some cases of hotspots being automatically detected by the program that were omitted by the manual hotspot detection. Upon review of each of these cases, a common characteristic was determined: despite the existence of USPIO uptake on the wall, the uptake only appeared within the inner layers of the aortic wall and did not reach the outer area, as described by the outmost pixels on the perimeter of the AAA. It must be noted here that the thickness of the aortic wall varies among different AAAs, while it can also vary within the same AAA, ranging from 1 pixel to several pixels, as depicted in Figure 5.13.
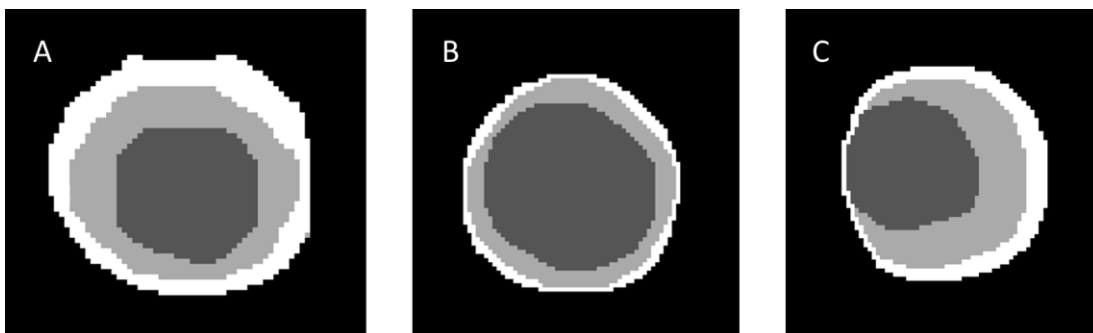
Figure 5.13: Examples of different-sized aortic walls. *Cross-sectional slices depicting the manually segmented ROIs corresponding to 3 different AAAs (A, B, C). The aortic wall is shown in white, the thrombus in light grey and the lumen in dark grey. The difference in the size of the aortic wall is very pronounced among these cases.*

The reason behind the failure of the manual processing to detect these hotspots lies on the limitations imposed by the visual examination. The manual assessment of inflammatory hotspots was performed on the %ΔT$_2$* colourmaps, which look like Figure 5.14 A, using the SliceOmatic 4.3 (TomoVision) software.

As a result, the observer would not have direct reference of the segmentations used for processing, as these could not be superimposed on the same image when using the SliceOmatic software used for manual segmentation. The position of the lumen was obvious, as it was always kept unmasked in the %ΔT$_2$* colourmaps, but the aortic wall thickness was not presented visually. This information is crucial for the observer to determine whether the candidate area lies within the aortic wall and therefore should be accepted as a hotspot, demonstrating a limitation in the manual hotspot process.

Within this study, and before this issue was identified, observers tended to regard the outer perimeter of the AAA as wall, namely a wall of approximately 1-pixel width.
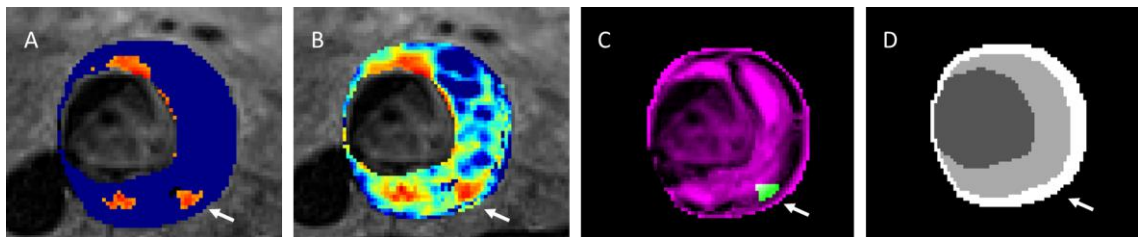
Figure 5.14: Example of hotspot found on the inner layers of aortic wall. A) %ΔT$_2$ colourmaps with 71% threshold B) %ΔT$_2$* colourmap without threshold. C) Hotspot which intersects with aortic wall, but not the outer perimeter of the wall, as detected by automatic algorithm. D) ROIs, with the aortic wall in white, the thrombus in light grey and the lumen in dark grey. The wall clearly appears to be thicker than 1 pixel at the location of the hotspot (C).*

Consequently, the manually segmented hotspots only included the cases in which the USPIO uptake was present in the outer part of the wall, leading to disagreements with the automatic processing, as the algorithm checked the entire wall area (as segmented by clinical observers) for hotspot co-localisation, accepting all cases of mural USPIO uptake, regardless of their exact location

within the wall, as shown in Figure 5.14, where the hotspot identified by the algorithm in Figure 5.14 C was not selected by the clinical observers, as it was not located on the outer perimeter of the AAA.

The manual segmentation issue could be potentially resolved by creating new $\%\Delta T_2^*$ colourmaps which would include wall-thickness information. As this issue was however only discovered with the application of the automatic segmentation on the data (processed after the manual segmentations had been completed and the study database closed), re-visiting and updating the manual processing was not an option during the work completed in this thesis.

The Automatic Replication algorithm was updated to ensure only hotspots found on the outer perimeter of the aortic wall would be accepted in order to best replicate manual processing for this stage of the algorithm development and testing. The option of including hotspots found within the inner layers of the aortic wall was included in the Evolution 2D Algorithm and Evolution 3D Algorithm which will be introduced in 5.4 and 5.5 respectively.

5.3.6 Anatomical artefacts

As mentioned previously, perhaps the most important factor that makes the automation and standardisation of AAA processing challenging is the variation in AAA shapes. Contrary to cases such as the brain and the human heart, which have a fairly well documented and reproducible anatomical features, and for which standardised segmentation techniques have been implemented, automatic processing of AAAs still requires human evaluation of the results produced.

A representative case from the MA[3]RS dataset is presented in Figure 5.15 A, where a large inflammatory area on the $\%\Delta T_2^*$ colourmap (with 71% threshold applied) fulfilled all the conditions to be considered a hotspot and was thus selected by the automatic hotspot detection algorithm (marked in Figure 5.15 B

with green colour). Interestingly, the specific case had been dismissed during the manual selection of hotspots by the clinicians involved in the MA³RS project. Their reasoning was that the shape and position of the specific candidate hotspot were suggestive of it being a part of the duodenum, which had mistakenly been included in the ROI during segmentation by the clinical observers. This additional anatomical information was not available to the algorithm and potential introduction of segmentations of organs external to the aorta, like the duodenum, was outwith the scope of this thesis. If automatic segmentation processes are eventually implemented, then exclusion of duodenum-related areas will need to be incorporated into the segmentation process and should also be implemented in future manual segmentations.
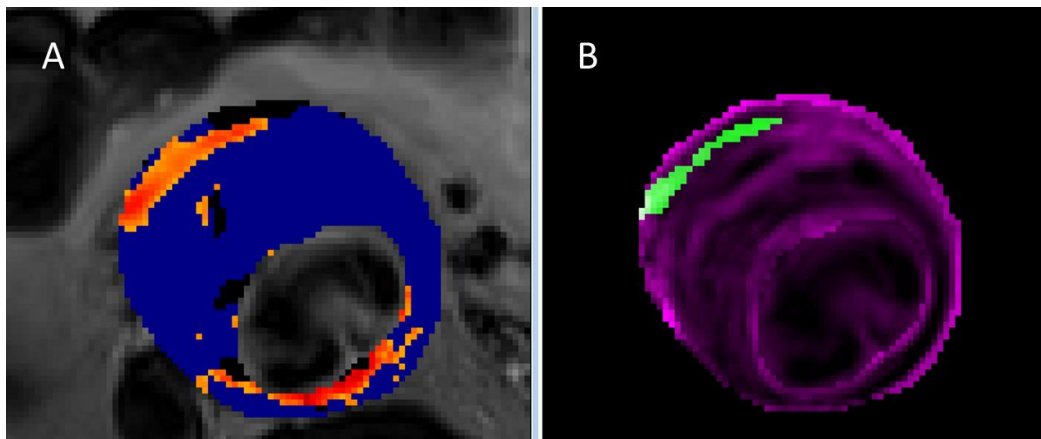
Figure 5.15: Representative case of duodenum included in ROI. *In the %ΔT₂* colourmap (with 71% threshold applied) presented in A, a large hotspot is clearly visible on the top left of the AAA. As such, it was selected by the automatic algorithm as shown marked with green colour in B.*

5.3.7 Automatic Replication Algorithm Pipeline

The steps followed by the Automatic Replication algorithm to imitate the manual hotspot segmentation are outlined in the flowchart in Figure 5.16.
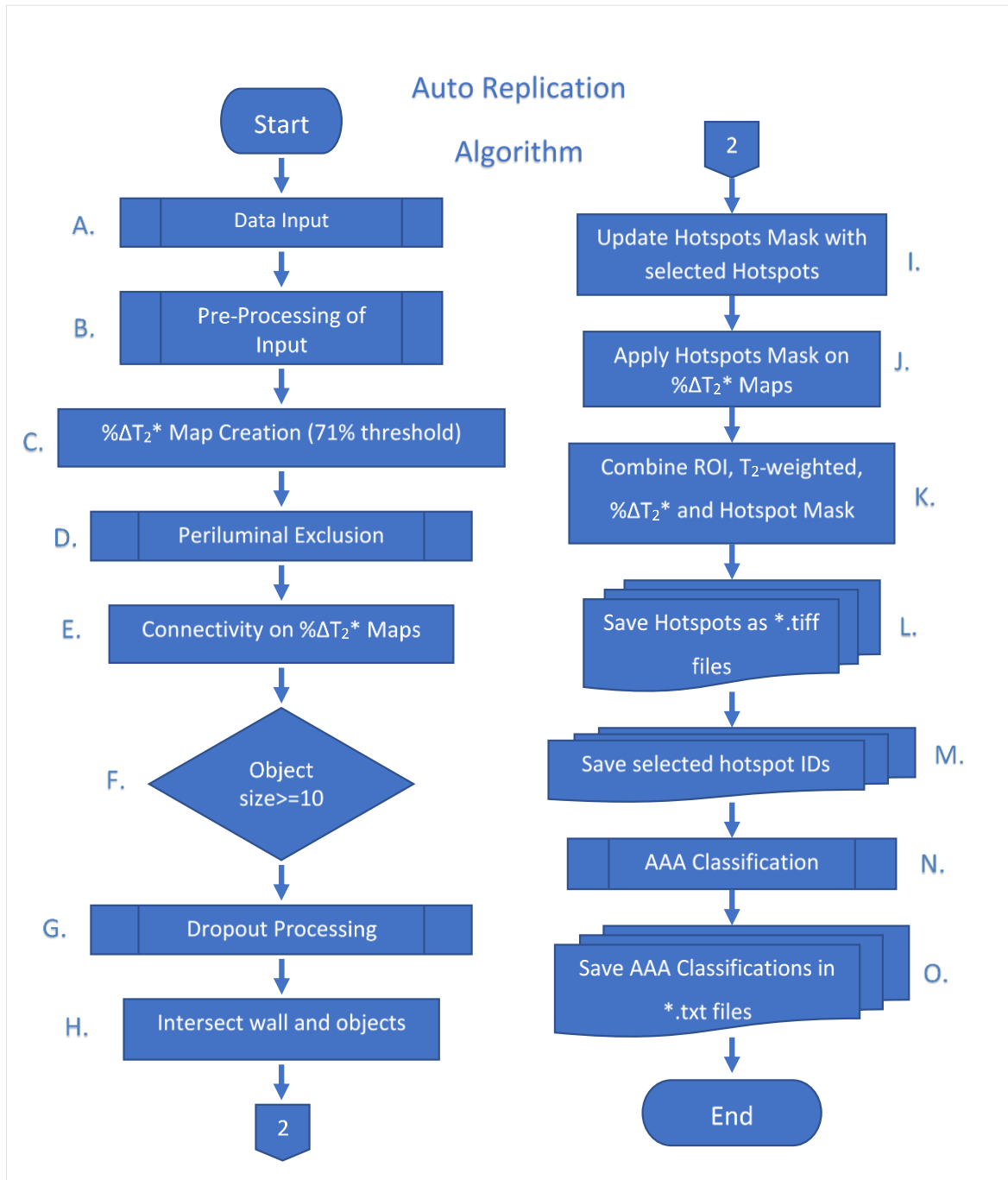
Figure 5.16: Flowchart of automatic replication algorithm

5.3.8 Classification of Hotspots

AAAs are divided into two groups, depending on the presence of hotspots within their volume. For each AAA, if at least one hotspot has been identified within it, the AAA is classified by the algorithm as USPIO-positive. Otherwise the AAA is classified as USPIO-negative.

A list of the hotspots identified is also saved for each AAA, as well as a folder with images of all the hotspots, individually superimposed on T_2-weighted MRI scans. The hotspots that were initially detected, then subsequently discarded based on the selection criteria were also saved as, for future reference, and to offer the option of visual inspection/confirmation by the clinical observers.

5.3.9 Algorithm Adaptations for different applications

The Automatic replication algorithm has four variables that can be adjusted so that it can be applicable to different datasets acquired with alternative protocols, derived from different trials or varying scanners.

The variables that can be adapted are:

1. The threshold applied on the $\%\Delta T_2^*$ maps.

2. The minimum number of pixels neighbouring the wall required for the inflammatory hotspot to be accepted.

3. The maximum number of pixels neighbouring to the periluminal area that would be accepted for the inflammatory area to be considered a separate hotspot.

4. The minimum number of connected pixels of inflammation per slice required for the area to be considered an inflammatory hotspot.

5.3.10   Application on Pilot Dataset

The Automatic Replication algorithm was applied on the Pilot dataset (see section 1.4) for evaluation and identification of any issues in the hotspot detection. I went through this process because we had a gold standard that had been published on this dataset. The disadvantage of this was that, as the dataset was historical, there were many limitations of the acquisition protocol that could have (and actually were) improved on the next datasets acquired in the MA^{3}RS trial.

5.3.10.1 Methods – Algorithm adaptations for Pilot dataset

The MRI datasets of a total of 25 AAAs I had access to from the Pilot study were used for the Automatic Replication algorithm to be tested. The ROIs had to be manually drawn again, as the original ROI data had been segmented following a different protocol than the one used in the MA^{3}RS study, as shown in Figure 5.17. Visual inspection of all slices concluded that no significant differences between the old and new ROIs that could potentially affect hotspot detection were present.
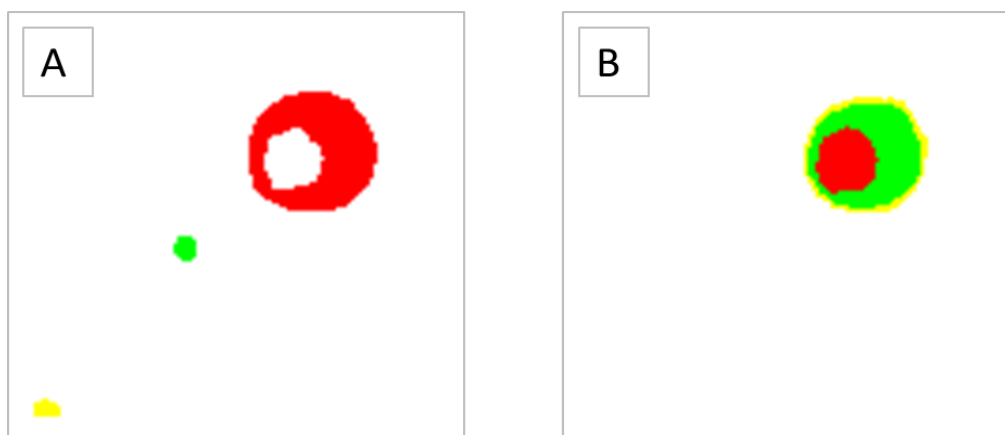
Figure 5.17: Example of old (A) and new (B) ROIs created for the pilot study dataset. A) *In the old ROI segmentations conducted during the pilot study, the area of the thrombus and the wall (in red) were segmented together as one ROI; the area of the lumen was not segmented separately, but rather inferred as the non-covered circular area within the AAA; and some reference regions external to the AAA were sometimes segmented as well (in yellow and green), which corresponded to known areas of fat or blood, for further comparison with areas of interest within the AAA.* ***B)*** *The new ROIs as identified to be used by the Replication algorithm identified the aortic wall (yellow), thrombus (green) and lumen (red).*

Following the protocol of the Pilot Study, a 59% threshold was applied to the %ΔT$_2$* maps. Furthermore, different adjustments of the following 2 variables were trialled, to identify the highest agreement levels between the manually selected hotspots and the automatically identified hotspots. The selected variables were:

1. The minimum number of neighbouring the wall pixels required for the inflammatory hotspot to be accepted was 1.

2. The maximum number of pixels neighbouring the periluminal area that would be accepted for the inflammatory area to be considered a separate hotspot was 1.

AAAs were classified by the Replication algorithm as "positive" (USPIO-positive) if they were found to contain at least 1 hotspot, otherwise they were classified as "negative" (USPIO-negative). As the manual classification for the pilot had also identified some AAAs as "diffuse USPIO uptake" (Group2), a decision had to be made as to whether these would correspond to the USPIO-positive or USPIO-negative of the Replication algorithm. The recommendation of the clinical observers was to consider these as USPIO-negative, as in most cases the diffuse inflammation did not fulfil the hotspot criteria (the inflammatory areas were smaller and/or not adjacent to the aortic wall).

5.3.10.2   Results

The automatic classifications were initially verified against the manual classifications that had previously been executed by the clinical observers, as summarised in the "manual outcome" of the confusion matrix in Table 5.2.

There was a total of three disagreements between the two methods, consisting of one false negative and two false positives. These three cases were subsequently

examined visually for the sources of the disagreements to be identified and new assessments for "ground truth" were included in Table 5.2.

The case reported as a false negative is presented in Figure 5.18: based on the areas marked as hotspots on slices A, B and C the clinical observers classified this AAA as USPIO-positive. The Replication algorithm however, classified it as USPIO-negative because none of the three candidate hotspots could be differentiated from the periluminal area that was in contact with the lumen. This case has been accepted as indeed a FN (false negative) and has been included as such in the "ground truth" section of the Table 5.2.

This problem, namely the existence of areas that might visually look separate than the periluminal area but exhibit too many contact points as to be distinguished by the algorithm, is further explored in section 5.4.4 and a new periluminal exclusion method is introduced there and later incorporated in the Evolution algorithms.

Table 5.2: Confusion matrix comparing auto and manual AAA classification based on hotspot detection. *The "Manual outcome" section depicts the initial agreement level between the auto and the manually classified AAAs by the clinical observers. The "Ground Truth" section depicts the agreement levels between the auto and the re-evaluated manual classifications. TP=True Positive, FP=False Positive, FN= False Negative, TN=True Negative; Sens=Sensitivity=TP/(TP+FN); Spec=Specificity= TN/(TN+FP), n=25.*

		Manual Outcome		Ground Truth Outcome	
		Positive	Negative	Positive	Negative
	Positive	TP = 10	FP = 2	TP = 12	FP = 0
	Negative	FN = 1	TN = 12	FN = 1	TN = 12
Auto Outcome	Sample size	25		25	
	Disagreements	3		1	
	Sensitivity	90.9%		92.3%	
	Specificity	85.7%		100%	
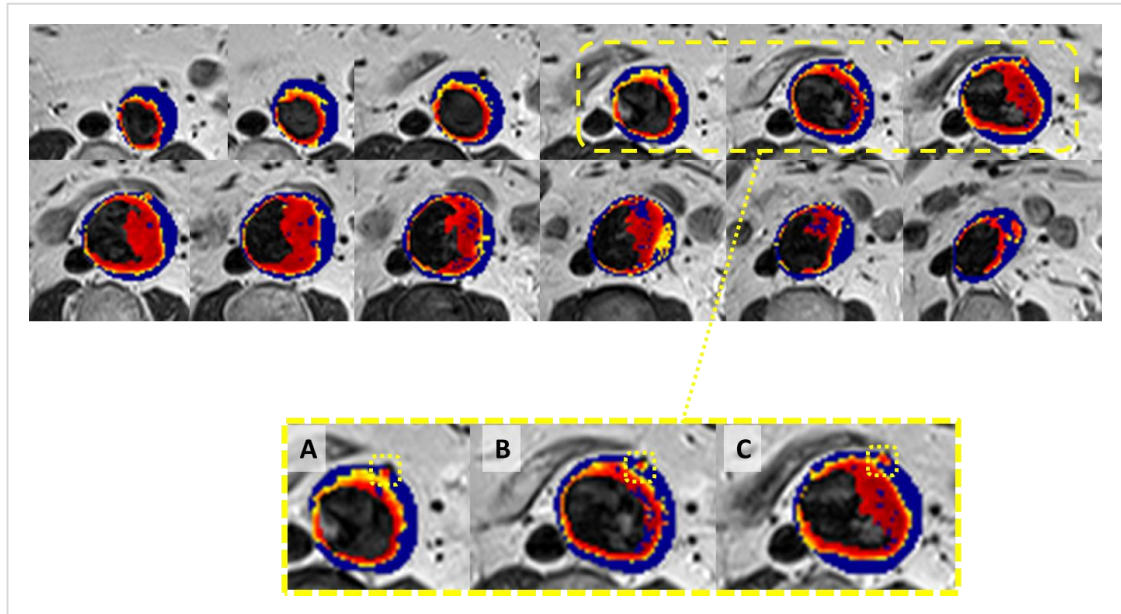
Figure 5.18: The case of a false negative AAA in the pilot dataset. *The marked areas within slices A, B, and C were identified as hotspots during the manual processing and thus the clinical observers classified this AAA as USPIO-positive. The automatic Replication algorithm classified this AAA as USPIO-negative, because the candidate hotspots were indistinguishable from the periluminal uptake.*

The two cases of the reported false positives were also visually inspected. The slices upon which the Replication algorithm detected hotspots (each slice corresponding to a different AAA) are presented in Figure 5.19. Based on these, the two corresponding AAAs were automatically classified as USPIO-positive. These AAAs had been classified as having "diffuse USPIO uptake" by the manual classification. This could have been due to the manual inspection of the entirety of the slices per AAA and the clinical observers may have based their decision on the diffused-looking USPIO uptake in the majority of the slices, rather than on the hotspots present in one unique slice.

However, assessed in isolation, the two cases depicted in Figure 5.19 would qualify as hotspots and therefore the corresponding AAAs would be considered USPIO-positive. For this reason, these cases have been accepted as positive in the "ground truth" section of Table 5.1 and as such, they have thus been included within the TP (true positive) cases of the table.
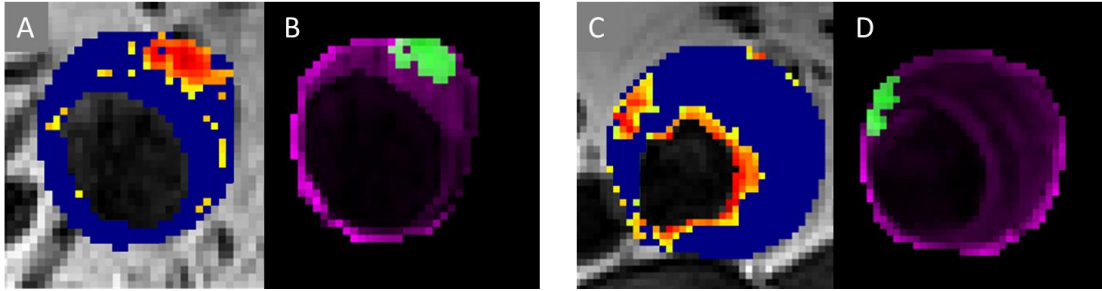
Figure 5.19: Additional hotspots detected by Automatic Replication algorithm. *A and C are %ΔT₂* colourmaps (with 59% threshold applied), corresponding to 2 different AAAs. They are accompanied by the automatically identified hotspot (in green) for each slice (B and D respectively).*

5.3.11 Application on MA³RS Dataset

As a next step, the Automatic Replication algorithm was applied to a subset of the MA³RS dataset and the results were verified against the manual processing previously performed by clinical observers.

5.3.11.1 Methods

A total of 176 randomly selected AAAs were used, for which the ROIs had been manually segmented previously. Following the protocol of the MA³RS study, a 71% threshold was applied to the %ΔT₂* maps. After trialling different combinations, the selected variables for the Replication algorithm to be applied to the MA³RS dataset were:

1. The minimum number of pixels neighbouring the wall required for the inflammatory hotspot to be accepted was 1.

2. The maximum number of pixels neighbouring the periluminal area that would be accepted for the inflammatory area to be considered a separate hotspot was 0.

As explained in 5.3.10.1, AAAs including at least one hotspot were classified by the Replication algorithm as USPIO-positive, otherwise as USPIO-negative. The MA³RS protocol included a small number of AAAs classified as having

"indeterminate USPIO enhancement". Those were considered as part of the USPIO-negative group for comparison with the automatic classifications.

5.3.11.2   Results

The automatic classifications were initially verified against the manual classifications previously performed by the clinical observers, as summarised in the "manual outcome" section of the confusion matrix in Table 5.3. There was a total of 16 initial disagreements between the two methods (among 176 samples), consisting of one false negative (FN) and 15 false positives (FP).

These cases were subsequently examined visually for the sources of the disagreements to be identified and new assessments for "ground truth" were included in the "ground truth outcomes" of Table 5.3, after agreement with the clinical observers.

Table 5.3: Confusion matrix comparing auto and manual AAA classification based on hotspot detection. *The "Manual outcome" section depicts the initial agreement level between the auto and the manually classified AAAs by the clinical observers. The "Ground Truth Outcome" section depicts the agreement levels between the auto and the re-evaluated manual classifications. The "Ground Truth ROI outcome" section depicts the agreement levels if the cases caused due to incorrect ROIs were excluded. TP=True Positive, FP=False Positive, FN= False Negative, TN=True Negative; Sens=Sensitivity=TP/(TP+FN); Spec=Specificity= TN/(TN+FP).*

<table>
<tr><td rowspan="2" colspan="2"></td><td colspan="2">Manual Outcome</td><td colspan="2">Ground   Truth Outc.</td><td colspan="2">Ground Truth ROI Outc.</td></tr>
<tr><td>Positive</td><td>Negative</td><td>Positive</td><td>Negative</td><td>Positive</td><td>Negative</td></tr>
<tr><td rowspan="8">Auto Outcome</td><td>Positive</td><td>TP = 77</td><td>FP = 15</td><td>TP = 88</td><td>FP = 4</td><td>TP = 88</td><td>FP = 0</td></tr>
<tr><td>Negative</td><td>FN = 1</td><td>TN = 83</td><td>FN = 1</td><td>TN = 83</td><td>FN = 1</td><td>TN = 83</td></tr>
<tr><td>Sample size</td><td colspan="2">176</td><td colspan="2">176</td><td colspan="2">172</td></tr>
<tr><td>Disagreem.</td><td colspan="2">16</td><td colspan="2">5</td><td colspan="2">1</td></tr>
<tr><td>Sensitivity</td><td colspan="2">98.7%</td><td colspan="2">98.9%</td><td colspan="2">98.9%</td></tr>
<tr><td>Specificity</td><td colspan="2">84.7%</td><td colspan="2">95.4%</td><td colspan="2">100%</td></tr>
</table>

The case of the AAA reported as a false negative is presented in Figure 5.20. As seen in Figure 5.20 B and Figure 5.20 D, two candidate hotspots were indeed identified by the Replication algorithm in two consecutive slices. However, these were then automatically dismissed because they were found to be in contact with the lumen. On the other hand, the clinical observers accepted these hotspots as valid, as they suggested that they appeared to be connected to each other in 3D. This case will be further explored in section 5.4.4.3. It was accepted as a false negative (FN) in the ground truth outcome in Table 5.3.
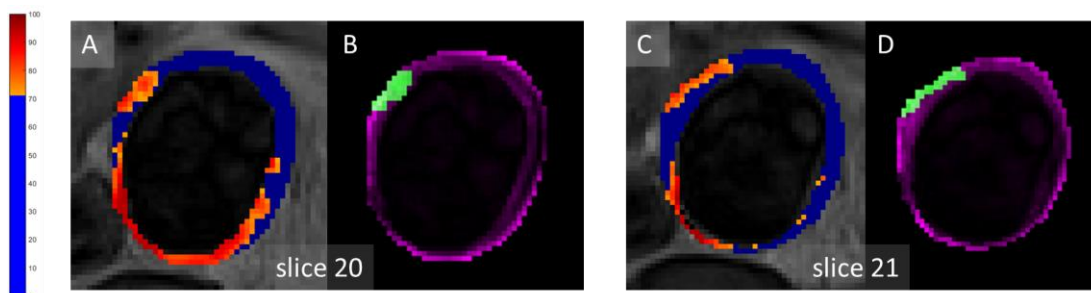
Figure 5.20: A case of disagreement between auto and manual: hotspots in contact with lumen. A and C are %ΔT$_2$* colourmaps (with 71% threshold applied) corresponding to two consecutive slices (20 and 21) within one AAA. In B and D, the automatically detected hotspots of the respective maps are illustrated; these were dismissed by the Replication algorithm, as they were in contact with the lumen, while the clinical observers accepted them as valid.

Visual inspection of the 15 cases that had been identified as false positives revealed that there were three reasons behind the disagreements: accidentally missed hotspots as depicted in example cases in Figure 5.21 (presence of these hotspots were agreed with the clinical observers after detection by my algorithm); hotspots of "uncommon" shapes which clinical observers suggested could be indicative of artefacts, as depicted in the examples in Figure 5.22; and hotspots detected on ROIs that, upon examination, were considered inaccurate, by e.g. including the duodenum as part of a ROI, as shown the examples in Figure 5.23. The manual classifications of the affected MA[3]RS datasets were consequently amended accordingly, incorporating the findings of the Replication algorithm and as shown in the "ground truth outcome" of Table 5.3, reducing the number of disagreements to just five. Furthermore, in the "ground truth ROI

outcome" section of the table, the 4 AAAs with ROI problems were excluded from the comparison.
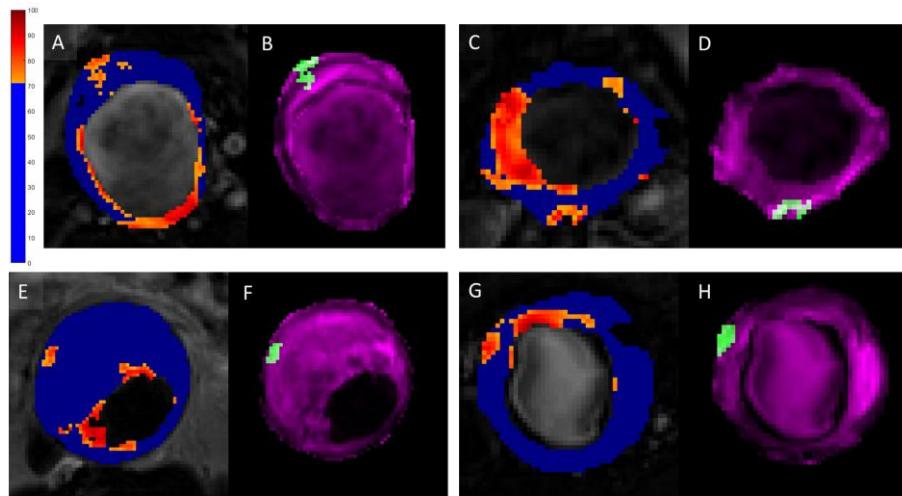
Figure 5.21: Examples of accidentally missed hotspots which were detected by Replication algorithm. *The hotspots on B, D, F and H were automatically detected on the %ΔT₂* colourmaps (with 71% threshold applied) of A, C, E and G, respectively. Each hotspot belongs to a different AAA.*
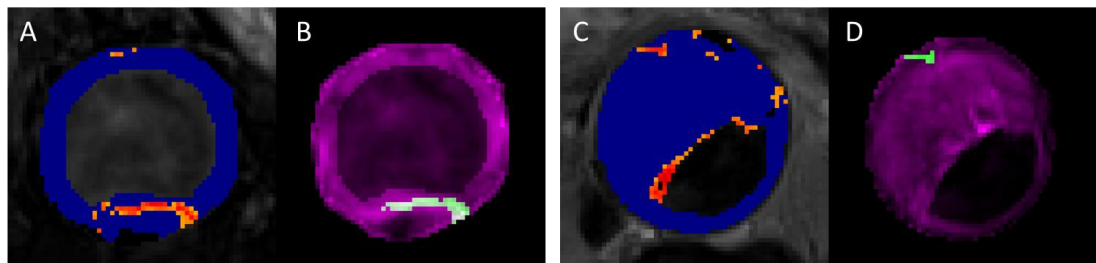
Figure 5.22: Examples of hotspots with "uncommon" shape, as detected by Replication algorithm. *The hotspots on B and D were automatically detected on the %ΔT₂* colourmaps (with 71% threshold applied) of A and C. They were dismissed by the clinical observers, because of their uncommon shape that they suggested was an artefact.*
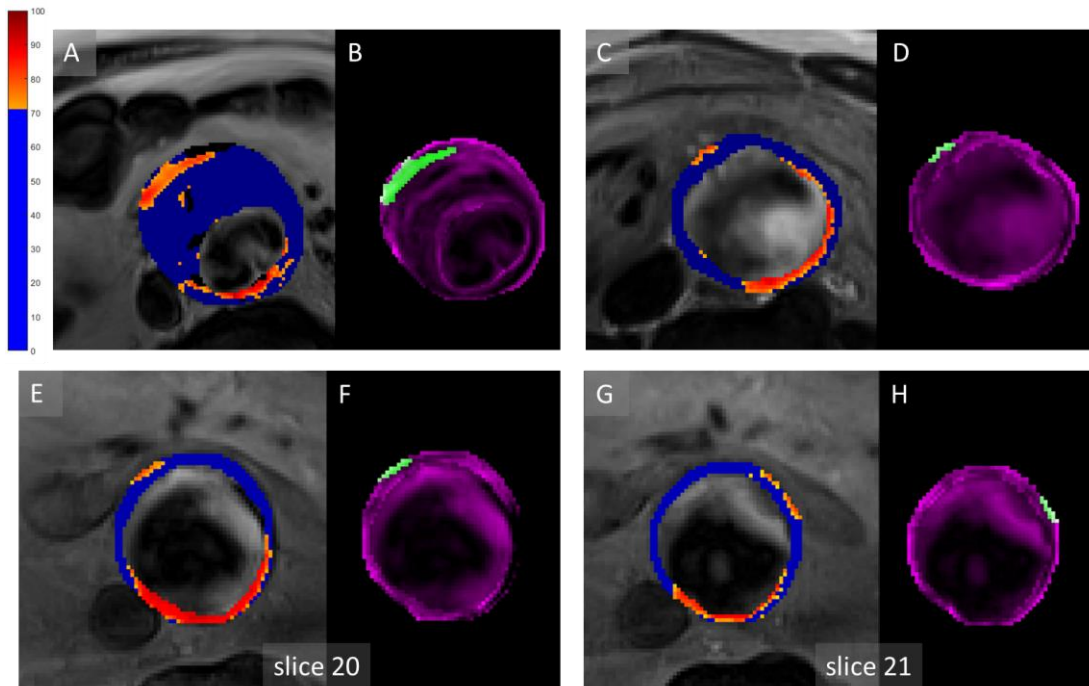
Figure 5.23: Disagreements between auto and manual hotspot detection because of ROI: duodenum. *The hotspots on B, D, F and H were automatically detected on the %ΔT$_2$* colourmaps (with 71% threshold applied) of A, C, E and G, respectively. Cases AB and CD belong to different AAAs (one case per AAA). Cases EF and GH belong to two consecutive slices of the same AAA. The clinical observers dismissed these hotspots, considering them part of the duodenum which they suggested had incorrectly been segmented as part of the three AAAs.*

5.4　　　"Evolution 2D" Algorithm

The next step after the development of the Replication Algorithm which reproduced the manual Hotspot detection, was towards the creation of a more advanced algorithm, hereby named "Evolution 2D Algorithm". The goal was to introduce alternative or additional methods which would assist in further stratifying the AAA patients in an automated way by providing a potentially more accurate detection of inflammation within the aneurysm. The differences between the basic functions of the Replication and the Evolution 2D algorithm are presented in Table 5.4.

Table 5.4: Differences between Replication algorithm and Evolution algorithm

	Replication Algorithm	**Evolution 2D Algorithm**
1	$\%\Delta T_2^*$ maps have 71% threshold	$\%\Delta T_2^*$ maps have 0% threshold
2	Hotspots not touching dropout areas neighbouring with lumen	Hotspots not touching dropout areas neighbouring with lumen
3	Hotspot Detection: connectivity on thresholded $\%\Delta T_2^*$ maps	2D Hotspot Detection: • k-means clustering (k=7) • 2D connectivity on thresholded $\%\Delta T_2^*$ maps
4	Hotspots >=10 contiguous voxels	Hotspots >=8 contiguous voxels
5	Hotspots within aortic wall (outer only)	Hotspots within aortic wall (outer or inner)
6	Periluminal function Detection of hotspots touching lumen	Updated Periluminal (k-means clustering) • Connectivity with lumen (n=8) • Periluminal area excluded on $\%\Delta T_2^*$ maps before hotspot detection
7	No metrics calculated	2D Metrics calculated

5.4.1 Percentage ΔT$_2$* Thresholding

The goal of the threshold application in the manual processing was to reliably allow only significant USPIO uptake to be depicted on the difference maps, in an effort to standardise the process: any focal area fulfilling the hotspot criteria would have to be selected by the observer, without any doubts over including or excluding any pixels. Thresholding the data also helped to speed up the manual classification process applied to both studies, which allowed the larger MA^{3}RS study to be performed using manual classification.

The major disadvantage of applying any threshold value on the data lies on the threshold's universality. AAAs inherently appear in many variations, hence the application of a global "cut-off point" introduces the risk of excluding valuable data, with some cases of AAAs being affected more than others.

It was obvious in some cases, that applying a threshold could exclude pixels of slightly lower USPIO uptake, which were possibly indicating lower but still significant inflammation and also function as "bridges" between two or more areas of high uptake: by removing these "bridges", the number of pixels of each area was not enough to reach the 10-pixel criterion for hotspot acceptance, as shown in Figure 5.24. In Figure 5.24 A, some high USPIO uptake areas can be seen in the 71% thresholded ΔT$_2$* map, but they are disconnected, while in Figure 5.24 B, the same areas appear connected in the non-thresholded ΔT$_2$* map, and are thus picked up by the algorithm as shown in Figure 5.24 C.
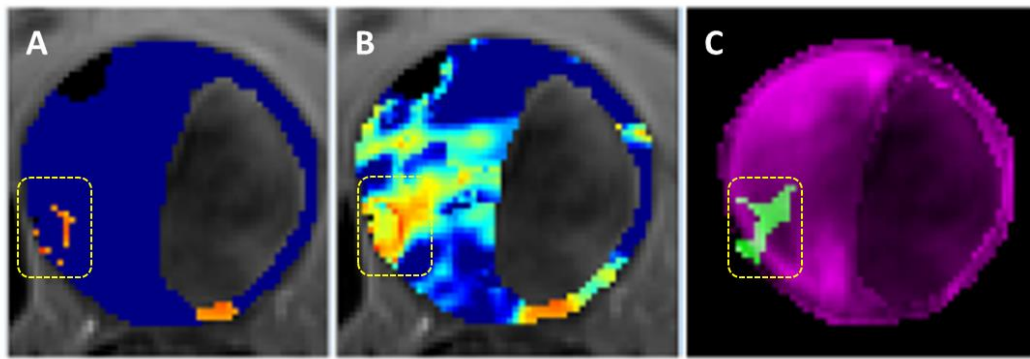
Figure 5.24: Differences in hotspot detection between different thresholds. A) *The marked areas of high USPIO uptake in this 71% thresholded ΔT_2* map are disconnected.* ***B)*** *The same marked areas appear connected in the non-thresholded ΔT_2* map.* ***C)*** *The automatic algorithm uses non-thresholded ΔT_2* maps, thus selects the aforementioned area as a hotspot.*

For such diverse datasets, introducing a level of adaptability in the image processing methods would be beneficial. For this reason, I chose to use non-thresholded data in the next stage of my processing.

5.4.1.1 Other Limitations of thresholding

The 71% threshold for the MA[3]RS dataset was chosen by checking the distribution of the specific datasets available (Figure 5.25). This approach is therefore not universal, as it depends on the imaging centre in which the scans take place: different scanners, imaging coils, spatial resolution, imaging sequences, different degree and type of image artefacts, etc. Importantly, data acquired from different patients may correspond to different ranges of signal intensity and using a more personalised approach is preferable.

On the other hand, as the automatic algorithm introduced here is using non-thresholded data, as shown in Figure 5.25 (a), it can be applied to any datasets available. Any thresholding happens at the final stages of the algorithm.
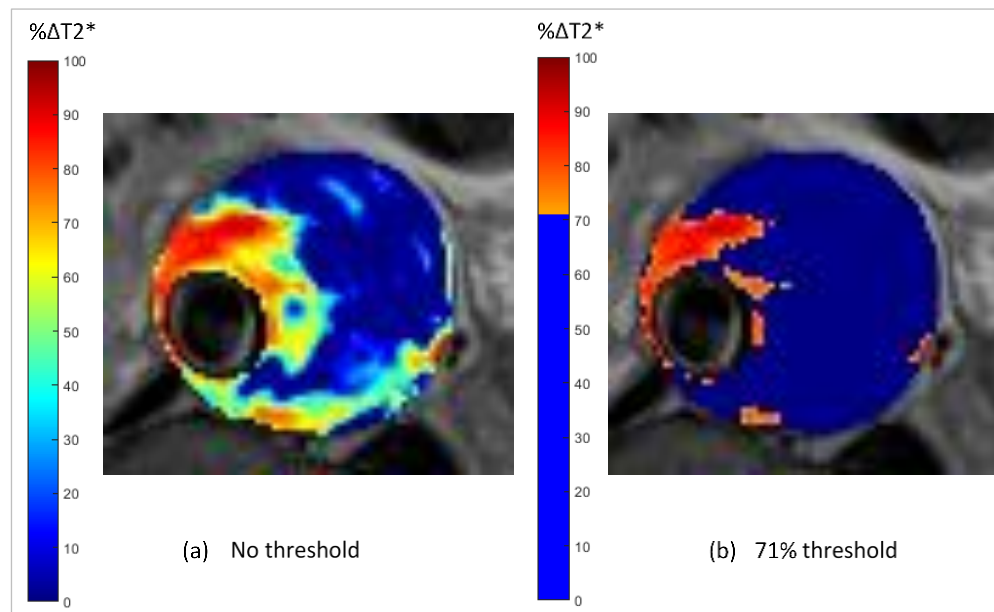
Figure 5.25: An example of %ΔT$_2$ maps without threshold (a) and with 71% threshold (b).*

5.4.2 Hotspot size

The criterion used in the pilot study for the hotspot size to be at least 10 pixels could be challenged, as it was suggested as a starting point in the pilot study which might be subsequently modified with more statistical evidence and larger patient numbers. In order to include a wider set of candidate hotspots in further analysis and possibly allow for further stratification of AAAs, the Evolution 2D Algorithm accepted hotspots comprising of a minimum of 8 pixels in the applications showcased in this thesis. The specific number was selected for the MA[3]RS trial, because within this dataset, many instances of isolated 8-pixel and 9-pixel areas adjacent to the aortic wall and not belonging to broader diffused inflammation had been visually detected and identified as potential smaller hotspots to further explore. The clinicians involved in the study agreed that the inclusion of these smaller areas in the automatic detection could identify previously missed regions which could potentially assist with further AAA stratification. For datasets of different spatial resolution, this number should be re-evaluated.

As will be outlined in 5.4.7, the hotspot size used in the Evolution 2D algorithm can be changed to accommodate different datasets.

5.4.3 Methods for Hotspot Detection on Un-thresholded data

A variety of methods were applied to the $\%\Delta T_2^*$ maps to explore their hotspot segmentation potential.

Initially, histograms of different AAAs were studied: histograms of $\%\Delta T_2^*$ values corresponding to slices containing manually identified hotspots were compared against histograms from slices without any inflammation. These were visually observed to identify potentially obvious patterns. To quantify the differences between the distributions, Earth Mover's Distance (EMD) [247]–[249] and Kolmogorov-Smirnov test [250], [251] were used. This histogram-based method pointed towards the existence of some patterns, but it did not prove to be scalable in an accurate way which could be implemented automatically.

The next method trialled was *Watershed segmentation*. This technique is based on the notion of visualising an image in three dimensions, in the form of a surface. The areas with high intensity values correspond to "high" values topographically, akin to watershed lines, while the areas with lower intensity correspond to "low" topographical areas, akin to catchment basins [178] as shown in Figure 5.26. The idea was to use the inverse image of the $\%\Delta T_2^*$ map (using the MATLAB function *imcomplement*) so that areas of high USPIO (potential hotspots) would be detected within deeper catchment basins.
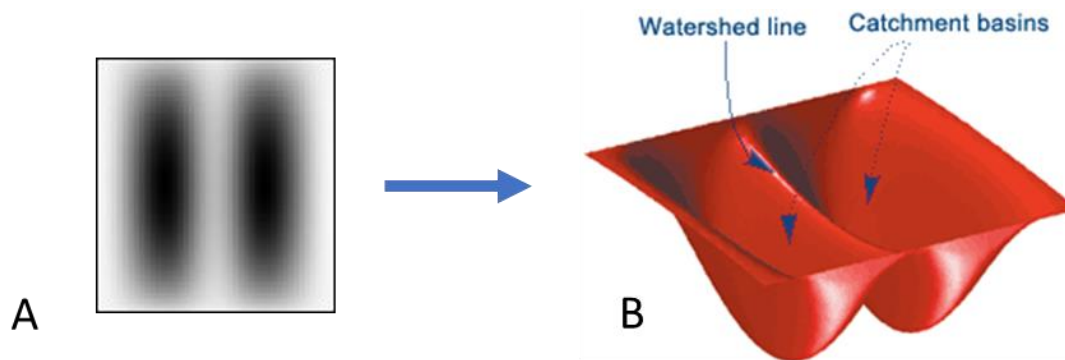
Figure 5.26: Watershed segmentation - basic concept. *A 2D image like the one depicted in A is imagined like a 3D surface, with higher intensity areas (brighter) on A corresponding to watershed lines in the surface in B and lower intensity (darker) areas corresponding to catchment basins. (Image adapted from MATLAB-Simulink Technical Articles and Newsletters, The MathWorks, Inc.).*

However, when applied to the $\%\Delta T_2^*$ maps, the watershed technique led to over-segmentation, which is a well-known problem of watershed segmentation. This type of over-segmentation happens because every local minimum, regardless of its significance, creates its own catchment basin. A commonly applied solution to over-segmentation is removing the local minima that are considered too shallow. This, however, requires a decision over a threshold to be applied on the $\%\Delta T_2^*$ values. As discussed previously in 5.3.1, the use of thresholding introduces many disadvantages I wanted to avoid in the Evolution algorithm. Consequently, the Watershed method was deemed inappropriate for the hotspot segmentation.

Region growing algorithms were not suitable for hotspot segmentation either, as they require an initial seed to be placed from which the region then grows, but in the case at hand there was no way to identify where to automatically place the seeds, as hotspots can appear at any region of the AAA. Additionally, more than one hotspot could exist per slice, thus more than one seed per slice would be required.

The next method employed was k-means clustering and will be described in the next sections.

5.4.3.1 K-means Clustering for Hotspot Detection

The background on Clustering and k-means clustering have been presented in Chapter 2.

The specification of the three parameters that are required by the user, namely cluster initialisation, number of clusters and distance metric [182], will be described in this section.

5.4.3.1.1 Cluster initialisation

The results produced with k-means clustering are highly dependent on the initialisation of the clusters. Given that k-means only converges to local minima, different initialisations are expected to lead to different clustering outcomes.

For the version of k-means used here, a deterministic approach was required, to ensure reproducibility of the outcomes. The $\%\Delta T_2{}^*$ data used were not thresholded and as the intensity histograms fluctuated significantly from case to case (some presenting with normal and some with skewed distributions), the initial centroids used were spaced uniformly along the grey level axis.

For each image processed with k-means, with k number of bins, $k_A = [1, k]$ and $m = \max(image) + 1$, the initial centroids C_A were calculated as shown in Equation 5.1:

$$C_A = k_A * m / (k + 1)$$

Equation 5.1

5.4.3.1.2 Number of bins/clusters

Most commonly, for the determination of the appropriate number of clusters, k-means is tested independently for different k values and the results are evaluated specifically for the domain in hand [182]. In the case of the automatic hotspot segmentations, the point of reference was not merely the manual segmentations performed by the trained observers. The additional goal was to incorporate more

information that was potentially missed in the manual process. In this adaptation of the k-means clustering, and given the initialisation described previously in 5.4.3.1.2, the number of bins selected would determine the level of intensity of areas considered as potential hotspots in each AAA. A larger number of bins would tend to identify smaller, more concentrated and higher-intensity areas as candidate hotspots. To identify the most appropriate number of bins, a randomly selected subgroup of the MA[3]RS trial was used as a "training set" (n=25 AAAs), upon which the k-means clustering algorithm was trialled with different cluster numbers (for k=4, k=5, k=6, k=7, k=8 bins) as shown in the example in Figure 5.27 and all the results were reviewed visually by me in the first stages and then presented to the clinicians participating in the MA[3]RS study. The different partitions produced by the different cluster numbers were compared against manually pre-defined hotspots. Upon agreement with the clinicians of the MA[3]RS study, it was concluded that k=6 was the best option, as indicated in Table 5.5. It should be noted that the detection of the hotspots was not the only factor considered, but also the size of the detected areas was taken into consideration, as large bin sizes tended to detect smaller areas and smaller bin sizes detected very large areas.

Table 5.5: Comparison between different k-means bin sizes and their effect on correct hotspot detection. Bin sizes from k=4 to k=8 were assessed on 25 cases, with the most successful being k=6.

	k=4	**k=5**	**k=6**	**k=7**	**k=8**
correct cases out of 25	17	20	23	21	18
% correct cases	68%	80%	92%	84%	72%

k=5, 5th cluster

k=6, 6th cluster
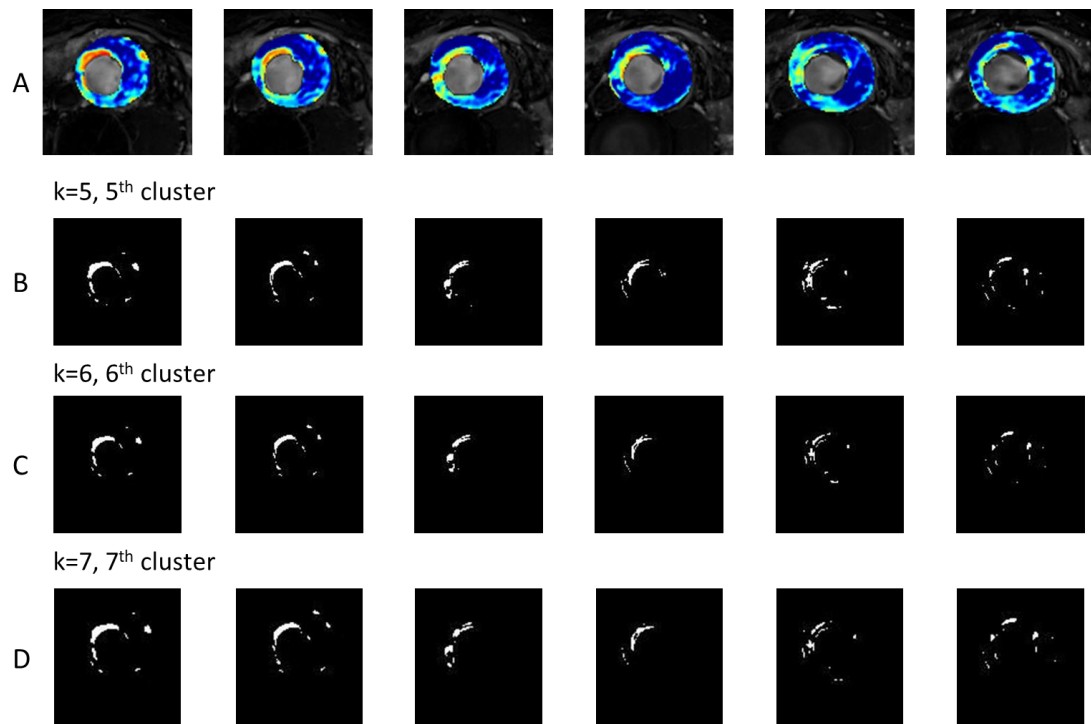
k=7, 7th cluster

Figure 5.27: Example of panel with different bin numbers used for k-means. A) %ΔT₂* maps (non- thresholded) of 6 consecutive slices of an AAA. B) The 5th cluster of all slices after applying k-means with 5 bins on the %ΔT₂* maps. C) The 6th cluster of all slices after applying k-means with 6 bins on the %ΔT₂* maps. D) The 7th cluster of all slices after applying k-means with 7 bins on the %ΔT₂* maps

5.4.3.1.3 Distance Metric

The Euclidean metric was chosen to be used in this version of k-means clustering algorithm because of the shorter processing time it needs compared to other commonly used distance metrics. Furthermore, as this metric is considered to be good at discerning "compact" clusters [184], [212], it was considered suitable for identifying potential hotspots, because they consist of pixels belonging to very similar signal intensities (thus forming "compact" clusters).

5.4.3.1.4 Advantages of k-means clustering

Using k-means clustering offers a variety of advantages. Firstly, this method works without imposing a universal threshold to the data, but instead it adapts to each AAA individually. It also offers the possibility of various adjustments (number of clusters, type of distance, etc. as detailed in 5.4.7) and can thus be applied to data from different trials and different scanners, altered to adjust for protocol and data quality variability. Furthermore, with k-means clustering, all inflammatory hotspots per slice are detected in the first stage (before being processed through the selection criteria), regardless of size, shape, etc., thus providing us with more data that can be used to extract supplementary characteristics or metrics for further AAA stratification as presented in 5.4.5. Finally, the speed of the k-means clustering was satisfactorily high, with processing times with the Evolution 2D algorithm of less than 45 seconds per AAA, compared to a total of more than 15 to 30 minutes per AAA for manual processing (total time depended on numbers of slices and AAA complexity in each case), which does not identify any metrics or produce visualisations.

5.4.4 Exclusion of periluminal area

In the course of detecting inflammatory hotspots, the algorithm faced a problem that had not been previously considered: In some slices of the non-thresholded $\%\Delta T_2^*$ maps there were instances of large areas of inflammation adjacent to the wall, but at the same time extending towards the luminal area, as in the case shown in Figure 5.28 and Figure 5.29.
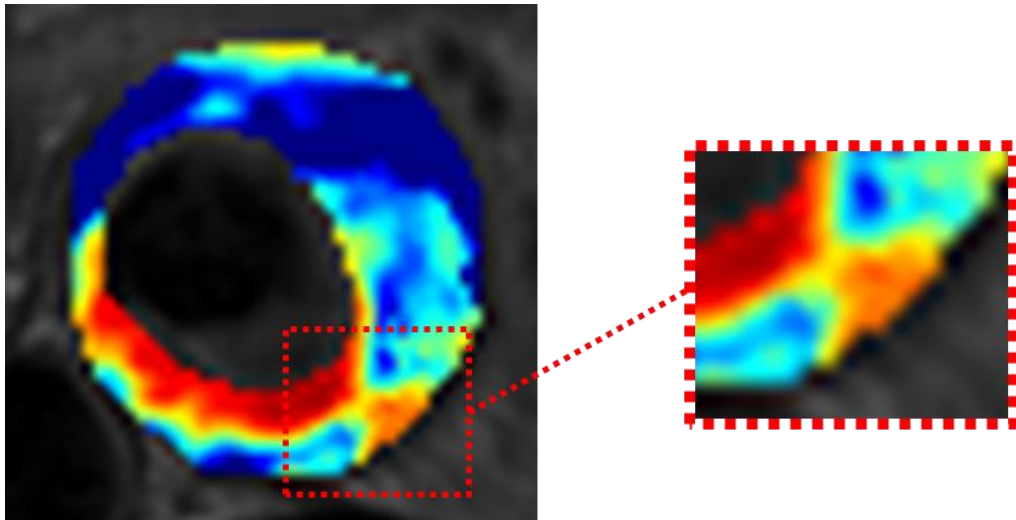
Figure 5.28: Example of application of periluminal exclusion algorithm. *The candidate hotspot depicted in the marked area of this non-thresholded ΔT_2^* map appears to be separate from the periluminal area upon visual inspection. The USPIO intensity decreases as proximity to periluminal area increases. The challenge was for the algorithm to be able to distinguish this case from cases where the hotspot clearly is part of the periluminal area and needs to be excluded.*

The algorithm would detect the proximity of these areas to the periluminal area and dismiss them as widespread inflammation rather than a concentrated hotspot.

Contrary to this, in the thresholded datasets used by the clinicians to visually identify the hotspots, the area would appear to be clearly distinct from the periluminal area, thus convincing the observers to classify the whole area of USPIO enhancement as a large hotspot. This problem was approached with the methods outlined in the following sections.

ΔT$_2$* map (71% threshold)   ΔT$_2$* map (0% threshold)   Auto Segmentation (0% thr.)
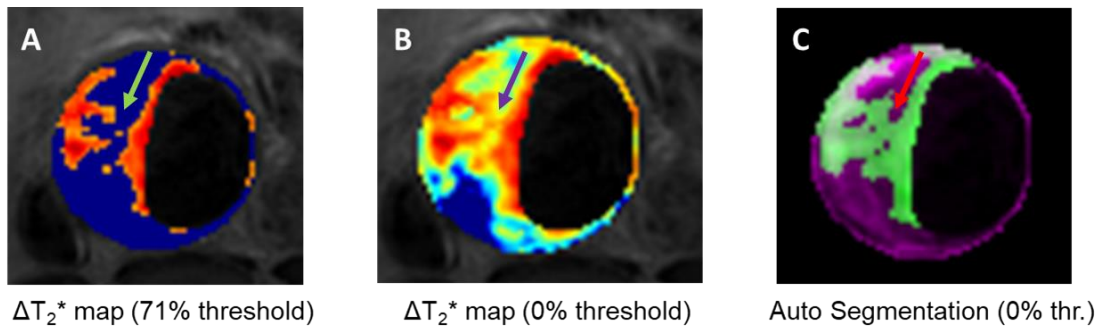
Figure 5.29: Example of periluminal area issue. A) *In the 71% thresholded ΔT$_2$* map, the periluminal USPIO uptake appears to be distinct from the uptake observed nearer to the wall, which consists of a candidate hotspot.* **B)** *In the non-thresholded ΔT$_2$* map however, the separation between the periluminal and the rest of the uptake does not appear to be as obvious. As the automatic algorithm uses non-thresholded data, it segments the entire area as one part and therefore rejects the potential hotspot* **(C).**

5.4.4.1 "*Improfile*" method for exclusion of periluminal area

The first method tested for periluminal exclusion utilised MATLAB's *improfile* function, which retrieves the intensity values of pixels along specified orientations in the image as shown in Figure 5.30 A and Figure 5.30 B and displays a plot of the intensity values, as shown in Figure 5.30 C.

The proposal was to employ *improfile* within the algorithm as a means of identifying the reduction in intensity that was observed in the problematic cases, as illustrated in Figure 5.30. For lines beginning from the lumen, then going through potential hotspots and finally meeting the wall, the intensity value plot demonstrated reductions in areas of reduced USPIO uptake, so it was investigated whether abrupt reductions in signal intensity throughout the profile could be used to separate areas of more significant USPIO uptake, thus helping to accept potential hotspots automatically which had been accepted in the manual classification of hotspots by clinical observers.
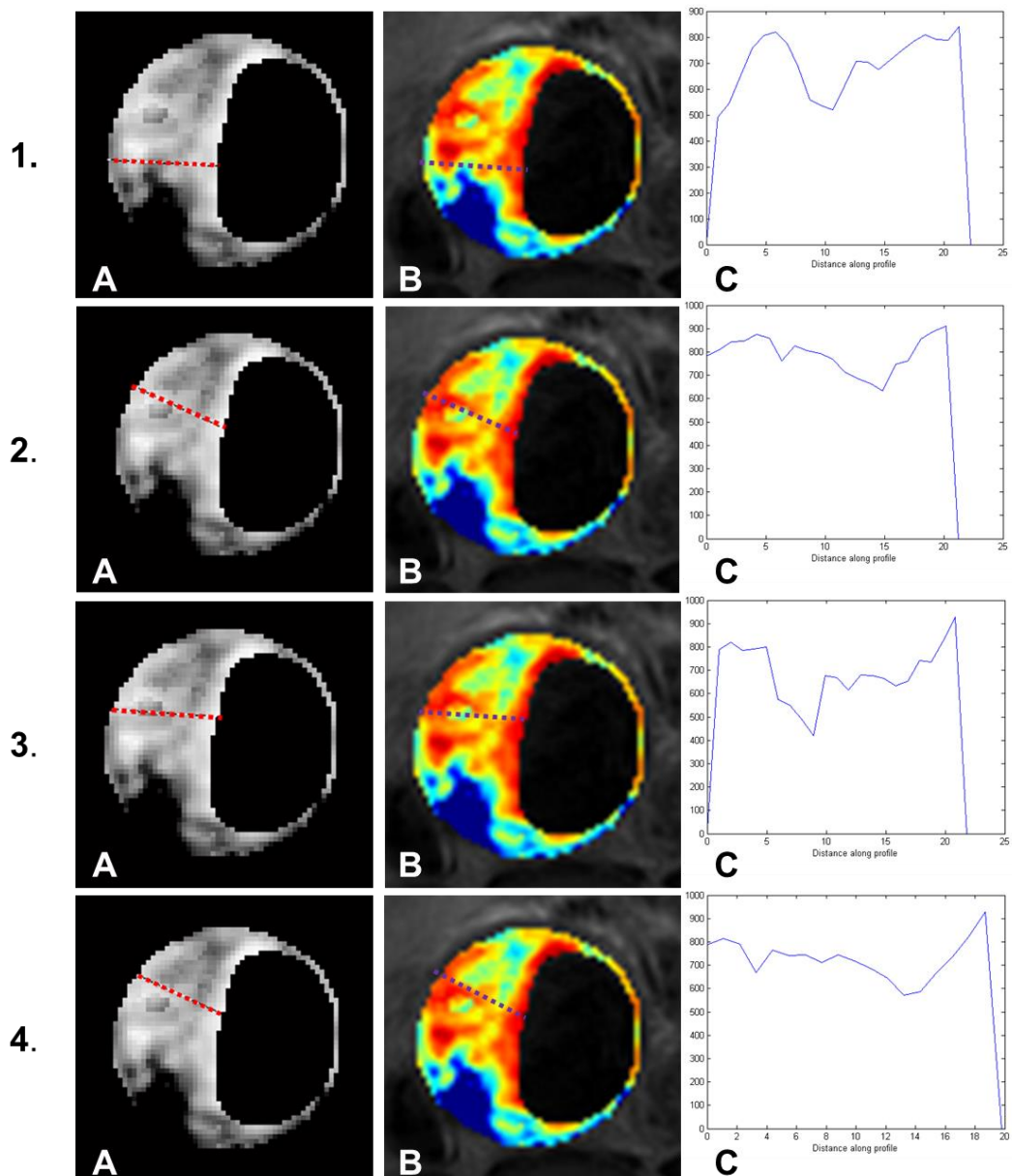
Figure 5.30: Application of MATLAB function 'improfile' to distinguish periluminal USPIO uptake from inflammatory hotspots. A) *Non-thresholded ΔT₂* map and* ***B)*** *Non-thresholded ΔT₂* map with colourmap applied, making USPIO uptake levels more visible.* ***C)*** *The resulting graph of the MATLAB improfile function, for the lines manually selected as seen on A and B. A reduction in signal intensity is obvious in all graphs, corresponding to the region where the periluminal area and the hotspot are connected via areas of lower USPIO uptake.*

In Figure 5.30 A and Figure 5.30 B, the lines across the AAA were manually

selected during the initial assessment of this method. This process was not taken

forward because it would require a threshold for signal intensity to be defined, which would restrict the adaptability of the algorithm to each specific AAA. Alternative methods were explored and k-means clustering produced satisfactory results in delineating areas of high and low uptake of USPIO to successfully address the issue raise in figure 4.22 and will be presented in 5.4.4.2.

5.4.4.2 K-means for Periluminal Area Segmentation

After none of the methods tested showed promising results for the segmentation of the periluminal area, mainly due to the area's complicated and not-reliably-connected shape, I hypothesised that excluding the lumen from the processing could be a needlessly introduced barrier and so investigated the option of not excluding the luminal area from the hotspot detection algorithm.

This is illustrated in the example case in Figure 5.31: if the lumen is excluded from the $\%\Delta T_2^*$ map as in Figure 5.31 A (excluded lumen area in black), it is challenging for the algorithm to detect the visually obvious "halo" of periluminal USPIO uptake marked with red arrows, because it is spread over a very thin area on the edge of the lumen without consistent signal intensity. If, however, the luminal segmentation is ignored and the $\%\Delta T_2^*$ maps are presented with the lumen included as depicted in Figure 5.31 B, a concentrated, usually fairly round area of high $\%\Delta T_2^*$ values is visible. This high signal intensity area includes the lumen and also extends to include the "problematic" periluminal area that I was trying to identify, both of which are assumed to have high signal intensity due to "passive" vascular supply of USPIO rather than macrophage/inflammation "active" delivery of USPIO. Within the $\%\Delta T_2^*$ maps, there seems to be no discernible border between the lumen and the periluminal area, since their signal intensity values are very similar.
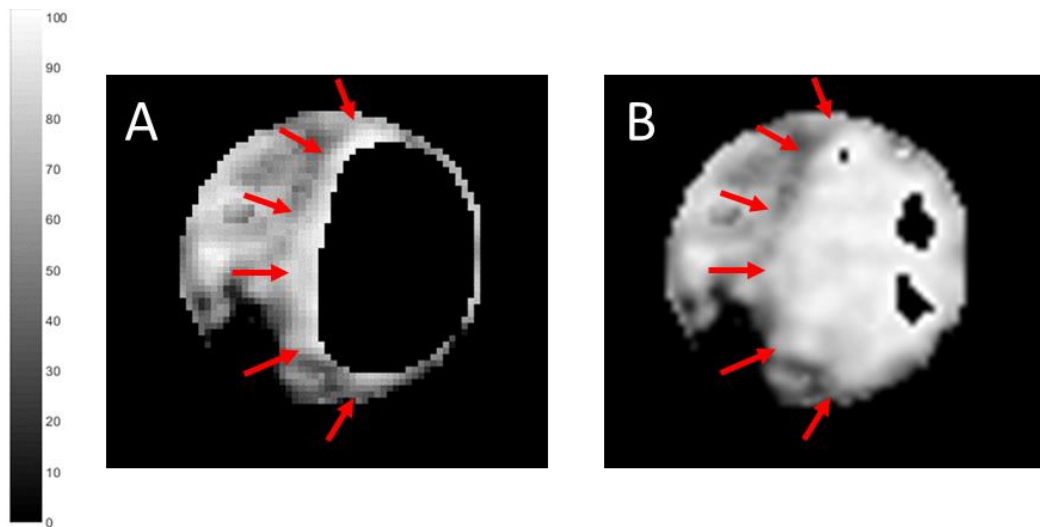
Figure 5.31: %ΔT$_2$* maps with light areas corresponding to higher USPIO uptake. *In A, the area of the lumen has been excluded (depicted in black) and a "halo" of periluminal USPIO is obvious, marked with the red arrows. In B, with the lumen included, the luminal and periluminal areas appear indistinguishable, as they have similar intensity values.*

Taking this observation into consideration, I tested inclusion of the lumen in the processing, so that it could be detected in combination with the periluminal area as a single large cluster of high signal intensity in the %ΔT$_2$* maps and thereupon the lumen could be excluded, leaving the periluminal area accurately marked.

Since the adapted k-means clustering combined with the connectivity process had performed well in identifying connected areas of high USPIO uptake for hotspot detection (see section 5.4.3.1), I tested this method for the purpose of periluminal detection, with a few adjustments. The experimental process to determine the best modifications was repeated for a range of periluminal areas from the population (Figure 5.32), with varying shapes, size, position within the AAA and USPIO uptake levels. K-means clustering was followed by the *bwconncomp* function to identify connected regions.
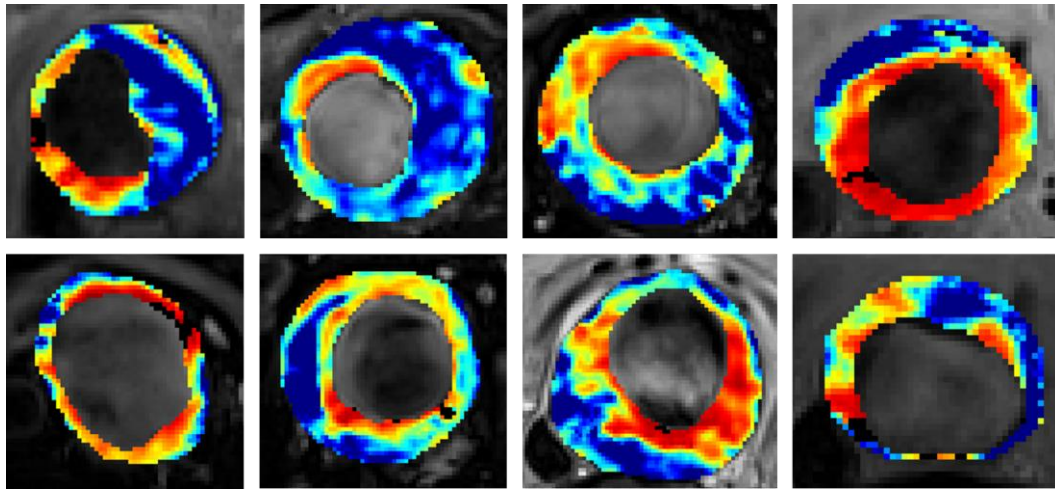
Figure 5.32: Different cases of periluminal USPIO uptake.

Of particular interest were the cases of AAAs presenting a hotspot in close proximity to the periluminal area. It was important to avoid missing potential hotspots by automatically clustering them as periluminal inflammation. For this reason, a balance had to be identified, between having a very conservative and restrictive area marked as periluminal, versus allowing the periluminal area selection to expand too much outside the lumen.

The level of definition (whether big blocks of pixels or more intricate/detailed shapes are segmented) is dependent on the binning size selected for the k-means clustering, as previously discussed in 5.4.3.1.2. A MA³RS subset of 10 representative cases of variable periluminal uptake was selected and different binning sizes were assessed experimentally (k=3, k=4, k=5 bins). Among these, the best compromise was achieved with the 4-bin processing, as shown in Table 5.6.

Table 5.6: Comparison between different k-means bin sizes and their effect on correct periluminal detection. *Bin sizes from k=3 to k=5 were assessed on 10 cases, with the most successful being k=4.*

	k=3	k=4	k=5
correct cases out of 10	7	9	7
% correct cases	70%	90%	70%

This choice was more conservative than the 3-bin version, which tended to cover larger areas, as shown in the example case of Figure 5.33, where the use of 3 bins (Figure 5.33 B) failed to distinguish between the marked hotspot and the periluminal area (Figure 5.33 C). With the application of the 4-bin version of the algorithm on the same slice (Figure 5.33 D), it was evident that there is a very good distinction of the hotspot (Figure 5.33 E).
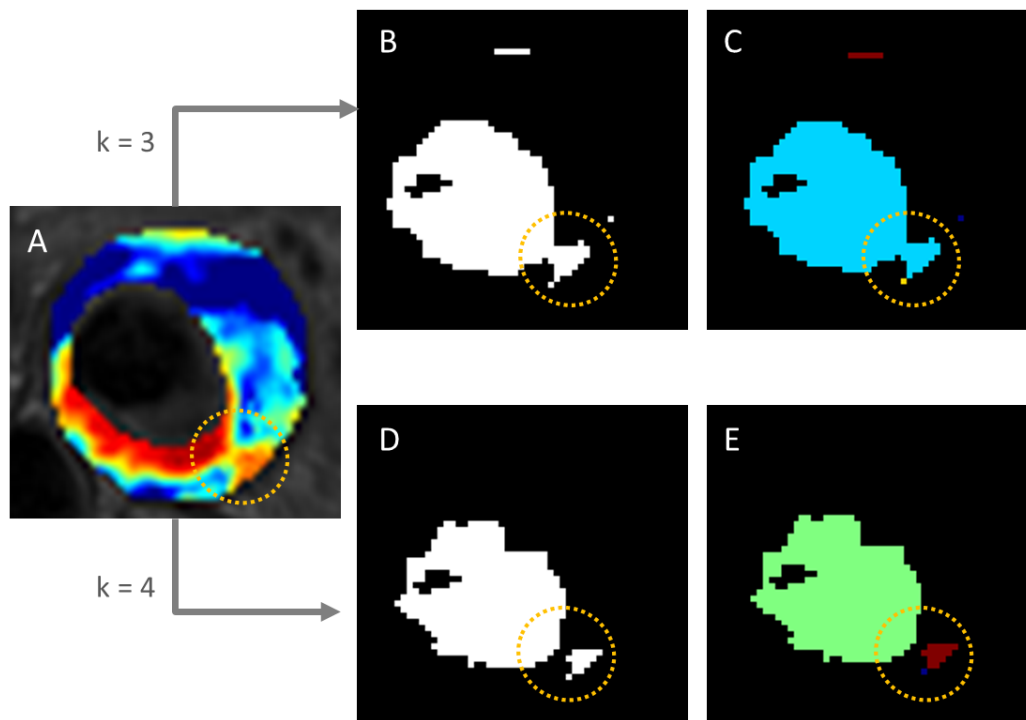
Figure 5.33: Example of different binning sizes of k-means for periluminal detection. A) *Non-thresholded %ΔT₂* map with colourmap applied and lumen area excluded.* ***B)*** *The 3rd cluster among the 3 clusters produced after the application of k-means clustering with 3 bins on the %ΔT₂* map of A.* ***C)*** *The resulting individual (unconnected) segments identified with the application of MATLAB's bwconncomp function on the 3rd cluster in B, marked in different colour per segment.* ***D)*** *The 4rd cluster among the 4 clusters produced after the application of k-means clustering with 4 bins on the %ΔT₂* map of A.* ***E)*** *The resulting individual (unconnected) segments identified with the application of MATLAB's bwconncomp function on the 4th cluster in D, marked in different colour per segment.*

These results were also discussed with the clinicians participating in the MA³RS project and the periluminal process gained their approval. Furthermore, the k-means clustering enabled the processing to be sufficiently fast (processing time of under 6 seconds per slice).

It should be noted that as the selection of the number of bins was experimentally defined for the specific dataset, it may need to be re-performed if the imaging protocol is changed, or the data is acquired on another scanner, as the data resolution/quality may change.

The entire periluminal processing methodology is summed up in the pipeline in Figure 5.34 and visually presented in Figure 5.35.

For each slice, adapted k-means clustering (described in 5.4.3.1) with k=4 bins was applied to the unthresholded $\%\Delta T_2^*$ map, segmenting the map into 4 clusters (Figure 5.34 A). MATLAB's *bwconncomp* function was then applied to the 4th cluster to identify all individual (un-connected) components (B) and a mask for them (bin4_Segments) was created (C). This mask was then intersected with the Lumen mask, which had been created based on the previously segmented (manually) ROIs (D).

From the intersection of the bin4_Segments mask and the Lumen mask (E), the segments which were in contact with the lumen were identified as parts of the periluminal area and were stored in a logical matrix called Periluminal (F).

These periluminal segments were then combined with the lumen to create the Total Mask (G). Any holes within the combined luminal and periluminal mask were filled using the *imfill* function of MATLAB (H) and the updated Total Mask was applied to the $\%\Delta T_2^*$ map.

This Total Mask would be returned to the algorithm to be used to exclude the lumen and the periluminal area of the AAA before running the hotspot detection algorithm, so that it would be ensured that periluminal areas wouldn't be wrongly selected as hotspots.
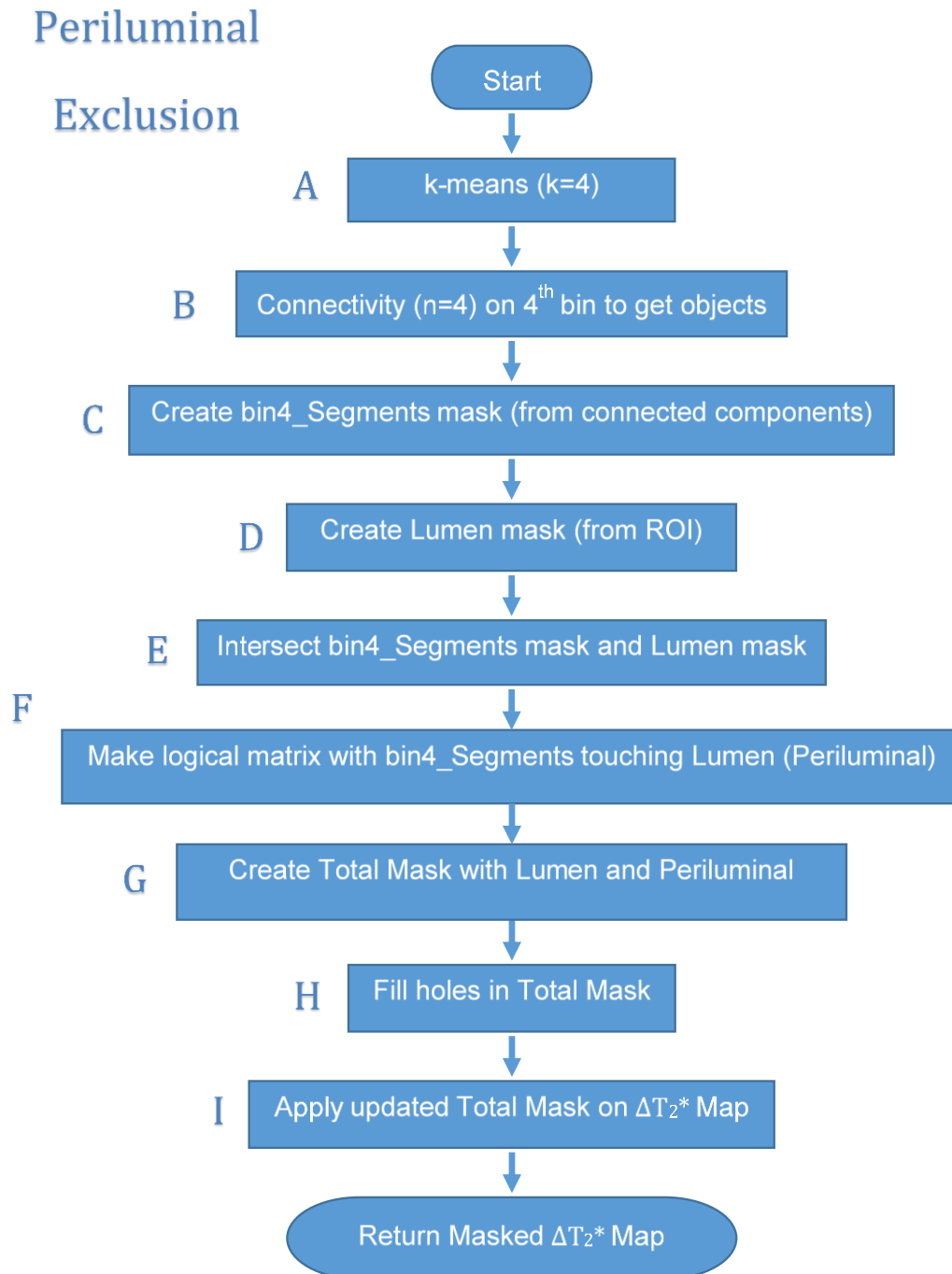
Figure 5.34: Flowchart of periluminal exclusion algorithm.
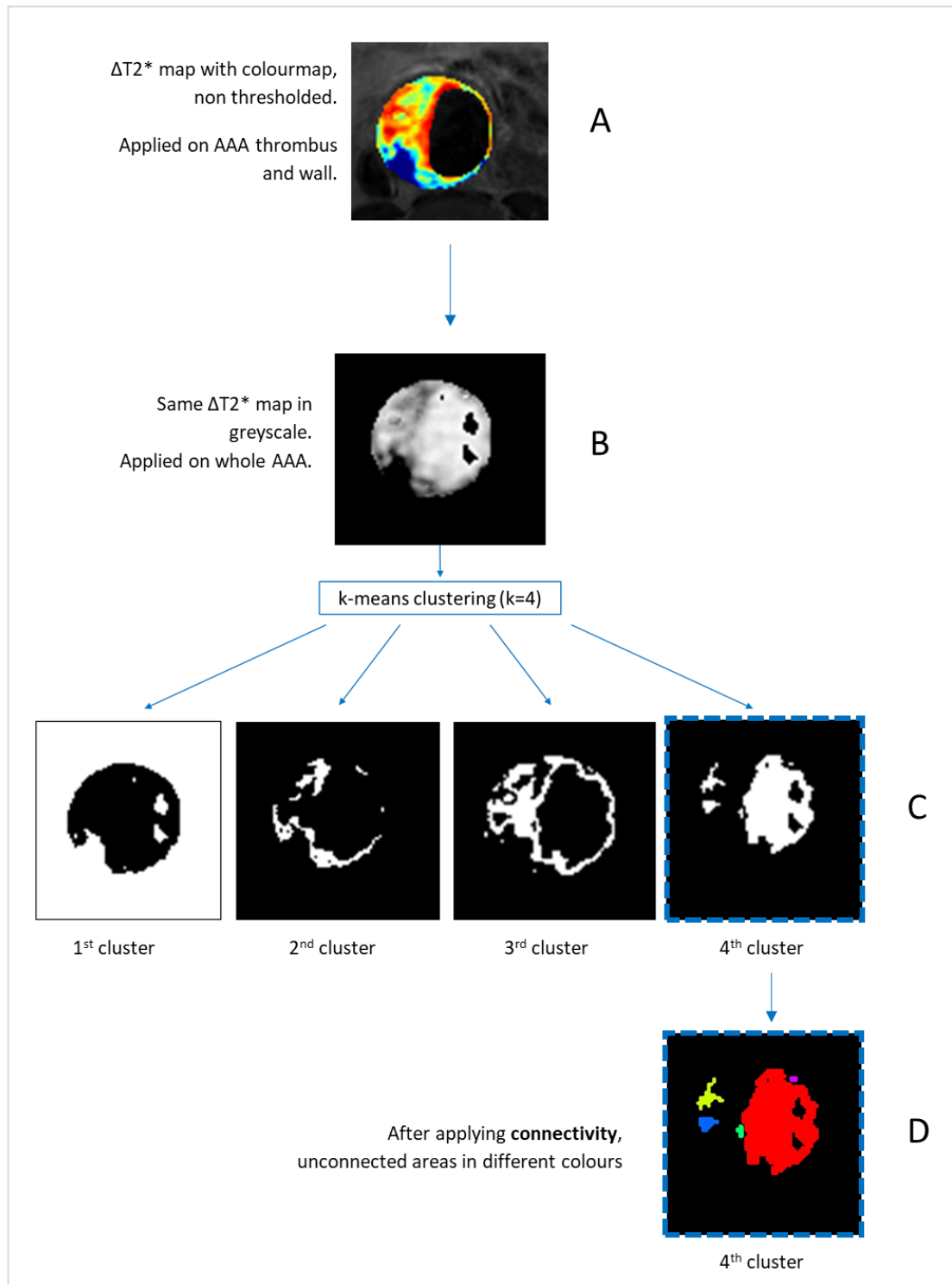
Figure 5.35: Diagram of k-means clustering for periluminal exclusion. A) Non-thresholded %ΔT₂* map with colourmap applied and lumen area excluded. B) Same non-thresholded %ΔT₂* map with lumen included. C) The 4 clusters resulting after applying k-means clustering with 4 bins on the

%ΔT₂ map seen on B. **D)** The resulting individual components, marked in different colours, of the 4ᵗʰ cluster after applying MATLAB's bwconncomp function for connectivity assessment.*

5.4.4.3 Exact number of pixels touching the periluminal area

The general rule was that hotspots should not be touching the area of the lumen and the periluminal area adjacent to it at all (zero neighbouring pixels). However, the trained observers would apply some additional criteria in some exceptional cases. For example, in the case shown in Figure 5.36, they accepted the candidate hotspot of slice 20 (Figure 5.36 A) as valid, despite the fact that 4 of its pixels were touching the lumen. Some degree of flexibility from one of the core rules allowed relevant clinical/anatomical information to be included in the classification decision-making process.
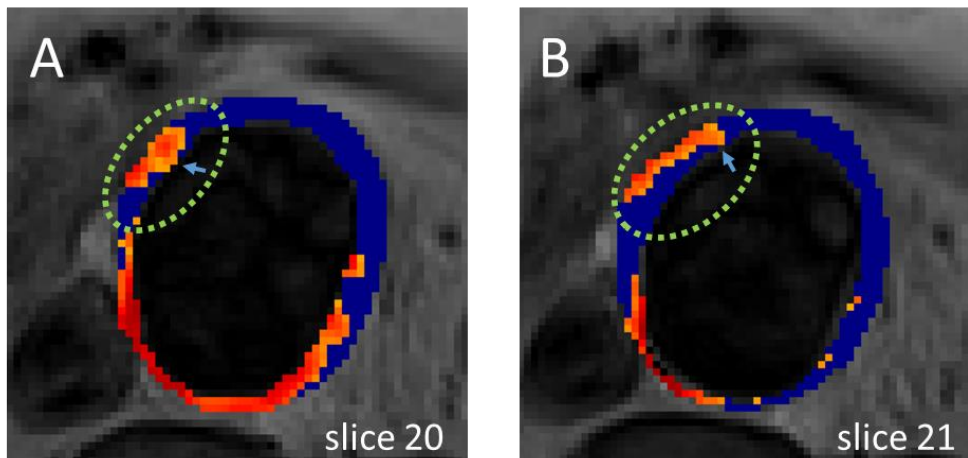
Figure 5.36: Example of exception to periluminal area neighbouring rule. *The marked hotspot in slice 20 in **A** is in contact with the lumen in 4 pixels, but it was accepted as a valid hotspot by the clinical observers, based on the existence of a hotspot on the consecutive slice (slice 21) in **B**, which indicated that the 2 hotspots were connected.*

In this particular case, the clinical observer's decision was based on the examination of the consecutive slice (slice 21) depicted in Figure 5.36 B, which presented a hotspot at the same region, thus they concluded that the candidate hotspot of slice 20 was an extension of the hotspot of slice 21. This sort of exception was not commonly applied in the MA³RS project, as the continuity of

hotspots between slices could not be accurately verified manually by the clinical observers in many cases.

This is an issue that could not be addressed in 2D automatic processing, and it became apparent that a 3D approach would be required in order to increase the sensitivity of the automatic hotspot identification, as will be described in section 5.5.1.

5.4.5 Hotspot Metrics

Within the Evolution 2D algorithm, a variety of metrics are automatically calculated for each hotspot detected, to enable sub-classification of the hotspots, which might be useful in future steps. The Hotspot metrics extracted for each hotspot are described here.

5.4.5.1 2D Hotspot Metrics

Metrics calculated using MATLAB's *regionprops* function, descriptions adapted from [252] are presented in Chapter 5-metrics:

- **Size**
- **Mean/Minimum/Maximum Intensity**
- **Eccentricity**
- **Equivalent Diameter**
- **Major/Minor Axis Length**
- **Orientation**

5.4.5.2 Additional 2D Metrics

- **Minimum Distance from Lumen:** This metric refers to the distance between the hotspot and the lumen at their closest instance. It is calculated by detecting the pixels on the perimeter of the lumen and the

pixels on the perimeter of the hotspot and calculating the distances of all the possible combinations between them, then selecting the smallest distance.

- **Position:** The position returned ranges between 9 values: North (N), East (E), South (S), West (W), NorthEast (NE), NorthWest (NW), SouthEast (SE), SouthWest (SW), Centre (C), which refer to the relative position of the coordinates of the centroid of the hotspot over the centroid of the AAA (in the specific slice). Centre refers to the extreme case in which the two centroids have the exact same coordinates.

5.4.6 Evolution 2D Algorithm Pipeline

The process followed by the Evolution algorithm in a bid to expand the manual segmentation is summarised in the flowchart in Figure 5.37.
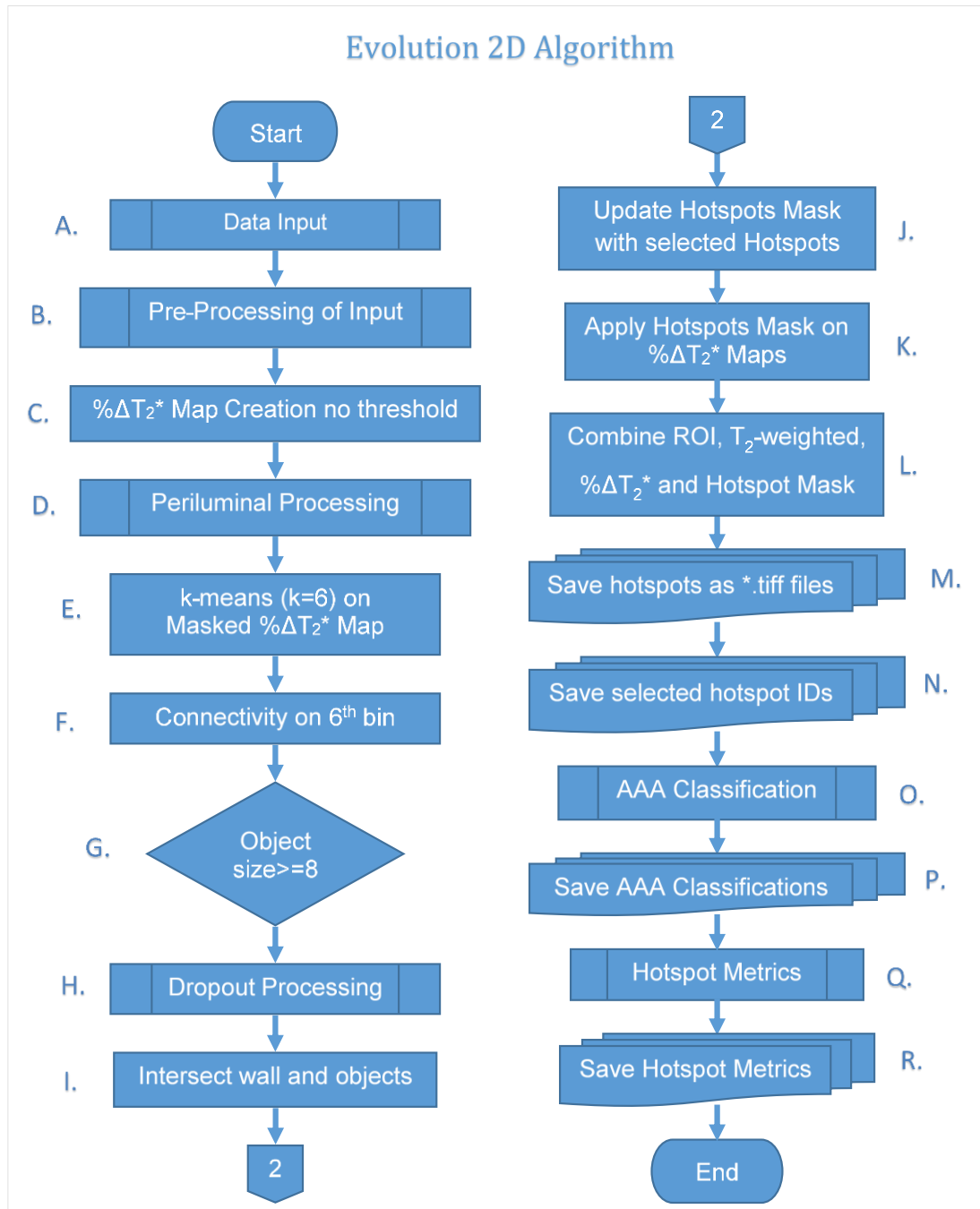
Figure 5.37: Evolution 2D Algorithm flowchart

5.4.7 Algorithm Adaptations for different applications

Similar to the Replication algorithm, the Evolution 2D algorithm has a (larger) number of variables that can be adapted so that it can be applicable to datasets obtained with alternative protocols, derived from different trials or different scanners.

The variables that can be adapted are:

1. The minimum number of connected pixels of inflammation per slice required for the area to be considered an inflammatory hotspot.

2. The number (k1) of clusters of k-means for Hotspot detection (see section 5.4.3.1.2)

3. The number (k2) of clusters of k-means for Periluminal Processing (see section 5.4.4).

4. The minimum number of pixels neighbouring the wall required for the inflammatory hotspot to be accepted.

5. The maximum number of pixels neighbouring the periluminal area that would be accepted for the inflammatory area to be considered a separate hotspot.

5.4.8 Application on MA³RS Dataset

The Evolution 2D algorithm was applied to a subset of the MA³RS dataset and the results were compared with the manual classifications previously produced by clinical observers as reference. However, the goal of the Evolution 2D was not to replicate manual results (as the Replication algorithm did, see 5.3), but rather to explore alternatives for the detection and measurement of hotspots.

5.4.8.1 Methods

A total of 173 randomly selected AAAs were used, for which the ROIs had been manually segmented previously. Following the protocol of the MA³RS study, the %ΔT_2* maps were created, but no threshold was applied on them. The variables used in the Evolution 2D to be applied on the MA³RS dataset were:

1. The minimum number of connected pixels of inflammation per slice required for the area to be considered an inflammatory hotspot was 8.

2. The number (k1) of clusters of the k-means for Hotspot detection (see section 5.4.3.1.2) was 6.

3. The number (k2) of clusters of the k-means for Periluminal Processing (see section 5.4.4) was 4.

4. The minimum number of pixels neighbouring the wall required for the inflammatory hotspot to be accepted was 1. In the first instance, only the hotspots in contact with the outer layer (perimeter) of the wall were accepted.

5. The maximum number of pixels neighbouring the periluminal area that would be accepted for the inflammatory area to be considered a separate hotspot was 0.

Similar to 5.3.10.1, AAAs including at least one hotspot were classified by the Evolution 2D algorithm as USPIO-positive, otherwise as USPIO-negative. The MA³RS protocol included a small number of AAAs classified as having "indeterminate USPIO enhancement". Those were considered as part of the USPIO-negative group for comparison with the automatic classifications.

5.4.8.2 Results

In Table 5.7, the manual classifications are compared with the classifications on the Evolution 2D algorithm: in a total of 173 AAAs, 90 true positives (TP), 20 false positives (FP), 61 true negatives (TN) and 2 false negatives (FN) were identified, amounting to 22 disagreements.

Table 5.7: Confusion matrix comparing auto and manual AAA classification based on hotspot detection. The Manual outcome correspond to results produced from the manual classification of AAAs by the clinical observers. TP=True Positive, FP=False Positive, FN= False Negative, TN=True Negative; Sens=Sensitivity=TP/(TP+FN); Spec=Specificity= TN/(TN+FP).

		Manual Outcome	
		Positive	Negative
Auto Outcome	Positive	TP = 90	FP = 20
	Negative	FN = 2	TN = 61
	Sample size	173	
	Disagreements	22	
	Sensitivity	97.8%	
	Specificity	75.3%	

The high number of "false positives" reflects the additional cases of hotspots suggested by the algorithm, based on the lack of data thresholding, the inclusion of smaller hotspots (8 pixels) and the differences in the processing method, as described in the previous sections.

Visual examination of the individual cases revealed the ways in which previously-discarded areas were now accepted as hotspots by the algorithm. As shown in

Figure 5.38, an inflammatory area adjacent to the aortic wall, that however appeared too small (only 3 pixels) in the 71%-thresholded %ΔT$_2$* map (Figure 5.38 A), was large enough in the non-thresholded %ΔT$_2$* data (Figure 5.38 B) to be accepted as a hotspot (Figure 5.38 C). Similarly, the area shown with the yellow arrow in Figure 5.38 D consisted of just 9 pixels in the 71%-thresholded %ΔT$_2$* map, while it appeared larger in the non-thresholded map of Figure 5.38 E and a 12-pixel hotspot was detected (Figure 5.38 F). The slice depicted in Figure 5.38 D had a second hotspot detected (white arrow), as seen in Figure 5.38 G, which did not appear at all in the thresholded map (Figure 5.38 D). This case of hotspot was of lower intensity and could be re-assessed later, with the intensity metrics taken into account.
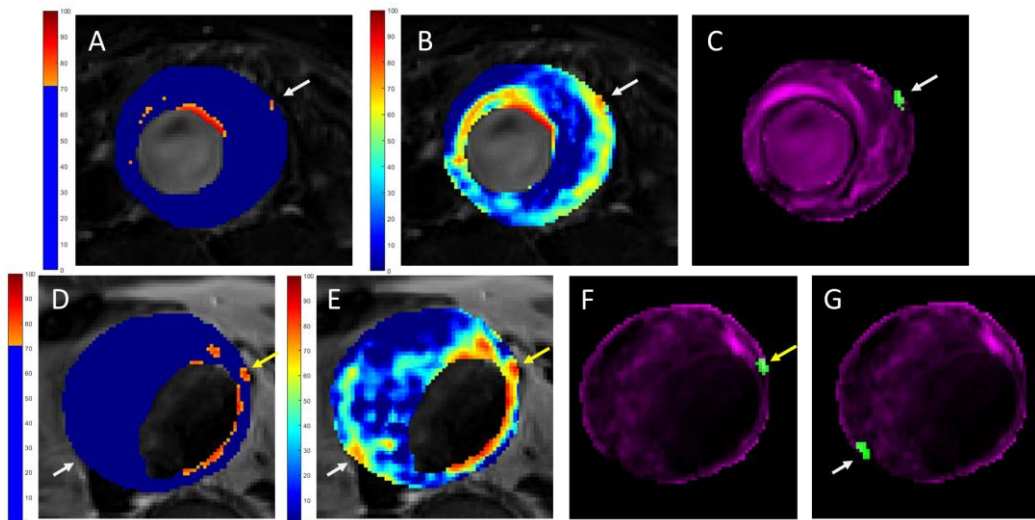
Figure 5.38: Examples of additional hotspots detected by Evolution 2D. *A and D are %ΔT$_2$* colourmaps (with 71% threshold applied). B and E are the corresponding non-thresholded %ΔT$_2$* colourmaps. In C, F and G, the automatically detected hotspots (arrows) of the respective maps are illustrated; both F and G correspond to the same slice.*

Another common finding was cases of inflammatory areas which in the thresholded %ΔT$_2$* maps appeared to be distinct from the aortic wall, as seen in Figure 5.39 A and Figure 5.39 D. Non-thresholded maps (Figure 5.39 B,E) revealed larger areas which expanded to the wall, therefore qualifying as

hotspots (Figure 5.39 C,F). In some cases, the inclusion of the previously thresholded data also allowed for "bridges" to be formed between smaller areas, to form a larger hotspot as depicted in Figure 5.39 D, E and F.
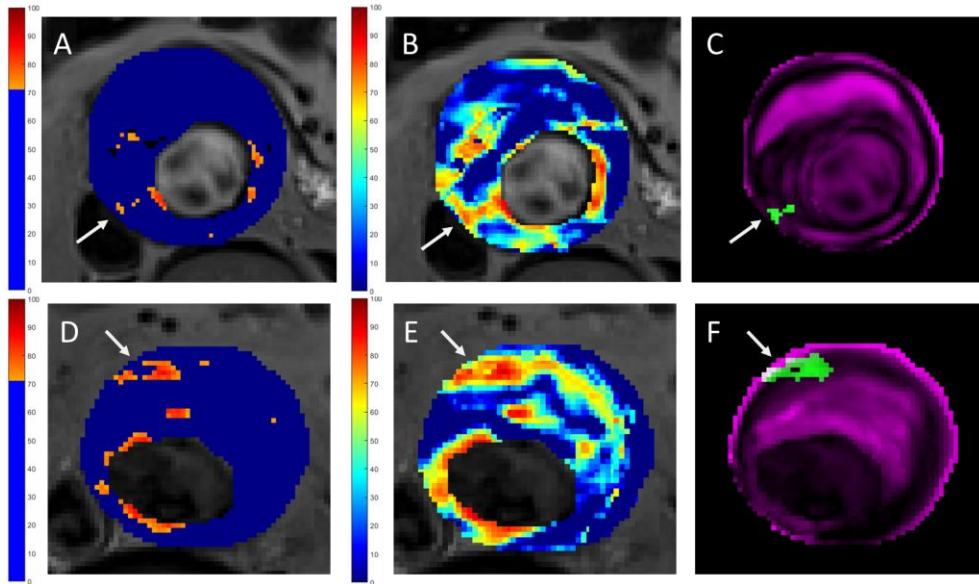
Figure 5.39: Examples of additional hotspots detected by Evolution 2D. *A and D are %ΔT$_2$* colourmaps (with 71% threshold applied). B and E are the corresponding non-thresholded %ΔT$_2$* colourmaps. In C and F, the automatically detected hotspots (arrow) of the respective maps are illustrated.*

A representative example of an interesting category of additional hotspots is presented in Figure 5.40. This type of USPIO uptake is challenging to manually classify in a reproducible way, as it could either be considered diffused USPIO, or, if a hotspot was identified, there would be no way of reproducibly defining its boundaries manually.
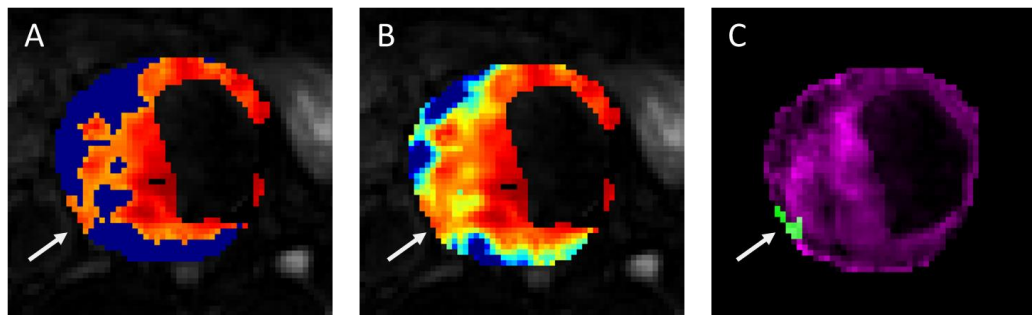
Figure 5.40: Example of additional hotspots detected by Evolution 2D. *A is a %ΔT₂* colourmap (with 71% threshold applied). B is the corresponding non-thresholded %ΔT₂* colourmap. In C, the automatically detected hotspot (arrow) is illustrated.*

Finally, some cases of accidental omission of hotspots during manual processing were also identified as shown in the examples in Figure 5.41, and the clinical observers were informed and the manually processed results were updated accordingly.
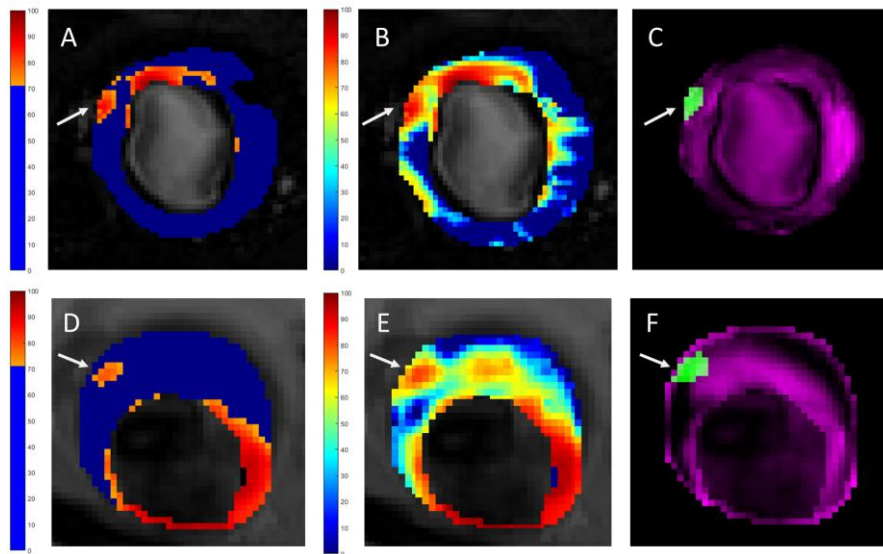
Figure 5.41: Examples of additional hotspots detected by Evolution 2D. *A and D are %ΔT₂* colourmaps (with 71% threshold applied). B and E are the corresponding non-thresholded %ΔT₂* colourmaps. In C and F, the automatically detected hotspots (arrow) of the respective maps are illustrated. These hotspots were accidentally missed by the clinical observers.*

Metrics on size, intensity of each hotspot and geometrical features were also recorded for all the AAAs processed. Even though a larger total number of potential hotspots are detected with the Evolution 2D algorithm, the additional information that accompanies each of them can enable us to sub-classify them and possibly discard some sub-categories. For example, by using the "mean intensity" metric to sub-classify hotspots, candidate hotspots with low mean values like the one depicted in Figure 5.38 E and G, can be identified as "non-very active" and be excluded, while cases with very high average values could be distinguished and assessed further.

5.4.8.2.1 Wall thickness

The first round of processing reported above accepted only hotspots that were found to be adjacent to the outer layer of the aortic wall, as calculated by finding the wall's perimeter. The same dataset was later re-processed to include the candidate hotspots that were only in contact with the inner wall layers. This change in the method lead to the identification of 5 additional hotspots, which then lead to 4 AAAs being classified as USPIO-positive. These AAAs could consequently be grouped together for further AAA stratification.

5.5   "Evolution 3D" Algorithm

In the initial analysis of the pilot study, the need for a 3-dimensional approach in detecting hotspots of inflammation had become apparent, as there were many cases in which the clinical observers noticed some continuity between the inflammation present in contiguous slices. The continuity was even more evident in the MA³RS datasets due to the improvements in the imaging protocol and raised the question of whether by only identifying hotspots in 2D (per slice), large inflammation areas spreading within a number of consecutive slices (in 3D) were being missed, or counted as smaller individual hotspots per slice, omitting information that may potentially be useful in further sub-classifying presence and degree of inflammation.

 Manually determining the existence of 3D hotspots in an accurate, reproducible and efficient way was not possible, as is suggested in the example in Figure 5.42: visual examination of the inflammatory areas (in green) of slices 7, 8 and 9 would not ascertain the fact that they were all inter-connected and as such, formed a 3D hotspot which extended within all three slices.

slice 7   slice 8   slice 9
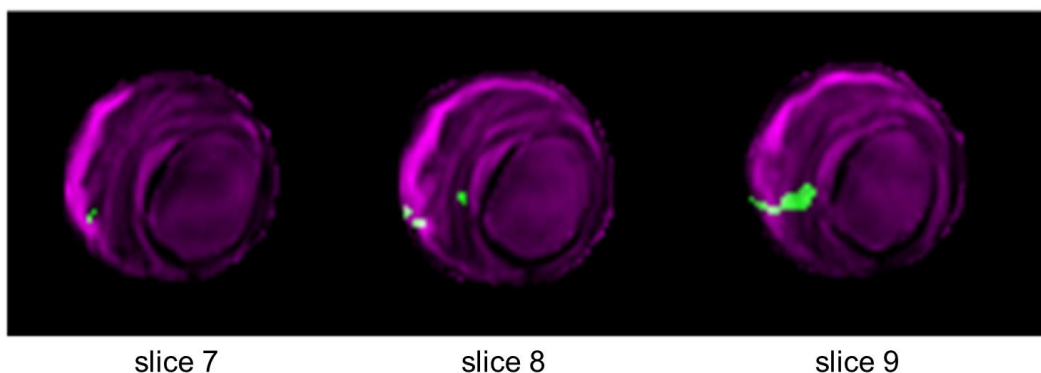
Figure 5.42: Example of 3D Hotspot detection. Using 3D connectivity with MATLAB's *bwconncomp function, the green areas of high USPIO concentration in slices 7 and 8 are found to be connected with the hotspot detected (in green) in slice 9, thus forming a 3D hotspot which extends within all three slices.*

Consequently, the Evolution 3D algorithm was developed, as an extension to the Evolution 2D algorithm, to detect and visualise 3D inflammatory hotspots for the first time and to allow more comprehensive analysis of the inflammation and further stratification with 3D metrics (describing size, geometrical features and signal intensity of each hotspot). The algorithm was developed and tested on the MA³RS dataset. While it could, practically, have been applied to the pilot dataset as well, the 5mm gap between consecutive slices of the pilot MRI acquisitions (see 1.4.4.) would render the 3D processing inaccurate. On the other hand, the MA³RS MRI dataset had been acquired without gaps between consecutive slices and its higher-quality MR images were more suitable for the 3D assessment.

As outlined in Table 5.8, the methods implemented for the Evolution 3D algorithm were largely the same as the ones used in the Evolution 2D algorithm, except for the hotspot detection (Table 5.8 F) and the metrics calculation (Table 5.8 G) which will be described in the following sections.

Table 5.8: Differences between Evolution 2D algorithm and Evolution 3D algorithm

	Evolution 2D Algorithm	**Evolution 3D Algorithm**
A	$\%\Delta T_2^*$ maps have 0% threshold	$\%\Delta T_2^*$ maps have 0% threshold
B	Hotspots not touching dropout areas neighbouring with lumen	3D Hotspots not touching dropout areas neighbouring with lumen
C	Updated Periluminal (k-means clustering) • Connectivity with lumen, n=8 • Periluminal area excluded on $\%\Delta T_2^*$ maps before hotspot detection	Updated Periluminal (k-means clustering) • Connectivity with lumen, n=8 • Periluminal area excluded on $\%\Delta T_2^*$ maps before hotspot detection
D	Hotspots >=8 contiguous voxels	Hotspots >=8 contiguous voxels

E	Hotspots within aortic wall (outer or inner)	Hotspots within aortic wall (outer or inner)
F	2D Hotspot Detection: • k-means clustering (k=7) • 2D connectivity (n=8) on thresholded %ΔT$_2$* maps	3D Hotspot Detection: • k-means clustering (k=7) • 3D connectivity (n=26) on thresholded %ΔT$_2$* maps
G	2D Hotspot Metrics	3D Hotspot Metrics

5.5.1 Detection of 3D Hotspots

The dropout exclusion method described in 5.3.2 (from the Replication algorithm methods) and the periluminal exclusion method described in 5.4.4 (from the Evolution 2D methods) were applied by the Evolution 3D algorithm on a slice-by-slice basis for each AAA being processed.

Furthermore, the same clustering technique (k-means clustering with k=6 bins) as the one implemented in the Evolution 2D algorithm was applied on the %ΔT$_2$* maps of each slice individually.

5.5.1.1 3D Connectivity

After all the slices per AAA had been segmented with the k-means clustering, 3D connectivity with MATLAB's function *bwconncomp* with n=26 was applied on the 3D volume consisting of the areas of the 6th cluster. This process is illustrated with two slices in Figure 5.43: for each slice, the corresponding 6th bin segmentation is depicted in Figure 5.43 B. With the application of the 3-D connectivity function to these, the interconnected areas of the two slices were

determined and marked with corresponding colours for illustration in Figure 5.43 C.
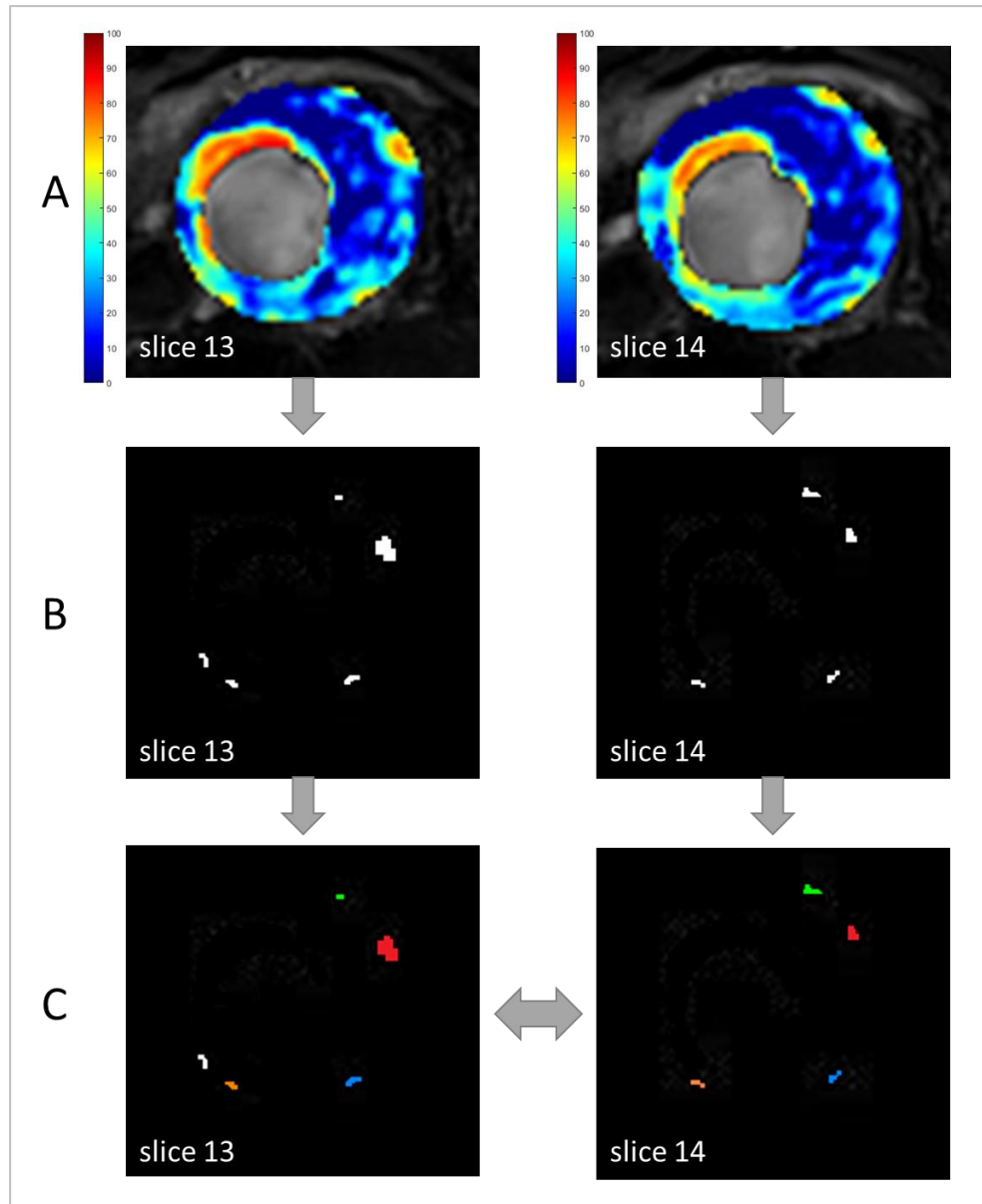
Figure 5.43: The identification of 3D-connected hotspots. A) *%ΔT₂* colourmaps (no threshold) of two consecutive slices (slices 13 and 14).* ***B)*** *The 6th cluster after application of k-means clustering (k=6) for each slice.* ***C)*** *3D connectivity applied on the two B slices identifies which pixels of slice 13 are connected with pixels of slice 14. Four neighbouring groups are identified (green, red, blue, orange); groups of the same colour are connected in 3D between the two slices.*

5.5.1.2 Visualisation of 3D Inflammatory Hotspots

The 3D hotspots detected by the Evolution 3D algorithm were automatically saved as series of consecutive 2D images as previously shown in Figure 5.42. As a supplementary way of visualising the USPIO uptake within the AAA volume, semi-automatic 3D reconstructions of the AAAs like the one presented in Figure 5.44 were also created.

For the 3D reconstruction of the AAAs, the manually defined ROIs were used for the lumen and thrombus areas and combined with maps of the 3D hotspots to create 3D volumes, while the wall region was not visualised for practical reasons.
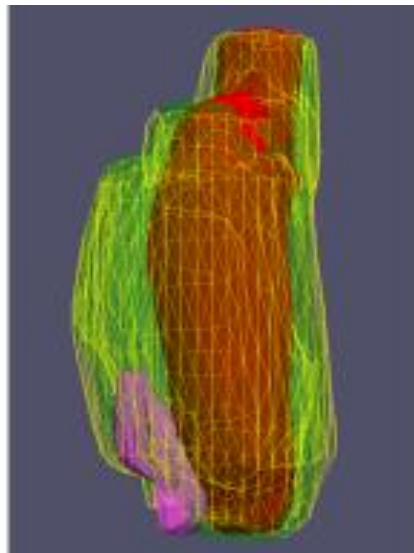
Figure 5.44: An example of a 3D hotspot visualised within an AAA. The hotspot is marked in magenta colour, while the lumen (bloodflow) is depicted in red, and the thrombus in green/yellow.

A protocol for the 3D reconstruction and visualisation was created, but the procedure was not yet fully automated at the time of writing. A combination of software packages was used, namely of MATLAB, Analyze and Paraview 4.0 (Kitware Inc., Los Alamos National laboratory).

5.5.2 Algorithm Adaptations for different applications

The set of variables described in section 5.4.7 for the Evolution 2D can also be adapted within the Evolution 3D algorithm for it to be usable with varying datasets acquired from different scanners and with alternative protocols. Additionally, the %ΔT$_2$* datasets can be thresholded at any level required.

5.5.3 3D Hotspot Metrics

The following 3D metrics were calculated with MATLAB's *regionprops3* function.

- **Volume:** the number of voxels comprising the hotspot.
- **Mean/Minimum/Maximum Intensity** of the %ΔT$_2$* values per hotspot.
- **Equivalent Diameter:** This value corresponds to the diameter that a sphere with the same volume as the hotspot would have. It is estimated as $\left(6 * \frac{Volume}{pi}\right)^{\frac{1}{3}}$.
- **Principal Axis Length:** Given by the length (in voxels) of the major axes of the ellipsoids that have the same normalised second central moments as the hotspot volume, returned as a 1-by-3 vector.
- **Orientation:** Given by Euler angles, returned as a 1-by-3 vector. As the angles are based on the right-hand rule, a positive angle represents a rotation in the counter-clockwise direction.

5.5.4 Application on MA^{3}RS Dataset

The Evolution 3D algorithm was applied on a subset of the MA^{3}RS dataset to explore new ways of identifying, visualising and quantifying 3D inflammation within AAAs. As this, to my knowledge, was the first time a 3D approach was being implemented within this specific context of detecting inflammation within

a 3D structure, there was no gold standard available for direct comparison of the results produced by the algorithm.

5.5.4.1 Methods

A total of 173 randomly selected AAAs were used, for which the ROIs had been manually segmented previously. As the 3D hotspots spanned more than one slice in most cases, the criteria of the mural and periluminal uptake (described in 5.3.5 and 5.4.4 respectively) had to be re-assessed for the 3D algorithm. For this assessment, a subset of 10 AAAs from the MA³RS study which had been automatically identified as having 3D hotspots were used, with zero contact points with the periluminal area and at least one contact point with the wall.

The selection of the hotspots was such that it included 5 cases that clearly had to be dismissed, as they mainly consisted of periluminal uptake and 5 cases with the USPIO mainly focused on the aortic wall.

Different combinations of mural contact sizes (minimum of 1 to 6 pixels) and periluminal contact sizes (maximum of 0 to 5 pixels) were trialled. The best combination, with 8/10 success rate was given for a minimum of 2 contact points with the wall and a maximum of 3 contact points with the periluminal area.

Is summary, the variables used in the Evolution 3D to be applied on the MA³RS dataset were:

1. The minimum number of connected pixels of inflammation per slice required for the area to be considered an inflammatory hotspot was 8.

2. The number (k1) of clusters of the k-means for Hotspot detection (see section 5.4.3.1.2) was 6.

3. The number (k2) of clusters of the k-means for Periluminal Processing (see section 5.4.4) was 4.

4. The minimum number of pixels neighbouring the wall required for the inflammatory hotspot to be accepted was 2. Only hotspots in contact with the outer layer (perimeter) of the wall were accepted.

5. The maximum number of pixels neighbouring the periluminal area that would be accepted for the inflammatory area to be considered a separate hotspot was 3.

6. The algorithm was applied both on thresholded $\%\Delta T_2$* maps (71% threshold) and on non-thresholded maps.

Similar to 5.3.10.1, AAAs including at least one hotspot were classified by the Evolution 3D algorithm as USPIO-positive, otherwise as USPIO-negative.

In order to examine the effects of 3D processing on the 71%-thresholded maps which were used by the clinical observers for manual processing and by the Replication algorithm, the Evolution 3D algorithm was first applied on thresholded data, to explore whether 3D hotspots could be detected despite the threshold application. Following this, the Evolution 3D algorithm was applied on non-thresholded data.

5.5.4.2 Results

When the Evolution 3D algorithm was applied to thresholded (71% threshold) $\%\Delta T_2$* maps, a total of 44 AAAs bearing at least one 3D hotspot each were identified. Application of the algorithm on non-thresholded $\%\Delta T_2$* maps resulted in the identification of 50 AAAs with 3D hotspots.

Applied on the thresholded data, this algorithm detected 3D hotspots which would be too small to be accepted as such per individual slice but were

adequately large if all the slices they occupied in 3 dimensions were included. A representative case is demonstrated in Figure 5.45 I. In A, the hotspot was identified in manual processing, but the inflammatory area in the next slice (B) did not qualify as a hotspot due to its small size. The Evolution 3D algorithm found that these areas defined in C and D were part of one 3D hotspot.

Additionally, by detecting 3D areas, the algorithm identified cases of inflammatory areas which were not adjacent to the aortic wall but were connected to other areas that were in contact with the wall, as illustrated in Figure 5.45 II. In this example, only the 10-pixel hotspot of E had been manually identified as a hotspot. The inflammatory area in F (arrow) fulfilled all the conditions to be a hotspot, except for the proximity to the aortic wall. The automatic processing revealed that the areas of both slices formed a single 3D hotspot (Figure 5.45 G and H).
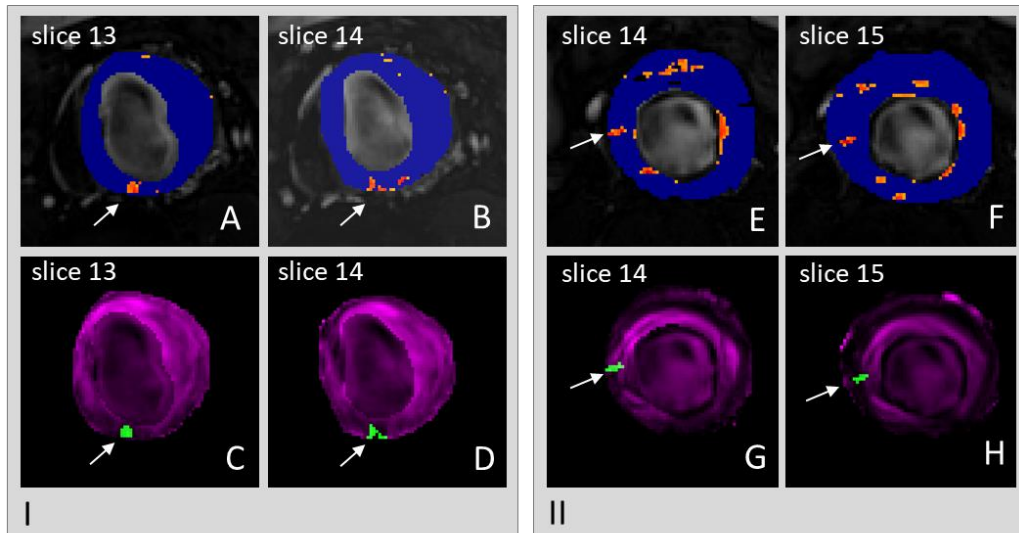
Figure 5.45: Example of 3D hotspots spanning within many consecutive slices. *Slices belonging to two AAAs, marked as I and II. A, B, E and F are %ΔT₂* colourmaps (with 71% threshold applied). The green areas marked on C, D correspond to the automatically detected 3D hotspot which extends on both slice 13 and slice 14 of I. The green areas marked on G, H correspond to the automatically detected 3D hotspot which extends on both slice 14 and slice 15 of II.*

The case depicted in Figure 5.46 was included here to demonstrate the difference between the manually detected hotspots in a series of slices (A) on thresholded data, against the automatically detected 3D hotspots which have been identified on non-thresholded $\%\Delta T_2^*$ maps. In A, six separate hotspots could be identified manually. With the Evolution 3D algorithm however, it is revealed that the previously defined hotspots actually belong to two large 3D hotspots that expand over several slices of the AAA: as shown in B, the first 3D hotspot spans from slice 11 to slice 17, while as shown in C, the second 3D hotspot is contained within slices 15 and 16.
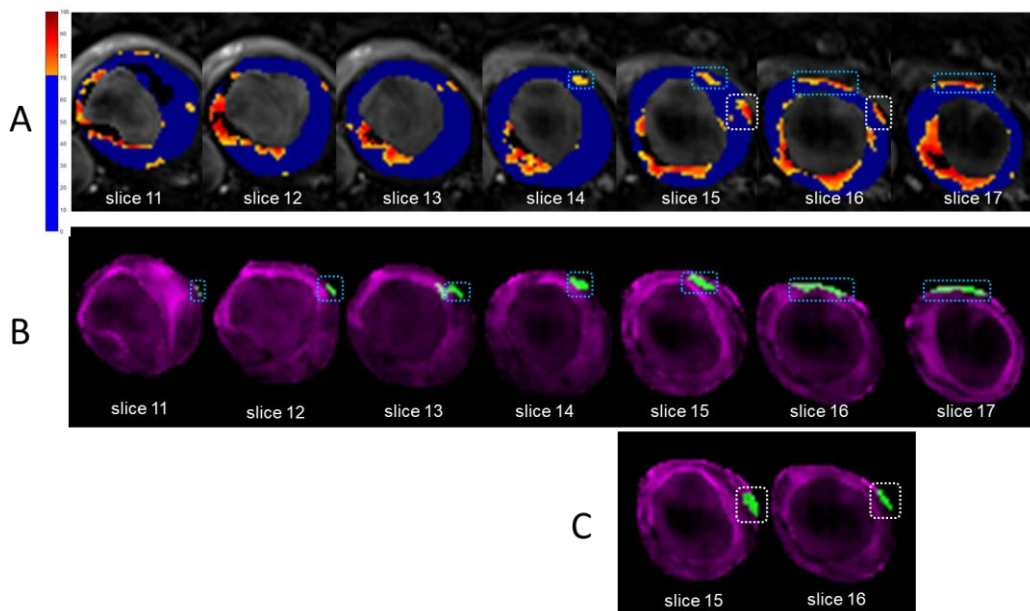
Figure 5.46: Comparison between manually detected 2D hotspots and automatically detected 3D hotspots. *A) $\%\Delta T_2^*$ colourmaps (with 71% threshold applied) of consecutive slices. Six manually identified hotspots are marked in slices 14, 15, 16 and 17. B) All marked areas on the seven consecutive slices correspond to one 3D hotspot, automatically detected by the Evolution 3D algorithm. C) The two areas marked in slices 15 and 16 belong to a separate 3D hotspot detected by the algorithm.*

The example in Figure 5.47 aims to highlight the fact that seemingly small, low-intensity areas of USPIO uptake which would be discarded in manual processing or if the 71% threshold was applied, can actually be part of a 3D "object" within

the AAA. In the specific example of Figure 5.47, the detected 3D hotspot spans 11 consecutive slices.
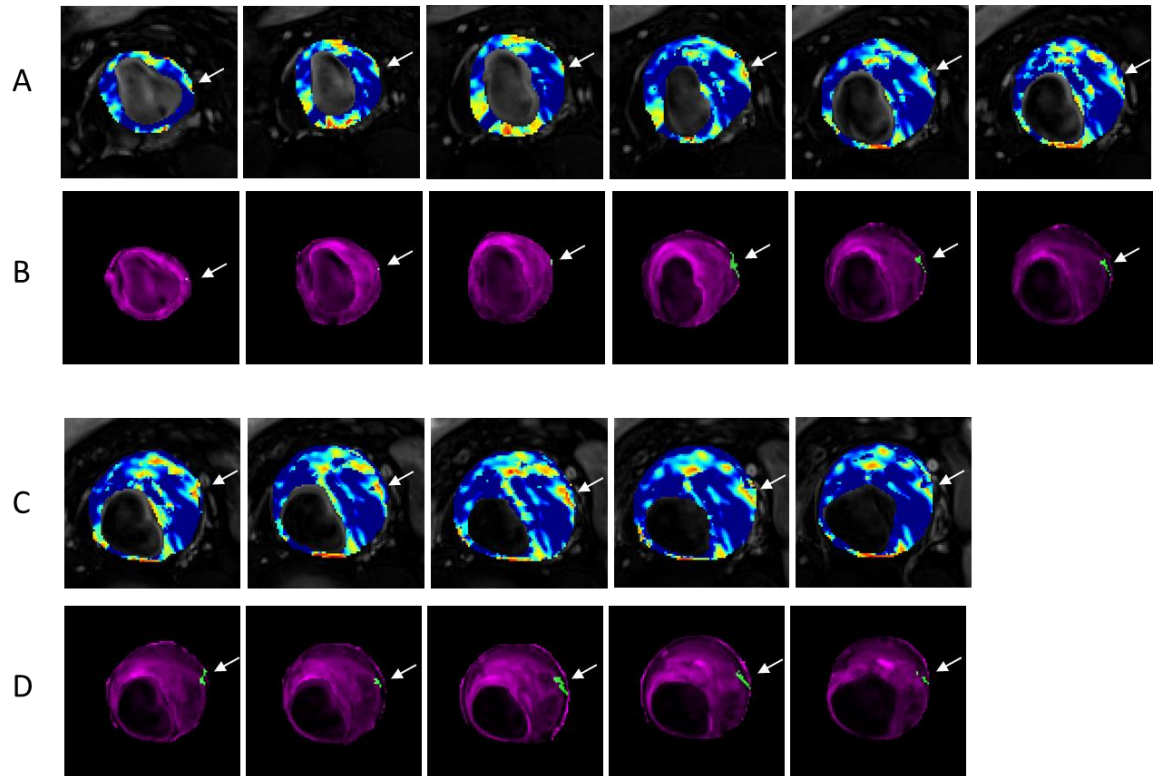
Figure 5.47: A and C are %ΔT$_2$* colourmaps (no threshold applied) of consecutive slices. In B and D, the green areas (arrows) of the total of 11 slices are part of one 3D hotspot, automatically detected by the Evolution 3D algorithm.

Furthermore, the 3D hotspot detection can potentially assist with cases of inflammation at the thinnest part of the thrombus in the AAA, where the lumen is in close proximity to the wall and therefore detecting hotspots is very challenging, as shown in Figure 5.48, where a 3D hotspot spanning the 3 slices is automatically detected.
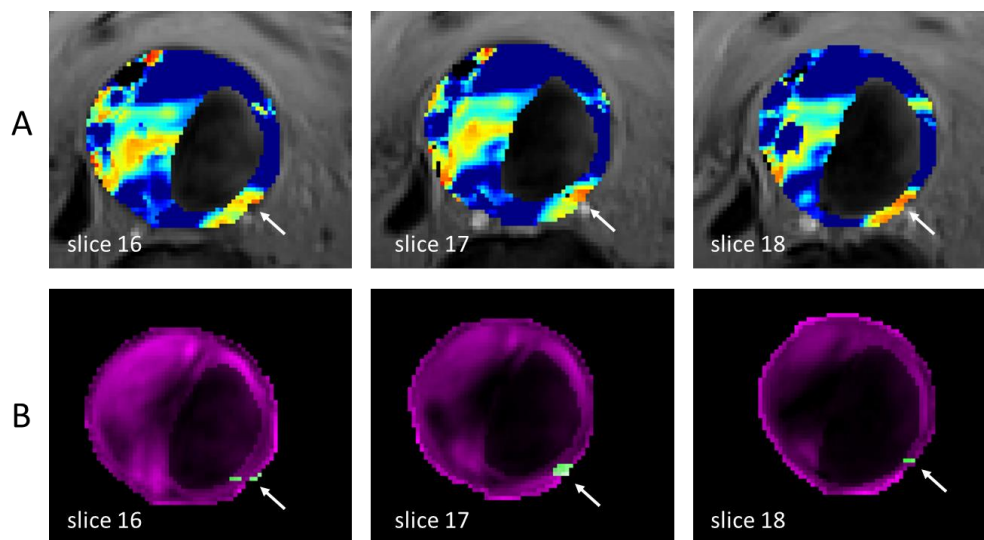
Figure 5.48: An example case of a 3D hotspot detected on the thinnest part of the thrombus.

Another variable revealed by running the 3D hotspot detection on the MA³RS dataset was the relative position of large 3D hotspots within AAAs. This has not been defined as one of the metrics currently calculated but could be implemented as future work. In the meantime, patterns of different positions can be visually studied on reconstructed 3D models. Among the MA³RS subset used for 3D hotspot detection, two patterns were easily discernible, namely 3D hotspots present either near the lower part of the AAA, as shown in Figure 5.49 A, or cases of them near the centre of the AAA, as shown in Figure 5.49 B. However, no quantitative assessment of different patterns was conducted within this work. This could be considered as something to be further developed in future work.
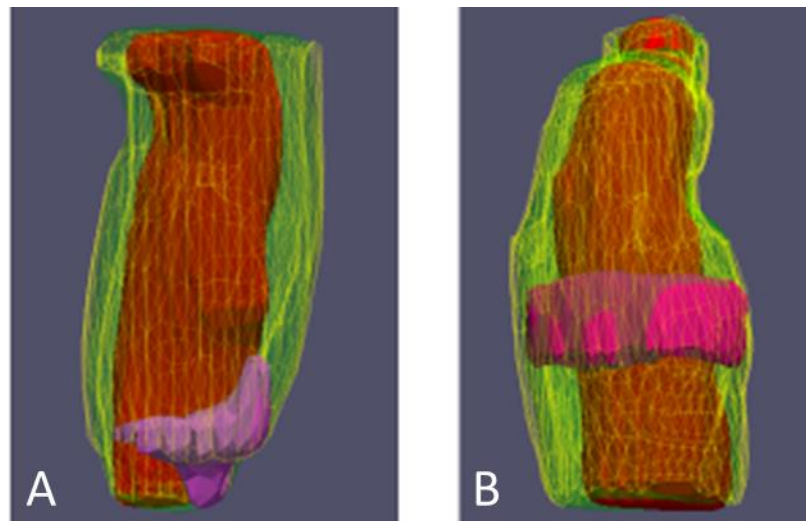
Figure 5.49: Examples of 3D-reconstructions of two AAAs with hotspots included. *These 3D models were made based on the 2D manually segmented ROIs for lumen (red) and thrombus (green/yellow). The wall is not depicted. The hotspots (magenta) have been identified automatically by the Evolution 3D algorithm. The 3D reconstruction was made in a semi-automatic way with a combination of MATLAB, Analyze and Paraview software.*

5.6　Graphical User Interface

5.6.1 Visualisation Graphical User Interface

As previously shown in the data input in 5.2.2, there was a variety of datasets required for the processing of each AAA, with many slices per AAA per dataset. Visually inspecting images from many sources in parallel for each slice was time consuming, laborious and occasionally prone to errors and was making manual processing and data assessment challenging.

In the first stages of the algorithm development, I also needed to have access to quick visualisations of the data for my own review, and to be easily accessible for review with the clinical team. I therefore created a MATLAB Graphical User Interface (GUI) which enabled easy visualisation of all available data per slice per AAA with just one click. A screenshot of the GUI can be seen in Figure 5.50.

The user would select a patient code from a drop-down list of all available patients with AAA scans and the specific slice they were interested in (Figure 5.50 A). By clicking "Load data", the $\%\Delta T_2^*$ map (no threshold) would appear on the left panel (Figure 5.50 B). Simultaneously, the corresponding T_2^* maps (Figure 5.50 F and K) and the four gradient echoes would appear on the panels on the right, for pre-USPIO (day1) and post-USPIO (day 2) data (Figure 5.50 K and L). The user could choose via radio-buttons between T_2^* and R_2^* maps (Figure 5.50 H and M) and the four gradient echoes (Figure 5.50 I and N).

Furthermore, the user could use the "Select Voxel" button (Figure 5.50 C) and choose any voxel of interest by clicking on the $\%\Delta T_2^*$ map (Figure 5.50 B). This would make the intensity value of the specific voxel appear, as well as the intensity values of the same voxel on the corresponding T_2^*/R_2^* maps. This tool was offered for quantitative assessment of any datapoints of interest.

Finally, a button for debugging was available, which gave access to the source code (Figure 5.50 D) for troubleshooting.
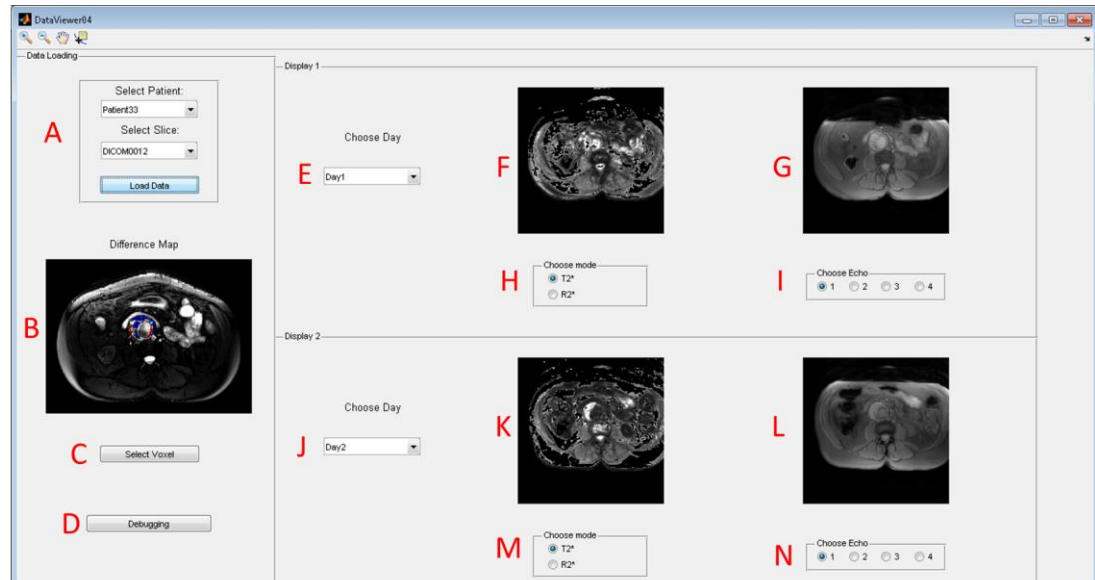
Figure 5.50: The visualisation GUI. *This GUI was created in MATLAB for efficient data visualisation and quality assessment.*

5.6.2 AAA Classification Graphical User Interface

After the finalisation of the Evolution 2D Algorithm, the code was incorporated into an improved version of the GUI. The new version did not require a specific slice number to be selected and loaded, but rather loaded the entire dataset for the AAA selected by the user (Figure 5.51 A). After the "Load Data" button was clicked, thresholded (71%) $\%\Delta T_2*$ maps (Figure 5.51 B) and non-thresholded maps (Figure 5.51 C) of the AAA were loaded, as well as T_2* maps and corresponding gradient echoes. Simultaneously to these, the classification result of the AAA according to the Evolution 2D algorithm was printed (Figure 5.51 L), as well as a list of all the hotspots detected and their location (slice number)

within the AAA (Figure 5.51 M). Additionally, the identified hotspots could be visualised one-by-one by clicking the button "Show Hotspots" (Figure 5.51 N).

The user could choose via radio-buttons between T_2* and R_2* maps (Figure 5.51 F and J) and the four gradient echoes (Figure 5.51 G and K) and use the slider under the loaded images to scroll through the different slices available per AAA.

Finally, a button for debugging was available, which gave access to the source code (Figure 5.51 0) for troubleshooting.
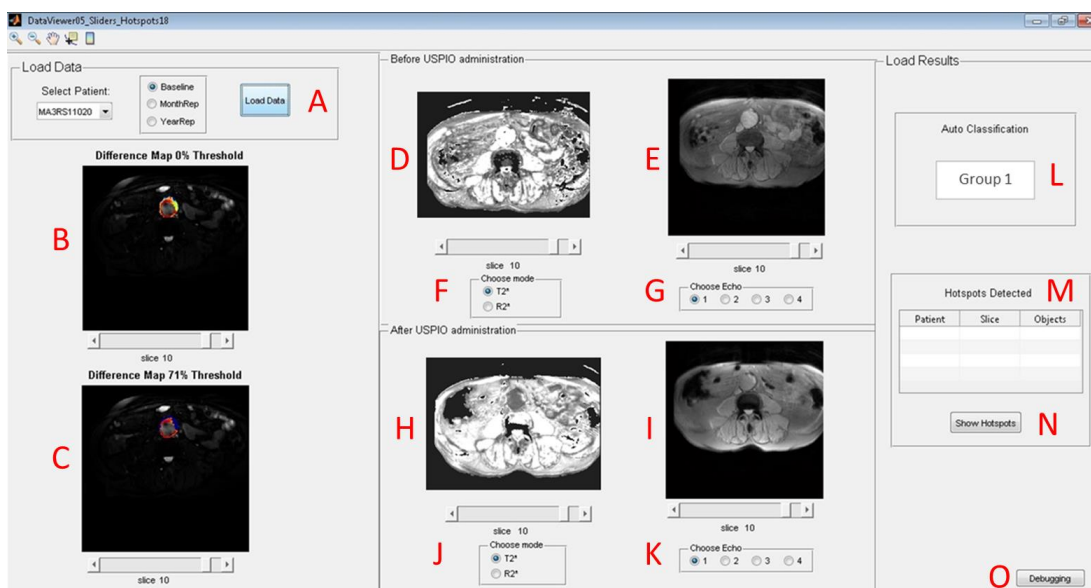
Figure 5.51: The improved, AAA classification GUI. *This GUI incorporated, additionally to the dataset visualisations, the code of the evolution 2D algorithm, thus presenting the classification result for the loaded AAA, as well as visualising the hotspots detected within it.*

The same GUI can also incorporate the Evolution 3D algorithm, but in its current form can only visualise the detected 3D hotspots in a slice-by-slice basis, rather than creating a 3D reconstruction.

5.7   Discussion

The detection of inflammatory hotspots was one of the core elements of the MA³RS trial and previously the pilot study. The methods employed for hotspot detection and classification of AAAs were performed manually in both studies. The manual processing, however, of such large and complex datasets introduced some challenges which I aimed to address by introducing automatic processing methods. The resulting three algorithms not only replicated the manual processing, but also introduced alternative hotspot detection techniques including the specific inclusion of detection and connectivity of hotspots in 3 dimensions, novel metrics and visualisations and a guided user interface which combined all the above.   The 3D combination of USPIO uptake had been highlighted as a requirement as early as the pilot study (refer to Richards et al pilot paper here).

5.7.1 Automatic Replication of Manual Processing

Given the fact that the MA³RS trial included 342 patients, with an average of approximately 30 slices per AAA needing individual review, manual processing was very time-consuming. Depending on the complexity of each AAA, manual hotspot detection could take between 15 to 30 minutes per AAA. Furthermore, the large amount of data involved introduced high chances of human error, while the nature of manual processing is inherently prone to low reproducibility levels.

The **Automatic Replication algorithm** was designed to be able to reproduce and speed up the manual processing. It imitated the manual protocol as closely as possible, by applying the same 71% threshold to $\%\Delta T_2^*$ maps, processing the AAAs on a slice-by-slice basis, incorporating controls for the exclusion of

"Dropout" areas, and accepting hotspots of at least 10 pixels, which were adjacent to the outer layers of the aortic wall and distinct from the periluminal area.

The outcome of the Replication algorithm was evaluated by being applied first to the Pilot dataset (sample size n=25) and with its outcomes compared against the previously produced manual outcomes, achieving a compelling 92.3% Sensitivity rate and 100% rate for Specificity after adjustments that accounted for some variability in the manual processing and were agreed with the clinical team. It was subsequently validated against the manual outcome of a subset of the MA³RS dataset (sample size n=173), with 98.9% Sensitivity rate and 100% Specificity (adjusted to account for manual processing variability, also agreed with the clinical team).

Along with the successful replication of manual processing, the algorithm was also very efficient, with processing time of less than 20 seconds per AAA, which was a substantial improvement compared to the 15-30 minutes of the manual method, while being fully reproducible.

These findings suggest that the Replication algorithm could successfully replace the manual processing in a reliable and reproducible manner, at a fraction of the currently required time. Additionally, this algorithm has the potential to be applicable to datasets that have been obtained with alternative scanning protocols or are derived from different trials and scanners.

5.7.2 Advanced Hotspot Analysis: The Evolution algorithms

5.7.2.1 Evolution 2D algorithm

The method followed in the manual processing and the Replication algorithm introduced some restrictions to the detection and analysis of hotspots, by imposing a universal 71% threshold on the %ΔT_2* maps, ignoring any USPIO-

uptake area of less than 10 pixels and discarding hotspots which were in contact only with the inner layers of the aortic wall rather than the outer layer (due to a lack of visualisation of the wall thickness in the manual process that I was replicating). Another issue was the lack of any more specific quantification methods to "qualify" the hotspots in terms of dimensions (hotspot "metrics"), other than the manual count of pixels per hotspot, which was not routinely recorded by the clinical observers. My hope was that additional metrics which could be made available using an automated analysis methodology could allow for the hotspots to be further assessed and sub-classified.

The Evolution 2D algorithm was therefore developed to tackle these issues and expand on the previous hotspot analysis. It did not apply a threshold to the %ΔT_2* maps, but instead used an adjusted k-means clustering technique for hotspot detection which adapted to every AAA case individually. This allowed me to potentially use all of the data available which reflected total USPIO distribution within these datasets, rather than restricting to thresholded data. More "subtle" or variable USPIO distribution information could therefore be incorporated into my analysis. This algorithm also incorporated smaller hotspots (>=8 pixels) and employed a more advanced periluminal-exclusion technique than the one used in the Replication algorithm. Crucially, this algorithm also identified hotspots adjacent to the inner layers of the aortic wall, aside from the ones in contact only with the outer layers. One of the key features of inflammation in relation to AAA wall stress that the clinical team valued highly was the presence of inflammation in the aortic wall. More accurately determining whether USPIO uptake was present in the full thickness of the aortic wall was therefore a key step forward for my algorithm. The aortic wall thickness was demonstrated to be highly variable in the study performed in Edinburgh in this population and the manual processing employed by the clinical was not able to take this into account.

Furthermore, with a large number of variables in the algorithm being adjustable, it can be applied to varying datasets/applications, or facilitate the investigation of the effects of different factors to the data being studied, in an automatic, efficient and reproducible way.

The Evolution 2D algorithm introduced additional hotspot metrics which were not employed in the previous manual processes, which could describe hotspot size, intensity and shape, and also the relative position of the hotspot within the AAA and its distance from the lumen area. These were all requests that came from the clinical team who performed the pilot study. A better understanding of USPIO uptake (and therefore inflammation) distribution throughout these aneurysms is highly desirable. Inflammation has been highlighted as an important pathological factor in AAA (provide some references here back from your introductory chapters, and the pilot and MA3RS papers). A more definitive description of the nature and distribution of inflammation within the aneurysms. These metrics may have some merit in the further stratification of AAA patient groups and potentially assist in the prediction of AAA growth and rupture (which will be explored in Chapter 5).

When applied to a MA^{3}RS subset (sample size n=173), twenty additional hotspots to the manually selected ones were identified. These included cases of: hotspots which had previously been too small because of the 71% intensity threshold or the 10-pixel threshold; hotspots that had appeared to be distinct from the aortic wall, but without the 71% threshold were expanding into the wall, hotspots of lower mean intensity (which could be further assessed with the metrics); hotspots formed as a composite of smaller areas when the lack of thresholding allowed "bridges" to interconnect them; and finally accidentally omitted hotspots. Importantly, this algorithm contributed to the effective distinction of hotspots which were found among diffuse USPIO uptake and were too challenging to segment manually. Lastly, separate application of the algorithm to

detect hotspots which were adjacent to the inner aortic wall layers introduced five extra hotspots.

5.7.2.2 Evolution 3D algorithm

The Evolution 2D algorithm introduced many improvements and additional insights to the previous hotspot detection techniques. It was however still confined to using only 2-dimensional techniques, while the MRI datasets of the MA³RS study, with their improved image quality over the pilot dataset and implementation of contiguous slices, offered more 3D information. The clinical MA³RS evaluation was developed using the pilot data methodology, and so was not designed to take into account 3D information, however the clinical team acknowledged that this was potentially useful information on the distribution of USPIO within the aneurysm.

The Evolution 3D algorithm was therefore developed as an expansion of the 2D version to incorporate additional 3D information available and offer better insights and opportunities for further AAA classifications. Using 3D connectivity to identify areas of high USPIO uptake that expanded beyond one slice to adjacent slices, this algorithm detected hotspots in three dimensions for the first time, allowing an assessment of hotspot volume. As with the 2D version, the Evolution 3D algorithm could be adapted for different datasets and scanning protocols using aa number of user-defined variables, with the ability to re-process multiple datasets rapidly.

Application of the 3D algorithm to the MA³RS subset (sample n=173) previously processed with the Evolution 2D algorithm, identified a total of 43 AAAs containing hotspots which spanned multiple slices (3D hotspots) when thresholded %ΔT$_2$* maps (71% threshold) were used, and 49 AAAs when non-thresholded data were used. As expected, these results were fundamentally

different than the outcomes of the 2D algorithms, since they described USPIO uptake in different ways. Some of the most representative ways in which the application of the Evolution 3D algorithm differed in detecting hotspots, were: high-USPIO areas previously considered too small per slice were identified as parts of larger 3D hotspots spanning more than one slice; candidate 2D hotspots that had appeared to be distinct from the aortic wall in one slice and dismissed, belonged to 3D hotspots which were in contact with the wall on another slice level; many individual 2D hotspots within an AAA were found to be part of one larger single 3D hotspot spanning multiple slices.

Importantly, 3D hotspot detection can potentially assist with complex cases of inflammation at the thinnest part of the thrombus which are challenging to segment. As the thrombus has been shown to potentially play a protective role for the AAA by decreasing wall stress [63], [80], [81], these areas can be extremely important, as they may be more prone to rupture. In cases of uncertainty over a slice, the automatically detected presence or absence of USPIO uptake on adjacent slices may have some potential in acting as guidance to the clinical observer.

Furthermore, the 3D processing may help differentiate between "diffuse" USPIO uptake and actual hotspots, by checking if the USPIO uptake is only present in small isolated areas in each slice, or expanding vertically to adjacent slices forming long, thin 3D hotspots.

Finally, the 3D hotspot metrics of size, shape and position produced by the Evolution 3D algorithm, may assist in AAA assessment if used as potential classifiers. If hotspot "size" is in fact a valuable descriptor of USPIO uptake, then volume of hotspot across slices, rather than area within a single slice is obviously an important factor to take into account.

5.7.2.3 GUI

As the detection of hotspots required the input of many datasets in parallel, a GUI for efficient data assessment and data visualisation was created. After the development of the algorithms presented in this chapter, the GUI was further improved and upgraded to incorporate the Evolution 2D algorithm. It proved useful in allowing rapid combinations of data assessment and visualisation options in hotspot detection.

5.7.2.4 ROI issues

A problem encountered by the automatic hotspot detection algorithms was ROI accuracy. All three algorithms included a pre-processing stage which successfully corrected small-scale inaccuracies, namely accidental marking of pixels as ROI and accidental omission of ROI pixels. However, in more complex cases, where the assessment of ROIs required anatomical information, human input was required, as was evident in the case of erroneous inclusion of the duodenum in the AAA.

Automating the ROI segmentation would potentially help prevent such problems, but it was outwith the scope of this thesis. Members of our research group have been working on this problem in parallel to the work presented in this thesis, and their algorithms could potentially be combined with this work in the future. AAA segmentation has proven challenging, particularly accurate segmentation of the aortic wall thickness, which can be highly variable across patients.

5.8   Summary

In this chapter, the detection of inflammatory hotspots in AAAs was investigated in depth. Three algorithms were developed:

1. The automatic Replication algorithm, which can successfully replace the previously employed manual hotspot detection, with faster, reliable and fully reproducible methods.
2. The Evolution 2D algorithm, which took hotspot detection a step further by using non-thresholded data and introducing hotspot metrics.
3. The Evolution 3D algorithm, which expanded on the 2D version by incorporating 3D information and identifying 3D distribution of hotspots for the first time, supplemented with useful visualisations and 3D hotspot metrics.

The Evolution 2D algorithm was subsequently incorporated into a data assessment and visualisation GUI, to provide clinical observers with a complete and useful tool for better AAA analysis.

The novel information and insights extracted from these algorithms may be useful classifiers for further AAA analysis and stratification. The effect of these newfound hotspot metrics on AAA growth will be explored in Chapter 5.

Chapter 6   Prediction of AAA Expansion

This chapter builds upon the work presented in the previous chapters to investigate prediction of AAA growth rate. The results from Chapter 3 on AAA measurement techniques using different modalities were applied here in order to calculate AAA size and AAA expansion rates. The classification of AAAs based on 2D and 3D hotspot detection, derived from the algorithms developed and presented in Chapter 4 (Hotspot detection) were used here to evaluate influence of detected USPIO uptake on AAA growth rate. Additionally, a number of anatomical metrics derived during the automatic processing of these datasets, for additional AAA stratification, are described and evaluated as potential AAA growth rate predictors. Finally, a multiple linear regression model for the prediction of AAA expansion rate is suggested as a starting point for further investigation using these methods with larger sample sizes in the future.

6.1   Introduction

One of the main goals of numerous imaging studies of AAAs is the identification of an accurate method to predict AAA expansion and rupture. It has been suggested in several studies that aneurysm diameter, the current criterion for AAA management, is an inadequately imprecise predictor [118], [253], [254]. Given the urgent need for additional growth and rupture predictors [255], [256], I focused on developing additional variables which could be extracted from the MA³RS cohort dataset and be assessed for their potential predictive power. This research dataset featured several novel imaging parameters acquired in a large surveillance patient population, which could be tested alongside these patients' clinical assessments of aneurysm size and growth as assessed with ultrasound.

6.2   Methods

6.2.1 Output (dependent variable)

First, the most suitable measurement of AAA growth and rupture outcome to assess the predictive variables for the MA³RS trial had to be defined. At the time of the data processing for this chapter, the sample size available for AAA rupture or AAA-related deaths was too small (6 ruptures) to be used as an outcome. Therefore, only AAA growth rate could be used as the outcome to investigate predictors.

The results presented in chapter 3 strongly indicated that CT and MRI measurements for AAA growth were interchangeable and were more accurate and reproducible than ultrasound. The CT scans available at the time of the processing of this chapter had not been segmented, so MRI-derived growth variables were used. Specifically, the max area metric was used to measure AAA growth rate, as it had been found to be more accurate than max AP diameter in chapter 3 section 3.5.4.

Therefore, only MA³RS subjects for which yearly growth from MRI could be estimated were selected; namely individuals who had a baseline MRI scan and a 1-year or 2-year follow-up MRI scan were included in this analysis, amounting to a sample of 79 patients.

The AAA growth rate (of max area) was calculated as shown in Equation 6.1.

$$AAA\ Growth\ rate = \frac{Change\ in\ \max area\ from\ baseline\ scan}{days\ from\ baseline\ to\ scan} * 365.25$$

Equation 6.1

The max area growth rate (mm²) variable corresponding to the 79-patient sample is presented in Table 6.1 and Figure 6.1.

Table 6.1: Basic statistics of Max Area Growth Rate (mm²).

Max Area Growth Rate		
N	Valid	79
	Missing	0
Mean		254.1
Median		226.1
Std. Deviation		200.3
Range		1022.5
Minimum		-87.3
Maximum		935.2
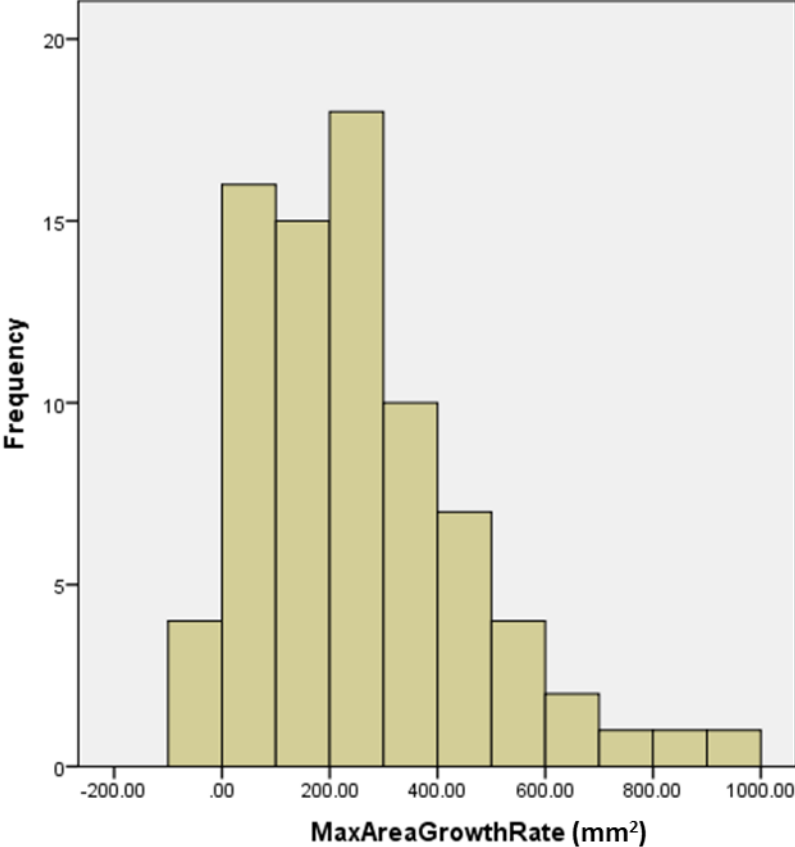
Figure 6.1: Histogram of max area growth rate (mm²) as measured with MRI.

6.2.2 Multiple Linear Regression Predictors

6.2.2.1 Available variables

Predictors of AAA rupture previously hypothesised and/or investigated by other groups were described in the Introduction chapter (1.1.3-1.1.6).

From those, the variables that had been acquired during baseline assessment of the patients and were examined in this chapter are:

Continuous variables (descriptive statistics in Table 6.2)**:**

- Diastolic blood pressure (in mmHg)
- Body Mass Index (BMI)

Categorical variables (frequencies in Table 6.3 and Figure 6.2)**:**

- Gender (male/female)
- Smoking (current/previous/never)
- Diabetes (positive/negative)
- Family history of AAA (positive/negative)

Table 6.2: Descriptive statistics of available continuous variables.

	N	Minimum	Maximum	Mean	Std. Deviation
BMI	79	19.2	36.3	27.3	3.4
BPdiast	79	62.0	118.0	80.8	10.2

Table 6.3: Frequencies of available categorical variables. For Gender: 0= female, 1=male; for Smoking: 0 = current smoker, 1=previous smoker, 2=never smoker; for Diabetes: 0=negative, 1=positive; for Family History of AAA: 0=negative, 1=positive; n=79 patients. These variables were collected during patient assessment at baseline.

	Gender	Smoking	Diabetes	Family History of AAA

		Freq.	Percent	Freq.	Percent	Freq.	Percent	Freq.	Percent
Valid	0	8	10.1	23	29.1	65	82.3	67	84.8
	1	71	89.9	45	57.0	14	17.7	12	15.2
	2	-	-	11	13.9	-	-	-	-
	Total	79	100.0	79	100.0	79	100.0	79	100.0
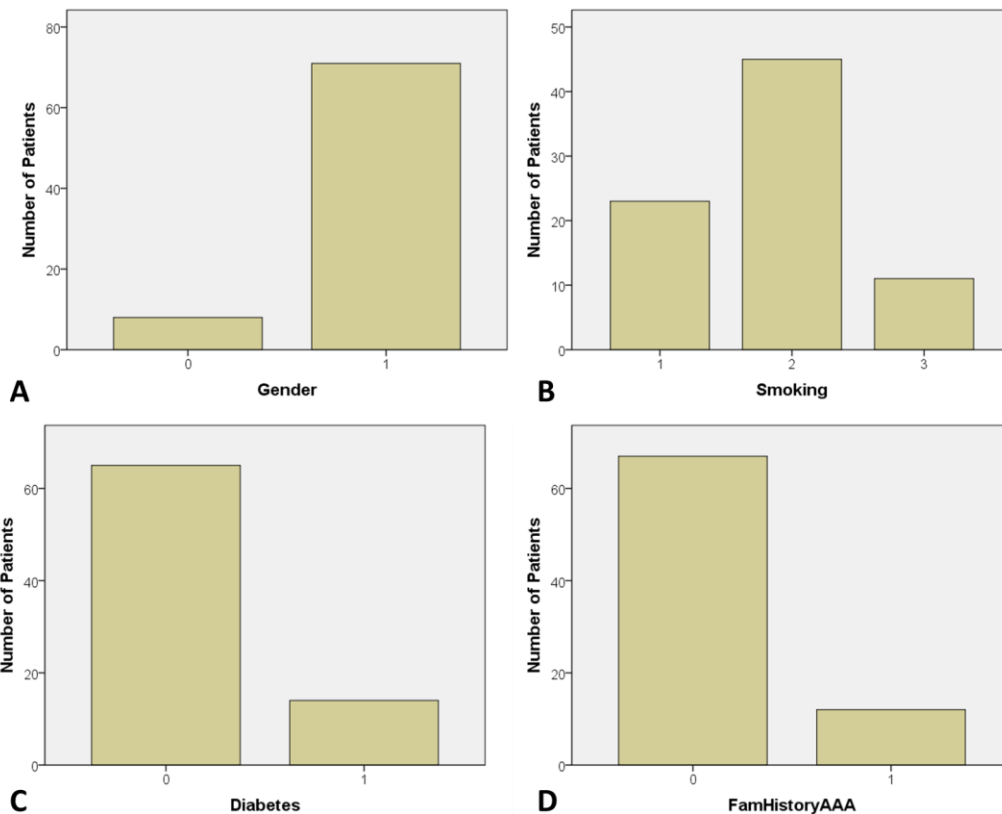
Figure 6.2: Frequencies of categorical variables. A) *Gender: 0= female (8 cases); 1=male (71 cases).* *B)* *Smoking: 0 = current smoker (23 cases), 1=previous smoker (45 cases), 2=never smoker (11 cases).* *C)* *Diabetes: 0=negative (65 cases), 1=positive (14 cases).* *D)* *Family History of AAA: 0=negative (67 cases), 1=positive (12 cases); n=79 patients. These variables were collected during patient assessment at baseline.*

Additionally, from the automatic hotspot detection algorithms presented in chapter 4, the following classifications were investigated as potential predictors (categorical variables) and are further described in Table 6.4 and Figure 6.3:

- o 2D hotspots on non-thresholded data (positive/negative)
- o 2D hotspots on 71%-thresholded data (positive/negative)
- o 3D hotspots on non-thresholded data (positive/negative)
- o 3D hotspots on 71%-thresholded data (positive/negative)

Table 6.4: Frequencies of categorical variables corresponding to 2D and 3D hotspots as detected in sample with or without 71% threshold; n=79.

		Class2D_0		Class2D_71		Class3D_0		Class2D_71	
		Freq.	Percent	Freq.	Percent	Freq.	Percent	Freq.	Percent
Valid	0	32	40.5	40	50.6	59	74.7	60	75.9
	1	47	59.5	39	49.4	20	25.3	19	24.1
	Total	79	100.0	79	100.0	79	100.0	79	100.0

The application of the automatic 2D and 3D hotspot detection algorithms on the current sample revealed that the 71% threshold had more impact on the 2D classifications than in the 3D. As shown in Figure 6.3 A and B, 47 cases of USPIO-positive AAAs were identified in 2D data without threshold, while the number of USPIO-positive cases was decreased to 39 with the threshold applied. 3D classification (Figure 6.3 C and D) determined 20 cases of USPIO-positive AAAs in the non-thresholded data and only 1 less (19 cases) in thresholded data.
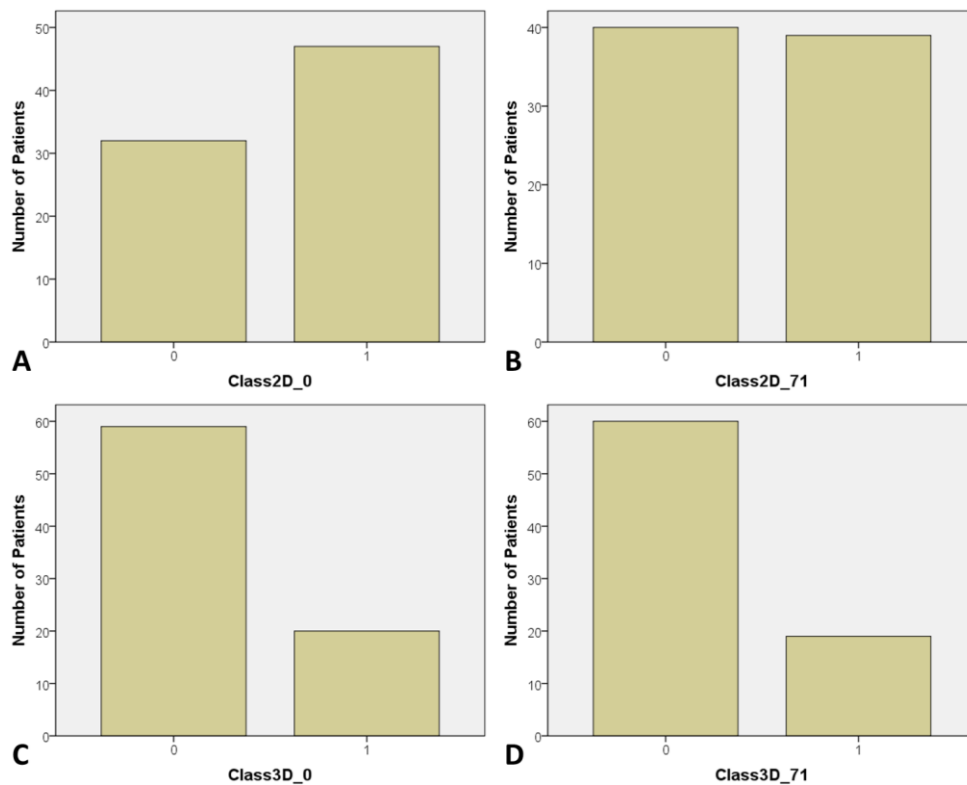
Figure 6.3: Frequencies of categorical variables. A) *2D Hotspots on 0% threshold: 0= negative (32 cases), 1=positive (47 cases).* ***B)*** *2D Hotspots on 71% threshold: 0= negative (40 cases), 1=positive (39 cases).* ***C)*** *3D Hotspots on 0% threshold: 0= negative (59 cases), 1=positive (20 cases).* ***D)*** *3D Hotspots on 71% threshold: 0= negative (60 cases), 1=positive (19 cases); n=79 patients. These variables have been produced with the automatic algorithms presented in chapter 4.*

Finally, a set of experimental anatomical AAA measurements were automatically extracted from the manually segmented MRI scans, using MATLAB's *regionprops* function.

The descriptions below have been adapted from [252]:

- **Size or Area (measured in pixels):** the number of pixels comprising the ROI.

- **Eccentricity:** This value corresponds to the eccentricity of the ellipse that has the same second-moments (or covariance matrix) as the ROI area. The eccentricity refers to the ratio of the distance between the foci of the ellipse and its major axis length. The range of the value is between 0 and

1, with 0 corresponding to the extreme case that the ellipse is a circle and 1 to the extreme case that the ellipse is a line.

- **Equivalent Diameter:** This value corresponds to the diameter that a circle with the same area as the ROI would have. It is estimated as $sqrt\left(4 * \frac{Area}{pi}\right)$.

- **Major/Minor Axis Length:** Given by the length (in pixels) of the major/minor axis of the ellipse that has the same normalised second central moments (or covariance matrix) as the ROI area.

- **Orientation:** Given by the angle between the x-axis and the major axis of the ellipse that has the same second-moments (or covariance matrix) as the ROI area. This value is presented in degrees, with a range between -90 to 90.

These metrics were calculated for every slice of each AAA, and separately per each region, for example the size for the lumen, thrombus and wall were calculated separately per slice. In this way, ratios between different regions of the AAA could be calculated, reflecting anatomical relationships between them, to be examined as predictors for AAA growth.

Average and maximum values were calculated for metrics of Eccentricity, Equivalent Diameter, Major Axis, Minor Axis and Orientation. The descriptive statistics for the average metric values calculated for this sample is presented in Table 6.5. and the descriptive statistics for the maximum metric values in Table 6.6.

Table 6.5: Descriptive Statistics of Mean values of automatically produced metrics.

	N	Minimum	Maximum	Mean	Std. Deviation
Lumen Mean Eccentricity	79	.29	.72	.51	.12
Lumen Mean EquivDiameter	79	18.2	45.3	32.5	6.0
Lumen Mean MajorAxis	79	21.5	48.0	36.0	6.1
Lumen Mean MinorAxis	79	15.8	44.4	29.9	6.2
Lumen Mean Orientation	79	-71.9	61.0	-9.8	28.5
Wall Mean Eccentricity	79	.24	.66	.41	.08
Wall Mean EquivDiameter	79	14.4	28.6	19.7	3.3
Wall Mean MajorAxis	79	51.7	114.6	67.2	9.8
Wall Mean MinorAxis	79	46.0	105.7	60.6	8.8
Wall Mean Orientation	79	-59.0	42.1	-7.1	24.0
Thrombus Mean Eccentricity	79	.23	.63	.40	.09
Thrombus Mean EquivDiameter	79	32.7	76.8	43.6	6.5
Thrombus Mean MajorAxis	79	35.0	81.0	46.0	6.8
Thrombus Mean MinorAxis	79	30.3	73.2	41.6	6.4
Thrombus Mean Orientation	79	-63.8	60.2	-5.5	29.3

Table 6.6: Descriptive Statistics of Max values of automatically produced metrics

	N	Minimum	Maximum	Mean	Std. Deviation
Lumen MaxEccentricity	79	.34	.89	.65	.14
Lumen MaxEquivDiameter	79	22.9	50.2	36.3	6.3
Lumen MaxMajorAxis	79	24.0	55.3	40.0	6.5

Lumen MaxMinorAxis	79	19.0	47.8	34.1	6.5
Lumen MaxOrientation	79	-61.24	89.28	44.4106	39.6
Wall MaxEccentricity	79	.35	.75	.55	.092
Wall MaxEquivDiameter	79	14.7	32.9	22.3	4.3
Wall MaxMajorAxis	79	57.1	125.0	73.6	11.2
Wall MaxMinorAxis	79	51.7	117.1	65.9	9.7
Wall MaxOrientation	79	-30.0	89.9	53.7	34.0
Thrombus MaxEccentricity	79	.32	.76	.54	.11
Thrombus MaxEquivDiameter	79	35.7	82.3	46.8	7.0
Thrombus MaxMajorAxis	79	37.0	86.4	49.9	7.8
Thrombus MaxMinorAxis	79	33.8	78.9	45.0	6.8
Thrombus MaxOrientation	79	-49.4	88.9	46.7	36.5

In Table 6.7, some cases where the ratios of the metrics corresponding to different ROIs per slice are shown. For example, for Mean WT pixels, it was calculated as: Mean (Wall size/Thrombus size). A more detailed formula is presented in 6.3.1.

Table 6.7: Descriptive Statistics for automatically produced metrics of Area (pixels) and Eccentricity ratios. *These metrics have been produced automatically with an algorithm applied on MRI data. N=79.*

	N	**Minimum**	**Maximum**	**Mean**	**Std. Deviation**
Mean WT pixels	79	.14	3.97	.81	.72
Mean WL pixels	79	.14	2.03	.44	.28
Mean TL pixels	79	.09	6.09	1.02	.94
Mean WT eccent	79	.66	2.15	1.13	.29
Mean WL eccent	79	.38	1.52	.86	.24
Mean TL eccent	79	.42	1.50	.85	.25

6.2.2.2 Limitations in Multiple Linear Regression

The variables described in 6.2.2.1 were tested with Multiple Linear regression (MLR) analysis in various combinations. Simultaneous examination of all the variables available with MLR analysis was not possible, as this would violate two statistical assumptions of MLR, multicollinearity and sample size.

The MLR assumption for multicollinearity states that no independent variables are highly correlated with each other. To meet this assumption, some variables could not be simultaneously included in the MLR model, e.g. MRI measurements of the baseline maxAP diameter had to be tested separately from max area measurements, as they were highly correlated. The Variance Inflation Factor (VIF) was used to quantitatively identify highly correlated variables in less obvious cases. The VIF creates an index which reflects the effects of collinearity on the variance of a predictor.

For the kth predictor of the multiple linear regression the VIF_k is:

$$VIF_k = \frac{1}{1 - R_k^2}$$

Equation 6.2

Where R_k^2 is the R^2-value obtained by regressing the kth predictor on the remaining predictors. A VIF of 1 can be interpreted as no correlation among the kth predictor and the rest of the predictor variables. Generally, values of $VIF > 4$ require further investigation, while values of $VIF > 10$ are indicative of severe multicollinearity problems.

Sample size also posed a challenge, as the available sample size determines the maximum number of predictors included in an MLR model to provide reliable estimates. To identify the maximum number of predictors for this sample, Green's formula 5.1 was used [257], [258]:

$$\min(sample\ size) = 50 + 8k, where\ k = number\ of\ predictors$$

Equation 6.3

According to this formula, 3 predictors would require a sample of at least 74 patients, while 4 predictors would require at least 82. For this sample of 79 patients therefore, MLR models with combinations of 3 predictors were primarily examined.

6.2.2.3 Statistical Methods

Multiple Linear Regression (MLR) analysis with SPSS version 22.0 (IBM Corp.) was used to examine whether AAA expansion could be significantly predicted by a combination of the available variables. A series of Stepwise and Enter method MLRs were used to identify the most significant combinations of predictors, in sets of 3.

6.3   Predictive Models

The three predictors which were initially identified as the most significant in predicting the yearly rate of max area growth were Diameter, Eccentricity WT and 3D Hotspots (non-thresholded data), as presented in 6.3.1. Two additional predictors were identified as significant, namely Family History of AAA and diastolic BP. Family History of AAA was added as a 4th predictor to create the 2nd model (6.3.2) and subsequently diastolic BP was added as a 5th predictor to build the 3rd model (6.3.3). However, it should be noted here that as the available sample is only 79 patients, and as highlighted in section 0, using a 4th and a 5th predictor does indeed "stretch" the MLR sample assumptions and may potentially be weakening the statistical "relevance" of the MLR models. The 2nd and 3rd model were therefore included for completeness and to suggest potential predictors that should be considered in the future for models with larger sample numbers.

6.3.1 First Model: 3 predictors

The dependent and independent variable of the first MLR model (created with "Enter" method) are described below.

Dependent Variable:

MaxAreaGrowthRate (mm² per year): Yearly growth rate of Maximum Area of AAA (calculated as average of 3 largest areas per AAA), measured with MRI.

Independent Variables:

1. **Diameter (mm):** Baseline maxAP diameter as measured with MRI
2. **3D Hotspots:** Binary (dichotomous) variable with value equal to 1 for subjects with at least one 3D hotspot detected (on 0%thresholded maps)

and 0 for subjects with no 3D hotspots (on 0%thresholded maps) detected.

Eccentricity WT: Mean (Wall eccentricity/Thrombus eccentricity) per slice ratio, measured with MRI:

$$\frac{1}{n} * \left(\frac{wall\ eccentricity_1}{thrombus\ eccentricity_1} + \frac{wall\ eccentricity_2}{thrombus\ eccentricity_2} + \cdots + \frac{wall\ eccentricity_n}{thrombus\ eccentricity_n} \right),$$

for n=number of slices per AAA.

> **Eccentricity:** A measure of how much a conic section deviates from being circular. Values ranging from 0 (circle) to 1 (highly elongated ellipse).

Table 6.8: Descriptive statistics of first MLR model

	Mean	Std. Deviation	N
MaxAreaGrowthRate (mm²/year)	254.11	200.30	79
Diameter (mm)	50.27	7. 58	79
Eccentricity WT	1.13	.29	79
3D Hotspots	.25	.44	79

For these, a modest but significant regression equation was found ($F_{(3,75)} = 5.643$, $p = .002$), with $R = .429$, $R^2 = .184$, $Adjusted\ R^2 = .152$ and Durbin-Watson = 2.206.
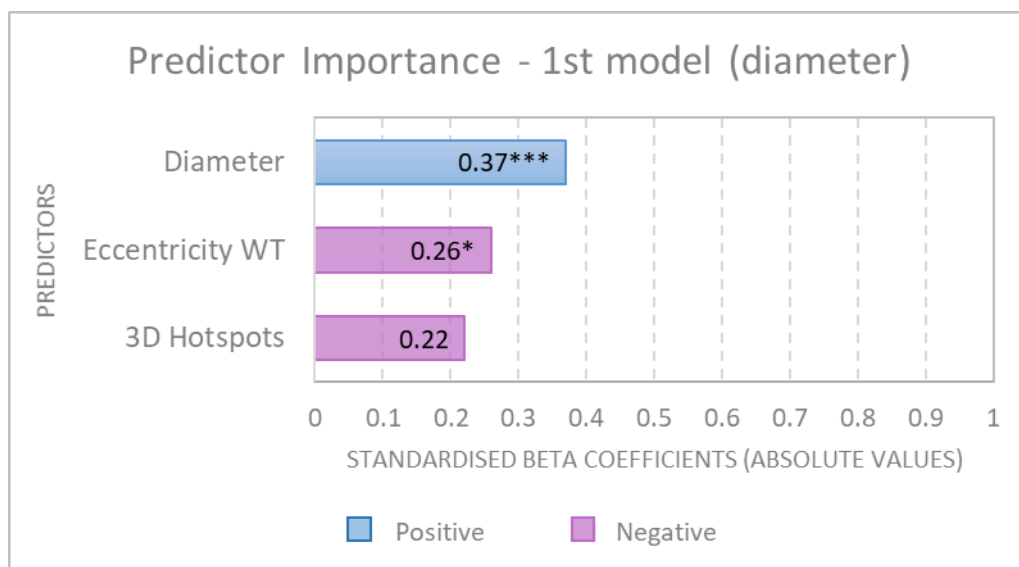
Figure 6.4: Predictor Importance of First Multiple Linear Model. *The absolute values corresponding to the standardised beta coefficients of each predictor are depicted on this graph for comparison, in descending order of "importance". The predictor depicted in blue (Diameter) with Beta=0.37 (p=0.001) is positive, while the predictors depicted in magenta (Eccentricity WT with Beta=-0.26 (p=0.16), 3D Hotspots with Beta=-0.22 (p=0.054)) are negative.*

The participants' predicted yearly max area growth is modelled by:

$$-6.167 + 9.747\,(Diameter) - 181.912\,(Eccentricity\ WT) - 98.383\,(3D\ Hotspots)$$

Collinearity was assessed for the three predictors, with $VIF(Diameter) = 1.113, VIF(Eccentricity\ WT) = 1.113\ and\ VIF(3D\ Hotspots) = 1.008.$

More detailed tables of the model are included in Appendix 2, section 2.1.1.

Following the development of the first MLR model and determining the high prediction level of the max AP diameter as measured with MRI, a series of potential alternatives to this were investigated to identify whether they would

predict growth rate with more accuracy. The results of the multi-collinearity analysis between the alternative variables, the max AP diameter and the max area growth rate are presented in maximum and average values for equivalent diameter, major axis and minor axis of the thrombus and the wall were investigated. The highest correlation was presented by the mean of the major axes of the thrombus (highlighted in Table 6.9).

The MLR model was also tested with the mean major axis of the thrombus instead of max AP diameter, as depicted in Figure 6.5

Table 6.9: Multicollinearity between alternatives to maxAP diameter and Max Area growth rate.

		MaxAP Diam	Wall (mean values)			Thrombus (mean values)			Wall (max values)			Thrombus (max values)		
			Equiv. Diam.	Major Axis	Minor Axis	Equiv. Diam.	Major Axis	Minor Axis	Equiv. Diam.	Major Axis	Minor Axis	Equiv. Diam.	Major Axis	Minor Axis
MaxAreaGrowthRate	Pearson Correlation	.288*	.042	.328**	.362**	.385**	.387**	.372**	-.055	.248*	.285*	.314**	.306**	.286*
	Sig. (2-tailed)	.010	.712	.003	.001	.000	.000	.001	.630	.027	.011	.005	.006	.011
	N	79	79	79	79	79	79	79	79	79	79	79	79	79

*. Correlation is significant at the 0.05 level (2-tailed).

**. Correlation is significant at the 0.01 level (2-tailed).

With the max AP diameter replaced with the thrombus major axis, an alternative, modest but significant regression equation was found ($F(3,75) = 8.482$, $p = .002$), with $R = .503$, $R^2 = .253$, $Adjusted\ R^2 = .223$ and Durbin-Watson = 2.295.
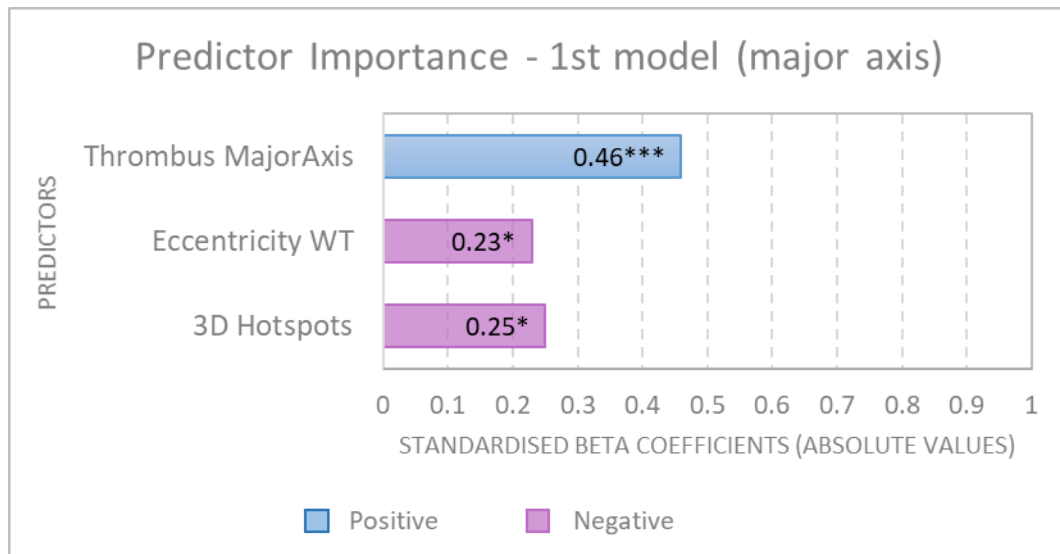
Figure 6.5: Predictor Importance of First Multiple Linear Model. *The absolute values corresponding to the standardised beta coefficients of each predictor are depicted on this graph for comparison, in descending order of "importance". The predictor depicted in blue (Thrombus major axis) with Beta=0.46 (p<0.001) is positive, while the predictors depicted in magenta (Eccentricity WT with Beta=-0.23 (p=0.023), 3D Hotspots with Beta=-0.25 (p=0.022)) are negative.*

The participants' predicted yearly max area growth is equal to:

$$-156.058 + 13.554\ (Thrombus\ major\ axis) - 163.513\ (Eccentricity\ WT)$$
$$- 112.967\ (3D\ Hotspots)$$

Collinearity was assessed for the three predictors, with $VIF\ (Thrombus\ major\ axis) = 1.114, VIF\ (Eccentricity\ WT) = 1.002\ and\ VIF\ (3D\ Hotspots) = 1.117$.

More detailed tables of the model are included in Appendix 2, section 2.1.2.

6.3.2 Second Model: 4 predictors

The dependent and independent variable of the second MLR model (created with "Enter" method) are described below.

Dependent Variable: **MaxAreaGrowthRate (mm² per year)**

Independent Variables (first three same as first model):

1. **Diameter (mm)**
2. **3D Hotspots**
3. **Eccentricity WT**
4. **Family History AAA:** Binary (dichotomous) variable with value equal to 1 for subjects with positive Family History of AAA and 0 for negative.

Table 6.10: Descriptive statistics of second MLR model

	Mean	Std. Deviation	N
MaxAreaGrowthRate (mm²/year)	254.11	200.27	79
Diameter (mm)	50.27	7.58	79
Eccentricity WT	1.13	.29	79
3D Hotspots	.25	.44	79
FamHistoryAAA	.15	.36	79

With **Family History AAA** added to the MLR model as a 4th predictor, a modest but significant regression equation was found ($F\,(4,74) = 6.394,\ p < .000$), with $R = .507,\ R^2 = .257,\ Adjusted\ R^2 = .217$ and Durbin-Watson = 2.151
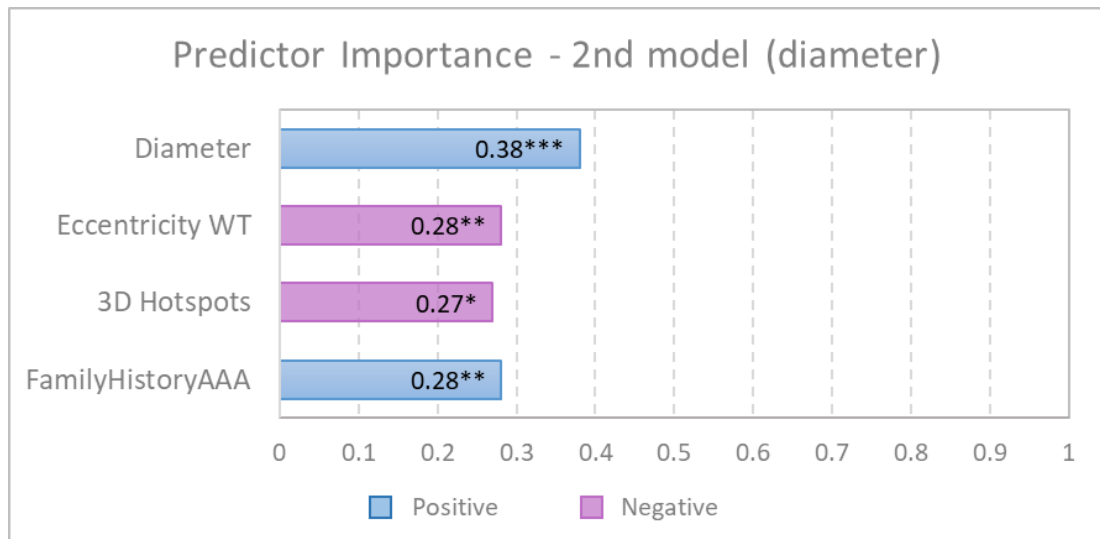
Figure 6.6: Predictor Importance of Second Multiple Linear Model. *The absolute values corresponding to the standardised beta coefficients of each predictor are depicted on this graph for comparison, in descending order of "importance". The predictors depicted in blue (Diameter with Beta=0.38 (p=0.001), Family History of AAA with Beta=0.28 (p=0.009)) are positive, while the predictors depicted in magenta (Eccentricity WT with Beta=-0.28 (p=0.007), 3D Hotspots with Beta=-0.27 (p=0.011)) are negative.*

Participants' predicted yearly max Area growth is equal to:

$$-14.945 + 9.994\,(Diameter) - 198.699\,(Eccentricity\,WT) - 130.927\,(3D\,Hotspots)$$
$$+ 154.651\,(FamilyHistoryAAA)$$

Collinearity was assessed for the three predictors, with $VIF(Diameter) = 1.114, VIF(Eccentricity\,WT) = 1.182\,and\,VIF(3D\,Hotspots) = 1.016, VIF(FamilyHistoryAAA) = 1.070$

More detailed tables of the model are included in Appendix 2, section 2.2.1.

With the thrombus major axis replacing the max AP diameter and the **Family History AAA** added to the MLR model as a 4th predictor, a significant regression equation was found ($F\,(4, 74) = 8.413,\,p < .000$), with $R = .559,\,R^2 = .313,\,Adjusted\,R^2 = .275$ and Durbin-Watson = 2.185
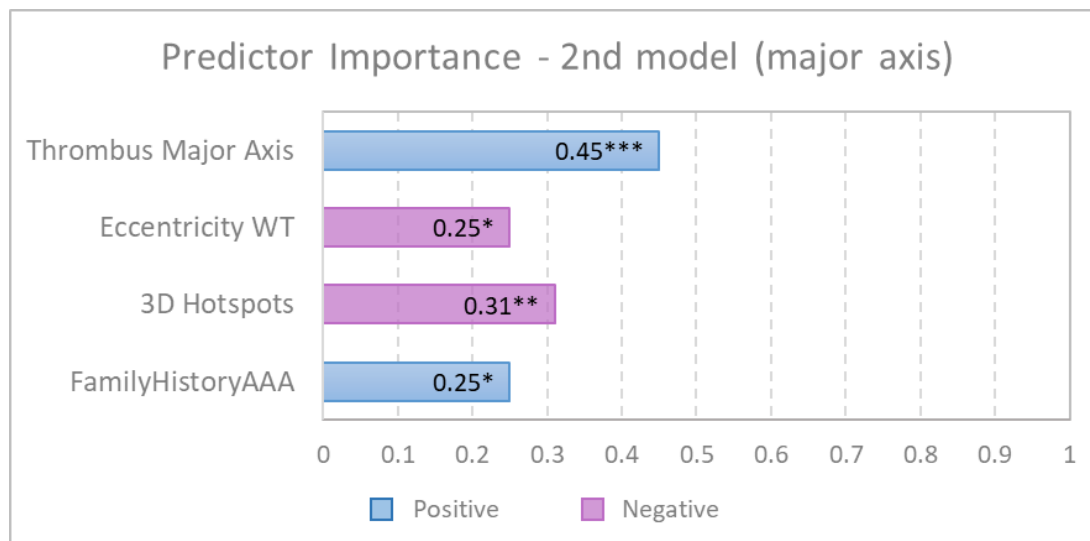
Figure 6.7: Predictor Importance of Second Multiple Linear Model. *The absolute values corresponding to the standardised beta coefficients of each predictor are depicted on this graph for comparison, in descending order of "importance". The predictors depicted in blue (Thrombus Major Axis Beta=0.45 (p<0.001), Family History of AAA with Beta=0.25 (p=0.014)) are positive, while the predictors depicted in magenta (Eccentricity WT with Beta=-0.25 (p=0.011), 3D Hotspots with Beta=-0.31 (p=0.005)) are negative.*

Participants' predicted yearly max Area growth is modelled by:

$$-142.238 + 13.301\,(Thrombus\ Major\ Axis) - 178.267\,(Eccentricity\ WT)$$
$$- 139.877\,(3D\ Hotspots) + 139.653\,(FamilyHistoryAAA)$$

Collinearity was assessed for the three predictors, with $VIF(Thrombus\ major\ axis) = 1.116, VIF(Eccentricity\ WT) = 1.010\ and\ VIF(3D\ Hotspots) = 1.175, VIF(FamilyHistoryAAA) = 1.070$

More detailed tables of the model are included in Appendix 2, section 2.2.2.

6.3.3 Third Model: 5 predictors

The dependent and independent variable of the third MLR model (created with "Enter" method) are described below.

Dependent Variable: **MaxAreaGrowthRate (mm² per year)**

Independent Variables:

1. **Diameter (mm)**
2. **3D Hotspots**
3. **Eccentricity WT**
4. **FamHistoryAAA**
5. **BPdiast (mmHg):** Diastolic Blood Pressure

Table 6.11: Descriptive Statistics of the third MLR model

	Mean	Std. Deviation	N
MaxAreaGrowthRate	254.11	200.27	79
Diameter (mm)	50.27	7.58	79
Eccentricity	1.13	.29	79
3D Hotspots	.25	.44	79
FamHistoryAAA	.15	.36	79

With **diastolic BP** added to the MLR model as a 5th predictor, an improved and significant regression equation was found ($F\ (5, 73)\ =\ 6.719,\ p\ <\ .000$), with $R = .561,\ R^2 = .315,\ Adjusted\ R^2 = .268$ and Durbin-Watson = 2.030
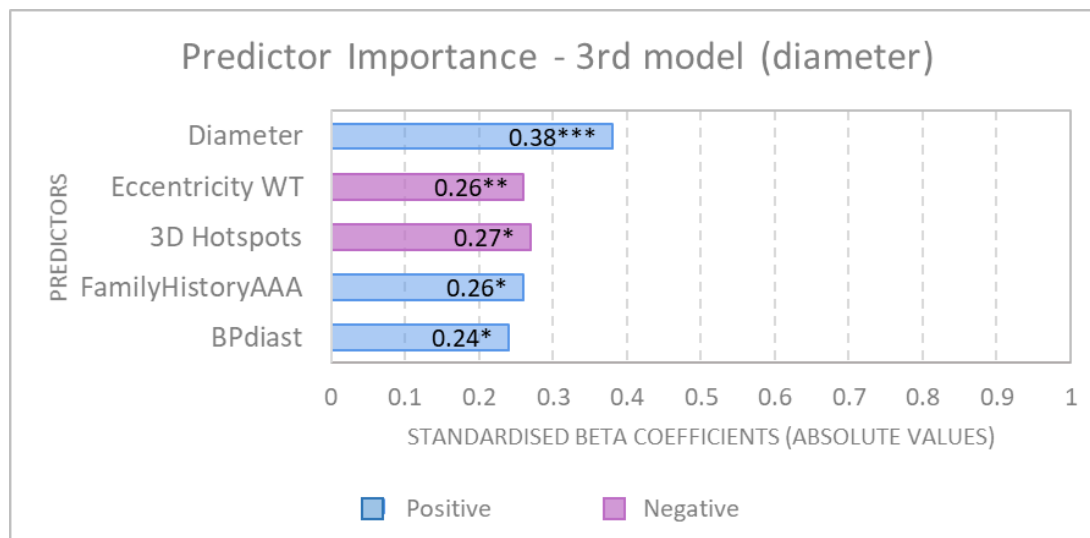
Figure 6.8: Predictor Importance of Third Multiple Linear Model. *The absolute values corresponding to the standardised beta coefficients of each predictor are depicted on this graph for comparison, in descending order of "importance". The predictors depicted in blue (Diameter with Beta=0.38 (p<0.001), Family History of AAA with Beta=0.26 (p=0.013), Diast.Blood Pressure with Beta=0.24 (p=0.015)) are positive, while the predictors depicted in magenta (3D Hotspots with Beta=-0.27 (p=0.013), Eccentricity WT with Beta=-0.26 (p=0.009),) are negative.*

Participants' predicted yearly max Area growth is modelled by:

$$-422.313 + 10.096 \, (Diameter) - 184.338 \, (Eccentricity \, WT)$$
$$- 122.378 \, (3D \, Hotspots) + 142.456 \, (FamilyHistoryAAA)$$
$$+ 4.776 \, (BPdiast)$$

Collinearity was assessed for the three predictors, with $VIF(Diameter) = 1.115$, $VIF(Eccentricity \, WT) = 1.188$, $VIF(3D \, Hotspots) = 1.023$, $VIF(FamilyHistoryAAA) = 1.079$, $VIF(BPdiast) = 1.017$

More detailed tables of the model are included in Appendix 2, section 2.3.1.

With the thrombus major axis replacing the max AP diameter and with **diastolic BP** added to the MLR model as a 5th predictor, an improved and significant

regression equation was found ($F(5,73) = 7.945$, $p < .000$), with $R = .594$, $R^2 = .352$, $Adjusted\ R^2 = .308$ and Durbin-Watson = 2.068
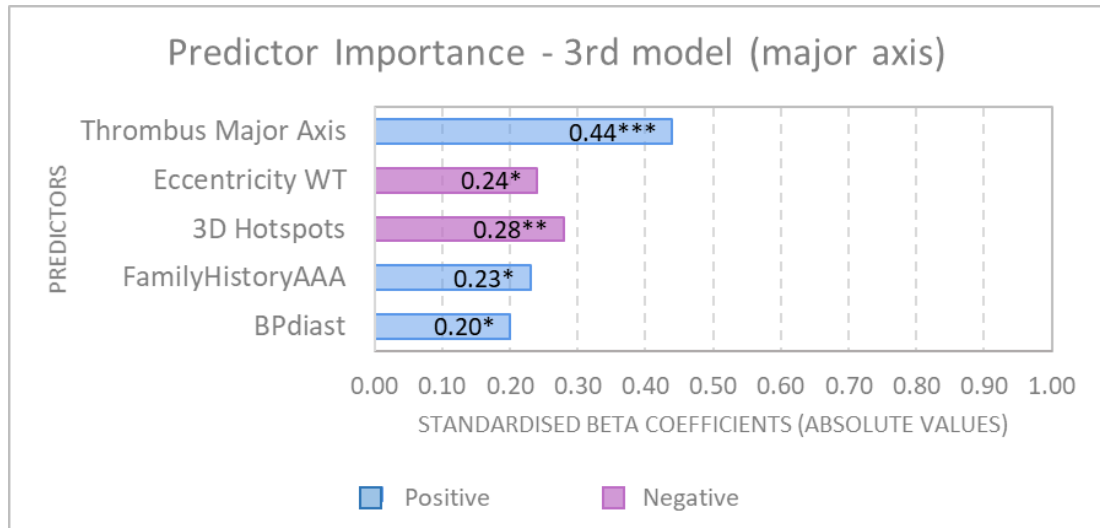
Figure 6.9: Predictor Importance of Third Multiple Linear Model. *The absolute values corresponding to the standardised beta coefficients of each predictor are depicted on this graph for comparison, in descending order of "importance". The predictors depicted in blue (Thrombus major axis with Beta=0.44 (p<0.001), Family History of AAA with Beta=0.23 (p=0.019), Diast.Blood Pressure with Beta=0.20 (p=0.038)) are positive, while the predictors depicted in magenta (3D Hotspots with Beta=-0.28 (p=0.007), Eccentricity WT with Beta=-0.24 (p=0.015),) are negative.*

Participants' predicted yearly max Area growth is modelled by:

$$-452.006 + 12.762\ (Thrombus\ Major\ Axis) - 166.244\ (Eccentricity\ WT)$$
$$- 129.690\ (3D\ Hotspots) + 129.817\ (FamilyHistoryAAA)$$
$$+ 3.961\ (BPdiast)$$

Collinearity was assessed for the three predictors, with $VIF(Thrombus\ major\ axis) = 1.124$, $VIF(Eccentricity\ WT) = 1.017$, $VIF(3D\ Hotspots) = 1.188$, $VIF(FamilyHistoryAAA) = 1.078$, $VIF(BPdiast) = 1.025$

More detailed tables of the model are included in Appendix 2, section 2.3.2.

6.4   Discussion

Among the collection of variables examined within the boundaries of MLR analysis of the sample at hand, the three most significant predictors of annual AAA growth rate were included in the first MLR model presented in this chapter. Those were Diameter, Eccentricity WT and 3D Hotspots.

As expected, the strongest predictor was found to be baseline size of the AAA. This finding is in agreement with the current AAA management practices by the NHS and supporting literature, as outlined in sections 1.1.3, 1.1.4 and 1.1.6.2. The size was initially included in the MLR models as max AP diameter, as the commonly used metric in current practice, and was found to be significant. However, further investigation into alternative size metrics revealed that the average size of the thrombus per AAA, noted here as Thrombus major axis (calculated as the mean of the major axes of all slices) predicted annual area growth more accurately than max AP diameter. The reason that the thrombus major axis appears to be a more accurate predictor may be due to the fact that as a multi-slice metric it provides a more comprehensive representation of the whole volume of the AAA, rather than focusing on one slice, as max AP diameter does. Furthermore, this metric does not include the wall ROI, which has been shown (see section 4.7.2.4) to be more error-prone during manual segmentation; it may thus include more accurate segmentations which provide more representative baseline sizes.

The second most significant predictor detected was **Eccentricity WT**, which represents an anatomical feature of the AAA by expressing the mean of the per-slice ratios of wall eccentricity over thrombus eccentricity. It was found to be a negative predictor in the AAA growth rate model. This suggests that in cases of

increasingly elliptically-shaped walls compared to the corresponding thrombi, the AAA growth rate would be lower.

To visually assist with the interpretation of this finding, two hypothetical cases were illustrated in Figure 6.10. Case A is a case where the wall (blue) closely approaches the value zero and thus the shape of a circle, while the thrombus (green) approaches the value one and thus the shape of an ellipse with a high degree of ovalness. According to the MLR, this would result in the WT variable most predictive of the highest AAA growth rate. Case B is a case where the wall closely approaches the value one and thus the shape of an ellipse, while the thrombus approaches the value zero and thus the shape of a circle. This case would contribute to a prediction of the lowest AAA growth rate.

In terms of AAA morphology, this finding could be pointing towards a delicate balance between the different levels of pressure imposed to the wall by the thrombus depending on the shape of each. The changes in the wall's shape may also be influenced by the environment surrounding the AAA (e.g. whether it expands towards rigid organs) and on the elasticity level on the wall [259]. No information about the size or shape of the lumen was incorporated in this metric.
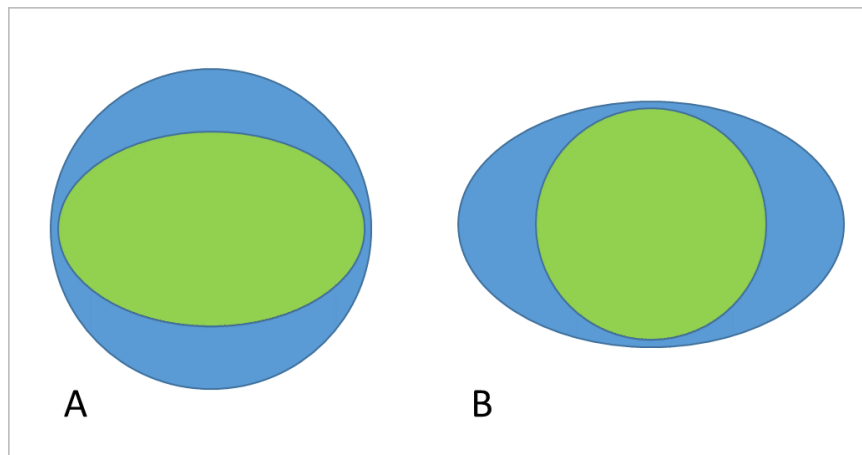
Figure 6.10: Two illustrations of the hypothetical extreme cases of the mean wall eccentricity over thrombus eccentricity ratio. *The wall is depicted in blue and the thrombus in green colour. In **A,** the ratio approaches its minimum value, with wall eccentricity close to value zero and thus close to circular shape and thrombus eccentricity close to value one and thus close to elliptical shape with high degree of ovalness. In **B**, the reverse is seen, with the ratio approaching its maximum value, with wall eccentricity close to value one and thus close to elliptical shape and thrombus eccentricity close to value zero and thus close to circular shape.*

The histogram of the Eccentricity WT values in Figure 6.11 demonstrates that the majority of AAAs are concentrated near value 1, therefore most AAAs have walls and thrombi that tend to have a shape of similar eccentricity. The cases of AAAs closer to the beginning of the axes correspond to faster growing rates. As the distance from the beginning of the axes increases, the AAA growth rate decreases.
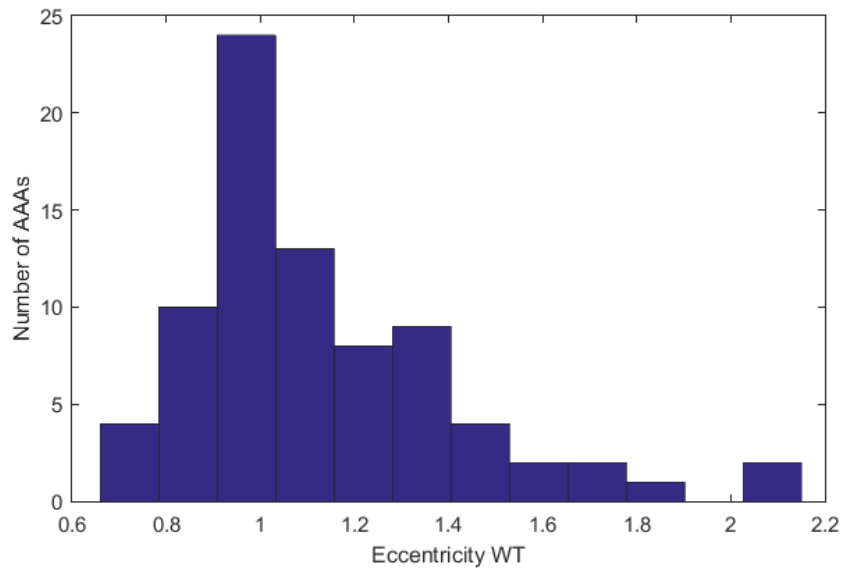
Figure 6.11: Histogram of Eccentricity WT values of all AAAs included in the MLR model (n=79).

Eccentricity of the lumen has previously been suggested as potentially [260] influential when combined with other parameters in exerting pressure load on the wall, but to my knowledge this is the first time that the ratio of eccentricities of wall and thrombus has been used and found to predict AAA growth rate. This anatomical measurement merits investigation in more depth and if possible with larger samples.

The third most significant predictor was **3D hotspots**, as detected on non-thresholded ΔT_2^* maps. Three more classifications of hotspots had been examined: 2D hotspots detected on non-thresholded data, 2D hotspots detected on 71%-thresholded data, and 3D hotspots detected on 71%-thresholded data, but none of these were found to have significant predictive power. Contrary to the expectations arising from the pilot study (see section 1.4) and the background described in section 1.3.2, the effect of the presence of 3D hotspots on the AAA growth rate was found to be negative.

As this finding was not consistent for 2D hotspots from previous analysis, the physiological differences between the presence of 2D and 3D hotspots, or the manner in which they are detected might describe different processes present in a range of AAA's. 3D hotspots (derived from non-thresholded data) represent comparatively narrow (per slice) but elongated (to adjacent slices), complicated inter-connected shapes which often span over large areas/many slices and often expanding to reach the aortic wall. This presentation may be consistent with the previous described network of channels within the thrombus described in [24], which were found to be of adequate size as to allow cellular passage. Histologic evaluation of these channels had suggested that they may be functioning as a delivery system for cells and macromolecules to the aortic wall of the AAA. In the original pilot study [15], USPIO uptake was classified into three groups, negative for hotspots, positive for hotspots, and a third group which demonstrated a "diffuse" presence of USPIO throughout the aneurysm in the thresholded data. It is possible that the 3D connectivity stage of the 3D hotspot detection is sensitive to the presence of this interconnected network of vascular supply throughout the aneurysm and that the presence of 3D hotspot parameter is in fact weighted towards the previously described diffuse uptake group of the pilot study. In the paper by Richards et al, this group demonstrated the same growth rate as the USPIO negative group. If the 3D hotspots are therefore sensitive to USPIO trapped within this vascular network system, it could be inferred that USPIO detected in this case is via blood flow. In this case, if blood could travel through this channel system, it may be assisting in the delivery of oxygen to the aortic wall, and thus actually decreasing its degradation process and expansion rate, as originally evidenced by the lack of increased growth rate in the pilot study diffuse uptake group. This hypothesis should be further investigated with larger sample sizes and more detailed morphological analysis of the 3D hotspots, which could be conducted with the application of the 3D hotspot metrics introduced in chapter 5.

Family history of AAA and **diastolic blood pressure** were identified as fourth and fifth significant predictor respectively, in agreement with the literature as presented in section 1.1.3 of the introduction chapter.

Predictors previously suggested in the literature, namely **smoking, sex, diabetes (negative predictor), and BMI** were also checked, but none of them was found to be a significant predictor of AAA expansion rate. This could be affected by the fact that MRI measurements were used to measure growth rate as output in the analysis presented in this chapter, while the majority of studies suggesting the aforementioned predictors (see sections 1.1.3 and 1.1.4) used ultrasound for output measurement. Whist MRI appears from the material presented in this thesis to be a more reliable assessment of AAA size, the ultrasound studies which suggest demographic factors such as smoking, sex etc. to be significant predictors are generally in very large scale epidemiological studies in AAA populations where MRI growth rate is, as yet, an untested outcome.

6.5   Summary

In this chapter, MLR analysis was employed to investigate possible predictive powers of the variables extracted from the MA³RS datasets. The relatively smaller sample size for which MRI growth rate outcome was available allowed for three significant predictors to be reliably identified, which were size (as either max baseline diameter or thrombus major axis), an anatomical metric (Eccentricity of mean wall/thrombus ratio) and the presence of 3D hotspots.

The role of baseline size as a predictor was expected and well- documented in the literature, but a novel way of calculating it was presented, namely the average thrombus major axis, which accounted for the entire volume of each AAA, instead of focusing on one slice.

Furthermore, this chapter introduced the eccentricity predictor which compared wall and thrombus shape and has not been used before; this introduces a new path to be explored in AAA growth rate prediction analysis, perhaps in combination with wall shear stress analysis.

An unexpected negative relationship between the presence of 3D hotspots and AAA expansion rates was detected and should be further investigated, potentially considering the possibility that 3D hotspots detected with my algorithms might not correspond to inflammation, but rather to vascular transport of USPIOs within inter-connected networks of capillaries throughout the AAA.

The MLR models also identified family history of AAA and high diastolic blood pressure as significant predictors of AAA growth rate, but these two findings should be further verified with larger sample sizes, as the sample available was not sufficient for reliably defining more than 3 predictors in the MLR models.

Chapter 7   Conclusion and Perspectives

The current clinical standard of care for patients with abdominal aortic aneurysms is to monitor the cross-section diameter of the aneurysm using ultrasound imaging. Despite this surveillance program, a significant number of aneurysms below the diameter threshold for intervention will rupture whilst patients are under surveillance (see chapter 1). Several approaches to better understand aneurysm progression have been attempted, pathophysiological, biomechanical, and molecular in nature. However, the prediction of aneurysm expansion and rupture remains a challenge (see sections 1.1.3, 1.1.4).

Previously, a pilot study undertaken in Edinburgh [15] described a novel application of MR imaging of AAA's using ultrasmall superparamagnetic iron oxide particles to track macrophages to site of inflammation in the aneurysms, inflammation having been previously identified as a key biological process occurring in tissue samples obtained from ruptured aneurysms [97], [102], [103]. More recently the MA^{3}RS trial, which started in parallel with the work described in this PhD thesis, expanded this pilot study in a larger multi-centre cohort of AAA patients under surveillance, attempting to determine whether USPIO-MRI could be a useful tool to investigate AAA development and the role of inflammation in its growth and potentially aid in rupture prediction in "at-risk" aneurysms. The image processing methods employed in these studies for the segmentation of images, and subsequent detection of inflammatory "hotspots" and AAA classification were performed manually. This is exceptionally time-consuming, involving appropriately qualified and experience clinical observers making repeated manual classifications of the aneurysms. The detection of "hotspots" of USPIO uptake in the aneurysms was based on application of a thresholding technique, determined from reproducibility data of repeated imaging with and without USPIO application. It was felt by the clinical team that whilst this

threshold manual approach was reliable to the degree that any USPIO uptake observed was reliable in terms of being above this threshold, that the threshold methodology was perhaps too restrictive and risked potentially discarding useful information about the full range of USPIO distribution within the aneurysm. Therefore, subtle information about inflammation within the aneurysms may have been neglected. The clinical team were also very keen to determine whether areas of inflammation could be observed to extend along the length of the aneurysm which was not possible using the 2D manual threshold methodology used (see section 1.5.2). The work presented in this thesis aimed to enhanced and adapt the image analysis pipeline to a) automate and therefore speed up detection of USPIO hotspots of inflammation within the aneurysms, b) determine whether an approach could be developed which was able to detect the presence of hotspot of inflammation from non-thresholded data, and finally c) to determine whether methods could be developed to detect the extent to which hotspots of inflammation extended along the length of the aneurysm. This work was performed in parallel to the MA³RS study with the clinical team working on MA³RS, to expand on the established methodology and complement the MA³RS study analysis.

Firstly, the existing methods for determining AAA size and expansion rate were assessed. The work presented in chapter 3 demonstrates that ultrasound tends to under-measure AAA diameter in comparison to both MRI and CT modalities, while MRI can be used essentially interchangeably with CT, which is currently used as a gold standard for surgical planning imaging in the AAA population where intervention is required. Furthermore, the use of the maximum Anterior-Posterior diameter for AAA measurements was shown to introduce a degree of variability, particularly for growth measurements. This was true to some extent for all modalities and was particularly present in the ultrasound data. An alternative and more reproducible measurement metric was suggested for growth calculations, namely maximum area, derived from MRI.

Automation of the manual analysis process for hotspot detection was also achieved, making it more reproducible and less prone to operator error as presented in chapter 4. The automatic processing was considerably faster and reached excellent levels of "agreement" with the manual process, also detecting inflammatory "hotspots" that the clinical team agreed they had missed upon subsequent review.

Further to the replication of the manual processing, and in a bid to incorporate as much of the AAA USPIO uptake data as was available, several methods for hotspot detection were evaluated and a k-means clustering approach adopted (chapter 4). Working with the clinical team, the clustering detection of hotspots was evolved to deal with problematic cases and introduce rules and exceptions to the initial clustering approach until a reliable replacement to the manual process was achieved (See section 4.3.11-4.4.4). As well as an automatic analysis of non-thresholded data, analysis of distribution of USPIO across multiple slices was introduced (see section 4.5-4.6), as well as novel visualisation of USPIO uptake throughout the AAA volume with 3D models. The lack of thresholding and the use of a clustering technique that adapted to each specific dataset, as well as the presence of a number of adjustable variables within the 2D and 3D automated algorithms developed make this process more easily applicable to datasets obtained with alternative acquisition protocols, or on different scanners, and crucially does not reduce reliability by removing user-derived thresholds of significance to USPIO uptake. Additionally, supplementary AAA and hotspot metrics were automatically derived from the MRI datasets in both the 2D and 3D algorithms developed which may have some potential in assisting further AAA stratification. The algorithms developed and presented in chapter 4 were incorporated into a GUI which may be used by clinicians to access the automatic algorithms, but also to assess and visualise datasets. This MATLAB-based GUI was used to assess performance of the algorithms and aid in their refinement.

This tool can be easily adapted for further algorithm development or the requirements of the clinical team for further evaluation.

In the last part of this thesis presented in chapter 5, the hotspot detection and metrics that were derived from my algorithms were applied in a subset of 79 patients from the MA³RS population, for which outcome could be calculated from MRI data in terms of growth rate over 12-24 months. The classifications derived from the automatic hotspot detections and the metrics were combined with size measurements acquired during baseline assessment of the patients, to investigate whether any of the derived parameters from my algorithms exhibited any potential in the prediction of annual AAA growth rate. Multiple linear regression models were investigated for this 79-patient cohort. This sample size allowed for the reliable identification of three significant predictors as presented in chapter 6: size, eccentricity and the presence of 3D hotspots. The "average thrombus major axis" was introduced as a novel size metric and it was shown to predict annual AAA growth more successfully than the maximum AP diameter, as it was representative of larger proportion of the AAA volume, rather than deriving the measurement from only a single 2D slice.

The "eccentricity" predictor was also introduced as a novel morphological metric describing the relationship between thrombus shape and wall shape and possibly representative of the effects of shear wall stress on AAA growth.

Contrary to expectations regarding the influence of focal USPIO uptake on AAA expansion, the MLR models developed identified a negative relationship between 3D hotspots and expansion rate. I hypothesise that these hotspots may be corresponding to transported USPIO within inter-connected vascular channels that have previously been hypothesised in previous work and the pilot imaging study here in Edinburgh [15] to allow cells to reach the aortic wall and supply it with necessary nutrients. If the 3D USPIO detection developed in this thesis is in fact sensitive to the presence of this vascular network, it has been previously

suggested that aneurysms exhibiting this vascular network may in fact be growing at a slower rate, hence the negative predictive value of this parameter with aneurysm growth rate.

Family history of AAA and high diastolic blood pressure were also identified as significant predictors of AAA growth rate in line with previous literature in larger epidemiological studies. However, no more than 3 predictors could reliably be incorporated in the MLR models in this work due to the relatively small sample size used to assess the algorithm variables, which is a limitation of this work. Furthermore, T_2* mapping of USPIO uptake has been demonstrated in cardiovascular imaging in particular to be prone to image artefacts, particular "blooming" of signal dropout around presence of USPIO [15], [261], [262]. Therefore, further development of acquisition protocols is required to minimise image artefacts in these datasets. The Edinburgh group are currently helping to develop application of a positive contrast USPIO imaging sequence which will help to reduce image artefacts in these datasets. One further limitation to this work that became obvious during algorithm development was the reliance of the current methods on manual segmentation of the original anatomical data by clinical observers. This was an arduous and time-consuming task, and therefore prone to some degree of operator error, as evidenced by the segmentation errors, both accidental (extra pixels segmented or not segmented in datasets) and morphological (the duodenum incorporated in aneurysm segments). An obvious improvement to the analysis pipeline would be the automating of anatomical segmentation of the datasets. Whilst that was desirable, it was outside of the scope of the work presented in this thesis. Initially, attempts were made to automate AAA segmentation in parallel with the MA³RS trial and the work presented in this thesis. However, reliable automatic segmentation of the aortic wall proved very difficult to implement, and manual segmentation was instead adopted into the MA³RS trial. The USPIO-MRI methodology was further implemented in assessment of inflammation in the myocardium, following

infarct, coronary artery bypass and myocarditis [261]–[263]. Reliable automated segmentation of the myocardium proved much easier to implement and it would be interesting to apply the algorithms developed in this thesis to the automatically segmented myocardial USPIO-MRI datasets in further work. Unfortunately, there was not enough time to implement this, with the myocardial data only arriving towards the end of the work presented here.

The MLR findings presented in chapter 5 present several parameters which exhibit at least some potential in the enhanced description of AAA's which may be considered "at risk". To properly assess the methods presented in this thesis and their potential for monitoring AAA and aiding in growth rate and rupture prediction, further investigations should be made with larger sample sizes that would afford the inclusion of more potential predictors in the models and a more robust assessment of variable significance in predictive models.

Furthermore, the inclusion of larger cohorts would potentially allow for sub-classifications of AAAs to be explored, for example with the use of the hotspot metrics introduced here to determine whether previously identified large diameter aneurysms could be labelled as "at risk" if they exhibited unusual characteristics. Additional hotspot metrics could also be relatively easily implemented using the data derived by the automated algorithms presented in this thesis. Hotspot volume, or numbers of hotspots present within an aneurysm could be derived and investigated as potential methods to sub-classify aneurysms. Unfortunately, there was no time to implement these in the work presented here.

Furthermore, more sources of AAA data could be incorporated into a multi-modality assessment of different aspects of aneurysm physiology, to enrich these investigations, including for example mechanical models of stress [3], [264], or information on appearance of calcification within AAAs as detected by positron emission tomography [255].

Finally, the algorithms developed in this thesis would benefit from an implementation in a lower-level programming language such as C++, which would make processing faster and would enable us to develop a stand-alone application which clinicians would be able to use. An executable file could be sent out to multiple sites for evaluation in hotspot detection, potentially in multiple clinical applications. This would help to obtain feedback and evolution of the algorithms for wider application in the detection of contrast uptake in medical imaging.

Appendix 1: Research Output

<u>The work described in this thesis has been presented in the following conferences</u>:

- "Automatic Classification and 3D Visualisation of Abdominal Aortic Aneurysms to Predict Aneurysm Expansion and Rupture", Conference Scientific Poster, International Society for Magnetic Resonance in Medicine Annual Meeting (ISMRM 2016), Singapore.
- "Automatic detection of inflammatory 'hotspots' in abdominal aortic aneurysms to identify patients at risk of aneurysm expansion and rupture", Oral Presentation and e-Poster in International Society for Magnetic Resonance in Medicine Annual Meeting (ISMRM 2015), Toronto, Canada
- Oral Presentation in European Society for Magnetic Resonance in Medicine and Biology (ESMRMB 2015) Congress, Edinburgh, UK
- Oral Presentation in ISMRM Workshop on "MRI Cell Tracking for Visualizing Cellular Therapeutics & Inflammation", La Jolla, CA, USA
- Oral Presentation and Traditional Poster in British Chapter of ISMRM Annual Scientific Meeting (2014), Edinburgh, UK

Scientific poster presentation, International Society for magnetic Resonance in Medicine Annual Meeting (ISMRM 2016) Singapore

Automatic Classification and 3D Visualisation of Abdominal Aortic Aneurysms to Predict Aneurysm Expansion and Rupture

Yolanda Georgia Koutraki[1,2], Rachael O. Forsythe[2], Olivia Mcbride[2], Chengjia Wang[1,3], Jennifer Robson[2], Tom J. MacGillivray[1], Calum D. Gray[1], David E. Newby[1,2] and Scott I. Semple[1,2]

[1] Clinical Research Imaging Centre, University of Edinburgh, Edinburgh, United Kingdom, [2] Centre for Cardiovascular Science, University of Edinburgh, Edinburgh, United Kingdom, [3] Toshiba Medical Visualization System-Europe, Edinburgh, United Kingdom

Introduction

Abdominal aortic aneurysms (AAA) are responsible for 1-3% of deaths in men aged 65 to 85 in the western world[1]. Currently decisions for AAA repairs are based on ultrasound measures of the aneurysm diameter (>5.5cm), which is an imperfect criterion since 60% of AAA>5.5 cm never rupture, while 10-20% of AAA< 5.5 cm do rupture[2,3]. Ruptured AAA cause 80%-90% mortality, so there is an imperative need for better methods to accurately predict AAA expansion and rupture.

Richards et al[4] demonstrated that uptake of Ultrasmall Superparamagnetic Particles of Iron Oxide (USPIO) in MRI identifies cellular inflammation, while differentiation in patterns of inflammation correlates with aneurysm growth-rate: AAA with distinct mural uptake of USPIO ("inflammatory hotspots") were found to expand significantly faster.

This processing of the data on a 2D slice-by-slice basis however is time-consuming and it uses an empirically-defined threshold which may exclude important information, while inter- and intra-observer variability are introduced by subsequent manual classification.

We previously suggested the use of a classification technique[6] which automatically detects hotspots of inflammation and classifies AAA.

We have now developed our algorithm to include 3D processing of the data. The inflammation throughout the whole volume of the AAA can be quantified and visualised for the first time; this enables us to begin sub-classification of the current groups and higher accuracy of growth prediction in our existing classification.

We are also incorporating anatomical measurements to further assist our classification with multivariate analysis.

Our algorithm is now included in a Graphical User Interface (GUI) and we have enabled batch processing to greatly reduce classification time.

Methods

350 patients were imaged using a 3-T MRI Verio (Siemens GmbH, Erlangen) before and 24+ hours after administration of USPIO (Rienso); sub-groups were randomly selected for our algorithm to be tested. A multi-echo, gradient-echo T_2*W sequence was used to produce T_2* maps to detect the accumulation of USPIO within the AAA. The percentage change in T_2* (%ΔT_2*) was calculated and displayed as a colour scale. The datasets were registered automatically using a previously described custom algorithm[5]. Our program was built in MATLAB-R2015a (Mathworks) and uses non-thresholded data. The periluminal area of the AAA is automatically masked. In order to detect 'hotspots' of USPIO uptake, an adapted k-means clustering (k=7) algorithm and 2D and 3D-connectivity are applied to the %ΔT_2* data. Metrics (e.g. lumen size and shape) are calculated using MATLAB and the 3D visualisations are created in MATLAB and Paraview (Kitware).

Results

In the subpopulation of 16 patients initially processed, classification of 12 out of 16 patients was in agreement between the automatic classification and the clinicians' manual classification (92% of hotspots agreed). However when we checked the outcome of the percentage US growth of the AAA at one year, the automatic classification was more predictive of growth than manual classification (Figure 1). This might be the result of using non-thresholded data in the automatic processing, so that the automatically detected 2D hotspots appear larger and therefore less potential hotspots are discarded (Figures 2, 3). We are now in the process of using the 3D-connectivity between hotspots of different slices and the metrics to subclassify the AAA according to hotspot size and shape. The total processing time with our program for each patient ranges between 70 to 95 seconds. The corresponding processing time by trained observers ranges between 45 to 65 minutes per patient per observer.

Discussion

Our automatic classification program appears to have a high success rate in reproducing the clinicians' manual classification, while introducing improvements to the process that increase aneurysm growth-rate prediction accuracy. This software may provide clinicians with more automated, robust and fast data processing and can effectively assist in the assessment of future AAA patients. By using non-thresholded data both in 2D and 3D, we obtain more reliable measurements of USPIO uptake, including areas missed in manual processing. The clustering technique used in our algorithm adapts to every individual patient, while the 71% threshold used in the manual processing is population-based. The processing time of the program is approximately 40 times faster than the manual processing, without taking into consideration the extra time needed for observer training. The results are fully reproducible removing inter-

and intra-observer variability. With the incorporation of anatomical metrics and 3D connectivity information we have the opportunity to investigate further sub-classifications within the AAA patients. Furthermore, these techniques can be adapted in the future to assist with the imaging of inflammation throughout the body in different clinical application, for example USPIO uptake targeting inflammation post myocardial infarction.
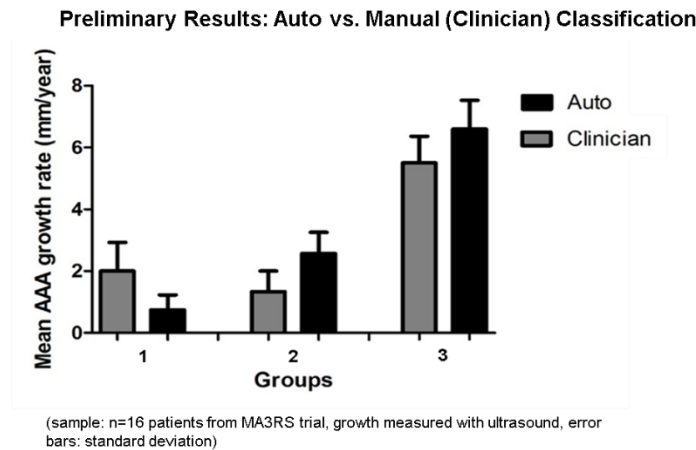
Figure 1: Mean AAA growth rate (mm/year) of AAAs as classified by clinicians (grey coloured bars and by automatic algorithm (black-coloured bars). Group 1 corresponds to AAAs with no mural or thrombus USPIO uptake, except for isolated periluminal T_2* enhancement, Group 2 corresponds to AAAs with diffuse USPIO uptake that was distinct from the periluminal thrombus and the aortic wall, and Group3 corresponds to AAAs presenting with "hotspots" of inflammation.
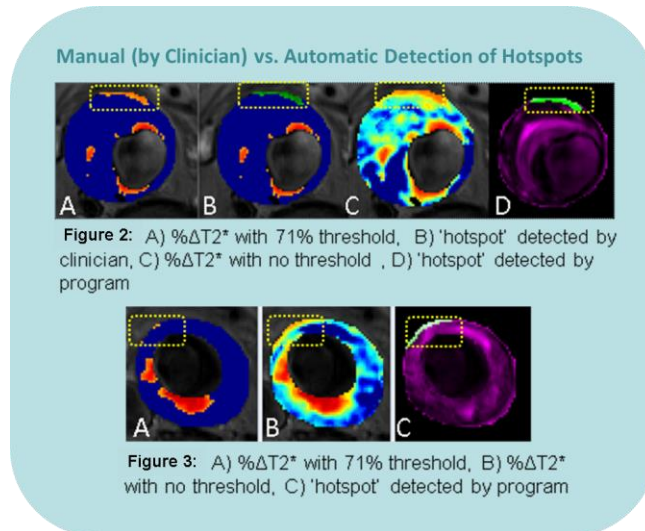
Figures 2 & 3: Comparison of manual (by trained observer) against automatic detection of inflammatory hotspots. The hotspots chosen by our automated process appear bigger on each slice and additional hotspots are detected, due to the absence of thresholding.
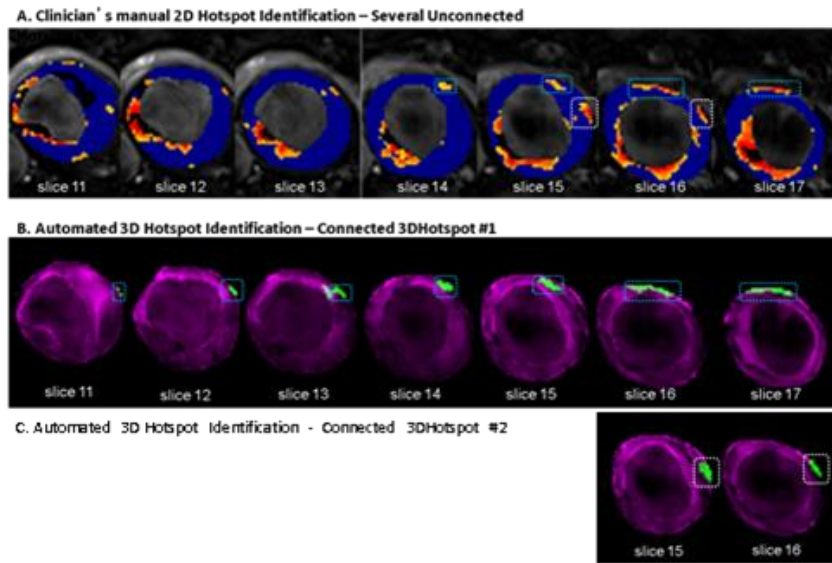
Figure 4: Automated 3D Hotspot Identification and 3D-connectivity *algorithms have been applied to the same difference map, with no threshold. The Hotspots identified by the clinician are now identified as 2 separate 3D Hotspots. The hotspots chosen by our automated process appear bigger on each slice, due to the absence of thresholding.*

References

1. Sakalihasan, N., R. Limet, and O.D. Defawe, *Lancet*, 2005.   **2.** Hardman, D., et al., International Journal for Numerical Methods in Biomedical Engineering, 2013. **3.** Scott, R.A.P., et al., European Journal of Vascular and Endovascular Surgery, 2001.
4. Richards, J.M.J., et al., 2011. **5**. Wang, et al., ISMRM annual meeting, 2014.
6. Y.G. Koutraki, et al., ISMRM annual meeting, 2015.

(Magna cum laude) Oral Presentation and e-poster, International Society for Magnetic resonance in medicine Annual meeting (ISMRM 2016), Toronto, Canada.

Automatic detection of inflammatory 'hotspots' in abdominal aortic aneurysms to identify patients at risk of aneurysm expansion and rupture

Yolanda Georgia Koutraki[1,2], Chengjia Wang[1,3], Jennifer Robson[2], Olivia Mcbride[2], Rachael O. Forsythe[2], Tom J. MacGillivray[1], Calum Gray[1], Keith Goatman[3], J. Camilleri-Brennan[2], David E. Newby[1,2] and Scott I. Semple[1,2]

[1] Clinical Research Imaging Centre, University of Edinburgh, Edinburgh, United Kingdom, [2] Centre for Cardiovascular Science, University of Edinburgh, Edinburgh, United Kingdom, [3] Toshiba Medical Visualization System-Europe, Edinburgh, United Kingdom

INTRODUCTION

Abdominal aortic aneurysms (AAA) are responsible for 1-3% of deaths in men between 65 and 85 years in the western world[1]. Repair of AAA is considered when the aneurysm diameter exceeds 5.5 cm as measured with ultrasound. However, diameter is an imperfect criterion since 60% of AAA >5.5 cm never rupture, while 10-20% of AAA < 5.5 cm do rupture[2,3]. Ruptured AAA cause 80%-90% mortality, so better criteria of AAA expansion and rupture are urgently required. Richards et al[4] in their pilot study, showed that uptake of Ultrasmall Superparamagnetic Particles of Iron Oxide (USPIO) in AAA identifies cellular inflammation and demonstrated that AAA with distinct mural uptake of USPIO (classified as group 3) have a 3-fold increase in aneurysm growth rate compared to AAA with no (group 1) or nonspecific (group 2) USPIO uptake. The classification of "inflammatory hotspots" to stratify patients into the 3 groups was performed manually by trained observers. This manual processing however is time consuming and introduces inter- and intra-observer variability. Due to the manual nature of this classification, the data were analysed on 2D slice-by-slice purely on the basis of presence or absence of hotspot. By automating this assessment, it is possible to assess inflammatory volume throughout the aneurysm which might provide a method to further sub-classify the group 3 patients and further optimise rupture prediction, based on hotspot size and distribution, rather than the manual "presence of hotspot" method alone. Furthermore, this pilot project is now being followed up in the MA3RS study of 350 AAA patients. Manual processing of this large dataset would be impractical so an automated method of AAA classification by hotspot detection is required. We suggest the use of a classification technique (programmed in-house in MATLAB R2013a, Mathworks) which can automatically detect hotspots of inflammation and consequently classify AAA in a robust and efficient way.

MATERIALS AND METHODS

350 patients with asymptomatic AAA >4.0 cm were recruited and imaged using a 3-T MRI Verio (Siemens, Germany) before and 24 to 36 hours after administration of USPIO. T_2-weighted imaging was acquired for anatomical data and a multi-echo, gradient-echo T_2*W sequence was used to produce T_2* maps to detect the accumulation of USPIO within the AAA. Regions or interest (ROI) for the lumen, thrombus and aortic wall were manually defined (SliceOmatic by TomoView) and automatic registration between datasets was applied[5]. The percentage change in T_2* value (%ΔT_2*) was calculated and displayed as a color scale. The AAAs were then assessed by trained clinicians to detect focal areas ('hotspots') of at least 10 contiguous voxels of USPIO uptake, within the aortic wall and distinct from the periluminal area. At this stage, a threshold of significance for %ΔT_2* of 71% was established for the manual classification (based on 95th centile of the %ΔT_2* of patients without USPIO). 12 patients classified as group 3 were selected to be processed with our technique for automatic classification. Our method does not use the 71% threshold introduced above, but it rather calculates the %ΔT_2* on non-thresholded data to potentially allow better assessment of total distribution of all USPIO within the aneurysm. Due to expected uptake of USPIO in the periluminal area (not corresponding to inflammation, but assumed to be passive transport and 'trapping' of USPIO in periluminal friable tissue[4]) in a significant number of AAA, it was deemed necessary to create a mask in order to exclude the lumen and the periluminal area. These areas had similar ranges of intensity; therefore were segmented together (with k-means clustering, k=4) and were included in a mask. The rest of the processing was applied to both masked and unmasked data, as each method appears to differentiate distributions of USPIO within the various geometries of AAA. In order to detect 'hotspots' of USPIO uptake, an adapted k-means clustering (k=7) algorithm was applied on the %ΔT_2* data (masked and unmasked). 2D connectivity was used to identify the 'hotspots' that consisted of at least 10 contiguous voxels and exclusion criteria were applied: the hotspots were rejected if they were in contact with the lumen and accepted only if they were within the aortic wall. The segmented hotspots are automatically saved in individual folders for each slice and the AAA can be automatically classified based on these findings.
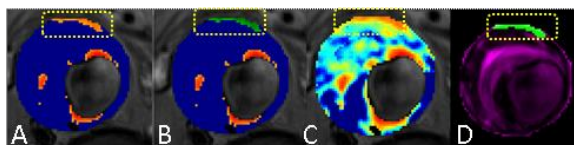
Figure 1: A) %$\Delta T2$* with 71% threshold, B) 'hotspot' detected by clinician, C) %$\Delta T2$* with no threshold , D) 'hotspot' detected by program
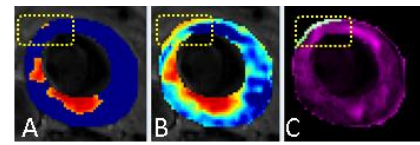
Figure 2: A) %$\Delta T2$* with 71% threshold, B) %$\Delta T2$* with no threshold, C) 'hotspot' detected by program

RESULTS

In the 12 patients from group 3 that were selected to process, the hotspots were identified by our program with a 92% agreement rate in individual hotspots (35 out of 38 hotspots detected) and 100% agreement in classification results (12 out of 12 patients classified as group 3). Importantly, because of the inclusion of non-thresholded data, the automatically detected hotspots appear to be larger (Figure 1). In addition, many extra hotspots were automatically detected and were later accepted as valid after assessment by the trained observers (Figure 2). The total processing time with our program for each patient ranged between 70 to 95 seconds. The corresponding processing time by the observers ranged between 45 to 65 minutes per patient per observer.

DISCUSSION/CONCLUSIONS

The automatic classification program appears to have a very high success rate in fully reproducing the clinicians' manual processing. This software may provide clinicians with more automated, robust and fast data processing and can effectively assist in the decision making process during the assessment of future AAA patients. By using non-thresholded data, extra 'hotspots' of USPIO uptake that were previously ignored by the observers can now be detected. Additionally the 'hotspots' in agreement with the clinicians appear to constitute larger areas. This happens partly due to the fact that the clustering technique adapts to every individual patient, while the 71% threshold used in the manual processing is universal. The processing time of the program is approximately 40 times faster than the manual processing, without taking into consideration the extra time needed for training the observers. The results are fully reproducible such that inter- and intra-observer variability are removed. Additionally, with the use of this tool we have the opportunity to investigate further sub-classification within group 3 of patients.

REFERENCES

1. Sakalihasan, N., R. Limet, and O.D. Defawe, *Lancet*. 2005: England. p. 1577-89.   **2.** Hardman, D., et al., International Journal for Numerical Methods in Biomedical Engineering. **29**(2): p. 165-178. **3.** Scott, R.A.P., et al., European Journal of Vascular and Endovascular Surgery, 2001. **21**(6): p. 535-540.
4. Richards, J.M.J., et al., 2011. **5**. Wang, et al., ISMRM annual meeting, 2014.

**Oral Presentation in European Society for Magnetic resonance in Medicine and Biology (ESMRMB 2015), Edinburgh, UK.**

INTRODUCTION

Abdominal aortic aneurysms (AAA) are responsible for 1-3% of deaths in men between 65 and 85 years in the western world[1]. Currently decisions for AAA repairs are based on ultrasound measures of the aneurysm diameter (>5.5cm) which is an imperfect criterion[2,3]. Richards et al[4], in their pilot study, showed that uptake of Ultrasmall Superparamagnetic Particles of Iron Oxide (USPIO) in MRI identifies cellular inflammation, and they demonstrated that differential USPIO uptake correlates with aneurysm growth-rate. The classification of patients in the pilot study was performed manually by trained observers. This processing of the data on 2D slice-by-slice however is time-consuming and it uses a user-defined threshold which may exclude important information, while inter- and intra-observer variability are also an issue.

We suggest the use of a classification technique which can automatically detect patterns of inflammation and classify AAA in a robust and efficient way.

SUBJECTS AND METHODS

350 patients had MRI scans before and after USPIO administration from which we have tested our algorithm on selected sub-populations. Regions of interest were manually defined and automatic registration between datasets was applied[5]. Our algorithm was built in MATLAB-R2013a(Mathworks), with automatic segmentations, special masks, k-means clustering and 2D- and 3D-connectivity applied on the percentage change in T_2* value (%ΔT_2*).

RESULTS

Our program has shown a 92% agreement rate in individual patterns selected by trained observers and 100% agreement in classification results in an initial group of 12 patients. Our method uses non-thresholded data and identifies more accurate inflammation patterns with a total processing time for each patient of 70-95 seconds. The corresponding manual processing time is over 70 minutes.

We are currently incorporating additional metrics (volumes within AAA, circularity, symmetry etc.) and using 3Dprocessing and visualisation of AAA in order to achieve further sub-classifications among the patients.

DISCUSSION

The automatic classification program appears to have a very high success rate in reproducing and developing the clinicians' manual processing. Our software provides faster, more automated and

fully reproducible processing which we are improving further by using 3D techniques. It is our aim to develop USPIO-MRI as an aneurysm rupture risk-stratification tool using this automated classification process.

REFERENCES

1. Sakalihasan, N., R. Limet, and O.D. Defawe, *Lancet*, 2005.   **2.** Hardman, D., et al., International Journal for Numerical Methods in Biomedical Engineering, 2013. **3.** Scott, R.A.P., et al., European Journal of Vascular and Endovascular Surgery, 2001.
4. Richards, J.M.J., et al., 2011. **5**. Wang, et al., ISMRM annual meeting, 2014.

Oral presentation in British Chapter of ISMRM Annual Scientific Meeting 2014 Edinburgh, UK

3D Visualisation of "Hotspots" of Inflammation in Abdominal Aortic Aneurysms (AAA): towards Automatic Classification

Georgia S. Koutraki[1,2], Chengjia Wang[1,3], Olivia Mcbride[2], Tom J. MacGillivray[1], Calum Gray[1], David E. Newby[1,2] and Scott I. Semple[1,2]

[1] Clinical Research Imaging Centre, University of Edinburgh, Edinburgh, United Kingdom, [2] Centre for Cardiovascular Science, University of Edinburgh, Edinburgh, United Kingdom, [3] Toshiba Medical Visualization System-Europe, Edinburgh, United Kingdom

Background

Abdominal Aortic Aneurysms (AAA) are responsible for 1-3% of deaths in men between 65 and 85 years in the western world[1]. Repair of AAA is considered when the diameter exceeds 5.5cm. However, diameter is an imperfect criterion since 60% of AAA > 5.5 cm never rupture, while 10-20% of AAA < 5.5 cm do rupture[2,3]. Ruptured AAA over 80%-90% mortality, so better criteria of AAA expansion and rupture are required. Richards et al[4] in their pilot study, showed that uptake of Ultrasmall Superparamagnetic Particles of Iron Oxide (USPIO) in AAAs identifies cellular inflammation and appears to distinguish those patients with more rapidly progressive AAA expansion.

In the MA3RS project, we are currently expanding on the pilot data with 350 patients involved. Since the manual data analysis was very time-consuming in the small pilot study, we are moving to automated analysis methods for the larger patient study currently being performed. Additionally, novel visualisation methods are being implemented and USPIO uptake (area of concentrated inflammation within the AAA, or 'Hotspot') is visualised in 3D for the first time.

Aims

- Implementation of software that will facilitate, automate and improve the visualisation (2D & 3D) and examination of AAA.
- Novel methods for the study of inflammatory induced R2* changes in AAA – Automated Hotspot identification and AAA classification.

Results

1. Automatic segmentation with k-means clustering

A. MRI data, k = 4

B. CT data, k = 3
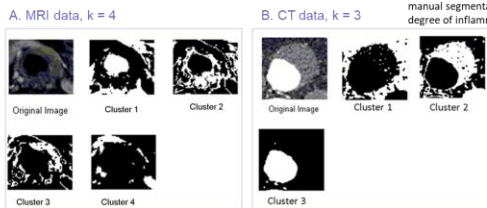
A. Automatic segmentation of MRI slice with k-means clustering algorithm, programmed in MATLAB R2013a. Different numbers of clusters were tested, k=4 appeared to be the best to facilitate MRI segmentation. In cluster 1 we can see how clearly the lumen is depicted, while in cluster 2 we can distinguish parts of the aortic wall. K-means can be applied more times on the same dataset to give more detailed results.

B. Automatic segmentation of CT slice with k-means clustering algorithm, programmed in MATLAB R2013a. K = 3 clusters were shown to be optimal for CT segmentation. The k-means algorithm appears to work more efficiently with CT rather than MRI data.

2. 3D-Connectivity

Slice 12

Slice 13
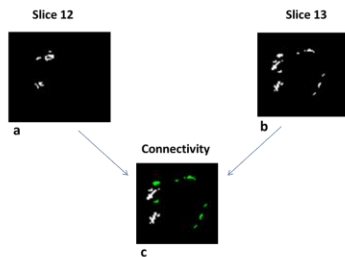
Connectivity

An algorithm checking for 3D connectivity is applied on all slices of each AAA (MATLAB). This allows us to identify whether previously manually defined 'separate' hotspots on individual 2D slices are actually part of a single larger larger hotspot in 3 dimensions.

In the above image, 3D (26 neighbours) connectivity between slice 12 (a) and slice 13 (b) is depicted. In (c) the 'common' or 'connected' voxels between the two slices are pictured in white and superimposed on the voxels of slice 13 (green).

3. Automated 3D Hotspot Identification

A. Clinician's manual 2D Hotspot Identification – Several Unconnected
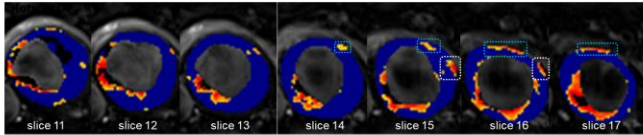
B. Automated 3D Hotspot Identification – Connected 3DHotspot #1
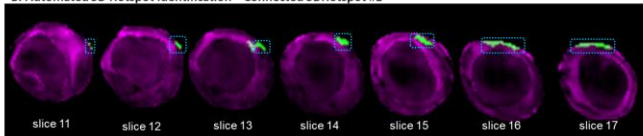
C. Automated 3D Hotspot Identification – Connected 3DHotspot #2

A. In image (A), the difference maps between Day1 and Day2 are depicted, reflecting USPIO uptake. A 65% threshold has been applied to the difference maps, thus eliminating differences smaller than 65%. The light blue area shows areas identified by the clinician as "Hotspots" according to the criteria of the pilot Study (10 contiguous voxels distinct from aortic lumen and adjacent to the aortic wall). Each slice is considered as a separate entity and no connection between Hotspots of contiguous slices is accounted for. The clinician has identified 1 Hotspot in slice14, 2 in slice15, 2 in slice16 and 1 in slice17.

B, C. Automated 3D Hotspot Identification and 3D connectivity algorithms have been applied on the same difference map but with no threshold. The Hotspots identified by the clinician are now identified as 2 separate 3D Hotspots: the first ranging from slice11 to slice17 and the second in slices 15 and 16. The Hotspots chosen by our automated process appear also bigger on each slice, because of the absence of thresholding. Furthermore, as can be seen in (B), areas smaller than 10 voxels that did not meet inclusion criteria during manual segmentation by the clinician are found to be connected with the larger hotspot, allowing more accurate categorisation of the degree of inflammation within the AAA.
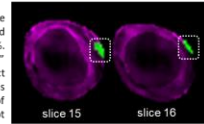
4. Novel 3D Visualisation of Hotspots (USPIO uptake)
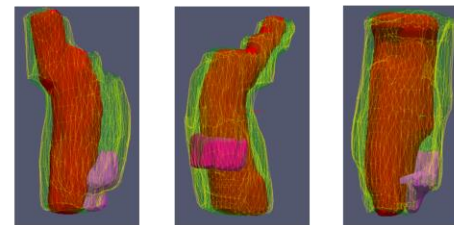
Novel 3D visualisation of Hotspots (areas with very high & concentrated USPIO uptake, denoting inflammation). The yellow wireframe corresponds to the aortic wall, the semi-trasparent green area to the thrombus, the red area to the lumen and the purple/magenta to the hotspot. AAA segmented manually on SliceOmatic software, 3D reconstruction using Analyze, MATLAB and Paraview.

Discussion

- Exploring the data in 3 dimensions allows better understanding of the distribution of USPIO hotspots (and therefore inflammation) in AAA. The application of 3D connectivity algorithms together with 3D visualisation enables us to better identify important characteristics of Hotspots: their size and shape, whether they are inter-connected, and their position within the AAA.
- The pilot study is currently being reproduced, and a direct comparison of manual and automatic segmentation will be presented.
- These visualisation and quantification techniques can provide clinicians with more automated, robust and fast data processing tool that can effectively assist in the decision making process during the assessment of future AAA patients.
- When fully implemented, this tool will be suitable for more general clinical application, both in AAA, and in other cardiovascular disease, such as post myocardial infarction.

References

1. Sakalihasan, N., R. Limet, and O.D. Defawe, *Abdominal aortic aneurysm*, in *Lancet*. 2005: England. p. 1577-89.
2. Hardman, D., et al., *Comparison of patient-specific inlet boundary conditions in the numerical modelling of blood flow in abdominal aortic aneurysm disease*. International Journal for Numerical Methods in Biomedical Engineering. 29(2): p. 165-178.
3. Scott, R.A.P., et al., *The Long-term Benefits of a Single Scan for Abdominal Aortic Aneurysm (AAA) at Age 65*. European Journal of Vascular and Endovascular Surgery, 2001. 21(6): p. 535-540.
4. Richards, J.M.J., et al., *Abdominal Aortic Aneurysm Growth Predicted by Uptake of Ultrasmall Superparamagnetic Particles of Iron Oxide*. 2011.

Appendix 2: Multiple Linear Regression Models

2.1   First Model: 3 predictors

2.1.1 Diameter

Multiple Linear Regression (3 predictors)

Descriptive Statistics

	Mean	Std. Deviation	N
MaxAreaGrowthRate	254.1073	200.27010	79
MRImaxAP	50.2691	7.57976	79
Class3D_0	.25	.438	79
MeanWTeccent	1.1257	.28505	79

Correlations

		MaxAreaGrowthRate	MRImaxAP	Class3D_0	MeanWTeccent
Pearson Correlation	MaxAreaGrowthRate	1.000	.288	-.087	-.228
	MRImaxAP	.288	1.000	.311	.054
	Class3D_0	-.087	.311	1.000	-.050
	MeanWTeccent	-.228	.054	-.050	1.000

Sig. (1-tailed)	MaxAreaGrowthRate	.	.005	.222	.021
	MRImaxAP	.005	.	.003	.318
	Class3D_0	.222	.003	.	.332
	MeanWTeccent	.021	.318	.332	.
N	MaxAreaGrowthRate	79	79	79	79
	MRImaxAP	79	79	79	79
	Class3D_0	79	79	79	79
	MeanWTeccent	79	79	79	79

Model Summary[b]

Model	R	R Square	Adjusted R Square	Std. Error of the Estimate	Durbin-Watson
1	.429[a]	.184	.152	184.47440	2.206

a. Predictors: (Constant), MeanWTeccent, Class3D_0, MRImaxAP

b. Dependent Variable: MaxAreaGrowthRate

ANOVA[a]

Model		Sum of Squares	df	Mean Square	F	Sig.
1	Regression	576122.614	3	192040.871	5.643	.002[b]
	Residual	2552310.284	75	34030.804		
	Total	3128432.897	78			

a. Dependent Variable: MaxAreaGrowthRate

b. Predictors: (Constant), MeanWTeccent, Class3D_0, MRImaxAP

Appendix 2: Multiple Linear Regression

Coefficients^a

Model		Unstandardized Coefficients		Standardized Coefficients	t	Sig.	Correlations			Collinearity Statistics	
		B	Std. Error	Beta			Zero-order	Partial	Part	Tolerance	VIF
1	(Constant)	-6.167	161.295		-.038	.970					
	MRImaxAP	9.747	2.907	.369	3.352	.001	.288	.361	.350	.898	1.113
	Class3D_0	-98.383	50.347	-.215	-1.954	.054	-.087	-.220	-.204	.899	1.113
	MeanWTeccent	-181.912	73.564	-.259	-2.473	.016	-.228	-.275	-.258	.992	1.008

a. Dependent Variable: MaxAreaGrowthRate

Residuals Statistics^a

	Minimum	Maximum	Mean	Std. Deviation	N
Predicted Value	-18.4611	596.5225	254.1073	85.94293	79
Residual	-374.54755	592.70245	.00000	180.89203	79
Std. Predicted Value	-3.172	3.984	.000	1.000	79
Std. Residual	-2.030	3.213	.000	.981	79

a. Dependent Variable: MaxAreaGrowthRate

Appendix 2: Multiple Linear Regression

Histogram

Dependent Variable: MaxAreaGrowthRate

Mean = 1.86E-16
Std. Dev. = 0.981
N = 79

Normal P-P Plot of Regression Standardized Residual

Dependent Variable: MaxAreaGrowthRate

Scatterplot

Dependent Variable: MaxAreaGrowthRate
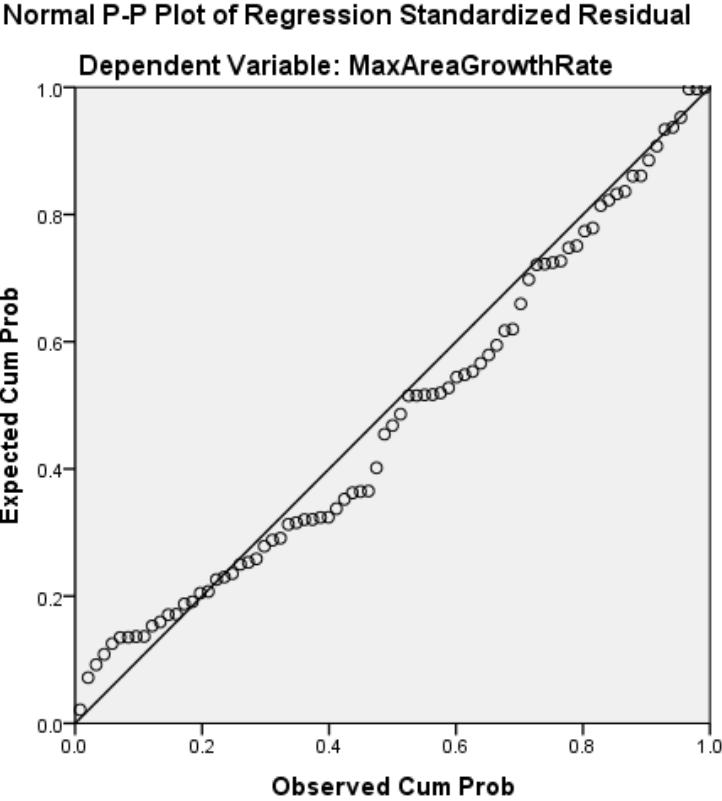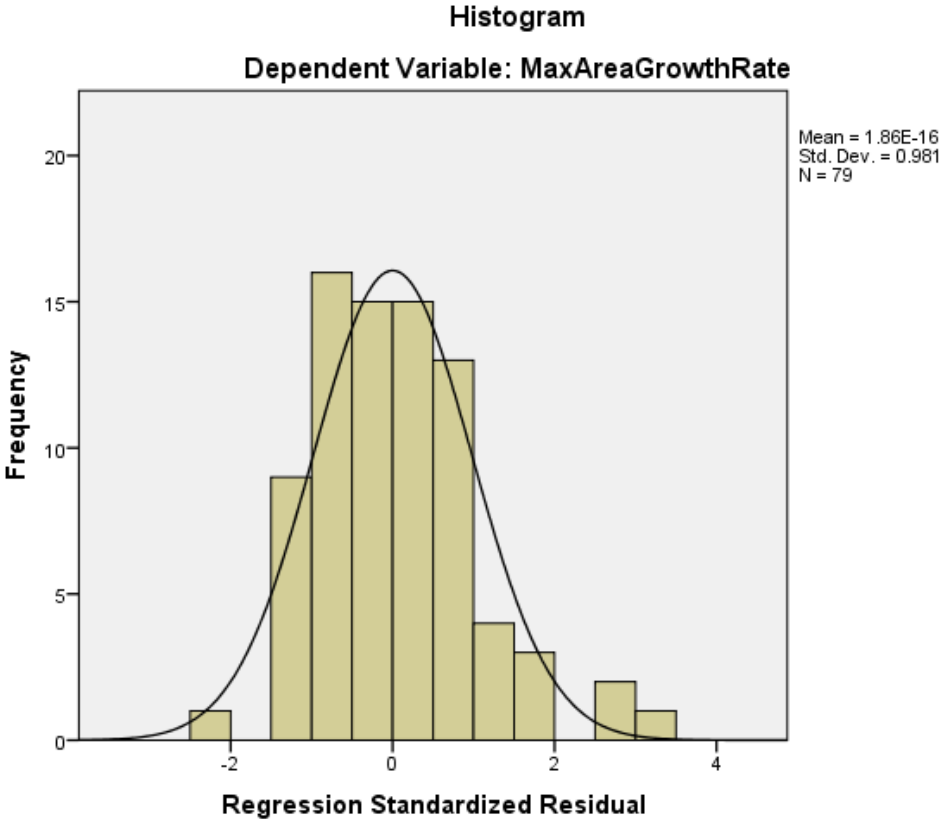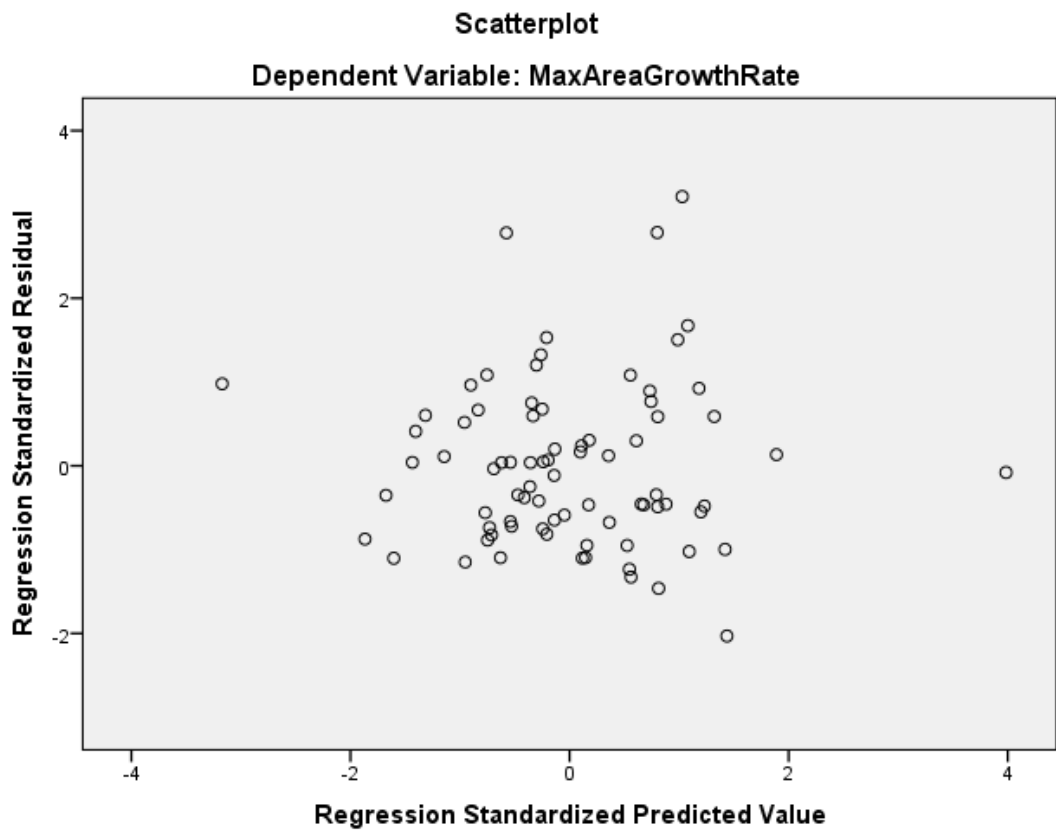
2.1.2 Mean thrombus major axis

Multiple Linear Regression (3 predictors)

Descriptive Statistics

	Mean	Std. Deviation	N
MaxAreaGrowthRate	254.1073	200.27010	79
thrMeanMajorAxis	45.9529	6.82428	79
MeanWTeccent	1.1257	.28505	79
Class3D_0	.25	.438	79

Correlations

		MaxAreaGrowthRate	thrMeanMajorAxis	MeanWTeccent	Class3D_0
Pearson Correlation	MaxAreaGrowthRate	1.000	.387	-.228	-.087
	thrMeanMajorAxis	.387	1.000	-.017	.320
	MeanWTeccent	-.228	-.017	1.000	-.050
	Class3D_0	-.087	.320	-.050	1.000
Sig. (1-tailed)	MaxAreaGrowthRate	.	.000	.021	.222
	thrMeanMajorAxis	.000	.	.441	.002
	MeanWTeccent	.021	.441	.	.332

	Class3D_0	.222	.002	.332	.
N	MaxAreaGrowthRate	79	79	79	79
	thrMeanMajorAxis	79	79	79	79
	MeanWTeccent	79	79	79	79
	Class3D_0	79	79	79	79

Model Summary[b]

Model	R	R Square	Adjusted R Square	Std. Error of the Estimate	Durbin-Watson
1	.503[a]	.253	.223	176.48132	2.295

a. Predictors: (Constant), Class3D_0, MeanWTeccent, thrMeanMajorAxis

b. Dependent Variable: MaxAreaGrowthRate

ANOVA[a]

Model		Sum of Squares	df	Mean Square	F	Sig.
1	Regression	792508.569	3	264169.523	8.482	.000[b]
	Residual	2335924.328	75	31145.658		
	Total	3128432.897	78			

a. Dependent Variable: MaxAreaGrowthRate

b. Predictors: (Constant), Class3D_0, MeanWTeccent, thrMeanMajorAxis

Coefficients^a

Model		Unstandardized Coefficients		Standardized Coefficients	t	Sig.	Correlations			Collinearity Statistics	
		B	Std. Error	Beta			Zero-order	Partial	Part	Tolerance	VIF
1	(Constant)	-156.058	161.145		-.968	.336					
	thrMeanMajorAxis	13.554	3.091	.462	4.385	.000	.387	.452	.438	.897	1.114
	MeanWTeccent	-163.513	70.188	-.233	-2.330	.023	-.228	-.260	-.232	.998	1.002
	Class3D_0	-112.967	48.256	-.247	-2.341	.022	-.087	-.261	-.234	.895	1.117

a. Dependent Variable: MaxAreaGrowthRate

Residuals Statistics^a

	Minimum	Maximum	Mean	Std. Deviation	N
Predicted Value	15.2245	682.3472	254.1073	100.79864	79
Residual	-333.96390	576.07855	.00000	173.05418	79
Std. Predicted Value	-2.370	4.248	.000	1.000	79
Std. Residual	-1.892	3.264	.000	.981	79

a. Dependent Variable: MaxAreaGrowthRate

Histogram

Dependent Variable: MaxAreaGrowthRate

Mean = -1.16E-15
Std. Dev. = 0.981
N = 79

Normal P-P Plot of Regression Standardized Residual

Dependent Variable: MaxAreaGrowthRate

Scatterplot

Dependent Variable: MaxAreaGrowthRate
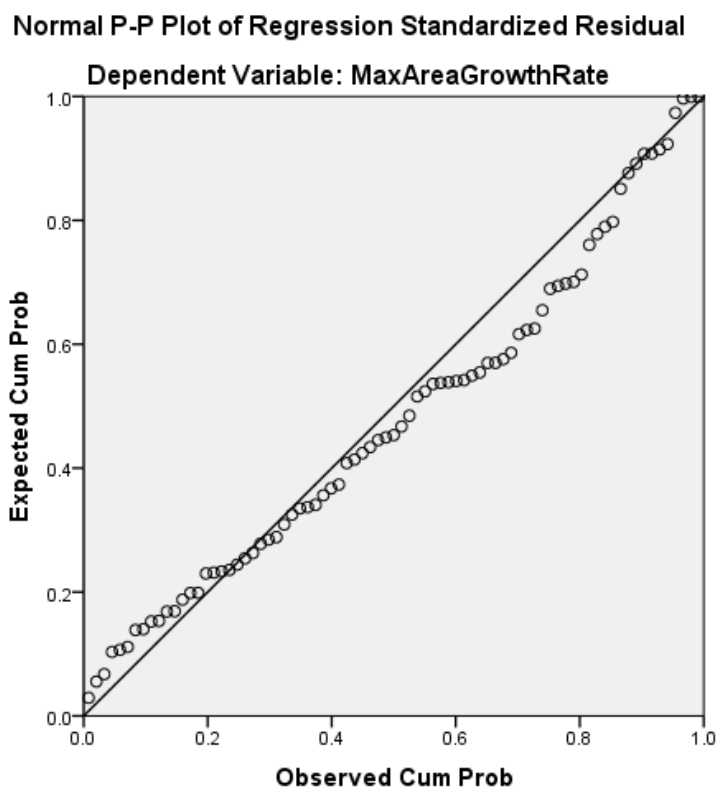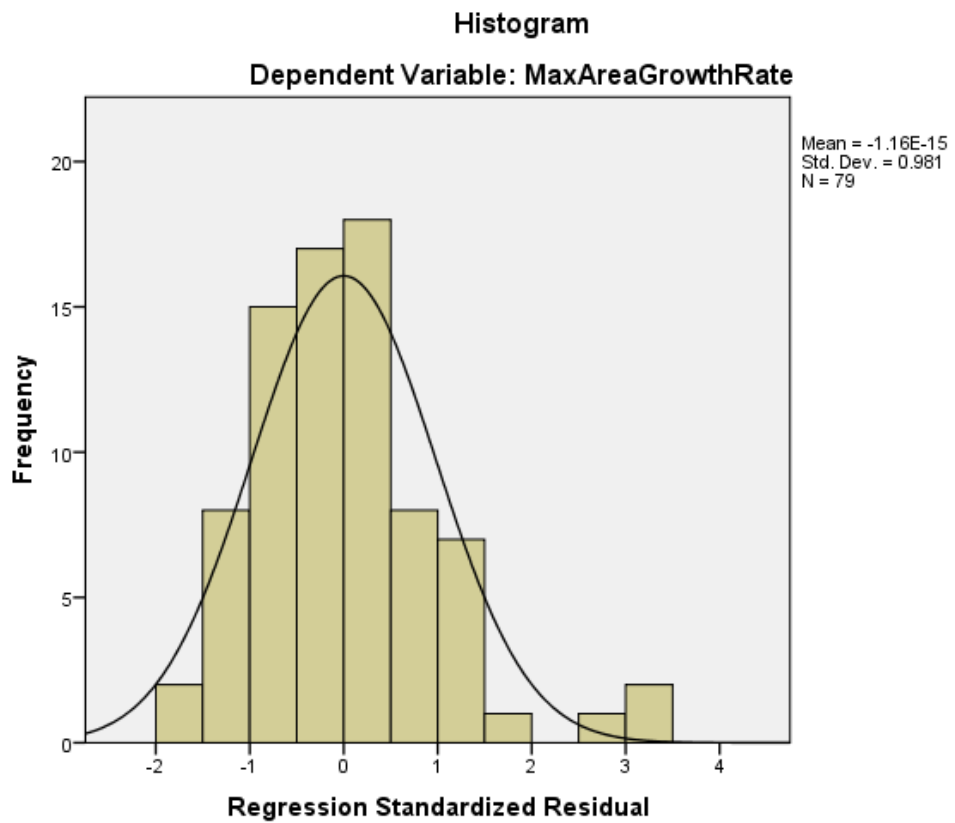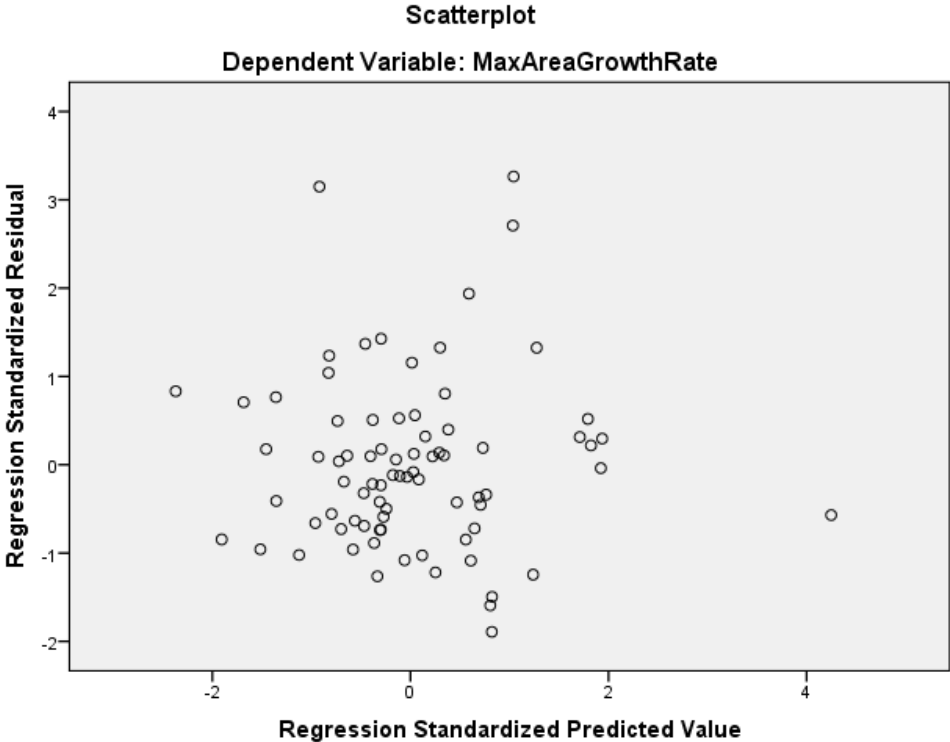
2.2   Second Model: 4 predictors

2.2.1 Diameter

Multiple Linear Regression (4 predictors)

Descriptive Statistics

	Mean	Std. Deviation	N
MaxAreaGrowthRate	254.1073	200.27010	79
MRImaxAP	50.2691	7.57976	79
Class3D_0	.25	.438	79
MeanWTeccent	1.1257	.28505	79
FamHistoryAAA	.15	.361	79

Correlations

		MaxAreaGrowthRate	MRImaxAP	Class3D_0	MeanWTeccent	FamHistoryAAA
Pearson Correlation	MaxAreaGrowthRate	1.000	.288	-.087	-.228	.209
	MRImaxAP	.288	1.000	.311	.054	.050
	Class3D_0	-.087	.311	1.000	-.050	.240
	MeanWTeccent	-.228	.054	-.050	1.000	.071

		MaxAreaGrowthRate	MRImaxAP	Class3D_0	MeanWTeccent	FamHistoryAAA
	FamHistoryAAA	.209	.050	.240	.071	1.000
Sig. (1-tailed)	MaxAreaGrowthRate	.	.005	.222	.021	.032
	MRImaxAP	.005	.	.003	.318	.330
	Class3D_0	.222	.003	.	.332	.016
	MeanWTeccent	.021	.318	.332	.	.267
	FamHistoryAAA	.032	.330	.016	.267	.
N	MaxAreaGrowthRate	79	79	79	79	79
	MRImaxAP	79	79	79	79	79
	Class3D_0	79	79	79	79	79
	MeanWTeccent	79	79	79	79	79
	FamHistoryAAA	79	79	79	79	79

Model Summary[b]

Model	R	R Square	Adjusted R Square	Std. Error of the Estimate	Durbin-Watson
1	.507[a]	.257	.217	177.24942	2.151

a. Predictors: (Constant), FamHistoryAAA, MRImaxAP, MeanWTeccent, Class3D_0

b. Dependent Variable: MaxAreaGrowthRate

ANOVA[a]

Model		Sum of Squares	df	Mean Square	F	Sig.
1	Regression	803548.559	4	200887.140	6.394	.000[b]

Residual	2324884.338	74	31417.356
Total	3128432.897	78	

a. Dependent Variable: MaxAreaGrowthRate

b. Predictors: (Constant), FamHistoryAAA, MRImaxAP, MeanWTeccent, Class3D_0

Coefficients[a]

Model		Unstandardized Coefficients		Standardized Coefficients	t	Sig.	Correlations			Collinearity Statistics	
		B	Std. Error	Beta			Zero-order	Partial	Part	Tolerance	VIF
1	(Constant)	-14.945	155.012		-.096	.923					
	MRImaxAP	9.994	2.795	.378	3.576	.001	.288	.384	.358	.897	1.114
	Class3D_0	-130.927	49.865	-.286	-2.626	.011	-.087	-.292	-.263	.846	1.182
	MeanWTeccent	-198.699	70.958	-.283	-2.800	.007	-.228	-.310	-.281	.985	1.016
	FamHistoryAAA	154.651	57.480	.279	2.691	.009	.209	.299	.270	.934	1.070

a. Dependent Variable: MaxAreaGrowthRate

Residuals Statistics[a]

	Minimum	Maximum	Mean	Std. Deviation	N
Predicted Value	46.0943	562.1419	254.1073	101.49830	79
Residual	-363.81204	530.00800	.00000	172.64475	79
Std. Predicted Value	-2.049	3.035	.000	1.000	79
Std. Residual	-2.053	2.990	.000	.974	79

a. Dependent Variable: MaxAreaGrowthRate

Appendix 2: Multiple Linear Regression

Scatterplot

Dependent Variable: MaxAreaGrowthRate

2.2.2 Mean thrombus major axis

Multiple Linear Regression (4 predictors)

Descriptive Statistics

	Mean	Std. Deviation	N
MaxAreaGrowthRate	254.1073	200.27010	79
thrMeanMajorAxis	45.9529	6.82428	79
MeanWTeccent	1.1257	.28505	79
Class3D_0	.25	.438	79
FamHistoryAAA	.15	.361	79

Correlations

		MaxAreaGrowthRate	thrMeanMajorAxis	MeanWTeccent	Class3D_0	FamHistoryAAA
Pearson Correlation	MaxAreaGrowthRate	1.000	.387	-.228	-.087	.209
	thrMeanMajorAxis	.387	1.000	-.017	.320	.108
	MeanWTeccent	-.228	-.017	1.000	-.050	.071
	Class3D_0	-.087	.320	-.050	1.000	.240
	FamHistoryAAA	.209	.108	.071	.240	1.000
Sig. (1-tailed)	MaxAreaGrowthRate	.	.000	.021	.222	.032
	thrMeanMajorAxis	.000	.	.441	.002	.173

	MeanWTeccent	.021	.441	.	.332	.267
	Class3D_0	.222	.002	.332	.	.016
	FamHistoryAAA	.032	.173	.267	.016	.
N	MaxAreaGrowthRate	79	79	79	79	79
	thrMeanMajorAxis	79	79	79	79	79
	MeanWTeccent	79	79	79	79	79
	Class3D_0	79	79	79	79	79
	FamHistoryAAA	79	79	79	79	79

Model Summary[b]

Model	R	R Square	Adjusted R Square	Std. Error of the Estimate	Durbin-Watson
1	.559[a]	.313	.275	170.47137	2.185

a. Predictors: (Constant), FamHistoryAAA, MeanWTeccent, thrMeanMajorAxis, Class3D_0

b. Dependent Variable: MaxAreaGrowthRate

ANOVA[a]

Model		Sum of Squares	df	Mean Square	F	Sig.
1	Regression	977956.815	4	244489.204	8.413	.000[b]
	Residual	2150476.083	74	29060.488		
	Total	3128432.897	78			

a. Dependent Variable: MaxAreaGrowthRate

b. Predictors: (Constant), FamHistoryAAA, MeanWTeccent, thrMeanMajorAxis, Class3D_0

Coefficients^a

Model		Unstandardized Coefficients		Standardized Coefficients	t	Sig.	Correlations			Collinearity Statistics	
		B	Std. Error	Beta			Zero-order	Partial	Part	Tolerance	VIF
1	(Constant)	-142.238	155.754		-.913	.364					
	thrMeanMajorAxis	13.301	2.987	.453	4.452	.000	.387	.460	.429	.896	1.116
	MeanWTeccent	-178.267	68.049	-.254	-2.620	.011	-.228	-.291	-.252	.990	1.010
	Class3D_0	-139.877	47.814	-.306	-2.925	.005	-.087	-.322	-.282	.851	1.175
	FamHistoryAAA	139.653	55.283	.252	2.526	.014	.209	.282	.243	.934	1.070

a. Dependent Variable: MaxAreaGrowthRate

Residuals Statistics^a

	Minimum	Maximum	Mean	Std. Deviation	N
Predicted Value	42.2000	635.6752	254.1073	111.97280	79
Residual	-321.50076	568.11584	.00000	166.04278	79
Std. Predicted Value	-1.892	3.408	.000	1.000	79
Std. Residual	-1.886	3.333	.000	.974	79

a. Dependent Variable: MaxAreaGrowthRate

Scatterplot

Dependent Variable: MaxAreaGrowthRate
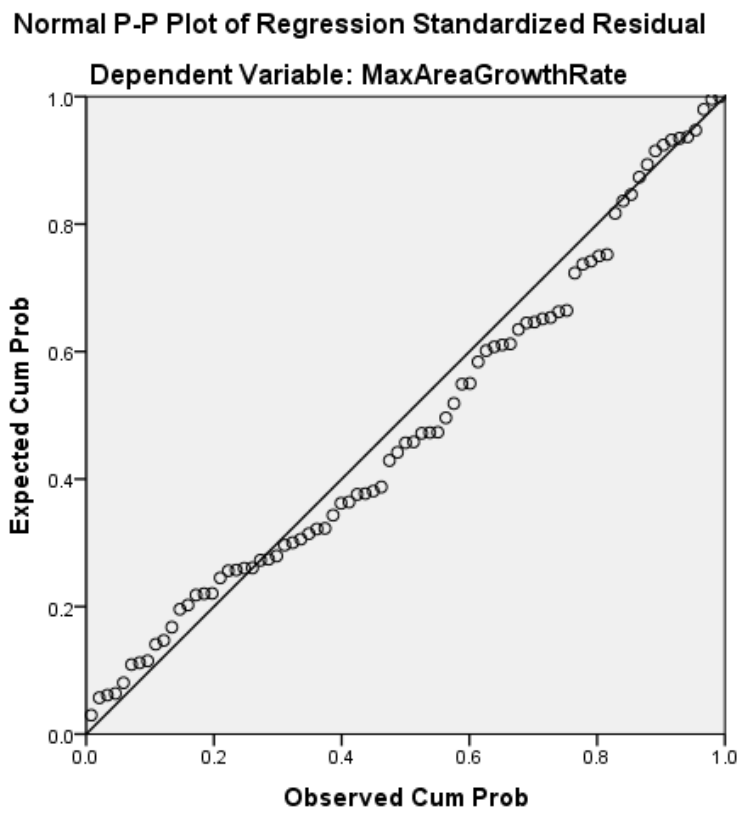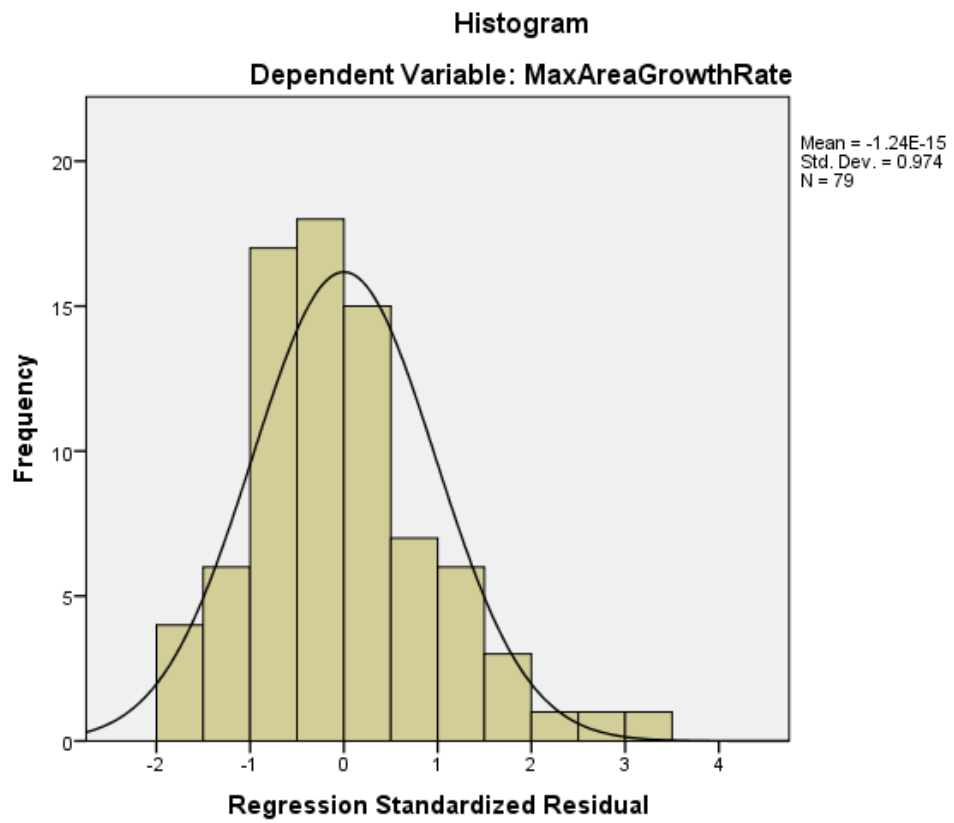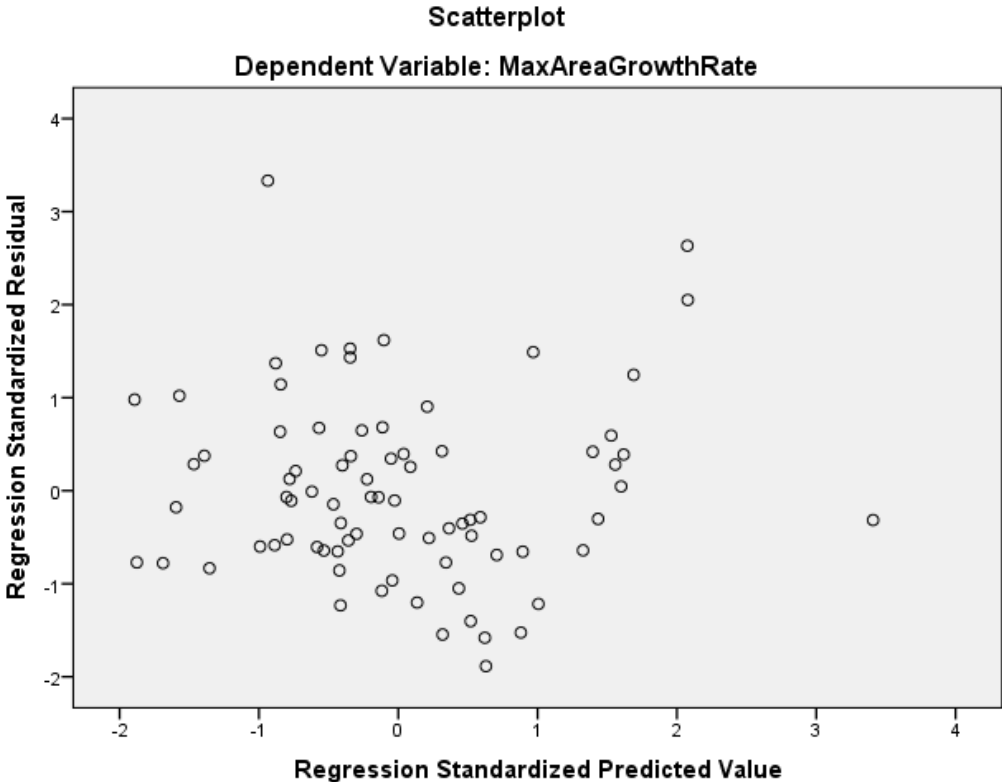
2.3   Third Model: 5 predictors

2.3.1 Diameter

Multiple Linear Regression (5 predictors)

Descriptive Statistics

	Mean	Std. Deviation	N
MaxAreaGrowthRate	254.1073	200.27010	79
MRImaxAP	50.2691	7.57976	79
Class3D_0	.25	.438	79
MeanWTeccent	1.1257	.28505	79
FamHistoryAAA	.15	.361	79
BPdiast	80.7722	10.21431	79

Correlations

		MaxAreaGrowthRate	MRImaxAP	Class3D_0	MeanWTeccent	FamHistoryAAA	BPdiast
Pearson Correlation	MaxAreaGrowthRate	1.000	.288	-.087	-.228	.209	.280
	MRImaxAP	.288	1.000	.311	.054	.050	-.040
	Class3D_0	-.087	.311	1.000	-.050	.240	-.056
	MeanWTeccent	-.228	.054	-.050	1.000	.071	-.075
	FamHistoryAAA	.209	.050	.240	.071	1.000	.065
	BPdiast	.280	-.040	-.056	-.075	.065	1.000

		MaxAreaGrowthRate	MRImaxAP	Class3D_0	MeanWTeccent	FamHistoryAAA	BPdiast
Sig. (1-tailed)	MaxAreaGrowthRate	.	.005	.222	.021	.032	.006
	MRImaxAP	.005	.	.003	.318	.330	.364
	Class3D_0	.222	.003	.	.332	.016	.313
	MeanWTeccent	.021	.318	.332	.	.267	.257
	FamHistoryAAA	.032	.330	.016	.267	.	.284
	BPdiast	.006	.364	.313	.257	.284	.
N	MaxAreaGrowthRate	79	79	79	79	79	79
	MRImaxAP	79	79	79	79	79	79
	Class3D_0	79	79	79	79	79	79
	MeanWTeccent	79	79	79	79	79	79
	FamHistoryAAA	79	79	79	79	79	79
	BPdiast	79	79	79	79	79	79

Model Summary[b]

Model	R	R Square	Adjusted R Square	Std. Error of the Estimate	Durbin-Watson
1	.561[a]	.315	.268	171.31397	2.030

a. Predictors: (Constant), BPdiast, MRImaxAP, FamHistoryAAA, MeanWTeccent, Class3D_0

b. Dependent Variable: MaxAreaGrowthRate

Automatic Classification and 3D Visualisation of AAAs to Predict Aneurysm Expansion

ANOVA^a

Model		Sum of Squares	df	Mean Square	F	Sig.
1	Regression	985994.136	5	197198.827	6.719	.000^b
	Residual	2142438.761	73	29348.476		
	Total	3128432.897	78			

a. Dependent Variable: MaxAreaGrowthRate

b. Predictors: (Constant), BPdiast, MRImaxAP, FamHistoryAAA, MeanWTeccent, Class3D_0

Coefficients^a

Model		Unstandardized Coefficients		Standardized Coefficients	t	Sig.	Correlations			Collinearity Statistics	
		B	Std. Error	Beta			Zero-order	Partial	Part	Tolerance	VIF
1	(Constant)	-422.313	221.678		-1.905	.061					
	MRImaxAP	10.096	2.702	.382	3.737	.000	.288	.401	.362	.897	1.115
	Class3D_0	-122.378	48.317	-.267	-2.533	.013	-.087	-.284	-.245	.842	1.188
	MeanWTeccent	-184.338	68.823	-.262	-2.678	.009	-.228	-.299	-.259	.978	1.023
	FamHistoryAAA	142.456	55.770	.257	2.554	.013	.209	.286	.247	.927	1.079
	BPdiast	4.776	1.915	.244	2.493	.015	.280	.280	.241	.983	1.017

a. Dependent Variable: MaxAreaGrowthRate

Appendix 2: Multiple Linear Regression

Residuals Statistics^a

	Minimum	Maximum	Mean	Std. Deviation	N
Predicted Value	21.7011	576.7721	254.1073	112.43198	79
Residual	-367.70242	534.71893	.00000	165.73220	79
Std. Predicted Value	-2.067	2.870	.000	1.000	79
Std. Residual	-2.146	3.121	.000	.967	79

a. Dependent Variable: MaxAreaGrowthRate

Histogram

Dependent Variable: MaxAreaGrowthRate

Normal P-P Plot of Regression Standardized Residual

Dependent Variable: MaxAreaGrowthRate

Scatterplot

Dependent Variable: MaxAreaGrowthRate

2.3.2 Mean thrombus major axis

Multiple Linear Regression (5 predictors)

Descriptive Statistics

	Mean	Std. Deviation	N
MaxAreaGrowthRate	254.1073	200.27010	79
thrMeanMajorAxis	45.9529	6.82428	79
MeanWTeccent	1.1257	.28505	79
Class3D_0	.25	.438	79
FamHistoryAAA	.15	.361	79
BPdiast	80.7722	10.21431	79

Correlations

		MaxAreaGrowthRate	thrMeanMajorAxis	MeanWTeccent	Class3D_0	FamHistoryAAA	BPdiast
Pearson Correlation	MaxAreaGrowthRate	1.000	.387	-.228	-.087	.209	.280
	thrMeanMajorAxis	.387	1.000	-.017	.320	.108	.066
	MeanWTeccent	-.228	-.017	1.000	-.050	.071	-.075
	Class3D_0	-.087	.320	-.050	1.000	.240	-.056
	FamHistoryAAA	.209	.108	.071	.240	1.000	.065
	BPdiast	.280	.066	-.075	-.056	.065	1.000
Sig. (1-tailed)	MaxAreaGrowthRate	.	.000	.021	.222	.032	.006

	thrMeanMajorAxis	.000	.	.441	.002	.173	.280
	MeanWTeccent	.021	.441	.	.332	.267	.257
	Class3D_0	.222	.002	.332	.	.016	.313
	FamHistoryAAA	.032	.173	.267	.016	.	.284
	BPdiast	.006	.280	.257	.313	.284	.
N	MaxAreaGrowthRate	79	79	79	79	79	79
	thrMeanMajorAxis	79	79	79	79	79	79
	MeanWTeccent	79	79	79	79	79	79
	Class3D_0	79	79	79	79	79	79
	FamHistoryAAA	79	79	79	79	79	79
	BPdiast	79	79	79	79	79	79

Model Summary[b]

Model	R	R Square	Adjusted R Square	Std. Error of the Estimate	Durbin-Watson
1	.594[a]	.352	.308	166.59007	2.068

a. Predictors: (Constant), BPdiast, Class3D_0, MeanWTeccent, FamHistoryAAA, thrMeanMajorAxis

b. Dependent Variable: MaxAreaGrowthRate

ANOVA^a

Model		Sum of Squares	df	Mean Square	F	Sig.
1	Regression	1102518.589	5	220503.718	7.945	.000^b
	Residual	2025914.308	73	27752.251		
	Total	3128432.897	78			

a. Dependent Variable: MaxAreaGrowthRate

b. Predictors: (Constant), BPdiast, Class3D_0, MeanWTeccent, FamHistoryAAA, thrMeanMajorAxis

Coefficients^a

Model		Unstandardized Coefficients		Standardized Coefficients	t	Sig.	Correlations			Collinearity Statistics	
		B	Std. Error	Beta			Zero-order	Partial	Part	Tolerance	VIF
1	(Constant)	-452.006	211.060		-2.142	.036					
	thrMeanMajorAxis	12.762	2.930	.435	4.355	.000	.387	.454	.410	.890	1.124
	MeanWTeccent	-166.244	66.741	-.237	-2.491	.015	-.228	-.280	-.235	.983	1.017
	Class3D_0	-129.690	46.972	-.283	-2.761	.007	-.087	-.307	-.260	.842	1.188
	FamHistoryAAA	129.817	54.223	.234	2.394	.019	.209	.270	.225	.927	1.078
	BPdiast	3.961	1.869	.202	2.119	.038	.280	.241	.200	.976	1.025

a. Dependent Variable: MaxAreaGrowthRate

Residuals Statistics[a]

	Minimum	Maximum	Mean	Std. Deviation	N
Predicted Value	20.6963	627.9628	254.1073	118.89009	79
Residual	-322.20560	567.41608	.00000	161.16222	79
Std. Predicted Value	-1.963	3.145	.000	1.000	79
Std. Residual	-1.934	3.406	.000	.967	79

a. Dependent Variable: MaxAreaGrowthRate

Histogram

Dependent Variable: MaxAreaGrowthRate

Mean = -1.39E-15
Std. Dev. = 0.967
N = 79

Normal P-P Plot of Regression Standardized Residual

Dependent Variable: MaxAreaGrowthRate

Appendix 2: Multiple Linear Regression   301
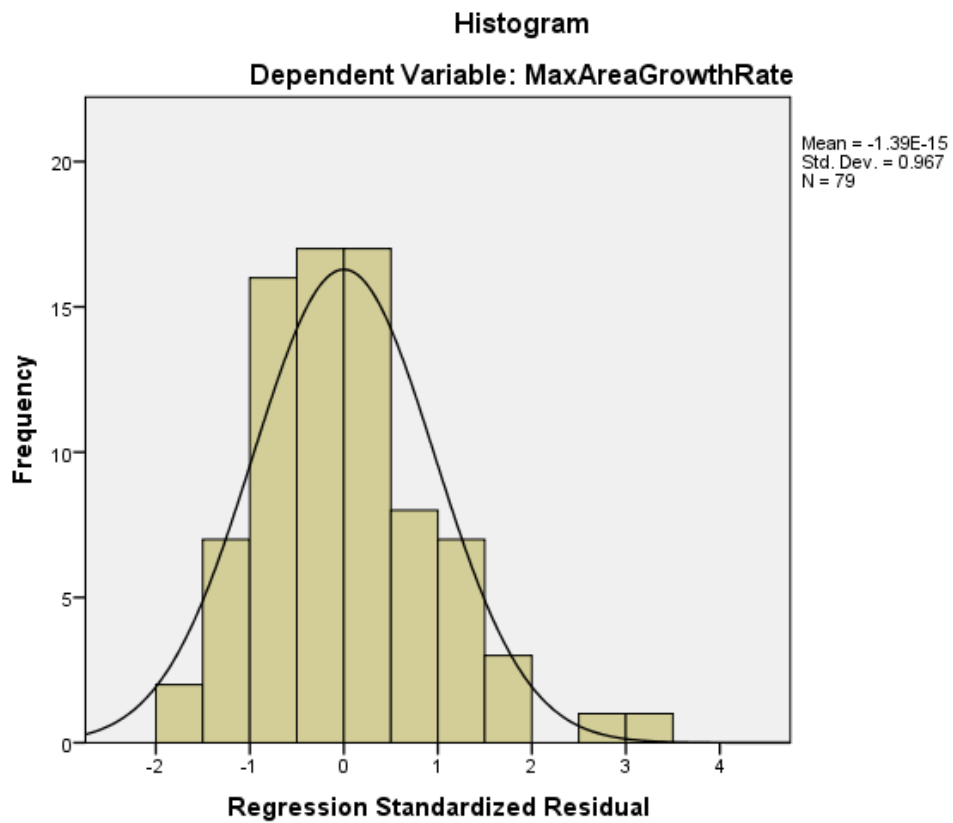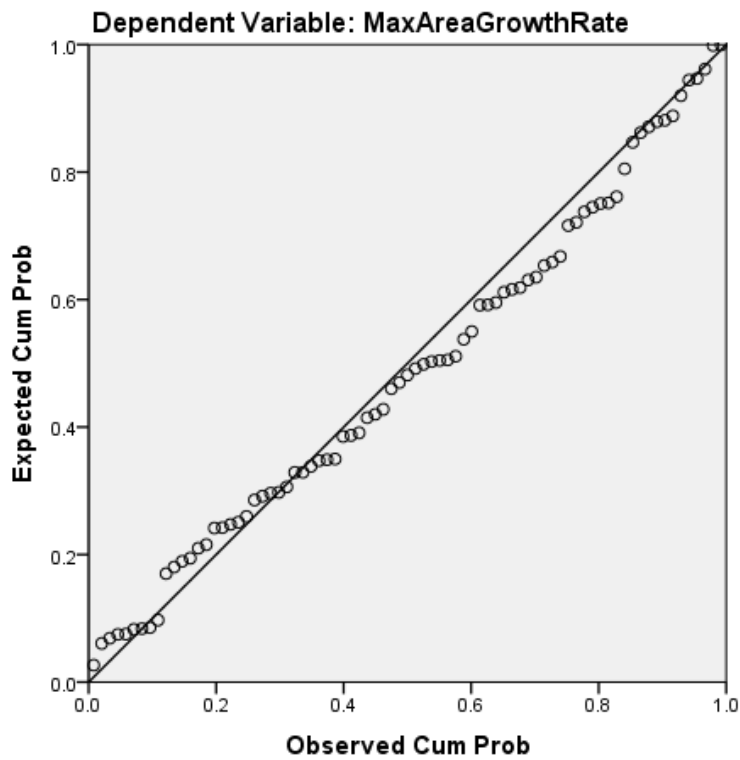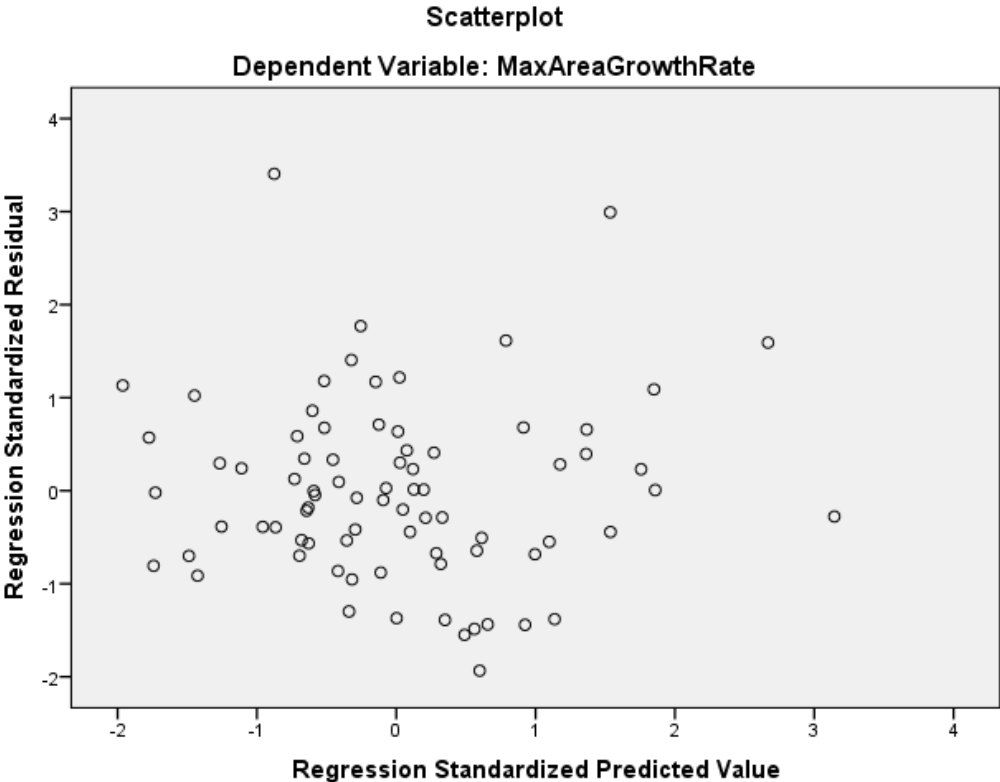
References

[1]   World Health Organization, "Global Health Estimates 2016: Disease burden by Cause, Age, Sex, by Country and by Region, 2000-2016.," *WHO*, 2018.

[2]   N. Townsend, M. Nichols, P. Scarborough, and M. Rayner, "Cardiovascular disease in Europe — epidemiological update 2015," *Eur. Heart J.*, p. ehv428, Aug. 2015.

[3]   D. Hardman, S. I. Semple, J. M. J. Richards, and P. R. Hoskins, "Comparison of patient-specific inlet boundary conditions in the numerical modelling of blood flow in abdominal aortic aneurysm disease.," *Int. j. numer. method. biomed. eng.*, vol. 29, no. 2, pp. 165–78, Feb. 2013.

[4]   E. Choke *et al.*, "A review of biological factors implicated in abdominal aortic aneurysm rupture.," *Eur. J. Vasc. Endovasc. Surg.*, vol. 30, no. 3, pp. 227–44, Sep. 2005.

[5]   N. Sakalihasan, R. Limet, and O. D. Defawe, "Abdominal aortic aneurysm.," *Lancet (London, England)*, vol. 365, no. 9470, pp. 1577–89, Jan. 2005.

[6]   R. A. Scott, K. A. Vardulaki, N. M. Walker, N. E. Day, S. W. Duffy, and H. A. Ashton, "The long-term benefits of a single scan for abdominal aortic aneurysm (AAA) at age 65.," *Eur. J. Vasc. Endovasc. Surg.*, vol. 21, no. 6, pp. 535–40, Jun. 2001.

[7]   A. Nakayama *et al.*, "Predictors of mortality after emergency or elective repair of abdominal aortic aneurysm in a Japanese population," *Heart Vessels*, vol. 29, no. 1, pp. 65–70, Jan. 2014.

[8]   S. Arya *et al.*, "Frailty increases the risk of 30-day mortality, morbidity, and failure to rescue after elective abdominal aortic aneurysm repair independent of age and comorbidities," *J. Vasc. Surg.*, vol. 61, no. 2, pp.

324–331, 2015.

[9]   A. W. Beck *et al.*, "Predicting 1-year mortality after elective abdominal aortic aneurysm repair.," *J. Vasc. Surg.*, vol. 49, no. 4, pp. 838-43; discussion 843–4, Apr. 2009.

[10]   F. J. V. V Schlösser *et al.*, "Mortality after elective abdominal aortic aneurysm repair," vol. 251, no. 1, Jan. 2010.

[11]   A.D.A.M. Inc., "A.D.A.M. Medical Encyclopedia; Abdominal aortic aneurysm," *Atlanta (GA)*, 2005. [Online]. Available: https://medlineplus.gov/ency/article/000162.htm. [Accessed: 15-Dec-2016].

[12]   H. W. Kniemeyer, T. Kessler, P. U. Reber, H. B. Ris, H. Hakki, and M. K. Widmer, "Treatment of ruptured abdominal aortic aneurysm, a permanent challenge or a waste of resources? Prediction of outcome using a multi-organ-dysfunction score.," *Eur. J. Vasc. Endovasc. Surg.*, vol. 19, no. 2, pp. 190–6, Feb. 2000.

[13]   F. A. Lederle *et al.*, "Immediate Repair Compared with Surveillance of Small Abdominal Aortic Aneurysms," *N. Engl. J. Med.*, vol. 346, no. 19, pp. 1437–1444, May 2002.

[14]   S. C. Nicholls, J. B. Gardner, M. H. Meissner, and K. H. Johansen, "Rupture in small abdominal aortic aneurysms," *J. Vasc. Surg.*, vol. 28, no. 5, pp. 884–888, Nov. 1998.

[15]   J. M. J. Richards *et al.*, "Abdominal aortic aneurysm growth predicted by uptake of ultrasmall superparamagnetic particles of iron oxide: a pilot study.," *Circ. Cardiovasc. Imaging*, vol. 4, no. 3, pp. 274–81, May 2011.

[16]   PEIR Digital Library, "GROSS: CARDIOVASCULAR: AORTA: Abdominal Aneurysm | PEIR Digital Library," *Pathology Education Instructional*

Resource (PEIR), University of Alabama at Birmingham, Department of Pathology. [Online]. Available:
http://peir.path.uab.edu/library/picture.php?/4062/categories.
[Accessed: 20-Feb-2017].

[17]   R. Erbel and H. Eggebrecht, "Aortic dimensions and the risk of dissection.," *Heart*, vol. 92, no. 1, pp. 137–42, Jan. 2006.

[18]   G. Y. H. Lip and J. E. (John E. Hall, *Comprehensive hypertension*. Mosby Elsevier, 2007.

[19]   B. A. Brown, H. Williams, and S. J. George, "Evidence for the Involvement of Matrix-Degrading Metalloproteinases (MMPs) in Atherosclerosis," *Prog. Mol. Biol. Transl. Sci.*, vol. 147, pp. 197–237, Jan. 2017.

[20]   J. Moini, *Phlebotomy : principles and practice*. Jones & Bartlett Learning, 2013.

[21]   E. L. Ritman and A. Lerman, "The dynamic vasa vasorum.," *Cardiovasc. Res.*, vol. 75, no. 4, pp. 649–58, Sep. 2007.

[22]   D. A. Vorp, W. A. Mandarino, M. W. Webster, and J. Gorcsan, "Potential influence of intraluminal thrombus on abdominal aortic aneurysm as assessed by a new non-invasive method.," *Cardiovasc. Surg.*, vol. 4, no. 6, pp. 732–9, Dec. 1996.

[23]   C. Behr-Rasmussen, N. Grøndal, M. B. Bramsen, M. D. Thomsen, and J. S. Lindholt, "Mural Thrombus and the Progression of Abdominal Aortic Aneurysms: A Large Population-based Prospective Cohort Study," *Eur. J. Vasc. Endovasc. Surg.*, vol. 48, no. 3, pp. 301–307, Sep. 2014.

[24]   R. Adolph, D. A. Vorp, D. L. Steed, M. W. Webster, M. V Kameneva, and S. C. Watkins, "Cellular content and permeability of intraluminal thrombus in abdominal aortic aneurysm.," *J. Vasc. Surg.*, vol. 25, no. 5, pp. 916–26, May

1997.

[25]   S. A. O'Leary, E. G. Kavanagh, P. A. Grace, T. M. McGloughlin, and B. J. Doyle, "The biaxial mechanical behaviour of abdominal aortic aneurysm intraluminal thrombus: Classification of morphology and the determination of layer and region specific properties," *J. Biomech.*, vol. 47, no. 6, pp. 1430–1437, Apr. 2014.

[26]   X. Houard *et al.*, "Topology of the fibrinolytic system within the mural thrombus of human abdominal aortic aneurysms," *J. Pathol.*, vol. 212, no. 1, pp. 20–28, May 2007.

[27]   X. Houard, V. Ollivier, L. Louedec, J.-B. Michel, and M. Bäck, "Differential inflammatory activity across human abdominal aortic aneurysms reveals neutrophil-derived leukotriene B $_4$ as a major chemotactic factor released from the intraluminal thrombus," *FASEB J.*, vol. 23, no. 5, pp. 1376–1383, May 2009.

[28]   M. Kazi *et al.*, "Influence of intraluminal thrombus on structural and cellular composition of abdominal aortic aneurysm wall," *J. Vasc. Surg.*, 2003.

[29]   J. V. Moxon, A. Parr, T. I. Emeto, P. Walker, P. E. Norman, and J. Golledge, "Diagnosis and Monitoring of Abdominal Aortic Aneurysm: Current Status and Future Prospects," *Curr. Probl. Cardiol.*, vol. 35, no. 10, pp. 512–548, 2010.

[30]   V. Fontaine *et al.*, "Involvement of the Mural Thrombus as a Site of Protease Release and Activation in Human Aortic Aneurysms," *Am. J. Pathol.*, vol. 161, no. 5, pp. 1701–1710, Nov. 2002.

[31]   A. Piechota-Polanczyk *et al.*, "The Abdominal Aortic Aneurysm and Intraluminal Thrombus: Current Concepts of Development and Treatment.," *Front. Cardiovasc. Med.*, vol. 2, p. 19, 2015.

[32] H. a Ashton *et al.*, "The Multicentre Aneurysm Screening Study (MASS) into the effect of abdominal aortic aneurysm screening on mortality in men: a randomised controlled trial.," *Lancet*, vol. 360, no. 9345, pp. 1531–1539, 2002.

[33] P. E. Norman *et al.*, "Population based randomised controlled trial on impact of screening on mortality from abdominal aortic aneurysm.," *BMJ*, vol. 329, no. 7477, p. 1259, Nov. 2004.

[34] J. S. Lindholt, S. Juul, H. Fasting, and E. W. Henneberg, "Screening for abdominal aortic aneurysms: single centre randomised controlled trial.," *BMJ*, vol. 330, no. 7494, p. 750, Apr. 2005.

[35] Office for National Statistics, "Mortality Statistics Series," 2013.

[36] N. Center for Health Statistics, "LCWK1. Deaths, percent of total deaths, and death rates for the 15 leading causes of death in 5-year age groups, by race and sex: United States, 2013," 2013.

[37] C. G. Solomon and K. C. Kent, "Abdominal Aortic Aneurysms," *N. Engl. J. Med.*, vol. 371, no. 22, pp. 2101–2108, Nov. 2014.

[38] S. Svensjo, M. Bjorck, M. Gurtelschmid, K. Djavani Gidlund, A. Hellberg, and A. Wanhainen, "Low Prevalence of Abdominal Aortic Aneurysm Among 65-Year-Old Swedish Men Indicates a Change in the Epidemiology of the Disease," *Circulation*, vol. 124, no. 10, pp. 1118–1123, Sep. 2011.

[39] D. Sidloff *et al.*, "Aneurysm Global Epidemiology Study: Public Health Measures can Further Reduce Abdominal Aortic Aneurysm Mortality," *Circulation*, 2013.

[40] S. M. Krishna, A. E. Dear, P. E. Norman, and J. Golledge, "Genetic and epigenetic mechanisms and their possible role in abdominal aortic aneurysm.," *Atherosclerosis*, vol. 212, no. 1, pp. 16–29, Sep. 2010.

[41]   M. Björck and A. Wanhainen, "Pathophysiology of AAA: heredity vs environment.," *Prog. Cardiovasc. Dis.*, vol. 56, no. 1, pp. 2–6, 2013.

[42]   H. Kuivaniemi, E. J. Ryer, J. R. Elmore, and G. Tromp, "Understanding the pathogenesis of abdominal aortic aneurysms.," *Expert Rev. Cardiovasc. Ther.*, vol. 13, no. 9, 2015.

[43]   D. Reed, C. Reed, G. Stemmermann, and T. Hayashi, "Are aortic aneurysms caused by atherosclerosis?," *Circulation*, vol. 85, no. 1, pp. 205–211, Jan. 1992.

[44]   S. H. Johnsen, S. H. Forsdahl, K. Singh, and B. K. Jacobsen, "Atherosclerosis in abdominal aortic aneurysms: a causal event or a process running in parallel? The Tromsø study.," *Arterioscler. Thromb. Vasc. Biol.*, vol. 30, no. 6, pp. 1263–8, Jun. 2010.

[45]   J. F. Blanchard, H. K. Armenian, and P. P. Friesen, "Risk Factors for Abdominal Aortic Aneurysm: Results of a Case-Control Study," *Am. J. Epidemiol.*, vol. 151, no. 6, pp. 575–583, Mar. 2000.

[46]   N. Katsiki, S. K. Papadopoulou, A. I. Fachantidou, and D. P. Mikhailidis, "Smoking and vascular risk: are all forms of smoking harmful to all types of vascular disease?," *Public Health*, vol. 127, no. 5, pp. 435–41, May 2013.

[47]   P. E. Norman and J. A. Curci, "Understanding the effects of tobacco smoke on the pathogenesis of aortic aneurysm.," *Arterioscler. Thromb. Vasc. Biol.*, vol. 33, no. 7, pp. 1473–7, Jul. 2013.

[48]   M. P. Reilly, "Tobacco-related cardiovascular diseases in the 21st century.," *Arterioscler. Thromb. Vasc. Biol.*, vol. 33, no. 7, pp. 1458–9, Jul. 2013.

[49]   W. Tang *et al.*, "Lifetime Risk and Risk Factors for Abdominal Aortic Aneurysm in a 24-Year Prospective StudyHighlights," *Arterioscler.*

Thromb. Vasc. Biol., vol. 36, no. 12, pp. 2468–2477, Dec. 2016.

[50] J. S. Lindholt, N. H. Heegaard, S. Vammen, H. Fasting, E. W. Henneberg, and L. Heickendorff, "Smoking, but not lipids, lipoprotein(a) and antibodies against oxidised LDL, is correlated to the expansion of abdominal aortic aneurysms.," *Eur. J. Vasc. Endovasc. Surg.*, vol. 21, no. 1, pp. 51–6, Jan. 2001.

[51] K. Singh, "Prevalence of and Risk Factors for Abdominal Aortic Aneurysms in a Population-based Study : The Tromso Study," *Am. J. Epidemiol.*, vol. 154, no. 3, pp. 236–244, Aug. 2001.

[52] K. A. Vardulaki, N. M. Walker, N. E. Day, S. W. Duffy, H. A. Ashton, and R. A. Scott, "Quantifying the risks of hypertension, age, sex and smoking in patients with abdominal aortic aneurysm.," *Br. J. Surg.*, vol. 87, no. 2, pp. 195–200, Feb. 2000.

[53] A. R. Brady, S. G. Thompson, F. G. R. Fowkes, R. M. Greenhalgh, and J. T. Powell, "Abdominal Aortic Aneurysm Expansion," *Circulation*, vol. 110, no. 1, 2004.

[54] S. Shantikumar, R. Ajjan, K. E. Porter, and D. J. A. Scott, "Diabetes and the Abdominal Aortic Aneurysm," *Eur. J. Vasc. Endovasc. Surg.*, vol. 39, no. 2, pp. 200–207, Feb. 2010.

[55] S. G. Thompson *et al.*, *Systematic review and meta-analysis of the growth and rupture rates of small abdominal aortic aneurysms: implications for surveillance intervals and their cost-effectiveness.*, vol. 17, no. 41. 2013, pp. 1–118.

[56] F. A. Lederle, "Should Abdominal Aortic Aneurysm Be Managed Differently in Women?," *Scand. J. Surg.*, vol. 97, no. 2, pp. 125–127, Jun. 2008.

[57] A. K. Vavra, M. R. Kibbe, M. J. Bown, J. T. Powell, T. L. Forbes, and A. Ross Naylor, "Debate: Whether evidence supports reducing the threshold diameter to 5 cm for elective interventions in women with abdominal aortic aneurysms," *J. Vasc. Surg.*, vol. 60, no. 6, 2014.

[58] R. C. Lo *et al.*, "Relative importance of aneurysm diameter and body size for predicting abdominal aortic aneurysm rupture in men and women," *J. Vasc. Surg.*, vol. 59, no. 5, pp. 1209–1216, May 2014.

[59] D. A. Sidloff *et al.*, "Sex differences in mortality after abdominal aortic aneurysm repair in the UK.," *Br. J. Surg.*, vol. 104, no. 12, pp. 1656–1664, Nov. 2017.

[60] J. Melrose, J. Whitelock, Q. Xu, and P. Ghosh, "Pathogenesis of abdominal aortic aneurysms: Possible role of differential production of proteoglycans by smooth muscle cells," *J. Vasc. Surg.*, vol. 28, no. 4, pp. 676–686, Oct. 1998.

[61] J. K-J. Li, "Comparative cardiac mechanics: Laplace's law," *J. Theor. Biol.*, vol. 118, no. 3, pp. 339–343, Feb. 1986.

[62] A. J. Hall, E. F. G. Busse, D. J. McCarville, and J. J. Burgess, "Aortic wall tension as a predictive factor for abdominal aortic aneurysm rupture: improving the selection of patients for abdominal aortic aneurysm repair.," vol. 14, no. 2, Mar. 2000.

[63] D. H. J. J. Wang, M. S. Makaroun, M. W. Webster, and D. A. Vorp, "Effect of intraluminal thrombus on wall stress in patient-specific models of abdominal aortic aneurysm," *J. Vasc. Surg.*, vol. 36, no. 3, pp. 598–604, Sep. 2002.

[64] M. L. Raghavan, D. A. Vorp, M. P. Federle, M. S. Makaroun, and M. W. Webster, "Wall stress distribution on three-dimensionally reconstructed models of human abdominal aortic aneurysm," *J. Vasc. Surg.*, vol. 31, no. 4,

pp. 760–769, Apr. 2000.

[65]   M. F. Fillinger, M. L. Raghavan, S. P. Marra, J. L. Cronenwett, and F. E. Kennedy, "In vivo analysis of mechanical wall stress and abdominal aortic aneurysm rupture risk," *J. Vasc. Surg.*, vol. 36, no. 3, pp. 589–597, Sep. 2002.

[66]   M. F. Fillinger, S. P. Marra, M. L. Raghavan, and F. E. Kennedy, "Prediction of rupture risk in abdominal aortic aneurysm during observation: Wall stress versus diameter," *J. Vasc. Surg.*, vol. 37, no. 4, pp. 724–732, Apr. 2003.

[67]   D. F. Elger, D. M. Blackketter, R. S. Budwig, and K. H. Johansen, "The influence of shape on the stresses in model abdominal aortic aneurysms.," *J. Biomech. Eng.*, vol. 118, no. 3, pp. 326–32, Aug. 1996.

[68]   M. M. Stringfellow, P. F. Lawrence, and R. G. Stringfellow, "The influence of aorta-aneurysm geometry upon stress in the aneurysm wall," *J. Surg. Res.*, vol. 42, no. 4, pp. 425–433, Apr. 1987.

[69]   A. . Venkatasubramaniam *et al.*, "A Comparative Study of Aortic Wall Stress Using Finite Element Analysis for Ruptured and Non-ruptured Abdominal Aortic Aneurysms," *Eur. J. Vasc. Endovasc. Surg.*, vol. 28, no. 2, pp. 168–176, Aug. 2004.

[70]   J. L. Cronenwett *et al.*, "The United Kingdom Small Aneurysm Trial: Implications for surgical treatment of abdominal aortic aneurysms," *J. Vasc. Surg.*, vol. 29, no. 1, pp. 191–194, Jan. 1999.

[71]   D. A. Vorp, M. L. L. Raghavan, and M. W. Webster, "Mechanical wall stress in abdominal aortic aneurysm: Influence of diameter and asymmetry," vol. 27, no. 4, Apr. 1998.

[72]   Z. Zhang *et al.*, "Comparison of the Young-Laplace Law and Finite Element

Based Calculation of Ventricular Wall Stress: Implications for Postinfarct and Surgical Ventricular Remodeling," *Ann. Thorac. Surg.*, vol. 91, no. 1, pp. 150–156, 2011.

[73]   D. A. Vorp, "Biomechanics of abdominal aortic aneurysm," *J. Biomech.*, vol. 40, no. 9, pp. 1887–1902, 2007.

[74]   F. Tanios *et al.*, "Interaction of Biomechanics with Extracellular Matrix Components in Abdominal Aortic Aneurysm Wall," *Eur. J. Vasc. Endovasc. Surg.*, vol. 50, no. 2, pp. 167–174, Aug. 2015.

[75]   S. Seyedsalehi, L. Zhang, J. Choi, and S. Baek, "Prior Distributions of Material Parameters for Bayesian Calibration of Growth and Remodeling Computational Model of Abdominal Aortic Wall," *J. Biomech. Eng.*, vol. 137, no. 10, p. 101001, Aug. 2015.

[76]   J. P. Vande Geest, D. H. J. Wang, S. R. Wisniewski, M. S. Makaroun, and D. A. Vorp, "Towards A Noninvasive Method for Determination of Patient-Specific Wall Strength Distribution in Abdominal Aortic Aneurysms," *Ann. Biomed. Eng.*, vol. 34, no. 7, pp. 1098–1106, Jul. 2006.

[77]   J. Biehler *et al.*, "Probabilistic noninvasive prediction of wall properties of abdominal aortic aneurysms using Bayesian regression," *Biomech. Model. Mechanobiol.*, vol. 16, no. 1, pp. 45–61, Feb. 2017.

[78]   P. Matusik, P. Mazur, E. Stępień, R. Pfitzner, J. Sadowski, and A. Undas, "Architecture of intraluminal thrombus removed from abdominal aortic aneurysm," *J. Thromb. Thrombolysis*, vol. 30, no. 1, pp. 7–9, Jul. 2010.

[79]   F. Riveros, G. Martufi, T. C. Gasser, and J. F. Rodriguez-Matas, "On the Impact of Intraluminal Thrombus Mechanical Behavior in AAA Passive Mechanics," *Ann. Biomed. Eng.*, vol. 43, no. 9, pp. 2253–2264, Sep. 2015.

[80]   L. Speelman *et al.*, "The mechanical role of thrombus on the growth rate of

an abdominal aortic aneurysm," *J. Vasc. Surg.*, vol. 51, no. 1, pp. 19–26, Jan. 2010.

[81] E. Georgakarakos, C. V Ioannou, S. Volanis, Y. Papaharilaou, J. Ekaterinaris, and A. N. Katsamouris, "The influence of intraluminal thrombus on abdominal aortic aneurysm wall stress.," *Int. Angiol.*, vol. 28, no. 4, pp. 325–33, Aug. 2009.

[82] J. Stenbaek, B. Kalin, and J. Swedenborg, "Growth of thrombus may be a better predictor of rupture than diameter in patients with abdominal aortic aneurysms.," *Eur. J. Vasc. Endovasc. Surg.*, vol. 20, no. 5, pp. 466–9, Nov. 2000.

[83] L. Virag, J. S. Wilson, J. D. Humphrey, and I. Karšaj, "A Computational Model of Biochemomechanical Effects of Intraluminal Thrombus on the Enlargement of Abdominal Aortic Aneurysms," *Ann. Biomed. Eng.*, vol. 43, no. 12, pp. 2852–2867, Dec. 2015.

[84] S. Polzer, T. C. Gasser, J. Swedenborg, and J. Bursa, "The Impact of Intraluminal Thrombus Failure on the Mechanical Stress in the Wall of Abdominal Aortic Aneurysms," *Eur. J. Vasc. Endovasc. Surg.*, vol. 41, no. 4, pp. 467–473, Apr. 2011.

[85] J. Roy, F. Labruto, M. O. Beckman, J. Danielson, G. Johansson, and J. Swedenborg, "Bleeding into the intraluminal thrombus in abdominal aortic aneurysms is associated with rupture," *J. Vasc. Surg.*, vol. 48, no. 5, pp. 1108–1113, Nov. 2008.

[86] C. F. Gonsalves, "The Hyperattenuating Crescent Sign," *Radiology*, vol. 211, no. 1, pp. 37–38, Apr. 1999.

[87] T. Arita *et al.*, "Abdominal aortic aneurysm: rupture associated with the high-attenuating crescent sign.," *Radiology*, vol. 204, no. 3, pp. 765–8, Sep. 1997.

[88] S. A. Schwartz, M. S. Taljanovic, S. Smyth, M. J. O'Brien, and L. F. Rogers, *CT findings of rupture, impending rupture, and contained rupture of abdominal aortic aneurysms.*, vol. 188, no. 1. American Roentgen Ray Society, 2007, pp. W57–W62.

[89] C. L. Siegel, R. H. Cohan, M. Korobkin, M. B. Alpern, D. L. Courneya, and R. A. Leder, "Abdominal aortic aneurysm morphology: CT features in patients with ruptured and nonruptured aneurysms.," *AJR. Am. J. Roentgenol.*, vol. 163, no. 5, pp. 1123–9, Nov. 1994.

[90] K.-N. Vu *et al.*, "Rupture signs on computed tomography, treatment, and outcome of abdominal aortic aneurysms.," *Insights Imaging*, vol. 5, no. 3, pp. 281–93, Jun. 2014.

[91] D. Vorp, "Potential influence of intraluminal thrombus on abdominal aortic aneurysm as assessed by a new non-invasive method," *Cardiovasc. Surg.*, vol. 4, no. 6, pp. 732–739, Dec. 1996.

[92] T. Freestone, R. J. Turner, A. Coady, D. J. Higman, R. M. Greenhalgh, and J. T. Powell, "Inflammation and matrix metalloproteinases in the enlarging abdominal aortic aneurysm.," *Arterioscler. Thromb. Vasc. Biol.*, vol. 15, no. 8, pp. 1145–51, Aug. 1995.

[93] H. Jalalzadeh, R. Indrakusuma, R. N. Planken, D. A. Legemate, M. J. W. Koelemay, and R. Balm, "Inflammation as a Predictor of Abdominal Aortic Aneurysm Growth and Rupture: A Systematic Review of Imaging Biomarkers," *Eur. J. Vasc. Endovasc. Surg.*, vol. 52, no. 3, pp. 333–342, Sep. 2016.

[94] R. P. Savarese, J. C. Rosenfeld, and D. A. DeLaurentis, "Inflammatory abdominal aortic aneurysm.," *Surg. Gynecol. Obstet.*, vol. 162, no. 5, pp. 405–10, May 1986.

[95] S. Anidjar, P. B. Dobrin, M. Eichorst, G. P. Graham, G. Chejfec, and J. T.

Powell, "Correlation of inflammatory infiltrate with the enlargement of experimental aortic aneurysms.," *J. Vasc. Surg.*, vol. 16, no. 2, pp. 139–47, Aug. 1992.

[96] W. R. W. Wilson, J. Evans, P. R. F. Bell, and M. M. Thompson, "HMG-CoA Reductase Inhibitors (Statins) Decrease MMP-3 and MMP-9 Concentrations in Abdominal Aortic Aneurysms," *Eur. J. Vasc. Endovasc. Surg.*, vol. 30, no. 3, pp. 259–262, Sep. 2005.

[97] W. R. W. Wilson *et al.*, "Matrix Metalloproteinase-8 and -9 Are Increased at the Site of Abdominal Aortic Aneurysm Rupture," *Circulation*, vol. 113, no. 3, pp. 438–445, Jan. 2006.

[98] M. L. McCormick, D. Gavrila, and N. L. Weintraub, "Role of Oxidative Stress in the Pathogenesis of Abdominal Aortic Aneurysms," *Arterioscler. Thromb. Vasc. Biol.*, vol. 27, no. 3, pp. 461–469, Mar. 2007.

[99] K. . Wilson, J. . Lindholt, P. . Hoskins, L. Heickendorff, S. Vammen, and A. . Bradbury, "The Relationship Between Abdominal Aortic Aneurysm Distensibility and Serum Markers of Elastin and Collagen Metabolism," *Eur. J. Vasc. Endovasc. Surg.*, vol. 21, no. 2, pp. 175–178, Feb. 2001.

[100] K. Wilson *et al.*, "Relationship between abdominal aortic aneurysm wall compliance and clinical outcome: a preliminary analysis," *Eur. J. Vasc. Endovasc. Surg.*, vol. 15, no. 6, pp. 472–477, Jun. 1998.

[101] D. A. Vorp *et al.*, "Wall strength and stiffness of aneurysmal and nonaneurysmal abdominal aorta.," *Ann. N. Y. Acad. Sci.*, vol. 800, pp. 274–6, Nov. 1996.

[102] S. R. Vallabhaneni, G. L. Gilling-Smith, T. V. How, S. D. Carter, J. A. Brennan, and P. L. Harris, "**Heterogeneity of Tensile Strength and Matrix Metalloproteinase Activity in the Wall of Abdominal Aortic Aneurysms**," *J. Endovasc. Ther.*, vol. 11, no. 4, pp. 494–502, Aug. 2004.

[103] E. Choke *et al.*, "Increased Angiogenesis at the Site of Abdominal Aortic Aneurysm Rupture," *Ann. N. Y. Acad. Sci.*, vol. 1085, no. 1, pp. 315–319, Nov. 2006.

[104] M. M. Thompson, A. Wills, E. McDermott, M. Crowther, N. Brindle, and P. R. Bell, "An in vitro model of aneurysmal disease: effect of leukocyte infiltration and shear stress on MMP production within the arterial wall.," *Ann. N. Y. Acad. Sci.*, vol. 800, pp. 270–3, Nov. 1996.

[105] J. C. Parodi, J. C. Palmaz, and H. D. Barone, "Transfemoral intraluminal graft implantation for abdominal aortic aneurysms.," *Ann. Vasc. Surg.*, vol. 5, no. 6, pp. 491–9, Nov. 1991.

[106] J. A. Curci, D. Petrinec, S. Liao, L. M. Golub, and R. W. Thompson, "Pharmacologic suppression of experimental abdominal aortic aneurysms: A comparison of doxycycline and four chemically modified tetracyclines," *J. Vasc. Surg.*, vol. 28, no. 6, pp. 1082–1093, Dec. 1998.

[107] S. R. Vallabhaneni and P. . Harris, "Lessons learnt from the EUROSTAR registry on endovascular repair of abdominal aortic aneurysm repair," *Eur. J. Radiol.*, vol. 39, no. 1, pp. 34–41, Jul. 2001.

[108] E. L. Chaikof *et al.*, "The care of patients with an abdominal aortic aneurysm: the Society for Vascular Surgery practice guidelines.," *J. Vasc. Surg.*, vol. 50, no. 4 Suppl, pp. S2-49, Oct. 2009.

[109] M. M. Farooq, J. A. Freischlag, G. R. Seabrook, M. R. Moon, C. Aprahamian, and J. B. Towne, "Effect of the duration of symptoms, transport time, and length of emergency room stay on morbidity and mortality in patients with ruptured abdominal aortic aneurysms," *Surgery*, vol. 119, no. 1, pp. 9–14, Jan. 1996.

[110] The UK Small Aneurysm Trial Participants *et al.*, "Mortality results for randomised controlled trial of early elective surgery or ultrasonographic

surveillance for small abdominal aortic aneurysms.," *Lancet (London, England)*, vol. 352, no. 9141, pp. 1649–55, Nov. 1998.

[111] C. Fleming, E. P. Whitlock, T. L. Beil, and F. A. Lederle, "Screening for Abdominal Aortic Aneurysm: A Best-Evidence Systematic Review for the U.S. Preventive Services Task Force," *Ann. Intern. Med.*, vol. 142, no. 3, p. 203, Feb. 2005.

[112] J. S. Lindholt, S. Juul, H. Fasting, and E. W. Henneberg, "Preliminary Ten Year Results from a Randomised Single Centre Mass Screening Trial for Abdominal Aortic Aneurysm," *Eur. J. Vasc. Endovasc. Surg.*, vol. 32, no. 6, pp. 608–614, Dec. 2006.

[113] Public Health England, "Population screening programmes: NHS abdominal aortic aneurysm (AAA) programme - GOV.UK," *Department of Health*, 2015. [Online]. Available: https://www.gov.uk/topic/population-screening-programmes/abdominal-aortic-aneurysm. [Accessed: 05-Mar-2017].

[114] R. A. P. Scott, S. G. Bridgewater, and H. A. Ashton, "Randomized clinical trial of screening for abdominal aortic aneurysm in women," *Br. J. Surg.*, vol. 89, no. 3, pp. 283–285, Mar. 2002.

[115] J. E. Starr and V. Halpern, "Abdominal aortic aneurysms in women," *Journal of Vascular Surgery*, vol. 57, no. 4 SUPPL. Mosby, p. 3S–10S, 01-Apr-2013.

[116] B. G. DeRubertis *et al.*, "Abdominal aortic aneurysm in women: Prevalence, risk factors, and implications for screening," *J. Vasc. Surg.*, vol. 46, no. 4, p. 630–635.e1, Oct. 2007.

[117] NHS Choices, "Abdominal aortic aneurysm screening - NHS Choices," *NHS choices*, 2014.

[118] H. Hong, Y. Yang, B. Liu, and W. Cai, "Imaging of Abdominal Aortic Aneurysm: the present and the future.," *Curr. Vasc. Pharmacol.*, vol. 8, no. 6, pp. 808–19, Nov. 2010.

[119] PEIR Digital Library, "cross-section- AORTA: Abdominal Aneurysm | PEIR Digital Library," *Pathology Education Instructional Resource (PEIR), University of Alabama at Birmingham, Department of Pathology.* [Online]. Available: http://www.wikidoc.org/index.php/File:Aortic_aneurysm_5.jpg. [Accessed: 20-Feb-2017].

[120] M. G. van der Vaart, R. Meerwaldt, R. H. J. A. Slart, G. M. van Dam, R. A. Tio, and C. J. Zeebregts, "Application of PET/SPECT Imaging in Vascular Disease," *Eur. J. Vasc. Endovasc. Surg.*, vol. 35, no. 5, pp. 507–513, May 2008.

[121] Public Health England, "Abdominal Aortic Aneurysm (AAA) Screening Programme - an important milestone | Public health matters," *Department of Health UK*, 2016. [Online]. Available: https://publichealthmatters.blog.gov.uk/2016/01/06/abdominal-aortic-aneurysm-aaa-screening-programme-an-important-milestone/. [Accessed: 21-Feb-2017].

[122] F. A. Lederle *et al.*, "The aneurysm detection and management study screening program: validation cohort and final results. Aneurysm Detection and Management Veterans Affairs Cooperative Study Investigators.," *Arch. Intern. Med.*, vol. 160, no. 10, pp. 1425–30, May 2000.

[123] L. Beales, S. Wolstenhulme, J. A. Evans, R. West, and D. J. A. Scott, "Reproducibility of ultrasound measurement of the abdominal aorta," *British Journal of Surgery*, vol. 98, no. 11. pp. 1517–1525, Nov-2011.

[124] K. A. A. Wilson, P. R. R. Hoskins, A. J. J. Lee, F. G. R. G. Fowkes, C. V. V

Ruckley, and A. W. W. Bradbury, "Ultrasonic measurement of abdominal aortic aneurysm wall compliance: a reproducibility study.," vol. 31, no. 3, Mar. 2000.

[125] P. Pavone *et al.*, "[Abdominal aortic aneurysms. Comparison of magnetic resonance, ultrasound, CT x-ray and angiography].," *Radiol. Med.*, vol. 76, no. 3, pp. 168–173, 1988.

[126] RSNA, "Ultrasound (Sonography)," *RadiologyInfo.org*. Radiological Society of North America, Inc. (RSNA)., 2016.

[127] P. Pavone *et al.*, "Abdominal aortic aneurysm evaluation: comparison of US, CT, MRI, and angiography.," *Magn. Reson. Imaging*, vol. 8, no. 3, pp. 199–204, 1990.

[128] L. R. Sprouse *et al.*, "Comparison of abdominal aortic aneurysm diameter measurements obtained with ultrasound and computed tomography: is there a difference?," *J. Vasc. Surg.*, vol. 38, no. 3, pp. 466–471, Sep. 2003.

[129] C. P. Ho *et al.*, "Systematic technique-dependent differences in CT versus MRI measurement of the tibial tubercle-trochlear groove distance.," *Am. J. Sports Med.*, vol. 43, no. 3, pp. 675–82, Mar. 2015.

[130] NHS Choices, "CT scan - NHS Choices," 2015.

[131] A. M. Kok *et al.*, "Feasibility of wall stress analysis of abdominal aortic aneurysms using three-dimensional ultrasound," *J. Vasc. Surg.*, vol. 61, no. 5, 2015.

[132] D. Kondziolka *et al.*, "A comparison between magnetic resonance imaging and computed tomography for stereotactic coordinate determination.," *Neurosurgery*, vol. 30, no. 3, pp. 402-6; discussion 406-7, Mar. 1992.

[133] M. Salerno and G. A. Beller, "Noninvasive Assessment of Myocardial

Perfusion," *Circ. Cardiovasc. Imaging*, vol. 2, no. 5, pp. 412–424, Sep. 2009.

[134] C. G. Stirrat, D. E. Newby, J. M. J. Robson, and M. A. Jansen, "The Use of Superparamagnetic Iron Oxide Nanoparticles to Assess Cardiac Inflammation," *Curr. Cardiovasc. Imaging Rep.*, vol. 7, no. 5, p. 9263, May 2014.

[135] Monitor and NHS England, "NHS national tariff payment system for 2014/15 - Consultations - GOV.UK," *NHS Consultations*, 2015. [Online]. Available: https://www.gov.uk/government/consultations/nhs-national-tariff-payment-system-for-2014-to-2015. [Accessed: 29-Dec-2016].

[136] B. J. Klopfenstein, M. S. Kim, C. M. Krisky, J. Szumowski, W. D. Rooney, and J. Q. Purnell, "Comparison of 3 T MRI and CT for the measurement of visceral and subcutaneous adipose tissue in humans.," *Br. J. Radiol.*, vol. 85, no. 1018, pp. e826-30, Oct. 2012.

[137] L. J. Erasmus, D. Hurter, M. Naudé, H. G. Kritzinger, and S. Acho, "A Short Overview of MRI Artefacts," *SA Journal of Radiology*, vol. 8, no. August. pp. 13–17, 2004.

[138] G. Liney, *MRI in clinical practice*. Springer-Verlag, 2006.

[139] J. Enders *et al.*, "Reduction of Claustrophobia with Short-Bore versus Open Magnetic Resonance Imaging: A Randomized Controlled Trial," *PLoS One*, vol. 6, no. 8, p. e23494, Aug. 2011.

[140] M. T. Vlaardingerbroek and J. A. Boer, *Magnetic Resonance Imaging : Theory and Practice*. Springer Berlin Heidelberg, 2003.

[141] C. Westbrook and C. K. Roth, *MRI in practice*. Blackwell Science, 1998.

[142] G. B. Chavhan, P. S. Babyn, B. Thomas, M. M. Shroff, and E. M. Haacke, "Principles, techniques, and applications of T2*-based MR imaging and its

special applications.," *Radiographics*, vol. 29, no. 5, pp. 1433–49, Jan. 2009.

[143] G.-P. Yan, L. Robinson, and P. Hogg, "Magnetic resonance imaging contrast agents: Overview and perspectives," *Radiography*, vol. 13, pp. e5–e19, Dec. 2007.

[144] G. J. Strijkers, W. J. M. Mulder, G. A. F. van Tilborg, and K. Nicolay, "MRI contrast agents: current status and future perspectives.," *Anticancer. Agents Med. Chem.*, vol. 7, no. 3, pp. 291–305, May 2007.

[145] M. H. Mendonça-Dias, E. Gaggelli, and P. C. Lauterbur, "Paramagnetic contrast agents in nuclear magnetic resonance medical imaging.," *Semin. Nucl. Med.*, vol. 13, no. 4, pp. 364–76, Oct. 1983.

[146] A. Bogdanov, M. L. Mazzanti, and M. L. Mazzanti, "Molecular magnetic resonance contrast agents for the detection of cancer: past and present.," *Semin. Oncol.*, vol. 38, no. 1, pp. 42–54, Feb. 2011.

[147] M. Freedman, E. H. Chang, Q. Zhou, and K. F. Pirollo, "Nanodelivery of MRI Contrast Agent Enhances Sensitivity of Detection of Lung Cancer Metastases," *Acad. Radiol.*, vol. 16, no. 5, pp. 627–637, May 2009.

[148] J.-F. Toussaint, G. M. LaMuraglia, J. F. Southern, V. Fuster, and H. L. Kantor, "Magnetic Resonance Images Lipid, Fibrous, Calcified, Hemorrhagic, and Thrombotic Components of Human Atherosclerosis In Vivo," *Circulation*, vol. 94, no. 5, pp. 932–938, Sep. 1996.

[149] M. P. Skinner *et al.*, "Serial magnetic resonance imaging of experimental atherosclerosis detects lesion fine structure, progression and complications in vivo.," *Nat. Med.*, vol. 1, no. 1, pp. 69–73, Jan. 1995.

[150] M. Shinnar *et al.*, "The Diagnostic Accuracy of Ex Vivo MRI for Human Atherosclerotic Plaque Characterization," *Arterioscler. Thromb. Vasc. Biol.*, vol. 19, no. 11, pp. 2756–2761, Nov. 1999.

[151] I. Laitinen *et al.*, "Evaluation of v 3 Integrin-Targeted Positron Emission Tomography Tracer 18F-Galacto-RGD for Imaging of Vascular Inflammation in Atherosclerotic Mice," *Circ. Cardiovasc. Imaging*, vol. 2, no. 4, pp. 331–338, Jul. 2009.

[152] C. M. Kramer, "Magnetic Resonance Imaging Identifies the Fibrous Cap in Atherosclerotic Abdominal Aortic Aneurysm," *Circulation*, vol. 109, no. 8, pp. 1016–1021, Feb. 2004.

[153] Z. Zhang *et al.*, "In vitro imaging of single living human umbilical vein endothelial cells with a clinical 3.0-T MRI scanner," *Magn. Reson. Mater. Physics, Biol. Med.*, vol. 18, no. 4, pp. 175–185, Sep. 2005.

[154] P. Robert, X. Violas, R. Santus, D. Le Bihan, and C. Corot, "Optimization of a blood pool contrast agent injection protocol for MR angiography," *J. Magn. Reson. Imaging*, vol. 21, no. 5, pp. 611–619, May 2005.

[155] A. Saleh, M. Schroeter, C. Jonkmanns, H.-P. Hartung, U. Modder, and S. Jander, "In vivo MRI of brain inflammation in human ischaemic stroke," *Brain*, vol. 127, no. 7, pp. 1670–1677, Jul. 2004.

[156] T. Tang *et al.*, "Assessment of Inflammatory Burden Contralateral to the Symptomatic Carotid Stenosis Using High-Resolution Ultrasmall, Superparamagnetic Iron Oxide-Enhanced MRI," *Stroke*, vol. 37, no. 9, pp. 2266–2270, Sep. 2006.

[157] T. Y. Tang *et al.*, "Comparison of the inflammatory burden of truly asymptomatic carotid atheroma with atherosclerotic plaques contralateral to symptomatic carotid stenosis: an ultra small superparamagnetic iron oxide enhanced magnetic resonance study," *J. Neurol. Neurosurg. Psychiatry*, vol. 78, no. 12, pp. 1337–1343, Dec. 2007.

[158] R. A. Trivedi *et al.*, "Identifying Inflamed Carotid Plaques Using In Vivo USPIO-Enhanced MR Imaging to Label Plaque Macrophages," *Arterioscler.*

Thromb. Vasc. Biol., vol. 26, no. 7, pp. 1601–1606, Jul. 2006.

[159] M. E. Kooi *et al.*, "Accumulation of Ultrasmall Superparamagnetic Particles of Iron Oxide in Human Atherosclerotic Plaques Can Be Detected by In Vivo Magnetic Resonance Imaging," *Circulation*, vol. 107, no. 19, pp. 2453–2458, May 2003.

[160] S. P. S. Howarth *et al.*, "Utility of USPIO-enhanced MR imaging to identify inflammation and the fibrous cap: A comparison of symptomatic and asymptomatic individuals," *Eur. J. Radiol.*, vol. 70, no. 3, pp. 555–560, Jun. 2009.

[161] U. Sadat *et al.*, "Ultrasmall Superparamagnetic Iron Oxide-enhanced Magnetic Resonance Imaging of Abdominal Aortic Aneurysms–A Feasibility Study," *Eur. J. Vasc. Endovasc. Surg.*, vol. 41, no. 2, pp. 167–174, Feb. 2011.

[162] T. Y. Tang *et al.*, "The ATHEROMA (Atorvastatin Therapy: Effects on Reduction of Macrophage Activity) Study," *J. Am. Coll. Cardiol.*, vol. 53, no. 22, pp. 2039–2050, Jun. 2009.

[163] G. H. Turner *et al.*, "Assessment of macrophage infiltration in a Murine model of abdominal aortic aneurysm," *J. Magn. Reson. Imaging*, vol. 30, no. 2, pp. 455–460, Aug. 2009.

[164] C. W. Jung and P. Jacobs, "Physical and chemical properties of superparamagnetic iron oxide MR contrast agents: ferumoxides, ferumoxtran, ferumoxsil.," *Magn. Reson. Imaging*, vol. 13, no. 5, pp. 661–74, 1995.

[165] C. Wilhelm, C. Billotey, J. Roger, J. N. Pons, J.-C. Bacri, and F. Gazeau, "Intracellular uptake of anionic superparamagnetic nanoparticles as a function of their surface coating.," *Biomaterials*, vol. 24, no. 6, pp. 1001–11, Mar. 2003.

[166] S. Aime and P. Caravan, "Biodistribution of gadolinium-based contrast agents, including gadolinium deposition.," *J. Magn. Reson. Imaging*, vol. 30, no. 6, pp. 1259–67, Dec. 2009.

[167] C. Corot, P. Robert, J. Idee, and M. Port, "Recent advances in iron oxide nanocrystal technology for medical imaging☆," *Adv. Drug Deliv. Rev.*, vol. 58, no. 14, pp. 1471–1504, Dec. 2006.

[168] M. Longmire, P. L. Choyke, and H. Kobayashi, "Clearance properties of nano-sized particles and molecules as imaging agents: considerations and caveats.," *Nanomedicine (Lond).*, vol. 3, no. 5, pp. 703–17, Oct. 2008.

[169] R. C. Semelka and T. K. G. Helmberger, "Contrast Agents for MR Imaging of the Liver," *Radiology*, vol. 218, no. 1, pp. 27–38, Jan. 2001.

[170] M. F. Bellin *et al.*, "Lymph node metastases: safety and effectiveness of MR imaging with ultrasmall superparamagnetic iron oxide particles--initial clinical experience.," *Radiology*, vol. 207, no. 3, pp. 799–808, Jun. 1998.

[171] Y.-X. J. Wang, S. M. Hussain, and G. P. Krestin, "Superparamagnetic iron oxide contrast agents: physicochemical characteristics and applications in MR imaging," *Eur. Radiol.*, vol. 11, no. 11, pp. 2319–2331, Nov. 2001.

[172] S. Metz, G. Bonaterra, M. Rudelius, M. Settles, E. Rummeny, and H. Daldrup-Link, "Capacity of human monocytes to phagocytose approved iron oxide MR contrast agents in vitro," *Eur. Radiol.*, vol. 14, no. 10, pp. 1851–8, Oct. 2004.

[173] I. Raynal, P. Prigent, S. Peyramaure, A. Najid, C. Rebuzzi, and C. Corot, "Macrophage Endocytosis of Superparamagnetic Iron Oxide Nanoparticles," *Invest. Radiol.*, vol. 39, no. 1, pp. 56–63, Jan. 2004.

[174] K. Morishige *et al.*, "High-Resolution Magnetic Resonance Imaging Enhanced With Superparamagnetic Nanoparticles Measures Macrophage

Burden in Atherosclerosis," *Circulation*, vol. 122, no. 17, pp. 1707–1715, Oct. 2010.

[175] O. M. B. McBride *et al.*, "MRI using ultrasmall superparamagnetic particles of iron oxide in patients under surveillance for abdominal aortic aneurysms to predict rupture or surgical repair: MRI for abdominal aortic aneurysms to predict rupture or surgery-the MA(3)RS study.," *Open Hear.*, vol. 2, no. 1, p. e000190, Apr. 2015.

[176] C. Wang *et al.*, "Automatic multi-parametric MR registration method using mutual information based on adaptive asymmetric k-means binning," in *Proceedings - International Symposium on Biomedical Imaging*, 2015, vol. 2015–July, pp. 1089–1092.

[177] A. P. Dhawan, "Medical Image Analysis," *Eng. Med. Biol.*, pp. i–xv, Jan. 2011.

[178] R. C. Gonzalez and R. E. Woods, "Image processing," *Digit. image Process.*, vol. 2, 2007.

[179] MA3RS Study Investigators *et al.*, "Aortic Wall Inflammation Predicts Abdominal Aortic Aneurysm Expansion, Rupture, and Need for Surgical Repair," *Circulation*, vol. 136, no. 9, pp. 787–797, Aug. 2017.

[180] A. K. Jain and R. C. Dubes, "Algorithms for clustering data," Jan. 1988.

[181] J. Bible, S. Datta, and S. Datta, *Informatics for Materials Science and Engineering*. Elsevier, 2013.

[182] A. K. Jain, "Data clustering: 50 years beyond K-means," *Pattern Recognit. Lett.*, vol. 31, no. 8, pp. 651–666, Jun. 2010.

[183] K. Krippendorff, "Clustering," *Multivariate Techniques in Human Communication Researc*. pp. 259–308, 1980.

[184] A. K. Jain, M. N. Murty, and P. J. Flynn, "Data clustering: a review," *ACM*

Comput. Surv., vol. 31, no. 3, pp. 264–323, Sep. 1999.

[185] A. K. Jain and R. Dubes, "Feature definition in pattern recognition with small sample size," *Pattern Recognit.*, vol. 10, no. 2, pp. 85–97, 1978.

[186] F. E. Eric, F. E. Eric, F. Gibou, and R. Fedkiw, "A Fast Hybrid k-Means Level Set Algorithm For Segmentation," *4TH Annu. HAWAII Int. Conf. Stat. Math.*, pp. 281--291, 2002.

[187] S. N. Sulaiman, N. A. Non, I. S. Isa, and N. Hamzah, "Segmentation of brain MRI image based on clustering algorithm," in *2014 IEEE Symposium on Industrial Electronics & Applications (ISIEA)*, 2014, pp. 60–65.

[188] H. Verma, R. K. Agrawal, and N. Kumar, "Improved fuzzy entropy clustering algorithm for MRI brain image segmentation," *Int. J. Imaging Syst. Technol.*, vol. 24, no. 4, pp. 277–283, Dec. 2014.

[189] H. P. Ng, S. H. Ong, K. W. C. Foong, P. S. Goh, and W. L. Nowinski, "Medical Image Segmentation Using K-Means Clustering and Improved Watershed Algorithm," in *2006 IEEE Southwest Symposium on Image Analysis and Interpretation*, 2006, pp. 61–65.

[190] W. Cai, S. Chen, and D. Zhang, "Fast and robust fuzzy c-means clustering algorithms incorporating local information for image segmentation," *Pattern Recognit.*, vol. 40, no. 3, pp. 825–838, Mar. 2007.

[191] L.-H. Juang and M.-N. Wu, "MRI brain lesion image detection based on color-converted K-means clustering segmentation," *Measurement*, vol. 43, no. 7, pp. 941–949, Aug. 2010.

[192] A. Gupta and G. Pahuja, "Hybrid Clustering And Boundary Value Refinement for Tumor Segmentation using Brain MRI," *IOP Conf. Ser. Mater. Sci. Eng.*, vol. 225, no. 1, p. 012187, Aug. 2017.

[193] E. Abdel-Maksoud, M. Elmogy, and R. Al-Awadi, "Brain tumor segmentation based on a hybrid clustering technique," *Egypt. Informatics J.*, vol. 16, no. 1, pp. 71–81, 2015.

[194] S. C. L. Deoni, B. K. Rutt, A. G. Parrent, and T. M. Peters, "Segmentation of thalamic nuclei using a modified k-means clustering algorithm and high-resolution quantitative magnetic resonance imaging at 1.5 T," *Neuroimage*, vol. 34, no. 1, pp. 117–126, 2007.

[195] D. Feng and C. Wu, "Advances in cryptography and information security-introduction of 2002-2006 progress of SKLOIS," *Front. Comput. Sci. China*, vol. 1, no. 4, pp. 385–396, 2007.

[196] S. W. Farraher, H. Jara, K. J. Chang, A. Hou, and J. A. Soto, "Liver and Spleen Volumetry with Quantitative MR Imaging and Dual-Space Clustering Segmentation," *Radiology*, vol. 237, no. 1, pp. 322–328, Oct. 2005.

[197] S. Nandagopalan, B. S. Adiga, C. Dhanalakshmi, and N. Deepak, "Automatic Segmentation and Ventricular Border Detection of 2D Echocardiographic Images Combining K-Means Clustering and Active Contour Model," in *2010 Second International Conference on Computer and Network Technology*, 2010, pp. 447–451.

[198] T. A. Reddy, "Chapter 8: Classification and Clustering Methods," in *Applied Data Analysis and Modeling for Energy Engineers and Scientists*, 2011, pp. 231–251.

[199] T. Pang-Ning, M. Steinbach, and V. Kumar, "Introduction to data mining," *Libr. Congr.*, p. 796, 2006.

[200] D. T. Pham, S. S. Dimov, and C. D. Nguyen, "Selection of K in K-means clustering," *Proceedings of the Institution of Mechanical Engineers, Part C: Journal of Mechanical Engineering Science*, vol. 219, no. 1. pp. 103–119, 2005.

[201] C. Fraley, "How Many Clusters? Which Clustering Method? Answers Via Model-Based Cluster Analysis," *Comput. J.*, vol. 41, no. 8, pp. 578–588, Aug. 1998.

[202] P. S. Bradley and U. M. Fayyad, "Refining Initial Points for K-Means Clustering," pp. 91–99, Jul. 1998.

[203] M. Steinbach, L. Ertoz, and V. Kumar, "The Challenges of Clustering High Dimensional Data," in *New Directions in Statistical Physics*, 2004, pp. 273–309.

[204] G. Kumar and P. K. Bhatia, "A Detailed Review of Feature Extraction in Image Processing Systems," in *2014 Fourth International Conference on Advanced Computing & Communication Technologies*, 2014, pp. 5–12.

[205] I. Guyon, S. Gunn, M. Nikravesh, and L. A. Zadeh, "Feature Extraction: Foundations and Applications (Studies in Fuzziness and Soft Computing)," Aug. 2006.

[206] H. Liu and H. Motoda, *Feature Selection for Knowledge Discovery and Data Mining*. Boston, MA: Springer US, 1998.

[207] O. Carugo, "Proximity measures for cluster analysis.," *Methods Mol. Biol.*, vol. 609, pp. 163–74, Jan. 2010.

[208] E. Diday and J. C. Simon, "Clustering Analysis," in *Communication and Cybernetics*, K. S. Fu, Ed. Sprin\-ger-Ver\-lag, 1976.

[209] M. R. Anderberg, *Cluster Analysis for Applications*. Elsevier, 1973.

[210] T. S. Madhulatha, "An Overview on Clustering Methods," *IOSR J. Eng.*, vol. 2, no. 4, pp. 719–725, 2012.

[211] M. M. Deza and E. Deza, *Encyclopedia of distances*. Springer Berlin Heidelberg, 2009.

[212] J. Mao and A. K. Jain, "A self-organizing network for hyperellipsoidal clustering (HEC).," *IEEE Trans. Neural Netw.*, vol. 7, no. 1, pp. 16–29, Jan. 1996.

[213] The MathWorks Inc., "Statistics and Machine Learning Toolbox: User's Guide (R2016b)," Natick, Massachusetts, 2016.

[214] T. Fawcett, "An introduction to ROC analysis," *Pattern Recognit. Lett.*, vol. 27, no. 8, pp. 861–874, Jun. 2006.

[215] D. G. Altman and J. M. Bland, "Diagnostic tests. 1: Sensitivity and specificity.," *BMJ*, vol. 308, no. 6943, p. 1552, Jun. 1994.

[216] P.-N. Tan, M. Steinbach, and V. Kumar, "Chap 8 : Cluster Analysis: Basic Concepts and Algorithms," *Introd. to Data Min.*, p. Chapter 8, 2005.

[217] M. E. Celebi and H. A. Kingravi, "DETERMINISTIC INITIALIZATION OF THE K-MEANS ALGORITHM USING HIERARCHICAL CLUSTERING," *Int. J. Pattern Recognit. Artif. Intell.*, vol. 26, no. 07, p. 1250018, Nov. 2012.

[218] U. M. F. Paul S. Bradley, "Refining Initial Points for K-Means Clustering."

[219] M. El Agha and W. M. Ashour, "Efficient and Fast Initialization Algorithm for K-means Clustering," *Int. J. Intell. Syst. Appl.*, vol. 4, no. 1, p. 21, 2012.

[220] M. Fawcett, "Histogram Analysis to Choose the Number of Clusters for K Means, lecture notes," Dept. of Computer Science and Engineering University of South Carolina, 2015.

[221] A. Long, L. Rouet, J. S. Lindholt, and E. Allaire, "Measuring the Maximum Diameter of Native Abdominal Aortic Aneurysms: Review and Critical Analysis," *Eur. J. Vasc. Endovasc. Surg.*, vol. 43, no. 5, pp. 515–524, 2012.

[222] B. J. Manning, T. Kristmundsson, B. Sonesson, and T. Resch, "Abdominal aortic aneurysm diameter: A comparison of ultrasound measurements

with those from standard and three-dimensional computed tomography reconstruction," *J. Vasc. Surg.*, vol. 50, no. 2, pp. 263–268, Aug. 2009.

[223] J. T. Powell, R. M. Greenhalgh, C. V Ruckley, and F. G. Fowkes, "The UK Small Aneurysm Trial.," *Ann. N. Y. Acad. Sci.*, vol. 800, pp. 249–51, Nov. 1996.

[224] The UK Small Aneurysm Trial Participants, "The U.K. small aneurysm trial: Design, methods and progress," *Eur. J. Vasc. Endovasc. Surg.*, vol. 9, no. 1, pp. 42–48, Jan. 1995.

[225] M. Ellis, J. T. Powell, and R. M. Greenhalgh, "Limitations of ultrasonography in surveillance of small abdominal aortic aneurysms.," *Br. J. Surg.*, vol. 78, no. 5, pp. 614–6, May 1991.

[226] M. P. Nevitt, D. J. Ballard, and J. W. Hallett, "Prognosis of Abdominal Aortic Aneurysms," *N. Engl. J. Med.*, vol. 321, no. 15, pp. 1009–1014, Oct. 1989.

[227] Multicentre Aneurysm Screening Study Group, "The Multicentre Aneurysm Screening Study (MASS) into the effect of abdominal aortic aneurysm screening on mortality in men: a randomised controlled trial.," *Lancet (London, England)*, vol. 360, no. 9345, pp. 1531–9, Nov. 2002.

[228] Y. Watanabe, H. Shigematsu, Y. Obitsu, N. Koizumi, N. Saiki, and T. Iwahashi, "Growth rates of abdominal aortic aneurysms in Japanese patients observed in one institute.," *Int. Angiol.*, vol. 31, no. 2, pp. 181–6, Apr. 2012.

[229] W. Karrowni, S. Dughman, G. P. Hajj, F. J. Miller, and Jr., "Statin therapy reduces growth of abdominal aortic aneurysms.," *J. Investig. Med.*, vol. 59, no. 8, pp. 1239–43, Dec. 2011.

[230] G. Martufi *et al.*, "Multidimensional growth measurements of abdominal aortic aneurysms," *J. Vasc. Surg.*, vol. 58, no. 3, pp. 748–755, Sep. 2013.

[231] M. Lindquist Liljeqvist, R. Hultgren, T. C. Gasser, and J. Roy, "Volume growth of abdominal aortic aneurysms correlates with baseline volume and increasing finite element analysis-derived rupture risk," *J. Vasc. Surg.*, vol. 63, no. 6, p. 1434–1442.e3, Jun. 2016.

[232] A. Delin, H. Ohlsén, and J. Swedenborg, "Growth rate of abdominal aortic aneurysms as measured by computed tomography," *Br. J. Surg.*, vol. 72, no. 7, pp. 530–532, Jul. 1985.

[233] M. J. Sweeting, S. G. Thompson, L. C. Brown, J. T. Powell, and RESCAN collaborators, "Meta-analysis of individual patient data to examine factors affecting growth and rupture of small abdominal aortic aneurysms," *Br. J. Surg.*, vol. 99, no. 5, pp. 655–665, May 2012.

[234] N. Kontopodis, S. Lioudaki, D. Pantidis, G. Papadopoulos, E. Georgakarakos, and C. V Ioannou, "Advances in determining abdominal aortic aneurysm size and growth," vol. 8, no. 2, Feb. 2016.

[235] K. Bredahl *et al.*, "Volume estimation of the aortic sac after EVAR using 3-D ultrasound-A novel, accurate and promising technique," *Eur. J. Vasc. Endovasc. Surg.*, vol. 45, no. 5, 2013.

[236] K. A. Vardulaki *et al.*, "Growth rates and risk of rupture of abdominal aortic aneurysms," *Br. J. Surg.*, vol. 85, no. 12, pp. 1674–1680, Dec. 1998.

[237] P. Jaakkola, M. Hippeläinen, P. Farin, H. Rytkönen, S. Kainulainen, and K. Partanen, "Interobserver variability in measuring the dimensions of the abdominal aorta: Comparison of ultrasound and computed tomography," *Eur. J. Vasc. Endovasc. Surg.*, vol. 12, no. 2, pp. 230–237, Aug. 1996.

[238] F. A. Lederle *et al.*, "Variability in measurement of abdominal aortic aneurysms," *J. Vasc. Surg.*, vol. 21, no. 6, pp. 945–952, Jun. 1995.

[239] L. . Sprouse, G. . Meier, F. . Parent, R. . DeMasi, M. . Glickman, and G. .

Barber, "Is Ultrasound More Accurate than Axial Computed Tomography for Determination of Maximal Abdominal Aortic Aneurysm Diameter?," *Eur. J. Vasc. Endovasc. Surg.*, vol. 28, no. 1, pp. 28–35, Jul. 2004.

[240] A. Wanhainen, D. Bergqvist, and M. Björck, "Measuring the Abdominal Aorta with Ultrasonography and Computed Tomography – Difference and Variability," *Eur. J. Vasc. Endovasc. Surg.*, vol. 24, no. 5, pp. 428–434, Nov. 2002.

[241] F. J. Foo *et al.*, "Agreement between Computed Tomography and Ultrasound on Abdominal Aortic Aneurysms and Implications on Clinical Decisions," *Eur. J. Vasc. Endovasc. Surg.*, vol. 42, no. 5, pp. 608–614, Nov. 2011.

[242] K. W. H. W. H. Chiu, L. Ling, V. Tripathi, M. Ahmed, and V. Shrivastava, "Ultrasound measurement for abdominal aortic aneurysm screening: A direct comparison of the three leading methods," *Eur. J. Vasc. Endovasc. Surg.*, vol. 47, no. 4, pp. 367–373, Apr. 2014.

[243] E. Di Cesare *et al.*, "CT and MR imaging of the thoracic aorta," *Open Med.*, vol. 11, no. 1, Jan. 2016.

[244] T. Saida *et al.*, "Prospective intraindividual comparison of unenhanced magnetic resonance imaging vs contrast-enhanced computed tomography for the planning of endovascular abdominal aortic aneurysm repair," *J. Vasc. Surg.*, vol. 55, no. 3, pp. 679–687, Mar. 2012.

[245] Public Health England, "AAA screening: standard operating procedures - Publications," 2015. [Online]. Available: https://www.gov.uk/government/publications/aaa-screening-standard-operating-procedures.

[246] J. Jacomelli, "Pathway Standards for NHS Abdominal Aortic Aneurysm Screening Programme Public Health England leads the NHS Screening

Programmes," 2016.

[247] Y. Rubner, C. Tomasi, and L. L. J. Guibas, "The Earth Mover's Distance as a Metric for Image Retrieval," *Int. J. Comput. Vis.*, vol. 40, no. 2, pp. 99–121, Nov. 2000.

[248] H. Ling and K. Okada, "An efficient Earth Mover's Distance algorithm for robust histogram comparison.," *IEEE Trans. Pattern Anal. Mach. Intell.*, vol. 29, no. 5, pp. 840–53, May 2007.

[249] O. Pele and M. Werman, "Fast and robust earth mover's distances," *Comput. vision, 2009 IEEE 12th …*, pp. 460–467, Sep. 2009.

[250] F. Lampariello, "On the use of the Kolmogorov-Smirnov statistical test for immunofluorescence histogram comparison," *Cytometry*, vol. 39, no. 3, pp. 179–188, Mar. 2000.

[251] I. T. Young, "Proof without prejudice: use of the Kolmogorov-Smirnov test for the analysis of histograms from flow systems and other sources.," *J. Histochem. Cytochem.*, vol. 25, no. 7, pp. 935–41, Jul. 1977.

[252] The MathWorks Inc, "Measure properties of image regions - MATLAB regionprops - MathWorks United Kingdom," *MATLAB Doc.*, 2018.

[253] J. Golledge, P. S. Tsao, R. L. Dalman, and P. E. Norman, "Circulating markers of abdominal aortic aneurysm presence and progression.," *Circulation*, vol. 118, no. 23, pp. 2382–92, Dec. 2008.

[254] R. C. Darling, C. R. Messina, D. C. Brewster, and L. W. Ottinger, "Autopsy study of unoperated abdominal aortic aneurysms. The case for early resection.," *Circulation*, vol. 56, no. 3 Suppl, pp. II161-4, Sep. 1977.

[255] R. O. Forsythe, D. E. Newby, and J. M. J. Robson, "Monitoring the biological activity of abdominal aortic aneurysms *Beyond Ultrasound*," *Heart*, vol.

102, no. 11, pp. 817–824, Jun. 2016.

[256] A. Wanhainen, K. Mani, and J. Golledge, "Surrogate Markers of Abdominal Aortic Aneurysm ProgressionSignificance," *Arterioscler. Thromb. Vasc. Biol.*, vol. 36, no. 2, pp. 236–244, Feb. 2016.

[257] S. B. Green, "How Many Subjects Does It Take To Do A Regression Analysis," *Multivariate Behav. Res.*, vol. 26, no. 3, pp. 499–510, Jul. 1991.

[258] B. G. Tabachnick and L. S. Fidell, *Using multivariate statistics, 5th ed.* Boston, MA: Allyn & Bacon/Pearson Education, 2007.

[259] B. J. Doyle, T. M. McGloughlin, K. Miller, J. T. Powell, and P. E. Norman, "Regions of high wall stress can predict the future location of rupture of abdominal aortic aneurysm," *Cardiovasc. Intervent. Radiol.*, vol. 37, no. 3, 2014.

[260] E. Di Martino *et al.*, "Biomechanics of abdominal aortic aneurysm in the presence of endoluminal thrombus: Experimental characterisation and structural static computational analysis," *Eur. J. Vasc. Endovasc. Surg.*, vol. 15, no. 4, pp. 290–299, Apr. 1998.

[261] C. G. Stirrat *et al.*, "Ferumoxytol-enhanced magnetic resonance imaging in acute myocarditis.," *Heart*, vol. 104, no. 4, pp. 300–305, Feb. 2018.

[262] S. R. Alam *et al.*, "Nanoparticle enhanced MRI scanning to detect cellular inflammation in experimental chronic renal allograft rejection.," *Int. J. Mol. Imaging*, vol. 2015, p. 507909, 2015.

[263] S. R. Alam *et al.*, "Perioperative elafin for ischaemia-reperfusion injury during coronary artery bypass graft surgery: a randomised-controlled trial.," *Heart*, vol. 101, no. 20, pp. 1639–45, Oct. 2015.

[264] N. Conlisk *et al.*, "Exploring the Biological and Mechanical Properties of

Abdominal Aortic Aneurysms Using USPIO MRI and Peak Tissue Stress: A Combined Clinical and Finite Element Study," *J. Cardiovasc. Transl. Res.*, Aug. 2017.